



HAL
open science

Studies of interactions between ions in ionic liquids electrolytes by nuclear magnetic resonance

Pierre Martin

► **To cite this version:**

Pierre Martin. Studies of interactions between ions in ionic liquids electrolytes by nuclear magnetic resonance. Other. Université d'Orléans, 2018. English. NNT : 2018ORLE2044 . tel-02165130

HAL Id: tel-02165130

<https://theses.hal.science/tel-02165130>

Submitted on 25 Jun 2019

HAL is a multi-disciplinary open access archive for the deposit and dissemination of scientific research documents, whether they are published or not. The documents may come from teaching and research institutions in France or abroad, or from public or private research centers.

L'archive ouverte pluridisciplinaire **HAL**, est destinée au dépôt et à la diffusion de documents scientifiques de niveau recherche, publiés ou non, émanant des établissements d'enseignement et de recherche français ou étrangers, des laboratoires publics ou privés.

ÉCOLE DOCTORALE
ENERGIE, MATERIAUX, SCIENCES DE LA TERRE ET DE L'UNIVERS

Laboratoire CEMHTI – UPR 3079 CNRS

THÈSE présentée par :
Pierre Martin

soutenue le : **12 Décembre 2018**

pour obtenir le grade de : **Docteur de l'université d'Orléans**

Discipline/ Spécialité : Chimie

**Studies of the interactions between ions in
ionic liquids electrolytes by nuclear magnetic
resonance**

THÈSE dirigée par :

Michaël DESCHAMPS
Maria FORSYTH
Luke O'DELL

Professor, Université d'Orléans, CNRS-CEMHTI
Professor, Deakin University
Senior lecturer, Deakin University

RAPPORTEURS :

Melanie BRITTON
Monika SCHOENHOFF

Senior Lecturer, University of Birmingham
Professor, Institut für Physikalische Chemie

JURY:

Melanie BRITTON
Michaël DESCHAMPS
Fabien FERRAGE
Maria FORSYTH
Luke O'DELL
Dominique MASSIOT
Monika SCHOENHOFF

Senior Lecturer, University of Birmingham
Professor, Université d'Orléans, CNRS-CEMHTI
Directeur de recherche, CNRS, ENS Chimie
Professor, Deakin University
Senior lecturer, Deakin University
Directeur de recherche, CNRS-CEMHTI
Professor, Institut für Physikalische Chemie

Acknowledgement

This co-supervising PhD project was conducted between France and Australia.

Firstly I would like to acknowledge both laboratory directors, Catherine Bessada and Franck Fayon in France, and Maria Forsyth in Australia, but also Deakin university and "Région centre Val de Loire", for the financial support.

Secondly, I would like to thank a lot my supervisors, Michael Deschamps, Maria Forsyth and Luke O'Dell, to have, first of all, believed in me and gave me the opportunity to carry on my PhD project, but also to have helped me out during this tiring life experience while enduring constant door knocking and questions.

A particular thought goes to Elodie Salager, which was my first internship supervisor, but also the first to welcome me at the CEMHTI lab.

It is with sincere emotion that I thank my chemistry High school teacher Jerome Cassiot, as it is due to his teaching and his passion for Physics and chemistry that I carried out these studies, up to the PhD.

As this PhD was conducted with multiple international collaboration, I'm addressing a big thanks to Prof Lou Madsen from Virginia Tech University for welcoming me in his team for 5 weeks. And also to Dr Frédéric Mentink-Vigier to have welcomed me for few weeks at the MagLab institute in Florida (I acknowledge the Maglab for their financial support also!)

I would like to address my deep appreciation to the jury members, Melanie Britton, Fabien Ferrage and Dominique Massiot to have accepted to come and listen to my defence. But also to my reviewers which weren't at the defence, but

who took the time to read my work and gave me fruitful feedback, Monika Schönhoff, Jean Le Bideau and Jason Harper.

Obviously, these three years of work, wouldn't be possible without a good team. Thus I would like to thanks colleagues from the CEMHTI, such as Pierre Florian for his fruitful discussion, but also Aydar Rakhmatullin and Vincent Sarou-Kanian (Sorry for the Dewar!). But also thanks colleagues from Deakin, Haijin Zhu for the NMR discussion, but also Ruhamah Yunis for the help with sample preparation, Fangfang Chen with the MD simulation, Urbi Pal for the help on experiments and also Matthias Hilder.

I would like also to thanks colleagues/friends who were by my side during this. Frédéric Deschêne-Allard, Kelly Machado, Abel Danezan, Charles-Emmanuel Dutoit, Marion Maravat, Vania Lourenco, Ludivine Afonso de Araujo, Marianna Porcino, Ghenima Oukali, Alexey Novikov, Andrew Basile, and much more. And friends, Joan Milon and Marie-Paule Sénié. But also everyone one who was at my side near or far!

Of course I would like to express a big thanks to my family, my brother and my sister, but even more to my parents, who believed in me, and always pushed me higher and to whom I dedicate this work.

Finally, every time a story is ending, a new one begins, thus I would like to thank Charlotte Monteiro to have supported me during these past years, and even more during the thesis writing and to have accepted to be my life partner for the next story.

Thanks to readers who have the courage to read this work,

and good luck!

Table of contents

Table of contents	5
List of figures.....	1
List of tables	1
Introduction	1
Chapter 1 Literature review.....	3
Overview	5
1.I.1 Lithium batteries.....	5
1.I.2 Ionic liquids as electrolytes.....	6
1.I.3 Structure and nanostructure in ionic liquids	7
1.I.4 Recent studies of liquid structure and speciation in ILs	8
1.II Characterization of ILs using NMR spectroscopy.....	10
1.II.1 Relaxation measurements	10
1.II.2 Diffusion.....	14
1.II.3 HOESY	19
1.II.4 ENMR	29
1.II.5 DNP	33
1.III Conclusion and perspectives.....	36
Chapter 2 Experimental NMR theory and methodology.....	37
2.I Introduction	39
2.II T_1 spin lattice relaxation.....	43
2.III Relaxation theory	44
2.III.1 Spectral density	44
2.III.2 Longitudinal relaxation against temperature.....	45
2.III.3 Transverse relaxation against temperature	46
2.III.4 Different relaxation interactions	47
2.IV Structural experiments.....	51
2.IV.1 Spin Echoes	51
2.IV.2 HMQC.....	53
2.IV.3 HSQC	54
2.IV.4 Diffusion measurements	55

2.IV.5	The Nuclear Overhauser Effect.....	57
2.IV.6	The NOESY experiments	59
2.IV.7	The HOESY experiment.....	61
2.IV.8	ENMR experiments	64
2.IV.9	DNP experiments	69
Chapter 3	Experimental details	73
3.I	Sample preparation.....	75
3.II	Diffusion measurements	75
3.III	Longitudinal relaxation (T1) measurements.....	76
3.IV	Molecular dynamics simulation details.....	76
3.V	DNP experiments	77
3.V.1	Sample preparation	77
3.V.2	NMR experimental details	77
Chapter 4	Results and discussion	79
PART 1:	Development of an automatic data fitting procedure	81
4.1.I	HOESY analysis method.....	83
4.1.I.1	The need for an improved equation for fitting the full HOESY build-up curve.....	83
4.1.I.2	Intensity decay due to diffusion	87
4.1.I.3	Extracting quantitative cross relaxation rates.....	90
4.1.I.4	Fitting code using Maple	93
4.1.I.5	Experimental time optimization	98
4.1.II	Conclusions.....	104
	Part 2: <i>N</i> -methyl- <i>N</i> -propyl pyrrolidinium bis(fluorosulfonyl)imide mixed with lithium bis(fluorosulfonyl)imide.....	105
4.2.I	Spin lattice relaxation.....	107
4.2.I.1	Spin lattice relaxation for ¹ H nuclei	109
4.2.I.2	Spin lattice relaxation for ¹⁹ F nuclei	114
4.2.I.3	Spin lattice relaxation for ⁷ Li nuclei	115
4.2.II	NOESY H-H measurements.....	117
4.2.III	Cross relaxation rates measurements.....	119
4.2.III.1	¹ H- ⁷ Li HOESY experiments	119

4.2.III.2	^1H - ^{19}F HOESY experiments.....	123
4.2.IV	Interpreting the cross-relaxation values in terms of spatial proximities.....	127
4.2.IV.1	Model A: Fluctuation of the intermolecular dipolar interaction with a single correlation time and a fixed distance, the strong ion pairing case	127
4.2.IV.2	Model B: Hard sphere model and distance of closest approach.....	129
4.2.IV.3	Model C: Inter molecular dipolar spin pair transfer: short to long range NOE	130
4.2.V	Application of these models to the HOESY data	131
4.2.V.1	^1H - ^7Li HOESY experiments	131
4.2.V.2	^1H - ^{19}F HOESY experiments.....	134
4.2.VI	Comparison with Molecular Dynamics simulations	139
4.2.VI.1	Cation-Cation interactions.....	139
4.2.VI.2	Cation-anion interactions	141
4.2.VII	Conclusions.....	144
Part 3:	Influence of ionic liquid cation structure	147
4.3.I	Effect of an additional carbon group on the alkyl chain	150
4.3.I.1	^1H - ^7Li HOESY experiments	150
4.3.I.2	^1H - ^{19}F HOESY experiments.....	151
4.3.II	Effect of an additional carbon group on the cycle	152
4.3.II.1	^1H peak assignment	152
4.3.II.2	^1H - ^7Li HOESY experiments	155
4.3.III	Effect of a methoxy group at the end of the alkyl chain	156
4.3.III.1	^1H - ^7Li HOESY experiments	156
4.3.III.2	^1H - ^{19}F HOESY experiments.....	157
4.3.III.3	Comparison with Molecular dynamics	159
4.3.IV	Conclusions.....	163
Part 4:	Structural studies of solid state <i>N</i> -methyl- <i>N</i> -propyl pyrrolidinium bis(fluorosulfonyl)imide mixed with lithium	165
4.4.I	DNP.....	167
4.4.I.1	Universal curve fitting.....	170
4.4.I.2	BS-REDOR curve fitting	173
4.4.I.3	Comparison with molecular dynamics	175
4.4.II	Comparison with HOESY.....	177

4.4.III	Conclusions.....	177
Chapter 5	Conclusions and outlook.....	179
5.I	Conclusions	181
5.I.1	An improved HOESY build-up curve fitting method	181
5.I.2	Quantitative comparison of cross-relaxation rates in ionic liquids.....	181
5.I.3	Correlating cross-relaxation rates with molecular dynamics simulations ...	182
5.I.4	Qualitative comparison with glassy state studies	182
5.II	Future work.....	183
5.II.1	Comparison with ^7Li - ^{19}F HOESY experiments	183
5.II.2	More accurate calculation of the spectral densities	184
5.II.3	Studies of the cross relaxation rate as a function of temperature	184
5.II.4	Developing ^{13}C - ^{23}Na REAPDOR experiments	185
5.II.5	Correlation with ENMR spectroscopy	185
	Bibliography	203

List of figures

Figure 1-1: Ragone chart showing the power and energy densities of various energy storage technologies. (Encarnaciòn Raymundo-Piñero talk).....	2
Figure 1-1: Illustration of a classical lithium-ion battery	5
Figure 1-2 : Examples of cations (on the left) and anions (on the right) which can be combined in order to make ionic liquids ⁹	6
Figure 1-3: The structure of the diethylimidazolium cation	7
Figure 1-4: Arrhenius plot of the ionic conductivity versus inverse temperature for P ₂₂₂₄ FSA, P ₂₂₂₅ FSA and P ₂₂₂₅ TFSA ⁵¹	9
Figure 1-5: Arrhenius plot of the conductivity versus inverse temperature for phosphonium based ionic liquids containing a methoxy group ⁵¹	9
Figure 1-6: Arrhenius plots of (a) ⁷ Li T ₁ and (b) the τ _c (Li) for C ₃ mpyr -TFSA-Li (black) and C ₃ mpyr -FSA-Li (blue). Lines show fits to BPP theory ⁵⁶	12
Figure 1-7 : a) ¹ H, b) ²³ Na and c) ¹⁹ F T ₁ relaxation times as a function of inverse temperature for the pure IL and the lowest and highest NaTFSI concentrations (0.2 and 2.0 mol.kg ⁻¹). The error bars are contained within the size of the data points. Lines show fits to BPP theory ⁵⁷	13
Figure 1-8: Arrhenius plots of the ion diffusion coefficients of the binary systems for a) C ₃ mpyr-FSI-Li and b) C ₃ mpyr-TFSI-Li. For comparison, <i>D</i> values of the neat P ₁₃ -FSA and P ₁₃ -TFSI samples are included in empty symbols	16
Figure 1-9 : Diffusivity of the different nuclei in P _{111i4} FSI as a function of LiFSI concentration at 22°C ⁷² , ¹ H nuclei for the cation, ¹⁹ F for the anion and ⁷ Li for the lithium cation.....	17
Figure 1-10: Ionicity plot of P _{111i4} FSI and various Li FSI concentrations at 22°C with the ideal molar conductivity presented as a block line. ⁷²	18
Figure 1-11: Contour plots of { ¹ H- ¹⁹ F} (top) and { ¹ H- ⁷ Li} (bottom) HOESY NMR spectra. The horizontal spectrum at the top shows the ¹ H NMR spectrum and C ₄ mpyr molecule labelled on the right. ⁷⁰ ...	20
Figure 1-12: { ¹ H- ¹⁹ F} HOESY build-up curves for C ₃ mpyrTFSI (left) and [LiTFSI] _{0.1} [C ₃ mpyrTFSI] _{0.9} (right). ¹⁷	21
Figure 1-13: Linear fit of HOESY intensities for C ₃ mpyrTFSI (left) and [LiTFSI] _{0.1} [C ₃ mpyrTFSI] _{0.9} (right). ¹⁷	21
Figure 1-14: Illustration of the normalized { ¹ H- ¹⁹ F} HOESY interaction strengths for C ₃ mpyrTFSI (left) and [LiTFSI] _{0.1} [C ₃ mpyrTFSI] _{0.9} (right) ¹⁷	22

Figure 1-15: Mathematical fits of the relative signal intensities for the H-2 proton of neat [Bmim] BF ₄ , corresponding to three different equation ⁸³	23
Figure 1-16: General assignment of the protons for imidazolium ⁸⁰	24
Figure 1-17: Relative cross relaxation rates between the protons and the ¹⁹ F nuclei on the anion. In each case the strongest interaction (H-2) has been used for normalization. * Unrealistic high value, most possibly due to an experimental error. ⁸⁰	25
Figure 1-18: ⁷ Li- ¹ H HOESY spectrum of N ₁₁₁₆ TFSI + LiTFSI measured at 313 K. ⁷ Li and ¹ H spectra are presented as 1D traces, with assignments (mixing time = 500 ms, T = 313 K). Inset: build-up magnetization for ammonium CH ₃ N site and EC site normalized by the effective number of hydrogens on each site. ⁵⁰	26
Figure 1-19: Representation and general assignment of different ions, Left: C ₄ mpyr cation. Right: TFSI- (top), BETI- (middle), and IM ₁₄ - (bottom) anions ²⁸	27
Figure 1-20: Contour plot of the ¹ H- ¹⁹ F HOESY experiment to C ₄ mpyr TFSI. Atom numbering according to Figure 1-19. ²⁸	27
Figure 1-21: Contour plot of the ¹ H- ¹⁹ F HOESY experiment on C ₄ mpyr BETI. Atom numbering according to Figure 1-19. ²⁸	28
Figure 1-22: Graphical sketch of the normalized { ¹ H- ⁷ Li}NOE intensity for the two mixtures 0.9 C ₃ mpyrTFSI-0.1 LiTFSI (left, PY9101) and 0.9 C ₃ mpyrFSI-0.1 LiTFSI (right, PY9191). The results for the intermediate composition 0.3 C ₃ mpyrTFSI-0.6 C ₃ mpyrFSI-0.1 LiTFSI (PY9461, central panel) are also reported. The numbers correspond to the extracted cross relaxation rates from the linear fitting. The shaded volumes are proportional to the “probability of presence” of the lithium atoms. The red color indicates normalized intensity values greater than 0.5. ¹⁷	29
Figure 1-23: Classical cell design with insulators for the electric cables (left) ⁹⁸ , similar cell design but with capillaries and shrink tubes in order to avoid the convection (right) ⁹⁷	31
Figure 1-24: Phase in dependence on the gradient strength in 0.25 mol L ⁻¹ LiBF ₄ /EmimBF ₄ for (a) ¹ H, (b) ¹⁹ F and (c) ⁷ Li with Δ _{Drift} = 300 ms for all nuclei. Errors are estimated at ± 3°. The red line results from a linear regression. ¹⁰⁰	32
Figure 1-25 : The electrophoretic mobility in (a) LiTFSA/EmimTFSA and (b) LiBF ₄ /EmimBF ₄ in dependence of the lithium salt concentration. Black squares: ¹ H, red circles: ¹⁹ F, blue triangles: ⁷ Li. Error bars are calculated from the standard deviation ¹⁰⁰	33
Figure 1-26: a) TEKpol bi radical and b) TOTAPOL bi radical molecular representation	34

Figure 1-27: Schematic polarization build-up curves derived from the Schematic polarization build-up curves derived from the analytical solution of the Solomon equations in the case of: a) either one of two non-interacting two-spin systems (each comprising a different nuclear spin but a common electron spin); and b) a three-spin system (two interacting nuclear spins and an electron spin that interacts with both). ¹⁰⁷	35
Figure 1-28: Polarization build-up curves of BMIM-TFSI with 15 mM galvinoxyl free radical for ¹⁹ F (a) and ¹⁹ F of a 1:1 v/v mixture of BMIM-TFSI and benzene (b). The inset in (a) displays ¹⁹ F spectra under Boltzmann conditions (“MW off”) and under ODNP enhanced conditions (“MW on” for 0.5 s and 5 s polarization time, respectively). b) Displays the monotonic exponential build-up of ¹⁹ F polarization ¹⁰⁷	36
Figure 2-1: Precession around the magnetic field ¹⁰⁸	39
Figure 2-2: Net magnetization along the external magnetic ¹⁰⁸	40
Figure 2-3: Sensitivity as a function of T ₁ relaxation and recovery time	41
Figure 2-4: Net magnetization in the xy plan (transverse magnetization) ¹⁰⁸	42
Figure 2-5: Inversion recovery pulse sequence (D ₁ corresponds to the recycle delay between each experiments, in order for the magnetisation to reach back equilibrium before the new scan).....	43
Figure 2-6: Evolution of the signal intensity due to longitudinal relaxation as function of D ₂ , with the zero crossing ⁶¹	43
Figure 2-7: Spectral density representation (with different correlation time number) as a function of the larmor frequency	45
Figure 2-8: The temperature dependence of the T ₁ parameter (figure taken from Dr Luke O’Dell lectures note)	46
Figure 2-9: Temperature dependence of T ₁ and T ₂ parameter (figure taken from Dr Luke O’Dell lectures note)	47
Figure 2-10: Energy level of a two spins system (figure taken from Dr Luke O’Dell lectures note)..	48
Figure 2-11: A spin echo experiment (figure taken from Dr Luke O’Dell lectures note).....	52
Figure 2-12: Effect of a 180° pulse	52
Figure 2-13: The effect of 180° pulses on a system of two coupled spins. (figure taken from Dr Luke O’Dell lectures note)	53
Figure 2-14: HMQC pulse sequence.....	54
Figure 2-15: HSQC pulse sequence	55

Figure 2-16: A basic diffusion NMR pulse sequence. The semi-circles represent field gradient pulses.	56
Figure 2-17: The effect of gradients during a diffusion experiment assuming no movement of the nuclei.....	56
Figure 2-18: The effect of gradients during a diffusion experiment assuming diffusion of the nuclei along the gradient direction.	56
Figure 2-19: Energy level and possible transitions of a two spins system (figure taken from Dr Luke O'Dell lectures note)	58
Figure 2-20: NOESY basic pulse sequence	60
Figure 2-21: ^1H - ^1H NOESY experiment realised on C_4mpyr FSI doped with 1 molal LiFSI sample, therefore corresponding to the hydrogen on the cation.	60
Figure 2-22: Representation of C_4mpyr cation with a colour labelling use later on for build up curves.	61
Figure 2-23: NOESYgtp pulse sequence	61
Figure 2-24: A basic 2D HOESY pulse sequence.....	62
Figure 2-25: Substraction of two HOESY scans, leading to extraction of the NOE enhancement (0 stand for the x position and 2 for -x position of the receiver).....	63
Figure 2-26: The HOESY pulse sequence used in this work	64
Figure 2-27: Pulsed-Gradient Spin Echo PGSE pulse sequence	65
Figure 2-28: Dephasing of signal due to mobility during the PGSE pulse sequence with E field ON	66
Figure 2-29: Pulsed-Gradient Double Spin Echo PGDSE pulse sequence	67
Figure 2-30: CPMG-like pulse gradient double spin echo.....	67
Figure 2-31: Double STimulated Echo (DSTE) pulse sequence	68
Figure 2-32: Electric overvoltage observe in situ on an oscilloscope.....	68
Figure 2-33: modified DSTE used in the following work.....	69
Figure 2-34: Rotational Echo DOuble Resonance REDOR pulse sequence.....	70
Figure 2-35: Theoretical representation of dephasing fraction of the signal as a function of τ	71
Figure 2-36: Rotational-Echo Adiabatic-Passage DOuble-Resonance REAPDOR pulse sequence	71
Figure 4-1: a) Simulated build-up curves T_1 values ranging from 0.5 (yellow) to 2 seconds (red), b) Linear fit of the build-up curves between 0 and 150 ms, c) Fitted cross-relaxation rates with confidence intervals, as a function of the T_1 values used for simulation.....	86

Figure 4-2: The ^7Li - ^1H HOESY pulse sequence used in this work, with phase cycling shown above pulses	87
Figure 4-3: Theoretical signal intensity decay due solely to diffusion during the HOESY pulse sequence (experimental parameters as specified in main text). This signal intensity can drop by 30% at the longest mixing time used in this work ($\tau_m = 5.5$ s, $D = 4.63 \times 10^{-11}$ m 2 .s $^{-1}$, $\delta = 1$ ms, $g = 0.5$ T/m and $\gamma_H = 2,68 \times 10^8$ rad.s $^{-1}$.T $^{-1}$).....	88
Figure 4-4: C ₃ mpyr cation with hydrogen sites numbering.....	89
Figure 4-5: Build-up curve fitted by taking into account diffusion (solid line) and not taking into account diffusion (dot line) realised on C ₃ mpyr FSI sample doped with 1 molal lithium FSI.....	89
Figure 4-6: Measured cross-relaxation rates for the different ^1H sites in C ₃ mpyrFSI with 1 mol.kg $^{-1}$ of LiFSI, with and without taking account diffusion effects. Without accounting for diffusion, the cross-relaxation rates are smaller by around 5%.	90
Figure 4-7: Theoretical HOESY build-up curves, with different M_0 and σ values. For small σ values, multiple solutions can give the same function shape. R_{1H} and R_{1Li} were both set to 1.0 s $^{-1}$ for all curves.	91
Figure 4-8: a) Quantitative single pulse ^1H spectrum with 4 scans corresponding to the pyrrolidinium cation (C ₃ mpyrFSI with 1 m. LiFSI), and b) 1D HOESY ^7Li - ^1H experiment at a mixing time of 700 ms, with 440 scans, normalized integrations show that the HOESY experiment is not only dependent of the number of protons.....	92
Figure 4-9: Single pulse ^1H spectrum of 1-methyl-1-(2-methoxyethyl) pyrrolidinium bis(fluorosulfonyl)imide, with peak assignment to the corresponding atom labelling.	94
Figure 4-10: Single pulse ^1H spectrum of 1-methyl-1-(2-methoxyethyl) pyrrolidinium bis(fluorosulfonyl)imide fitted using Maple	94
Figure 4-11: The top left figure correspond to the ^1H inversion recovery data set, follow by the fits of two different slices, corresponding to two different recovery delays. The right column corresponds to the ^7Li spin lattice relaxation	95
Figure 4-12: 2D ^1H - ^7Li HOESY data set obtained from 1-propyl-1-methylpyrrolidinium bis(fluorosulfonyl)imide doped with 1 m of lithium bis(fluorosulfonyl)imide.	96
Figure 4-13: Build-up curves extracted from the ^1H - ^7Li HOESY experiment on 1-propyl-1-methylpyrrolidinium bis(fluorosulfonyl)imide doped with 1 m of lithium bis(fluorosulfonyl)imide	97
Figure 4-14: Build-up curves fitted to the ^1H - ^7Li HOESY data of 1-propyl-1-methylpyrrolidinium bis(fluorosulfonyl)imide, with the diffusion taken into account	97

Figure 4-15: 1-propyl-1-methylpyrrolidinium cation with colour coding corresponding to the cross-relaxation rates in $(\times 10^{-4}) \text{ s}^{-1}$ between lithium and hydrogen for each hydrogen site (hydrogens sites were reduce to their corresponding carbon sites for clarity).....	98
Figure 4-16: Six experiments carried out on the same sample, N-methyl-N-propyl pyrrolidinium ($\text{C}_3\text{mpyr FSI}$) doped with 1 m of Lithium FSI, with different recycling delays (1.5s, 3s, 4.5s, 5s, 6.5s, 10s). The six graphs present the extracted ^7Li - ^1H cross-relaxation rates for the six hydrogen sites present on the pyrrolidinium cation, with and without taking into account the correction accounting for incomplete relaxation. (uncertainty of 2.5% for each cross relaxation rates)	101
Figure 4-17: Extracted cross-relaxation values using 22 (in blue) and 12 (in red) mixing times as a function of the rates obtained with 32 mixing times, assuming these are the most exact ones. The lines are linear fits $y = ax$ (equation displayed on the graph with the coefficient of determination R^2). We showed the results obtained for samples $\text{C}_3\text{mpyr FSI}$ at 20°C doped with 1 m Li FSI in a) and 3.2m Li FSI in b). (uncertainty of 2.5% for each cross relaxation rates)	102
Figure 4-18: Extracted cross-relaxation values when 80 (blue), 200 (red) and 440 transients (green) are recorded, plotted as a function the theoretically better rates obtained with 800 transients recorded for each of the 22 mixing times and a recovery delay of 6.5 s. The lines corresponds to the linear fit $y = ax$ fit, displayed on top with the corresponding coefficient of determination R^2 . The sample was $\text{C}_3\text{mpyr FSI}$, doped with 1 m LiFSI at 50°C (uncertainty of 2.5% for each cross relaxation rates).	103
Figure 4-19: a) C_3mpyr cation with ^1H sites color coding and number and b) ^1H Spin lattice relaxation at 300 MHz as a function of temperature for sample $\text{C}_3\text{mpyr FSI}$ with 3.2 m LiFSI	110
Figure 4-20: Correlation times τ_c obtained from the ^1H relaxation curves, as a function of $1000/T$ for sample $\text{C}_3\text{mpyr FSI}$ at 3.2 m LiFSI.	111
Figure 4-21: a) C_3mpyr cation with ^1H sites color coding and number and b) ^1H spin-lattice relaxation rates measured at 500 MHz as a function of temperature for sample $\text{C}_3\text{mpyr FSI}$ with 1 m LiFSI.	112
Figure 4-22: Correlation time τ_c calculated from ^1H longitudinal relaxation rates plotted as a function of $1000/T$ for sample $\text{C}_3\text{mpyrFSI}$ with 1 m LiFSI.....	113
Figure 4-23 : ^{19}F longitudinal relaxation rates at 300 MHz as a function of temperature for $\text{C}_3\text{mpyrFSI}$ at 1 m and 3.2 m of LiFSI, using the intermolecular heteronuclear dipolar relaxation.....	114
Figure 4-24: ^{19}F calculated correlation time τ_c as a function of $1000/T$ for sample $\text{C}_3\text{mpyr FSI}$ at 1 m and 3.2 m Li FSI in the intermolecular heteronuclear dipolar relaxation.....	115

Figure 4-25: ^7Li spin lattice relaxation at 300MHz as a function of temperature for sample C_3mpyr FSI at 1 m and 3.2 m of Li FSI	116
Figure 4-26: ^7Li calculated correlation time τ_c as a function of $1000/T$ for sample C_3mpyr FSI at 1 m and 3.2 m Li FSI	117
Figure 4-27: ^1H spectrum corresponding to the C_3mpyr FSI IL doped with 1 m LiFSI	118
Figure 4-28: ^1H - ^1H NOESY experiments realized at a) 17.61 T and b) 11.74 T	119
Figure 4-29: ^1H - ^7Li HOESY build-up curves for C_3mpyr FSI with 1 m LiFSI at 50°C	120
Figure 4-30: ^1H - ^7Li Overhauser rates for the C_3mpyr and lithium cations (1 molal LiFSI). Cross-relaxation rates are in $.10^{-4} \text{ s}^{-1}$ and the colour coding corresponds to the relative intensities of the NOE at a) 50°C and b) 20°C (uncertainty of 2.5% for each cross relaxation values)	121
Figure 4-31: Cross-relaxation rates measured for C_3mpyr FSI doped with 1 molal and 3.2 molal Li FSI at 20°C and 50°C (uncertainty of 2.5% for each cross relaxation values)	122
Figure 4-32: ^1H - ^7Li Overhauser rates for the C_3mpyr and lithium cations (3.2 molal LiFSI). Cross-relaxation rates are in $.10^{-4} \text{ s}^{-1}$ and the colour coding corresponds to the relative intensities of the NOE at a) 50°C and b) 20°C (uncertainty of 2.5% for each cross relaxation values)	123
Figure 4-33: ^1H - ^{19}F Overhauser build-up curves for C_3mpr FSI doped with 1 m LiFSI at 40°C , with the corresponding fits.	125
Figure 4-34: Cross-relaxation rates as a function of temperature extracted for C_3mpyr FSI with 1 mol.kg $^{-1}$ LiFSI (C_3mpyr FSI cation with hydrogen sites colours and numbers in insert) (uncertainty of 2.5% for each cross relaxation values).....	126
Figure 4-35: Representation of the spectral density as a function of $\log(\omega)$ according to the GSW model (reproduction of the figure from the original work ⁸¹).....	130
Figure 4-36: 3D representation of the cross-relaxation rate expression in the case of an intramolecular spin pair transfer with two theoretical spin pair example.....	132
Figure 4-37: Representation of C_3mpyr cation with the hard sphere model corresponding to the region of closest approach for the lithium to each hydrogen sites.....	133
Figure 4-38: 3D representation of the cross-relaxation rate expression in the case of a fixed distance r between spins and a single correlation time describing the fluctuation of the dipolar vector's orientation (two different views).....	135
Figure 4-39: Plot of the cross-relaxation rate as a function of the correlation time (log scale) assuming a fixed distance $r=1\text{\AA}$ between the ^1H and ^{19}F spins.....	135

Figure 4-40: 3D representation of the cross-relaxation rate expression in the case of a fixed distance r between spins and a single correlation time describing the fluctuation of the dipolar vector's orientation with correlation time range corresponding to range extracted from T_1 experiments.	136
Figure 4-41: 3D representation of the cross-relaxation rate in the case of a fixed distance r between spins and a single correlation time describing the fluctuation of the dipolar vector's orientation. The lines show the positions of the minimum and maximum.	137
Figure 4-42: Magnitude of cross-relaxation rates extracted for the C_3 mpyrFSI sample doped with 1 molal LiFSI at 20°C (uncertainty of 2.5% for each cross relaxation values).....	138
Figure 4-43: C_3 mpyr cation with numbering, colour coding and experimental cross-relaxation rates ($\times 10^{-4} s^{-1}$) between 1H and 7Li for C_3 mpyrFSI with 1 molal LiFSI at 50°C.....	140
Figure 4-44: Carbon-lithium radial distribution functions (RDF) in solid line, and coordination numbers (CN) in dashed line obtained from the MD simulations for C_3 mpyrFSI with 1 molal LiFSI at 50°C	140
Figure 4-45: Graphical illustration of the correlations between the experimentally measured 1H - 7Li cross relaxation rates and carbon-lithium distance derived from the MD, corresponding to Figure 4-43 and Figure 4-44 data respectively.	141
Figure 4-46: C_3 mpyr cation with numbering, colour coding and experimental cross-relaxation rates ($\times 10^{-4}$) of 1H - ^{19}F experiments for C_3 mpyr FSI with 1 molal Li FSI at 20°C (uncertainty of 2.5% for each cross relaxation values).....	142
Figure 4-47: Carbon-fluorine radial distribution functions (RDF) and coordination numbers (CN) obtained from the MD simulations for C_3 mpyrFSI with 1 molal LiFSI at 20°C.....	142
Figure 4-48: Graphical illustration of the correlations between the experimentally measured 1H - ^{19}F cross-relaxation rates and carbon-lithium coordination numbers (CN) derived from the MD, corresponding to Figure 4-46 and Figure 4-47 data respectively.....	143
Figure 4-49: 1H - 7Li cross relaxation rates for the C_4 mpyr and lithium cations (1 molal LiFSI at 50°C). Cross-relaxation rates are in $\cdot 10^{-4} s^{-1}$ and the colour coding corresponds to the relative intensities of the NOE. (uncertainty of 2.5% for each cross relaxation values)	151
Figure 4-50: 1H - ^{19}F Overhauser rates for the C_4 mpyr and FSI anions (1 molal LiFSI at 50°C). Cross-relaxation rates are in $\cdot 10^{-4} s^{-1}$ and the colour coding corresponds to the relative intensities of the NOE. (uncertainty of 2.5% for each cross relaxation values)	152

Figure 4-51: Single pulse ^1H experiments corresponding to the cation structure of the N-methyl-N-propyl Piperidinium bis(fluorosulfonyl)imide ($\text{C}_3\text{mpip FSI}$) doped with LiFSI at 1 mol.kg $^{-1}$	153
Figure 4-52: ^1H single spectrum of the N-methyl-N-propyl Piperidinium bis(fluorosulfonyl)imide in red and the N-propyl-N-methyl Pyrrolidinium in black, with the hydrogens sites correspondence.....	153
Figure 4-53: Zoom of an ^1H - ^{13}C HSQC experiments with a ^{13}C single pulse experiments as an external projection for the indirect dimension.....	154
Figure 4-54: Assigned ^1H spectrum of N-methyl-N-propyl piperidinium bis(fluorosulfonyl)imide ($\text{C}_3\text{mpip FSI}$) cation	155
Figure 4-55: ^1H - ^7Li Overhauser rates for the C_3mpip and lithium cations (1 molal LiFSI at 50°C). Cross-relaxation rates are in $.10^{-4} \text{ s}^{-1}$ and the colour coding corresponds to the relative intensities of the NOE. (uncertainty of 2.5% for each cross relaxation values)	156
Figure 4-56: ^1H - ^7Li Overhauser rates for the $\text{C}_{201}\text{mpyr}$ and lithium cations (1 molal LiFSI at 50°C). Cross-relaxation rates are in $.10^{-4} \text{ s}^{-1}$ and the colour coding corresponds to the relative intensities of the NOE. (uncertainty of 2.5% for each cross relaxation values)	157
Figure 4-57: ^1H - ^{19}F Overhauser rates for the $\text{C}_{201}\text{mpyr}$ and FSI anions (1 molal LiFSI at 50°C). Cross-relaxation rates are in $.10^{-4} \text{ s}^{-1}$ and the colour coding corresponds to the relative intensities of the NOE. (uncertainty of 2.5% for each cross relaxation values)	158
Figure 4-58: $\text{C}_{201}\text{mpyr}$ cation with numbering, colour coding and experimental cross-relaxation rates ($\times 10^{-4} \text{ s}^{-1}$) between ^1H and ^7Li for $\text{C}_{201}\text{mpyrFSI}$ with 1 molal LiFSI at 50°C (uncertainty of 2.5% for each cross relaxation values).....	159
Figure 4-59: Carbon-lithium radial distribution functions (RDF) and coordination numbers (CN) obtained from the MD simulations for $\text{C}_{201}\text{mpyrFSI}$ with 1 molal LiFSI at 50°C	160
Figure 4-60: Graphical illustration of the correlations between the experimentally measured ^1H - ^7Li cross relaxation rates and carbon-lithium distance derived from the MD, corresponding to Figure 4-58 and Figure 4-59 data respectively.	160
Figure 4-61: C_3mpyr cation with numbering, colour coding and experimental cross-relaxation rates ($\times 10^{-4}$) of ^1H - ^{19}F experiments for $\text{C}_3\text{mpyr FSI}$ with 1 molal LiFSI at 20°C (uncertainty of 2.5% for each cross relaxation values).....	161
Figure 4-62: Carbon-fluorine radial distribution functions (RDF) and coordination numbers (CN) obtained from the MD simulations for $\text{C}_{201}\text{mpyrFSI}$ with 1 molal LiFSI at 20°C.....	161

Figure 4-63: Graphical illustration of the correlations between the experimentally measured ^1H - ^{19}F cross-relaxation rates and carbon-lithium coordination numbers (CN) derived from the MD, corresponding to Figure 4-46 and Figure 4-47 data respectively.....	162
Figure 4-64: (a) The molecular structure of the $\text{C}_3\text{mpyrFSI}$ ionic liquid with the six inequivalent carbon sites labelled. ^{13}C CPMAS spectra obtained from the solid state $\text{C}_3\text{mpyrFSI}$ - $^6\text{LiFSI}$ -TEKPol solution are shown with (b) DNP enhancement and ^1H decoupling, (c) no DNP enhancement and ^1H decoupling, and (d) DNP enhancement but no ^1H decoupling. All spectra were acquired at 9.4 T and 8 kHz MAS with 80 scans acquired, a 6s recycle delay, and a sample temperature of approximately 92 K. The peak assignment is shown in (b), where S denotes the signal from the silicone plug. ...	168
Figure 4-65: Spectrum with and without the pi pulse train, and the spectrum corresponding to the subtraction of both, extracted from a REDOR experiment realised on the $\text{C}_3\text{mpyr FSI}$ sample doped with 1 molal $^6\text{Li FSI}$ at 8 ms of dephasing time	170
Figure 4-66: ^{13}C - ^6Li dephasing data fitted according to Equation 4-20.	172
Figure 4-67: ^{13}C - ^6Li REDOR dephasing plots for the six ^{13}C signals of the C_3mpyr cation (left) fitted using the BS-REDOR method with extracted C-Li distance distributions (right).	173
Figure 4-68: The molecular structure of the $\text{C}_3\text{mpyrFSI}$ ionic liquid with the six inequivalent carbon sites labelled.....	174
Figure 4-69: Plots of Li^+ spatial distribution around the C_3mpyr cation constructed from (a) the 92 K solid-state ^{13}C - ^6Li REDOR distance data in Table 2 and (b) a molecular dynamics simulation carried out on a liquid-phase $[\text{C}_3\text{mpyrFSI}]_{0.9}[\text{LiFSI}]_{0.1}$ system with a simulated temperature of 298 K. As a reference for scale, the carbon-carbon bond lengths on the C_3mpyr cation are 1.23 Å.	176

List of tables

Table 3-1 : Extracted activation energy E_a (in kJ/mol) and correlation time τ_0 at infinite temperature for ^1H T_1 measurements on $\text{C}_3\text{mpyrFSI}$ with 3.2 m LiFSI, measured at 300 MHz.	111
Table 3-2: Extracted activation energies E_a and correlation times at infinite temperature for ^1H T_1 measurements on $\text{C}_3\text{mpyrFSI}$ with 1 m LiFSI at 500 MHz.	113
Table 3-3: Extracted activation Energy and correlation time at infinite temperature for ^{19}F T_1 measurements on $\text{C}_3\text{mpyr FSI}$ at 1 m and 3.2 m of Li FSI.	115
Table 3-4: Extracted activation Energy and correlation time at infinite temperature for ^7Li T_1 measurements on $\text{C}_3\text{mpyr FSI}$ at 1 m and 3.2 m of Li FSI.	116
Table 3-5: Distance of closest approach between lithium and the different hydrogen sites for $\text{C}_3\text{mpyr FSI}$ with LiFSI 1 molal at 20°C and 50°C.	133
Table 3-6: Distance of closest approach between lithium and the different hydrogen sites for $\text{C}_3\text{mpyrFSI}$ with LiFSI 3.2 molal at 20°C and 50°C.	134
Table 3-7: ^{13}C Isotropic Chemical Shifts (δ_{iso}), Peak Widths ($\Delta\delta$), Polarization Buildup Times (T_1^*), and DNP Enhancement Levels (ϵ_{DNP}) for the six Carbon Sites on the Pyrrolidinium Cation (as indicated in Figure 3-64 (a)).....	169
Table 3-8: Li-C distances d and scaling factors f extracted from the ^{13}C - ^6Li dephasing data using the universal REDOR dephasing curve.	172
Table 3-9: Lithium-carbon distances (d_n), distribution widths (Δd_n) and relative fractions (f_n) extracted for each of the carbons on the C_3mpyr cation using BS-REDOR analysis. The distribution widths Δd_n for C1, C2 and C3 are unspecified due to the 9 Å cut-off used in the fitting.	175

Introduction

Finite fossil fuel resources and concerns over climate change have led to the requirement of improved ways to produce, use and store energy. On one hand, fossil fuels can still be extracted and distributed easily and at a relatively low cost, but unfortunately on the other hand, as our society consumes huge quantities of these resources, the reserves begin to be more and more complicated to access. Moreover, the combustion of fossil fuels pollutes the air and is overwhelmingly considered responsible for climate change, while the more difficult extraction methods create additional environmental issues¹.

By using alternative and renewable energy such as solar or wind we can limit the problem of climate change through the reduction of carbon dioxide emissions as well as reduce polluting smog that overwhelms many high population density cities such as Beijing, thereby helping to mitigate dangerous health issues. However, these cleaner energy sources have the problem of intermittency and/or inconsistent production. Moreover, as modern technology evolves rapidly, the energy demand becomes harder and harder to sustain. In fact some studies such as DESERTEC² have shown that the main current problem is not the energy generation or conversion, but energy storage. For example, in six hours, the deserts of the earth receive as much energy as all humanity uses in a year. Unfortunately current energy storage devices such as batteries, super-capacitors or even fuel cells (Figure 0-1: Ragone chart showing the power and energy densities of various energy storage technologies. (Encarnaciòn Raymundo-Piñero talk)Figure 0-1), are not yet reliable enough to make the most of such energy generation sources.

During the last several decades, much research has focused on developing these energy storage devices in order to support renewable energy sources³. Improvements have been made to all components of these devices, such as the electrodes, separators and electrolytes, making them safer, more eco-friendly, more conductive and also cheaper. This work is focused on the electrolytes,

specifically ionic liquids (ILs)⁴, and involves the use of magnetic resonance-based experimental characterisation⁵ to improve our understanding of the ion transport mechanisms within them, with the ultimate aim of being able to design new ILs with improved properties for use in energy storage applications.

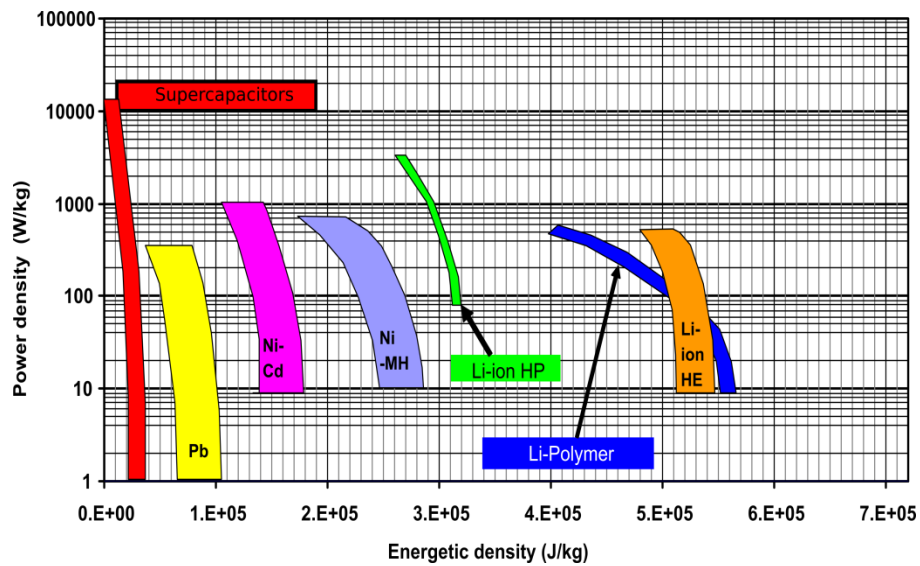


Figure 0-1: Ragone chart showing the power and energy densities of various energy storage technologies. (Encarnación Raymundo-Piñero talk)

Chapter 1

Literature review

Literature review

Overview

1.1.1 Lithium batteries

Lithium ion batteries have become one of the most commonly used energy storage devices due to the demand of ever thinner and lighter products⁶. Indeed lithium has the lightest weight, with a density of 0.534 gcm^{-3} , highest nominal voltage ($\sim 3.6 \text{ V}$), and greatest energy density ($\sim 240 \text{ Whkg}^{-1}$) of all metals. Currently lithium batteries are used in a very wide range of devices, from cell phones and laptops, to airplanes, trains or cars. Unfortunately these batteries suffer drawbacks, due for example to the volatile and highly flammable electrolyte, and several accidents have occurred due to the ignition of the batteries⁷.

A lithium battery, as shown below, consists of three main components, the cathode, the anode and an electrolyte (usually a lithium salt dissolved in a non-aqueous solvent). Lithium ions move from the positive electrode to the negative one during the charge of the battery, and in the other way during the discharge.

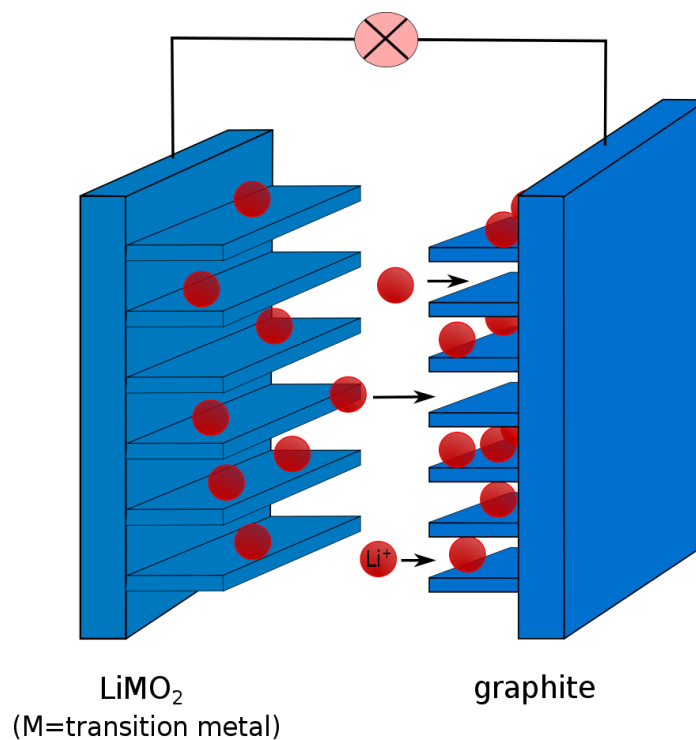


Figure 1-1: Illustration of a classical lithium-ion battery

For the anode, graphite is the most widely used material thanks to the lamellar host structure for lithium intercalation, good cycling ability and a small irreversible capacity. Example cathode materials include layered compounds LiMO_2 ($M=\text{Co}, \text{Ni}, \text{Mn}, \text{etc.}$), spinel compounds LiM_2O_4 ($M= \text{Mn}, \text{etc.}$) and olivine compounds LiMPO_4 ($M= \text{Fe}, \text{Mn}, \text{Ni}, \text{Co}, \text{etc.}$).

1.1.2 Ionic liquids as electrolytes

Ionic liquids (ILs) can be classified as pure salts with a melting temperature below 100°C . Some of them are liquid at room temperature, and are called room temperature ionic liquids (RTILs)⁸.

The number of potential ionic liquids is enormous because of the possibility to mix a large number of different anions and cations together. A small number of example cation and anion structures are shown in Figure 1-2. It is therefore crucial to understand how the molecular structures determine the various properties of the ILs (for example, the ionic conductivity) for choosing an IL for a specific application.

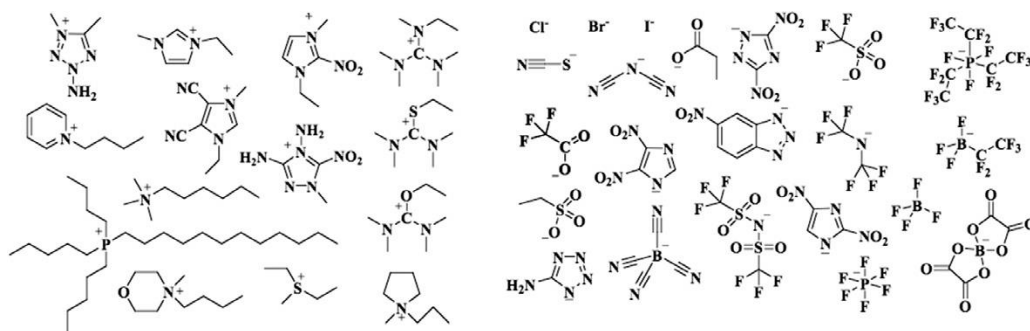


Figure 1-2 : Examples of cations (on the left) and anions (on the right) which can be combined in order to make ionic liquids⁹

Many ILs share similar properties, such as a very low vapor pressure, high stability at high temperature, a low combustibility, and the ability to dissolve a wide range of compounds^{10,11}. They are also, for the most part, good ionic conductors^{4,12}. These properties make ILs potentially advantageous as electrolytes for lithium batteries, especially when compared with the volatile or flammable solvents commonly used.¹³

The first IL was discovered during the 19th century¹⁴, however, the name “ionic liquid” was only coined in the 1980s to qualify the term molten salts that is now

predominantly reserved for inorganic, high melting point salt systems. Furthermore, it was only in 1992 that the first IL based on the imidazolium cation was synthesized (Figure 1-3).

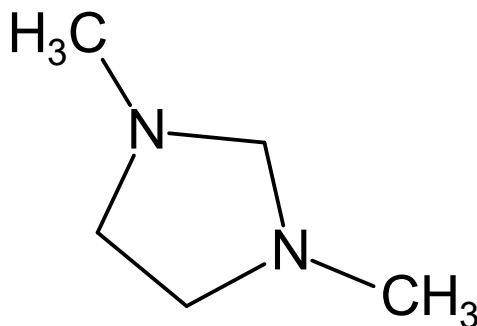


Figure 1-3: The structure of the diethylimidazolium cation

Thanks to their unique properties, ILs are currently used for applications in many sectors, from gas absorption to nanoparticle synthesis, including biocatalysts. In particular, their high conductivities make them very good candidates for electrochemistry applications, for example as electrolytes in batteries or fuel cells¹⁸ as mentioned above. However their main current applications are as “eco-friendly” solvents, because of their negligible vapor pressure, which avoids the evaporation of many volatile organic compounds. Indeed ILs have a very good capacity to dissolve a wide range of organic compounds while protecting their chemical function and reactivity¹⁵. They are also good solvents for inorganic compounds or polymers¹⁶ because their properties of dissolution depend on the relatively strong associations of cations and/or anions present in the IL with the desired solute molecules.

1.1.3 Structure and nanostructure in ionic liquids

Over the past years, a large amount of IL research has focused on the pyrrolidinium or imidazolium cations^{17–37}. Pyrrolidinium ions are often referred as Pyr_{1n}, “n” corresponding to the number of methyl groups on the alkyl chain, 1 to the methyl group on the nitrogen and “Pyr” standing for pyrrolidinium, or also C_nmpyr with the same coding for “n” and “pyr” and m to the methyl group on the nitrogen. For imidazolium samples the coding refers to the length of the alkyl chains thus the 1-Ethyl-3-

methylimidazolium will be coded as EMIM, “E” for ethyl, “M” for methyl and “IM” for imidazolium.

On the other hand, new types of ionic liquids are beginning to emerge. Phosphonium and ammonium based cations with various alkyl chains^{27,29,38–42}, mixed with trifluorosulfonylimide (TFSI, also referred to in the literature as TFSa or NTf₂)^{31,35,36,43–46} or fluorosulphonylimide (FSI, also referred to as FSA) anions^{18,20,21,47,48}, have shown improved properties such as lower viscosity or improved ion transport. The common notation for describing these cations is X where X = P or N and the subscripts a-d are the numbers of carbons on each of the four organic groups attached to the central atom, such as the *N,N*-Diethyl-*N*-methyl-*N*-propylammonium, which will be written N₂₂₁₃.

1.1.4 Recent studies of liquid structure and speciation in ILs

Many studies investigating how IL properties depend on the chemical structures of the cations or anions have been published. For example, a study by Carvalho⁴⁹ investigated the impact of the central cation atom (P or N with the rest of the cation having the same structure) on the ionic liquid behavior. They showed in this study that all of the properties investigated, including density, viscosity, melting temperatures, refractive indices, or even infinite dilution activity coefficients, are pronouncedly affected by the cation’s central atom nature. Furthermore, a similar study by Castner *et al*⁵⁰, by NMR found that, in the ammonium-based ILs (N₂₂₂₈⁺), the anion preferentially interacts with the head group of the cation while for the phosphonium based ILs the anions are more evenly distributed around the cations. This, according to the authors, can explain the higher densities, viscosities and melting temperatures of the ammonium based IL, as the tail is almost “free” of TFSI anions.

Studies of pure phosphonium-based ionic liquids were carried out by Tsunashima⁵¹, showing the impact of the anion (FSI or TFSI) on the structure and therefore the properties.

Literature review

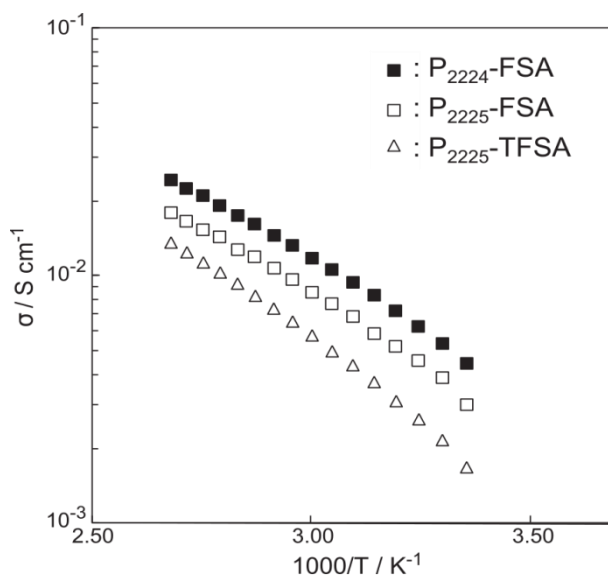


Figure 1-4: Arrhenius plot of the ionic conductivity versus inverse temperature for P_{2224} FSA, P_{2225} FSA and P_{2225} TFSA⁵¹

As shown in Figure 1-4, in this study the FSI-based phosphonium IL exhibited a higher conductivity than the corresponding TFSI-based one. Interestingly, they also investigated phosphonium based ionic liquids but containing a methoxy group on the cation, which showed a very low viscosity and were highly conductive compared to the equivalent cation without the methoxy group (Figure 1-4 vs. Figure 1-5).

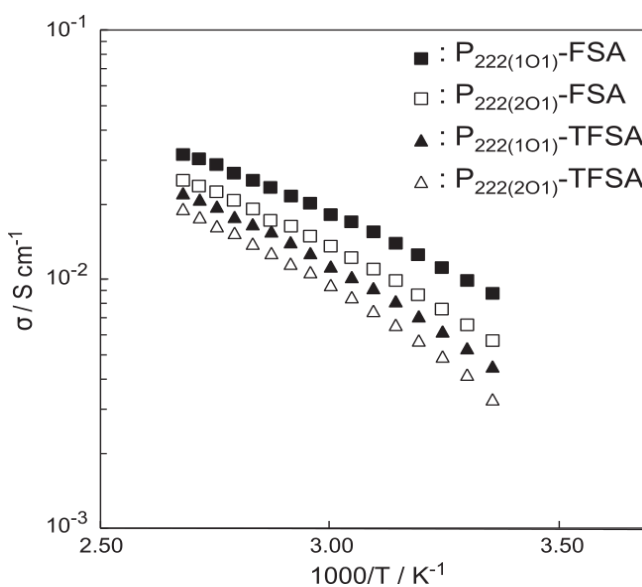


Figure 1-5: Arrhenius plot of the conductivity versus inverse temperature for phosphonium based ionic liquids containing a methoxy group⁵¹

1.II Characterization of ILs using NMR spectroscopy

Nuclear magnetic resonance (NMR) spectroscopy is a useful tool to characterize ILs^{5,52}. First of all NMR can allow the confirmation of the chemical structure of the samples studied, but also can verify the purity, and identify any contaminants such as a water. The investigation of NMR relaxation times can lead to a better understanding of the fast and short range dynamics, while the measurement of diffusion coefficients can give access to long range dynamics. Also, one of the biggest advantages of NMR spectroscopy and the main focus of this work, is the ability to study site-specific molecular associations, which can lead to an improved understanding of intermolecular proximities and therefore provide detailed information on ion associations and interactions. In this section, some recent examples of these types of NMR spectroscopy experiments as applied to ILs are discussed, as well as two more advanced and less commonly utilised NMR spectroscopy methods, electrophoretic NMR⁵³ spectroscopy and dynamic nuclear polarisation⁵⁴.

1.II.1 Relaxation measurements

NMR relaxation measurements are a very common and useful NMR spectroscopy tool for investigating localised dynamics in materials. Different relaxation rates such as T_1 , $T_{1\rho}$ and T_2 can be measured and correlated with molecular dynamics at different timescales. Herein we will focus on T_1 , also known as the spin-lattice relaxation time or longitudinal relaxation time. It relates to the time it takes for the excited nuclear spins to return to their thermal equilibrium state. The relaxation mechanism is strongly dependent on the dynamics and the surrounding structural environment as a number of specific relaxation mechanisms allow nuclear spins to exchange energy with their surroundings (such as the NOE effect⁵⁵).

In order to describe this relaxation process, theory was developed by Nicolaas Bloembergen, Edward Mills Purcell and Robert Pound, so called the BPP theory

Literature review

(Bloembergen-Purcell-Pound theory). This theory quantifies the relaxation rate in terms of the random molecular tumbling and molecular motions (quantified by τ_c , the correlation time). More details about the BBP theory and the spin lattice relaxation will be given in section 2. By studying T_1 s of different nuclei as a function of temperature, the correlation time, and also the activation energy of the molecular motion responsible for the relaxation can be quantified for the different species present in the ionic liquid.

There is a considerable volume of work in the literature that studies ionic liquids through spin lattice relaxation experiments. For example, Hayamizu *et al*⁵⁶ studied the translational and rotational motions in a pyrrolidinium system, with either TFSI or FSI anion as a counter ion and mixed (or not) with lithium FSI. Using different techniques including the T_1 spin lattice relaxation experiments they looked at the mobility of the lithium ion and how it varied with the counter ion. As shown in Figure 1-6, the T_1 parameter of the lithium was extracted at different temperatures and then, using the BPP equation for quadrupolar nuclei, they extracted the corresponding correlation time (τ_c) and activation energy (E_a). Through these experiments, they concluded that the lithium moved much faster in the C₃mpyr Li FSI system than in the C₃mpyr Li TFSI system.

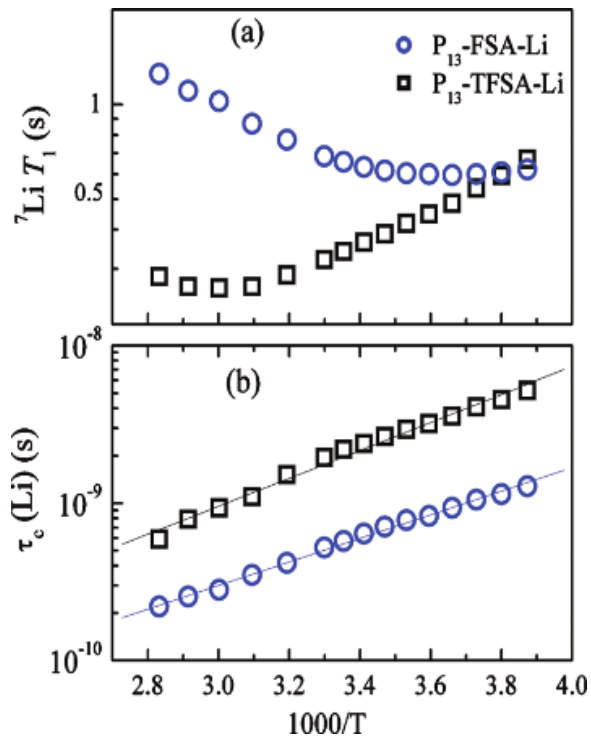


Figure 1-6: Arrhenius plots of (a) ${}^7\text{Li } T_1$ and (b) the $\tau_c(\text{Li})$ for $\text{C}_3\text{mpyr-TFSA-Li}$ (black) and $\text{C}_3\text{mpyr-FSA-Li}$ (blue). Lines show fits to BPP theory ⁵⁶

Other authors have focused on sodium containing ionic liquids. For example Pope *et al*⁵⁷ used ${}^1\text{H}$, ${}^{19}\text{F}$ and ${}^{23}\text{Na}$ spin lattice relaxation measurements as well as other techniques such as Differential Scanning Calorimetry (DSC), Electrochemical Impedance Spectroscopy (EIS), and Pulsed-Field Gradient diffusion NMR (PFG-NMR) to study sodium salt based ionic liquid electrolytes..

Literature review

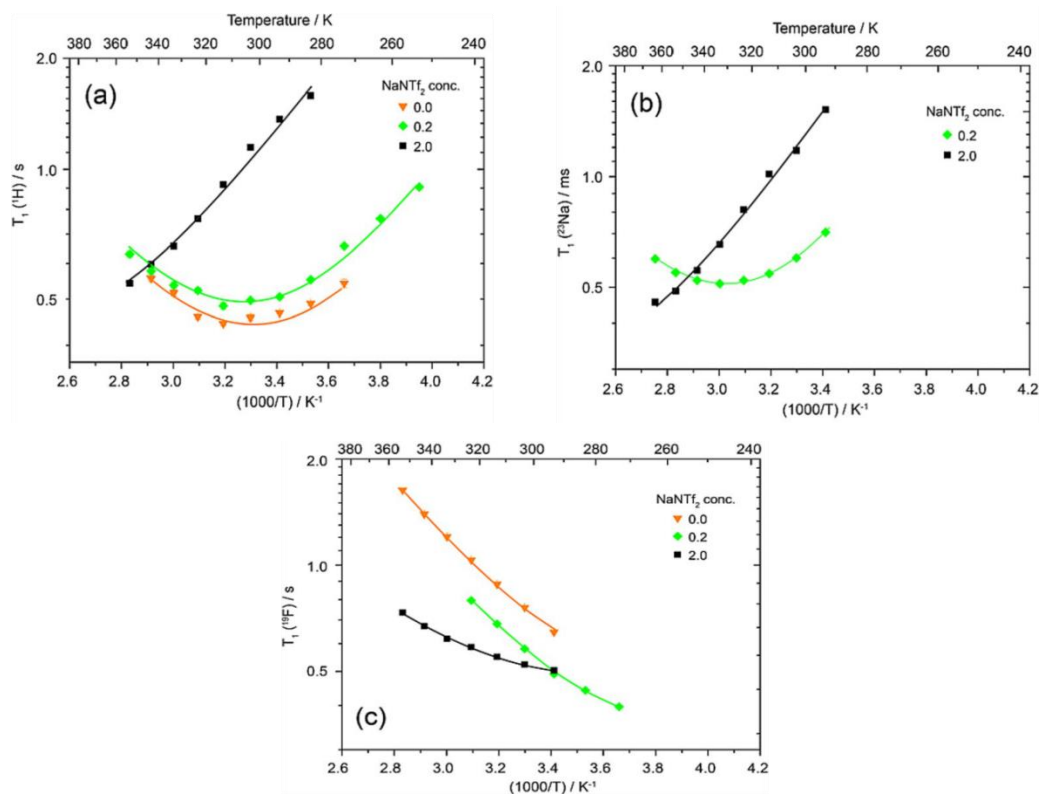


Figure 1-7 : a) 1H , b) ^{23}Na and c) ^{19}F T_1 relaxation times as a function of inverse temperature for the pure IL and the lowest and highest NaTFSI concentrations (0.2 and 2.0 mol.kg⁻¹). The error bars are contained within the size of the data points. Lines show fits to BPP theory⁵⁷

From fitting the 1H , ^{19}F and ^{23}Na T_1 s using BPP theory, the authors deduced the correlations time and activation energies for the quaternary tri-alkoxy ammonium [N₂(₂₀₂₀₁)(₂₀₂₀₁)(₂₀₂₀₁)], the bis(trifluoromethylsulfonyl)imide TFSI and also the sodium. These measurements implied a correlated dynamics between the IL cation and the sodium, with the anions being very different. This was interpreted as strong ion associations between the IL cation and the sodium, with sodium acting as a cross-link between multiple ammonium cations.

Many studies on other IL systems can be found, such as a study by Hayamizu et al⁴¹ on an ammonium based ionic liquid, or their study in 2011 of an imidazolium based ionic liquid. Some groups have focused on different anions^{58,59}, such as PF₆⁻ or BF₄⁻, while others have studied the impact of the cation alkyl chain lengths.⁶⁰

1.II.2 Diffusion

Diffusion is the random translational motion of molecules, also known as Brownian motion. It is mostly driven by the internal thermal energy and can be driven by molecular spatial distributions, but also the self-molecular motion in a compound. Diffusion in ionic liquids is important to study, as it plays a central role in ion transport and will be strongly related to the inter-ionic and molecular interactions. Even more importantly from the point of view of lithium-based electrolytes, as the diffusion coefficient describes the translational dynamics it can be used to understand the relative dynamics of say the lithium ions relative to other ions/molecules in an electrolyte⁶¹.

This self-diffusion coefficient can be measured by NMR⁶² (more details in Chapter 2 Experimental NMR spectroscopy theory and methodology), and is given in units of $\text{m}^2\cdot\text{s}^{-1}$. Usually larger for small molecules or non-viscous samples, typical diffusion coefficients range from 10^{-7} to $10^{-14} \text{m}^2\cdot\text{s}^{-1}$ ^{39,43,63}. For example the diffusion coefficient of water molecules in pure water is $2.57 \times 10^{-9} \text{m}^2\cdot\text{s}^{-1}$ at 25°C ⁶⁴. In the case of ionic liquids, providing the ions have different active nuclei, diffusion coefficients can be extracted as different ionic species are present (c.f. ionic liquids as electrolytes).

NMR spectroscopy based diffusion measurements are commonly made for ionic liquids, and a lot of work has been published quantifying ion diffusion in ILs. For example, in work by Tokuda *et al*, different ionic liquid systems were studied by choosing the same cation BMIM (butyl imidazolium), but with different types of anions⁶⁵, such as BF_4 , PF_6 , TFSI, CF_3CO_2 or $(\text{C}_2\text{F}_5\text{SO}_2)_2\text{N}$. In another work they investigated the impact of the alkyl chain of the imidazolium cation with TFSI as the anion⁶⁶, and in the last paper of the series, they changed the cation structure with TFSI as the anion⁶⁷. These works aimed to understand how ionic liquid structures can impact the ionic liquid properties, in others words, how the microscopic ion dynamics relate to the macroscopic properties⁶⁸. In fact, the huge variety of ionic liquids implies an ocean of potential studies with comparisons of ILs containing various different anions or cations such as in the study carried out by Noda *et al*⁶⁹. They presented a study of different lithium TFSI addition on two specific system, ie. $\text{C}_3\text{mpyr TFSI}$ ³⁷ or

C₄mpyr TFSI³¹, including different solvent addition to improve the electrochemical windows³⁹.

In fact, in most of these studies, the measured diffusion coefficients are very similar even if the system and its macroscopic properties can be very different. Usually, the diffusion coefficients ranged from 10^{-10} to $10^{-12} \text{ m}^2.\text{s}^{-1}$ depending on the temperature. A series of studies realised by Castiglione *et al*, reported studies of C₄mpyr, with some using different techniques such as conductivity and viscosity measurements²⁸, but mostly reporting diffusion and Nuclear Overhauser Effect (NOE) experiments (see below). Similarly to Tokuda *et al*, they studied the C₄mpyr cation, with different anions, TFSI, (trifluoromethanesulfonyl)(nonafluorobutanesulfonyl)imide (IM₁₄) and bis(pentafluoroethanesulfonyl)imide (BETI) and reported that the diffusion of the cation is faster than the anion in all three systems. As they were trying to understanding the anion-cation correlation in different systems, they also studied the C₄mpyr TFSI system mixed with different concentrations of lithium salts⁷⁰, followed by a study of C₄mpyr BETI and C₄mpyr IM₁₄ also doped with lithium salt⁴³, stating that mixing these ionic liquids with a lithium salt decreased the ionic conductivity.

It is also interesting to mention some studies realised by Hayamizu *et al*. Indeed, among their different studies, such as the study of an ammonium cation with an oxygen on one alkyl chain and mixed with Li TFSI⁴¹, they made a series of publications on the rotational and translational motions in ionic liquids. They began the study with the C₃mpyr cation with either FSI or TFSI mixed (or not) respectively with Li FSI and Li TFSI⁵⁶, highlighting a strong correlation between the diffusional motion and the viscosity. An example of the extracted diffusion coefficients is presented in Figure 1-8, with diffusion values between 10^{-10} to 10^{-12} , in the temperature range from 353 to 253 K. This worked was followed by a similar study, but this time on EMIM TFSI/FSI sample⁷¹ but also on EMIM and BMIM cation with BF₄.

Literature review

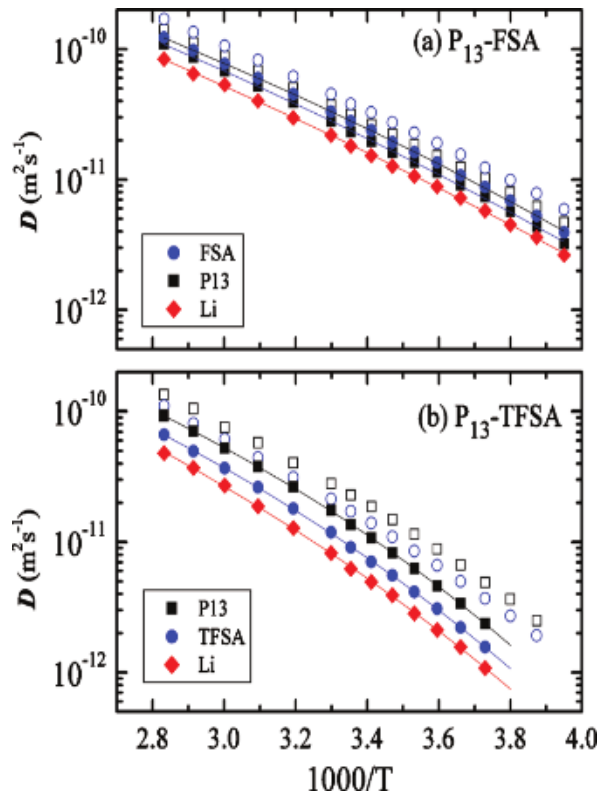


Figure 1-8: Arrhenius plots of the ion diffusion coefficients of the binary systems for a) C₃mpyr-FSI-Li and b) C₃mpyr-TFSA-Li. For comparison, D values of the neat P₁₃-FSA and P₁₃-TFSA samples are included in empty symbols

As another example, Girard⁷² and co-workers investigated the electrochemical and physicochemical properties of P_{111i4}FSI (i4 = isobutyl) (P=phosphorus) based ionic liquids. This sample was able to dissolve high concentrations of the Li FSI salt, up to 3.8 mol.kg⁻¹. This study showed some interesting Li cation behavior. As can be seen in Figure 1-9, the diffusivity of all ions decreases as the Li⁺ concentration in the IL electrolyte increases, attributed to an increase in viscosity. However, at high concentrations the lithium diffuses faster than the phosphonium cations, permitting a higher transport number of Li⁺ above 2 mol.kg⁻¹, and suggesting promising properties of concentrated IL electrolytes for battery applications.

Literature review

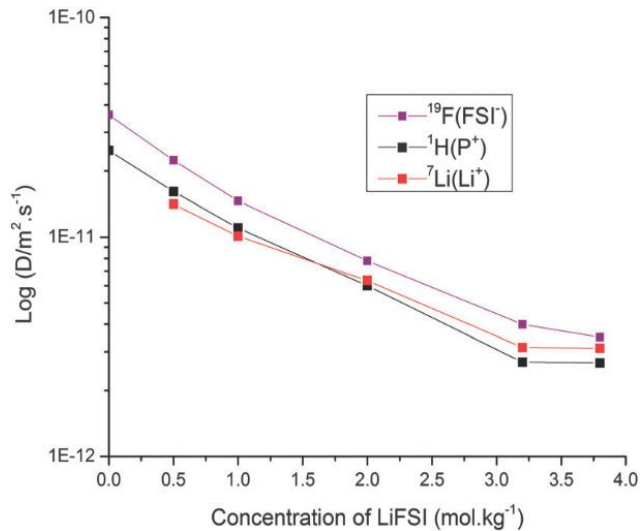


Figure 1-9 : Diffusivity of the different nuclei in P₁₁₁₄ FSI as a function of LiFSI concentration at 22°C⁷², ¹H nuclei for the cation, ¹⁹F for the anion and ⁷Li for the lithium cation.

The self-diffusion coefficients can also provide access to additional information. For example, from the self-diffusion coefficients of all of the species present in the liquid, the viscosity parameter can be extracted by using the Stokes-Einstein equation (Equation 1-1, where η is the viscosity and r the particle radius and C a constant that ranges from 6π under no-slip boundary conditions for the fluid on the particle surface to 4π under slip boundary conditions^{73,74}) or the ionic conductivity of the sample can be calculated using the Nernst Einstein equation (Equation 1-2). This calculated value is usually higher than that measured from impedance spectroscopy because in diffusion experiments even neutral ionic clusters are measured.

$$D = \frac{k_B T}{C \eta r}$$

Equation 1-1

$$\sigma = \frac{D z^2 e^2 c}{k_B T}$$

Equation 1-2

Where σ represent the conductivity, z the number of charge, e the elementary charge, C the molar concentration, k_B the Boltzmann constant, and T the temperature in Kelvin.

For example, Girard and co-workers used the extracted diffusion parameters, to calculate the ionic conductivity using the Nernst-Einstein equation. As shown on

Figure 1-10, the comparisons of the conductivity calculated by impedance spectroscopy (Λ_M) with those extracted *via* these self-diffusion coefficients (Λ_{NE}), show a difference between the two values. Indeed the diffusion coefficients determined by NMR spectroscopy represent an average mobility over all the ions whether an isolated ion, an aggregate or even when there is ion pairing, contrary to the conductivity measurements which measures only the mobility of the charged species (this matter will be discussed in the ENMR section below). Therefore the calculation of molar conductivity determined by NMR spectroscopy is usually higher than the experimental conductivity values. However this can provide information on transference numbers and ion pairing, through the calculation of the ionicity, which corresponds to Λ_M over Λ_{NE} .

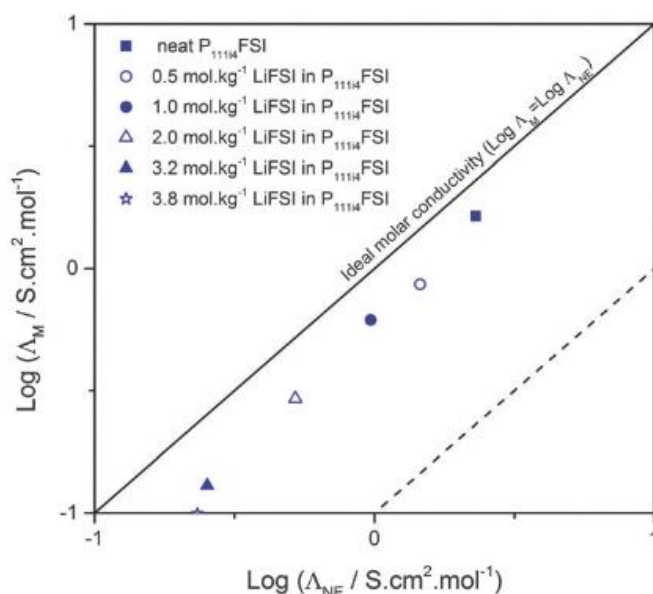


Figure 1-10: Ionicity plot of P₁₁₁₄ FSI and various Li FSI concentrations at 22°C with the ideal molar conductivity presented as a block line.⁷²

For example, a study carried out by Lee et al³⁹ showed the influence of the solvent addition on the properties of ionic liquids. Among other studies, they measured self-diffusion coefficients for all the species (also the solvent) of quaternary ionic liquids with and without solvent and with or without lithium FSI salt. By measuring the conductivity, and also by using the self-diffusion coefficients, they showed that the ratio of these quantities is less than unity, and therefore concluding that all the diffusive species within the IL do not contribute to the overall ionic conduction,

probing the presence of aggregates or ions pairings in the IL. Secondly, using the self-diffusion coefficients, they calculated the cationic transference numbers and lithium transference numbers showing that the cationic transference numbers are not affected by the addition of lithium, even if the lithium transference number is very low.

Some other work^{45,75} also reported self-diffusion calculations to understand different ion association but also factors like the solvation sphere around the lithium.

1.II.3 HOESY

While ionic conductivities and even diffusion coefficients for individual ionic species can be measured experimentally in ILs relatively easily as shown above, these do not provide much insight into the molecular-level ionic transport mechanism or how that is related to the IL structure. Molecular dynamics (MD) simulations are extremely useful in this regard, but in this case some form of experimental verification is important. In order for a better fundamental understanding of the ion transport mechanisms of ionic liquids, NMR spectroscopy is a powerful tool. Numerous research groups have focused on NMR spectroscopy in order to study the ion associations in ILs. One of these NMR techniques, called HOESY (Heteronuclear Overhauser Effect Spectroscopy, see section 5), gives information on through-space interactions between different nuclei, which can theoretically provide information on how the ions are arranged relative to one another, their average distances and their dynamics.^{17,76,76-82}

An example HOESY IL study is that carried out by Castiglione et al⁷⁰ on the C₄mpyrTFSI system with LiTFSI salt added. As shown in Figure 1-11, some two-dimensional ¹H-¹⁹F and ¹H-⁷Li HOESY NMR spectra were obtained. Each peak on the top represents a different ¹H environment on the pyrrolidinium cation, while the peaks on the left represent the ¹⁹F or ⁷Li NMR signals (only one chemical environment in each case).

Literature review

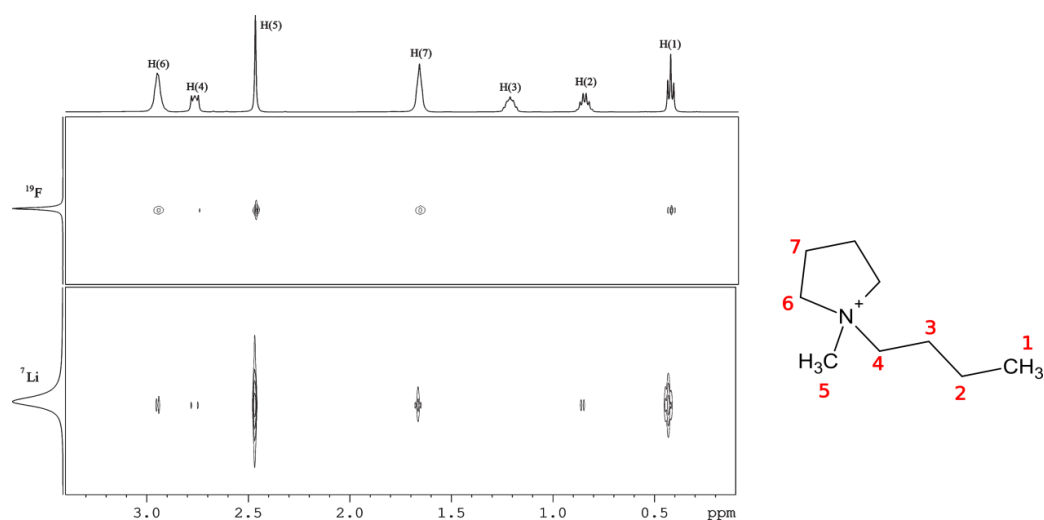


Figure 1-11: Contour plots of $\{^1\text{H}-^{19}\text{F}\}$ (top) and $\{^1\text{H}-^7\text{Li}\}$ (bottom) HOESY NMR spectra. The horizontal spectrum at the top shows the ^1H NMR spectrum and C₄mpyr molecule labelled on the right.⁷⁰

The cross-peaks, *i.e.*, the signals shown as contours in Figure 1-11, occur when the corresponding hydrogen site is close in space to the lithium or fluorine, allowing the magnetization to be transferred between them. The assumption made is that the stronger the cross-peak intensity, the closer these nuclei are on average. These experiments were carried out on a system $[\text{LiTFSI}]_{0.1}[\text{C}_4\text{mpyrTFSI}]_{0.9}$ and suggest that the molecular environment experienced by the Li^+ and TFSI^- ions are similar. However, the cross peak intensity also depends on the relative numbers of protons present and no quantitative analysis was carried out.

Another more recent study, also carried out by Castiglione et al.¹⁷, considered $[\text{LiTFSI}]_{0.1}[\text{C}_3\text{mpyrTFSI}]_{0.9}$ and $[\text{LiTFSI}]_{0.1}[\text{C}_3\text{mpyrFSI}]_{0.9}$. This time a more quantitative analysis was carried out. Multiple HOESY experiments were made with different mixing times, *i.e.*, the time over which the magnetization transfers from one nucleus to the other. Some examples of $^1\text{H}-^{19}\text{F}$ HOESY results plotted as cross-peak intensity against mixing time (called a build-up curve) are shown in Figure 1-12.

Literature review

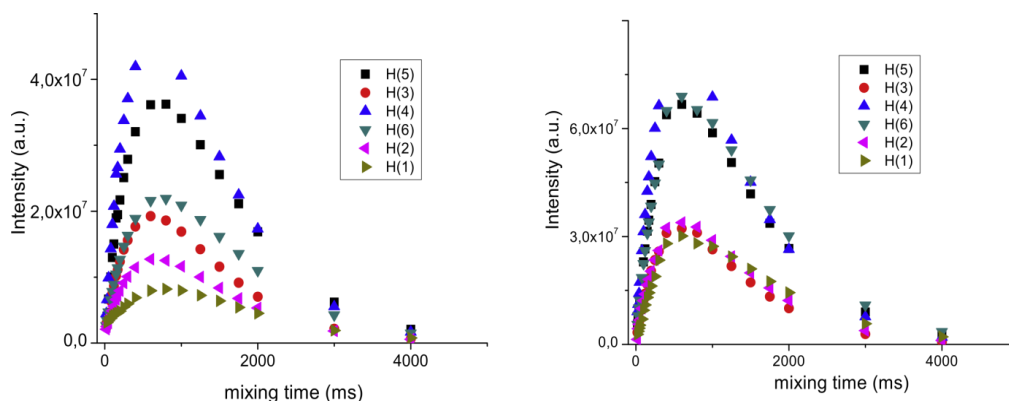


Figure 1-12: $\{^1\text{H}-^{19}\text{F}\}$ HOESY build-up curves for $\text{C}_3\text{mpyrTFSI}$ (left) and $[\text{LiTFSI}]_{0.1}[\text{C}_3\text{mpyrTFSI}]_{0.9}$ (right).¹⁷

In the initial part of the build-up curve, the signal intensity increases due to the magnetization transfer between the nuclei. At longer mixing times, the intensity decreases due to nuclear relaxation. In order to avoid the relaxation effects, Castiglione et al. fitted the beginning of the build-up curve from 25 to 150 ms of mixing time by a linear function in order to extract a measure of the interaction strength from the slope as shown in Figure 1-13.

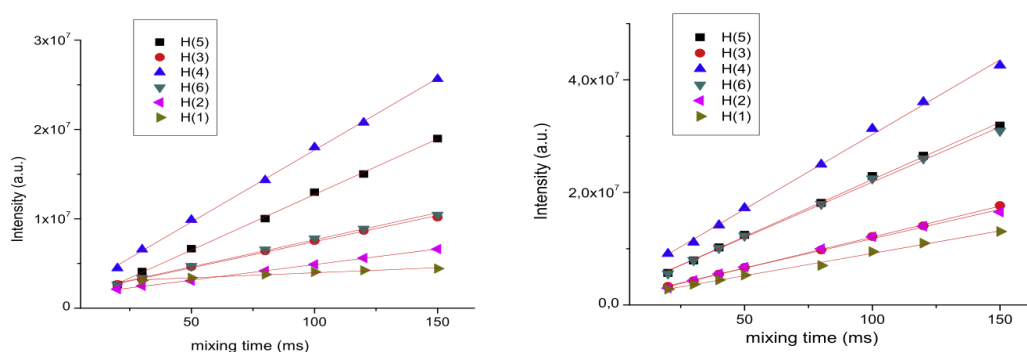


Figure 1-13: Linear fit of HOESY intensities for $\text{C}_3\text{mpyrTFSI}$ (left) and $[\text{LiTFSI}]_{0.1}[\text{C}_3\text{mpyrTFSI}]_{0.9}$ (right).¹⁷

These interaction strengths (measured directly from the slope of the linear fits) were normalized to the highest value. In Figure 1-14 the molecular structure of the cation is wrapped in shaded ellipsoids with a color code corresponding to the strength of the $^1\text{H}-^{19}\text{F}$ interaction determined in this way, red for strong and blue for medium/weak. These numbers were then interpreted as reflecting the average $^1\text{H}-^{19}\text{F}$ distances, with higher numbers reflecting closer $^1\text{H}-^{19}\text{F}$ associations. This interpretation suggests that the addition of LiTFSI induces structural change in the IL,

causing the anions to show greater associations with the whole pyrrolidinium ring rather than just with the sites closest to the nitrogen.

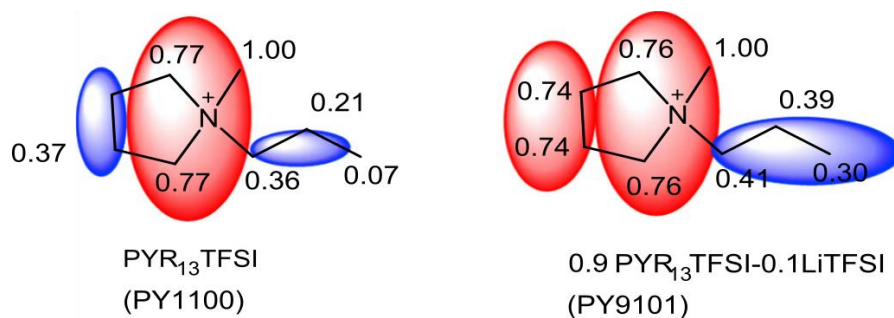


Figure 1-14: Illustration of the normalized $\{^1\text{H}-^{19}\text{F}\}$ HOESY interaction strengths for $\text{C}_3\text{mpyrTFSI}$ (left) and $[\text{LiTFSI}]_{0.1}[\text{C}_3\text{mpyrTFSI}]_{0.9}$ (right)¹⁷.

In 2012, Giernoth et al.⁸³ showed that these HOESY build-up curves can be fitted more reliably using a non-linear function that takes into account the NMR relaxation rates of the nuclei involved. The original equation, derived from the fundamental Solomon equations⁸⁴, uses a single relaxation rate (R).

$$NOE_H\{F\}(\tau) = \frac{1}{2} e^{-(R-\sigma_{HF})\tau} (1 - e^{-2\sigma_{HF}\tau})$$

Equation 1-3

In this equation, it is assumed that all protons and fluorine-19 nuclei have the exact same relaxation rate. The quantity σ is known as the “cross relaxation rate” with dimensions of s^{-1} . This parameter quantifies the HOESY interaction strength, and is discussed more in chapter 2. III. M_0 represents the total magnetization involved in the transfer.

Giernoth modified the HOESY equation to take into account the different relaxation rates of the nuclei:

$$NOE_H\{Li\}(\tau) = M_0\sigma \frac{2\sinh(\Delta\tau)}{\Delta} e^{-\frac{(R_{H,1}+R_{Li,1})\tau}{2}}$$

$$\Delta = \sqrt{\frac{R_{(H,1)}^2 - 2R_{H,1}\cdot R_{Li,1} + R_{Li,1}^2 + 4\sigma_{H,Li}^2}{2}}$$

Equation 1-4

By fitting the build-up curve using this equation, Giernoth et al. demonstrated that a better fit can be obtained than with the first equation (Figure 1-15). The approximation of linear behaviour is then only appropriate for very short mixing times and was suggested to be suitable for a qualitative interpretation of the interaction strength or inter-nuclear distance.

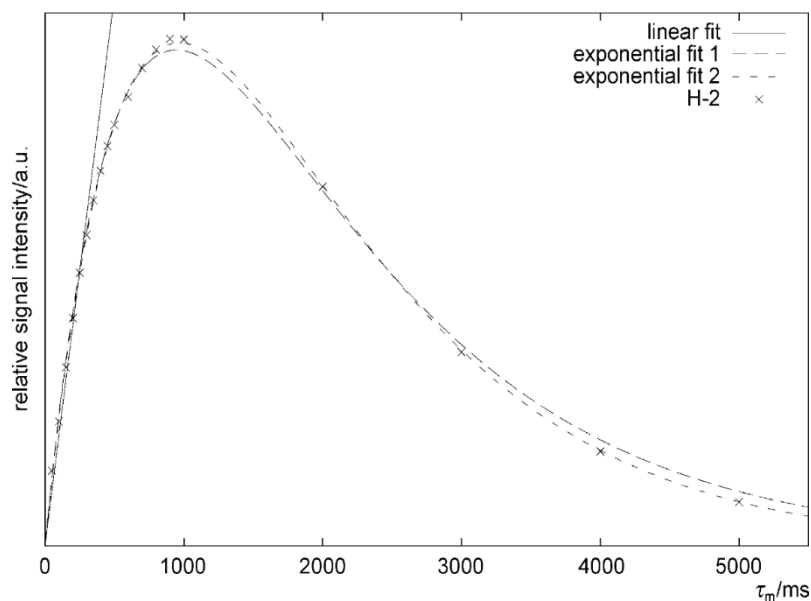


Figure 1-15: Mathematical fits of the relative signal intensities for the H-2 proton of neat [Bmim] BF₄, corresponding to three different equation⁸³

However, while this fitting allows the HOESY interaction strength to be determined *via* the extraction of a value for σ , there remains some uncertainty that this value can be simplistically interpreted as a qualitative measure of the average distance between the nuclei involved.

In 2013 a study by Gabl⁸¹ et al highlighted a new theory regarding the interpretation of HOESY data in liquids and in particular in ILs. The magnetization transfer in HOESY is mediated by the dipolar coupling interaction, which has an r^{-6} dependence where r

is the inter-nuclear distance. It is therefore commonly assumed that this is a highly localized interaction and that the magnetization transfer will not occur between nuclei that are far apart. Interestingly, the theory by Gabl et al reveals that for nuclei on different ionic species with close resonance frequencies, this rule may not be followed and a long range effect can appear and follow a r^{-n} dependence with n between 1 and 6. This implies that HOESY data obtained from nuclei like ^1H and ^{19}F (which are close in frequency) will in fact be much more difficult to analyse, and the cross relaxation rate σ extracted from the fitting much more difficult to interpret.

Even more challenging is to convert the experimentally obtained σ values into inter-nuclear distances. Since the ions in ILs are dynamic and the HOESY magnetization transfer occurs *via* nuclear relaxation processes driven by these dynamics, the use of data obtained from MD simulations (specifically the spectral densities of these motions) will be needed to achieve this. To the best of our knowledge, HOESY data has not been quantitatively linked with MD simulations in IL studies thus far.

In addition to the few examples described above, some other HOESY studies were carried out on ionic liquids samples. In order to get more insights about ion correlations in ionic liquids, we can consider the publication of Lingscheid *et al.*⁸⁰ who studied different imidazolium systems, choosing the butyl-imidazolium and the ethyl-imidazolium with either BF_4 or PF_6 , and with different solvents, either CD_2Cl_2 or $\text{DMSO-}d_6$. General proton notation can be seen in Figure 1-16.

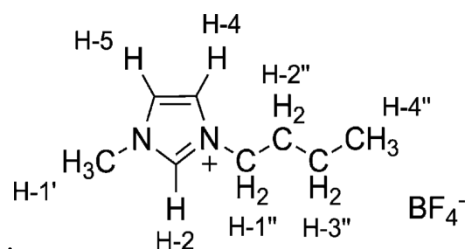


Figure 1-16: General assignment of the protons for imidazolium⁸⁰

For these systems, ^1H - ^{19}F experiments were carried out, and cross relaxation values were extracted as shown in Figure 1-17. Two main conclusions were made by the authors. First, no significant differences in terms of cross relaxation rates NOE intensities were observed between samples with BF_4 as a counter anion and those with PF_6 . However, differences were found when changing the solvent, first of all the

Literature review

signal is a bit more intense in CD_2Cl_2 as opposed to those in $\text{DMSO-}d_6$, which can be explained by the lower polarity of the solvent CD_2Cl_2 , leading to stronger ion pairings and thus stronger NOE signal. Nevertheless, authors explained that in comparison to a dilute sample, the neat sample shows more intense signal and greater differences between individual cross signals. Secondly, they noticed that the cross relaxation rates trends for the neat and the solution ILs are very similar as we can see in Figure 1-17. The strongest correlations between the cation and the anions are seen for H2 and then H1' protons, and then followed by H4 and H5. In fact the weakest interaction can be observed from the protons on the alkyl chain. However, this way of comparing normalized cross relaxation rate by the highest cross relaxation rate value is controversial. This thesis will in fact point out that normalizing cross relaxation rates with the maximum value on each specific system can't be meaningful and can lead to misunderstanding.

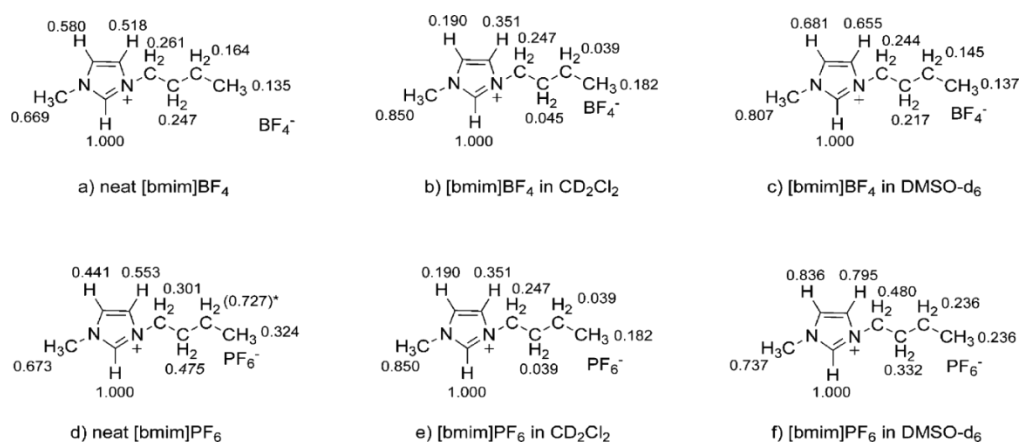


Figure 1-17: Relative cross relaxation rates between the protons and the ^{19}F nuclei on the anion. In each case the strongest interaction (H-2) has been used for normalization. * Unrealistic high value, most possibly due to an experimental error.⁸⁰

Another interesting publication by Le *et al*³⁹, reports the interactions in a dilute ionic liquids system, an ammonium TFSI (N_{1116} TFSI) doped with Li TFSI and diluted with ethylene carbonate (EC). The cation structure is represented and labeled on Figure 1-18, alongside a $^1\text{H-}^7\text{Li}$ HOESY experiments. A strong correlation with the N-CH₃ can be observed, as well as a correlation with the solvent, but no transfer is observable on the alkyl chain. According to the authors, after having recorded the HOESY experiment at different mixing time, as shown in the inset of Figure 1-18, the two sites correlating with the lithium have a similar intensity, highlighting that in this

specific system, the lithium is solvated with the EC but also that there are ionic clusters with the TFSI anion.

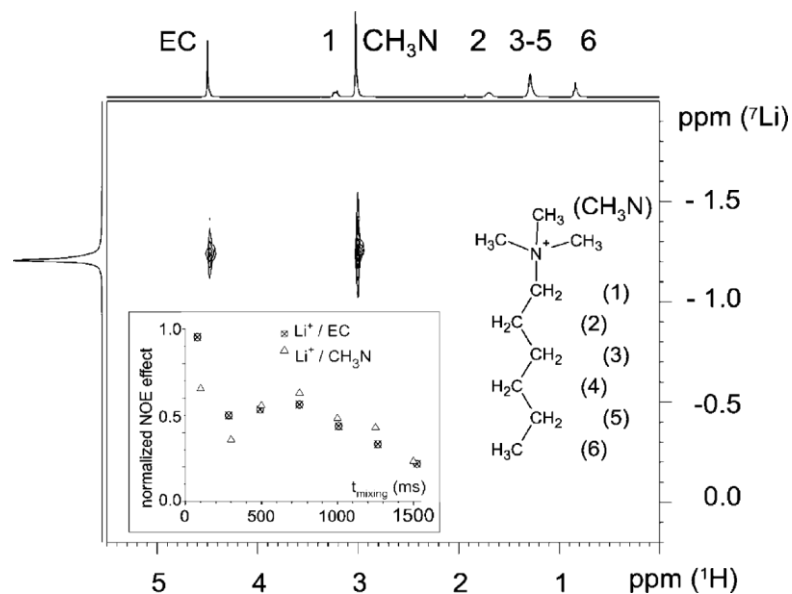


Figure 1-18: ^7Li - ^1H HOESY spectrum of $\text{N}_{1116}\text{TFSI} + \text{LiTFSI}$ measured at 313 K. ^7Li and ^1H spectra are presented as 1D traces, with assignments (mixing time = 500 ms, $T = 313$ K). Inset: build-up magnetization for ammonium CH_3N site and EC site normalized by the effective number of hydrogens on each site.⁵⁰

In fact the two described publications from Castiglione *et al*^{17,70}, come from a series of works^{17,28,43,70} following an interesting progression. In these works, they began to focus on three samples²⁸ as shown in Figure 1-19, the *N*-methyl-*N*-butyl-pyrrolidinium (C_4mpyr) cation, with three different types of anion, bis(trifluorosulfonyl)imide (TFSI), the bis(pentafluoroethanesulfonyl)imide (BETI) and the (trifluoromethanesulfonyl)(nonafluorobutanesulfonyl)imide (IM_{14}). As shown on Figure 1-20 and Figure 1-21, they carried out some ^1H - ^{19}F HOESY experiments on these samples.

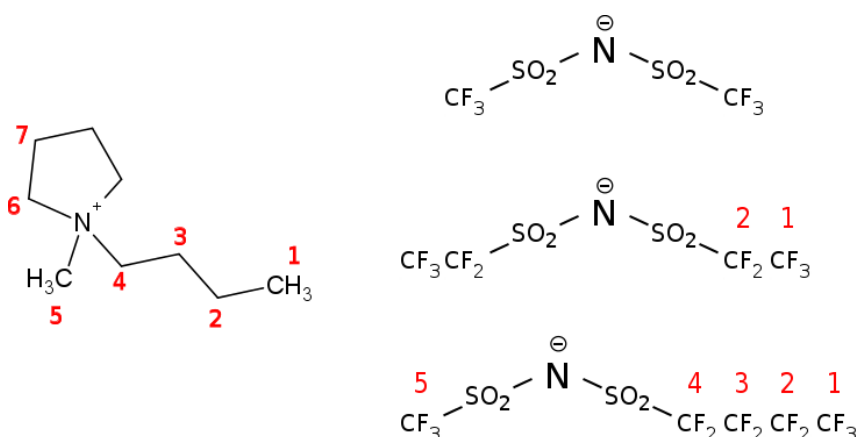


Figure 1-19: Representation and general assignment of different ions, Left: C₄mpyr cation. Right: TFSI- (top), BETI- (middle), and IM₁₄- (bottom) anions²⁸

From the HOESY spectra for C₄mpyr TFSI at one specific mixing time, shown in Figure 1-20, they concluded that the TFSI anion is close to the hydrogen sites H₆, H₇ and H₅, thus close to the protons belonging to the pyrrolidinium group and the N-methyl group of the cation (Figure 1-19), and as the NOE intensities related to the interactions with H₂, H₃ and H₄ are below the noise level, authors suggest that thus there is almost no interactions with the tail of the alkyl chain. In fact, according to the HOESY results, similar conclusions can therefore be reached about the two other samples as similar HOESY patterns are observed on both CF₂ and CF₃ groups of sample 2 (C₄mpyr BETI), but also on the isolated CF₃ group of sample 3 (C₄mpyr IM₁₄). Therefore authors suggest that these results highlight that the different anions studied are all interacting with the C₄mpyr cation. Furthermore, they are showing the anion belong indeed to the coordination shell of the cation, but at a specific place, around the nitrogen.

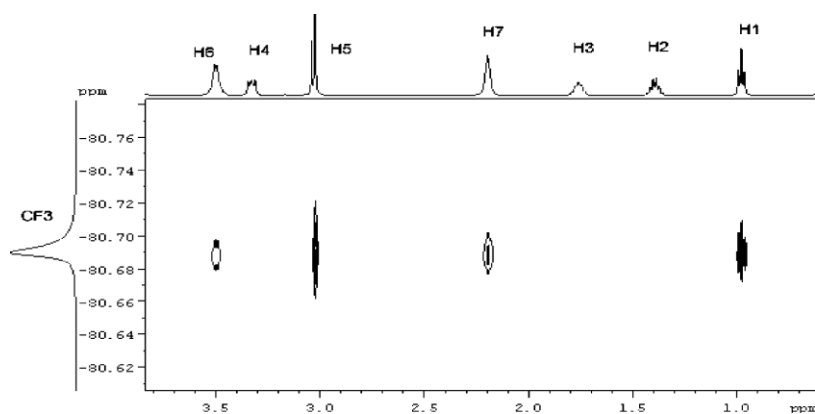


Figure 1-20: Contour plot of the ¹H-¹⁹F HOESY experiment to C₄mpyr TFSI. Atom numbering according to Figure 1-19.²⁸

Literature review

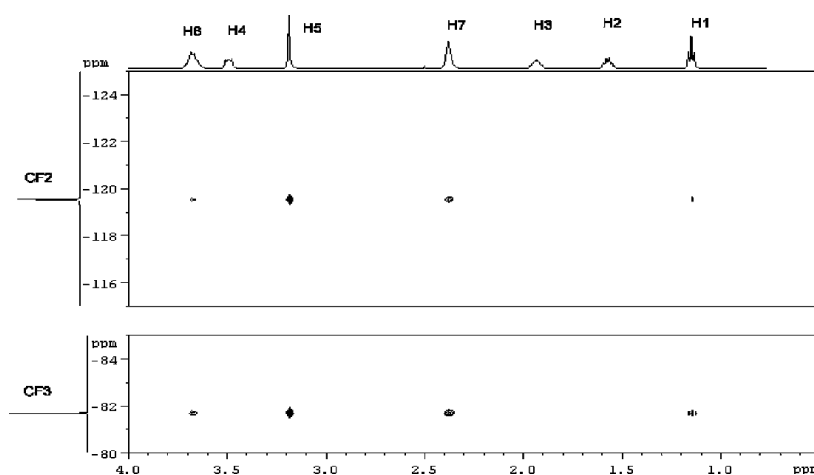


Figure 1-21: Contour plot of the ^1H - ^{19}F HOESY experiment on Campyr BETI. Atom numbering according to Figure 1-19.²⁸

This work was followed by a study of the specific C_4mpyr TFSI system⁷⁰, but this time, also mixed with Li TFSI. These results were explained earlier, and as shown in Figure 1-11, they are confirming the previous HOESY ^1H - ^{19}F results of the corresponding neat sample. But interestingly, here, as still shown on Figure 1-11, we can see that the ^1H - ^7Li HOESY experiments show the same trend as the ^1H - ^{19}F HOESY experiments. Therefore, the authors suggest that despite the presence of the positive charge on both cations, the lithium is strongly coordinated to the TFSI, and thus the TFSI and the lithium, experience a similar spatial coordination with the C_4mpyr .

The next publication following these works⁴³, presented similar results but this time on the C_4mpyr BETI and C_4mpyr IM₁₄ samples doped with respectively Li BETI and Li IM₁₄. As a NOE correlation can be extracted between the lithium and cation, despite the positive charge on both, the authors claimed that these results confirmed that the negatively charged complexes such as $[\text{Li}(\text{X})_2]^-$ ($\text{X}=\text{TFSI}, \text{BETI}, \text{IM}_{14}$) exist in these electrolytes.

The last publication of the series has already been mentioned¹⁷. This time Castiglione *et al*, studied the C_3mpyr TFSI and C_3mpyr FSI systems mixed or not with Li TFSI, and a mixture between the C_3mpyr TFSI, the C_3mpyr FSI and the Li TFSI this time by doing a series of HOESY experiments and extracting the cross relaxation rates by linearly fitting the first few points. Both ^1H - ^{19}F HOESY and ^1H - ^7Li HOESY experiments were reported, and the ^1H - ^{19}F HOESY experiments show a similar trend to the previously studied samples with (as explained earlier) a greater anion-cation association when

Li TFSI is added. However, by taking a look at the ^1H - ^7Li HOESY experiments an interesting feature and conclusion can be found. Indeed, in Figure 1-22 (the nomenclature corresponding to the sample composition is detailed in the figure), data of the PY9101 (left panel) suggest that the Li show great association to the hydrogen close to the nitrogen, which can be explained by chelation by TFSI ligands which are preferentially located around the positive charge of the nitrogen. These results are supported by lithium cation associations on sample PY9191 (right panel), as this shows similar association, albeit slightly weaker, which can be explained by the lesser hydrogen bonding properties of the FSI ligand compare to the TFSI ligand.

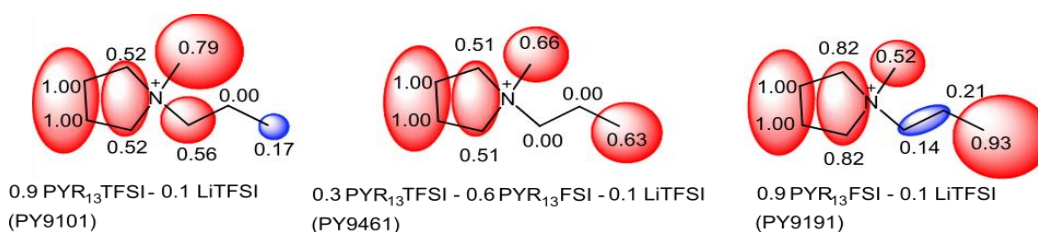


Figure 1-22: Graphical sketch of the normalized $\{^1\text{H}-^7\text{Li}\}$ NOE intensity for the two mixtures 0.9 C₃mpyrTFSI-0.1 LiTFSI (left, PY9101) and 0.9 C₃mpyrFSI-0.1 LiTFSI (right, PY9191). The results for the intermediate composition 0.3 C₃mpyrTFSI-0.6 C₃mpyrFSI-0.1 LiTFSI (PY9461, central panel) are also reported. The numbers correspond to the extracted cross relaxation rates from the linear fitting. The shaded volumes are proportional to the “probability of presence” of the lithium atoms. The red color indicates normalized intensity values greater than 0.5.¹⁷

However, when the authors comparing PY9101 and Py9191 (respectively left and right panel), one can note, that a striking feature arises; indeed, in Py9191, a high NOE intensity can be seen on the hydrogens at the end of the alkyl chain. In fact this feature can be also seen on PYR9461 (middle panel) although somewhat weaker. Thus, the authors suggest that this interaction involving the end of the alkyl chain is modulated by the TFSI/FSI ratio, potentially having consequences on the structure and on the size of the first solvation shell of the ions. However, one should note that again, normalizing cross relaxation rates from the highest value on each specific system is not appropriate if we want to compare one system to another.

1.II.4 ENMR

Literature review

Electrophoretic NMR spectroscopy was first shown experimentally by Holz et al^{85–89} and Johnson et al^{90–92}, but despite being its obvious benefits for studying ionic systems, is not a widely used technique due to the lack of commercial instrumentation as well as significant experimental challenges, such as electro-osmosis, convection, weak signal strengths and so on. In recent years much effort has been put into overcoming these technical problems. ENMR spectroscopy experiments are similar to traditional pulse field gradient diffusion experiments, using spin echoes with gradient pulses in order to detect the displacement of the moving nuclei along the magnetic field gradient, due to loss of intensities created by an incomplete refocusing. In ENMR spectroscopy an electric field is also used which results in a coherent component due to the migration of the nuclei along the electric field. Therefore, this displacement will induce a phase shift corresponding to the mobility of the studied ions under the applied electric field.

As explained above, in the case of fully dissociated ions, such as in diluted salt solutions, the self-diffusion coefficients can be used to calculate the conductivity. Concentrated ionic liquids, however, can show strong associations leading to species such as neutral ion pairs or clusters, causing huge discrepancies between the conductivity observed by impedance spectroscopy and that calculated using the self-diffusion parameters. Therefore, the electrophoretic mobility parameter should be more relevant to conductivity, as it corresponds only to the charged species. The conductivity can be thus derived directly from the ENMR, and in turn be used to calculate the transference numbers and potentially ion pairing, if compared with conductivity extracted from self-diffusion parameters.

As a deeper understanding of ion association and transference numbers can lead to a better understanding on the conduction mechanism, several studies have reported the calculation of transference number through self-diffusion measurements or mobility measurements^{12,75,93–95}. The calculations of the mobility using ENMR experiments^{53,75,92,93,96–99}, are still tricky. Indeed, a small phase shift is complicated to extract. In fact, due to the presence of metal electrodes in the cell, a lot of electrical noise can be picked up by the radiofrequency NMR coil. In addition, non-electrophoretic artefacts, mostly thermal convection or electro-osmosis, can be

important. One easy way to improve the phase shift is to increase the gradient, but unfortunately increasing the gradient further reduces the extracted signal, and exacerbates convection effects. The other potential parameters, like the distance between the electrodes or the applied voltage, can create additional problems such as increasing the electro-osmosis or increasing convection. Thus there is a need for improved cell designs and improved pulse sequences for ENMR^{96–99}.

For example, one current cell design is a cylindrical sample, as shown in Figure 1-23 (left), with palladium electrodes at the top and bottom. Insulation tubes around the wires avoid short circuits. As can be seen, in Figure 1-23 (right), Zhang et al completed this cell by adding capillaries between electrodes to avoid convection.

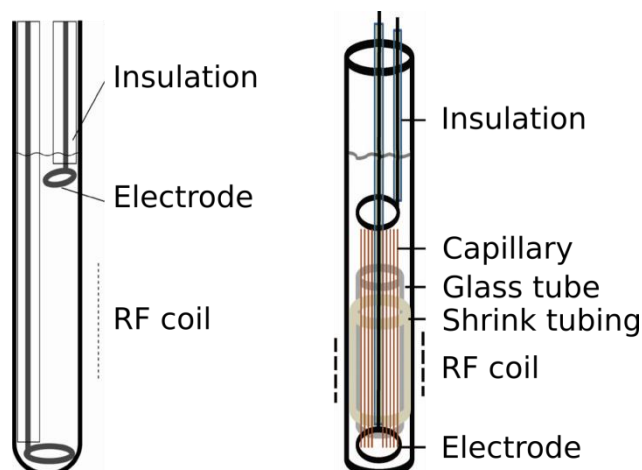


Figure 1-23: Classical cell design with insulators for the electric cables (left)⁹⁸, similar cell design but with capillaries and shrink tubes in order to avoid the convection (right)⁹⁷

A recent study carried out by Gouverneur *et al*¹⁰⁰ shows a very interesting observation of Li ion transport in lithium based ionic liquids. They studied by ENMR the mobility and transference numbers of ions in two different ionic liquids, LiTFSI/EMIMTFSI and LiBF₄/EMIMBF₄. In order to extract the mobilities for all types of ions, they carried out the experiments as shown in Figure 1-24 with an applied magnetic field gradient. As the phase shift of the signal is due to the mobility which is magnetic field dependent, the stronger the gradient is, the bigger the phase shift will be. Thus they recorded experiments at different gradient strengths in order to extract a wide range of phase shifts. By doing a linear regression of these curves, they could extract the mobility with only a series of spectra at different gradient strength. Furthermore, this data representation allows the distinction of the drift direction of

the species due to the sign of the slope of phase shifts values as the phase shift is also dependent on the ion directions (towards the cathode or anode).

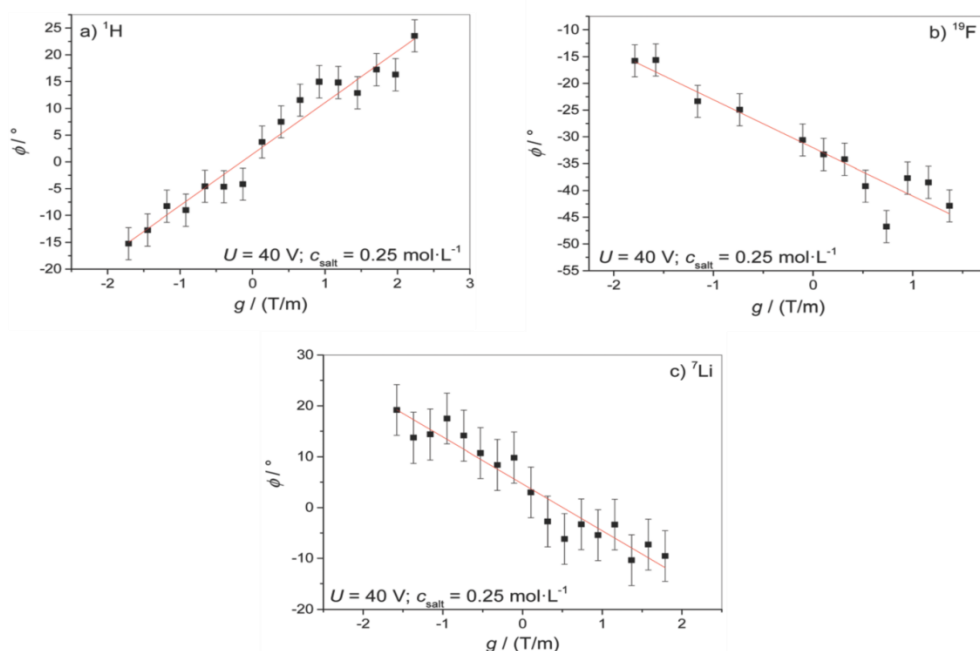


Figure 1-24: Phase in dependence on the gradient strength in $0.25 \text{ mol L}^{-1} \text{ LiBF}_4/\text{EmimBF}_4$ for (a) ^1H , (b) ^{19}F and (c) ^7Li with $\Delta D_{\text{drift}} = 300 \text{ ms}$ for all nuclei. Errors are estimated at $\pm 3^\circ$. The red line results from a linear regression.¹⁰⁰

By taking the modulus of the mobilities, one can notice from Figure 1-25 that the mobility of the cation is similar in both samples, but the mobility of the anion is higher with BF_4 rather than TFSI. This can be explained by the relative smaller size of BF_4 compared to the TFSI. Now we can discuss the mobility values of both systems, upon lithium addition. In case of the TFSI system, the addition of 25% of lithium salt led to a decrease of the EMIM mobility by 25%, but had no further influence upon 50% of lithium salt addition. Interestingly, this effect is the reverse on the anion, which was not significantly affected by a 25% of salt addition, but decreased by almost 50% on the addition of 50% of lithium salt. These effects can be related to the formation of large clusters at high concentrations, probably involving lithium.

In regard to the BF_4 system shown in Figure 1-25 b), compared to the TFSI system in Figure 1-25 a), the mobility of the cation is almost unaffected upon lithium addition, compared to the anion mobility with increasing lithium addition. This impact on the anion mobility alone can be explained by strong coulombic interactions between lithium and BF_4 . One should note that all of these results indicate a correlated

migration between the lithium and the anion, but also that these results are consistent with previous studies of ion diffusion^{28,100,101}. Furthermore in Figure 1-24 b) we can see that the anion travels in the opposite direction to the cation EMIM on Figure 1-24a), but interestingly, as shown in Figure 1-24 c), the lithium travels in the same direction as the cation.

Additional parameters were extracted in this work such as transference numbers or the effective charge of the ions, all of which can lead to a better understanding of the Li transport mechanism.

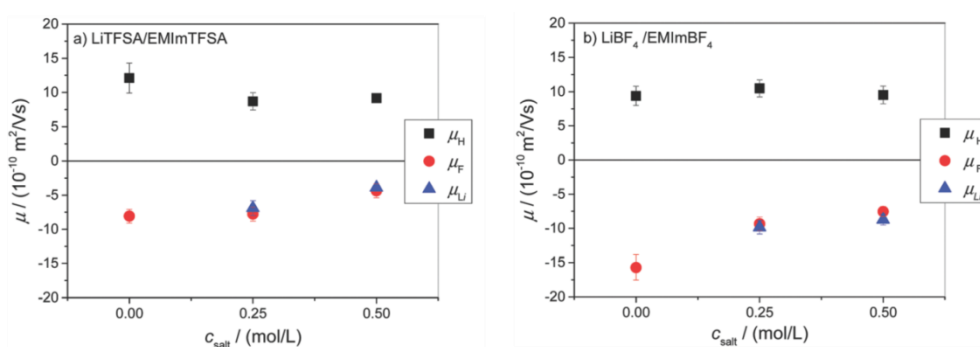


Figure 1-25 : The electrophoretic mobility in (a) LiTfSA/EMImTfSA and (b) LiBF₄/EMImBF₄ in dependence of the lithium salt concentration. Black squares: ¹H, red circles: ¹⁹F, blue triangles: ⁷Li. Error bars are calculated from the standard deviation¹⁰⁰

Despite the work described above, many challenges remain in developing ENMR apparatus and techniques for IL studies. Indeed, a very high voltage as still used for ionic liquids, such as 100-200 V and a big distance between electrodes, up to 4-5 cm which currently does not correspond to realistic enough cell parameters. Also, compared to standard diffusion experiments, the signal to noise ratio is usually very low, due to some field inhomogeneity created by the electrical current flow⁹⁹, but also due to the presence of the electrodes. Therefore, slow diffusion and mobility are difficult to measure, particularly for viscous sample such as ionic liquids.

1.II.5 DNP

NMR can suffer from the insensitivity of certain nuclei, either due to their low gyromagnetic ratios or low abundance of the observable isotopes. One way to

overcome this problem is to use higher magnetic field strengths, but these results in only incremental gains in polarisation. Another way is to use hyperpolarization techniques, where the nuclear polarization is enhanced far beyond the Boltzmann equilibrium by the manipulation of the spin state. The most popular current method is dynamic nuclear polarization (DNP), originally predicted by Albert Overhauser in 1953¹⁰², and first demonstrated experimentally by Carver and Slichter¹⁰³. DNP uses gyrotron microwave (MW) sources in order to enhance the polarization of nuclei in samples containing radicals (unpaired electrons). This enhancement is due to the irradiation of the electron spin, usually added through radicals such as TEKPOL or TOTAPOL (1-(TEMPO-4-oxy)-3-(TEMPO-4-amino)propan-2-ol), resulting in a transfer of polarisation to the nuclei *via* one or more potential mechanisms such as the Overhauser Effect, the solid effect, the cross effect or thermal mixing. Despite being discovered and verified more than half a century ago, DNP was until relatively recently not a widely used technique due to the lack of high power microwave sources. The new development and implementation of high field gyrotrons up to the terahertz frequency range led to the creation of high field DNP spectrometers, enabling the study of either liquid or solid state samples, the latter using Magic Angle Spinning (MAS)-DNP.

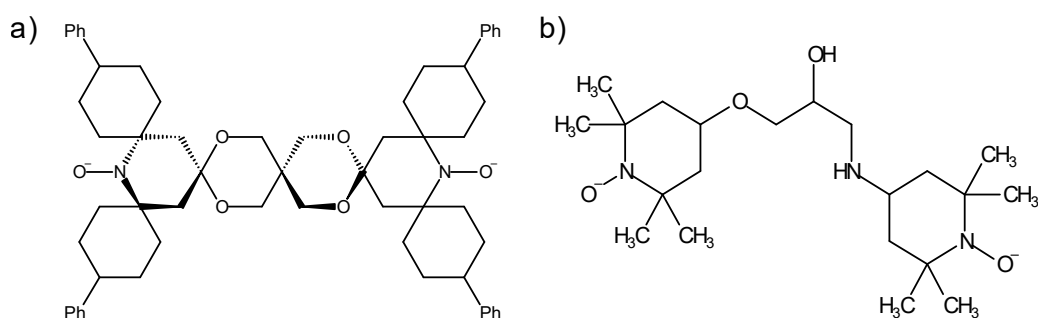


Figure 1-26: a) TEKpol bi radical and b) TOTAPOL bi radical molecular representation

As DNP is still a rapidly developing technology and methodology, a lot of current studies aim at developing the technique in terms of sensitivity. For example, researchers have reported improved signal enhancements, such as 50000 for fast dissolution DNP (dDNP)¹⁰⁴. One way to improve the signal enhancement is *via* the development of new radicals to increase the transfer¹⁰⁵. Also as the DNP transfer is generally much more efficient at very low temperatures (*e.g.*, 100 K which is achieved

by cooling with liquid nitrogen), one other area of research is to carry out DNP at even lower temperatures by using liquid helium¹⁰⁶. Such developments have enabled NMR spectroscopy studies of new systems that otherwise would not have been possible due to the lack of sensitivity, such as low concentration biological samples, solid surfaces, or insensitive nuclei such as ^{17}O .

Chandrakumar *et al*¹⁰⁷, carried out DNP NMR spectroscopy studies on ionic liquids using the electron-nuclear Overhauser DNP effect. In a three spin system as seen in Figure 1-27 a) one can observe a simple exponential build-up polarization curve of the signal enhancement due to the transfer from the electron spin to the nuclear spin. If an NOE transfer between the two nuclear spins is included the ODNP build-up curve will exhibit maxima or minima. This behaviour is due to the cross relaxation transfer occurring between the two nuclear spin, which is also an indication of nucleus proximity (similar to HOESY as described above).

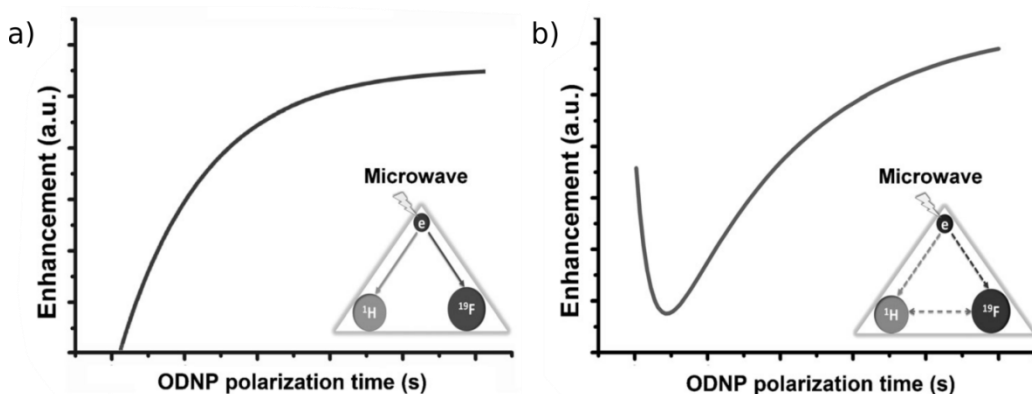


Figure 1-27: Schematic polarization build-up curves derived from the analytical solution of the Solomon equations in the case of: a) either one of two non-interacting two-spin systems (each comprising a different nuclear spin but a common electron spin); and b) a three-spin system (two interacting nuclear spins and an electron spin that interacts with both).¹⁰⁷

Chandrakumar *et al.* studied different IL samples, as shown on Figure 1-28. They observed that for the samples at 1:1 v/v mixture of BMIM-TFSI and benzene with 15 mM of galvinoxyl free radical, the ^{19}F build up was exponential, corresponding to the fact that the electron spin to nuclear spin transfer is predominant. When the same experiment was carried out on the pure BMIM-TFSI sample, without dilution, the build-up curve exhibited a minimum, which can be explained by ion clustering inducing some nuclear spin to nuclear spin transfer, *i.e.* the NOE effect.

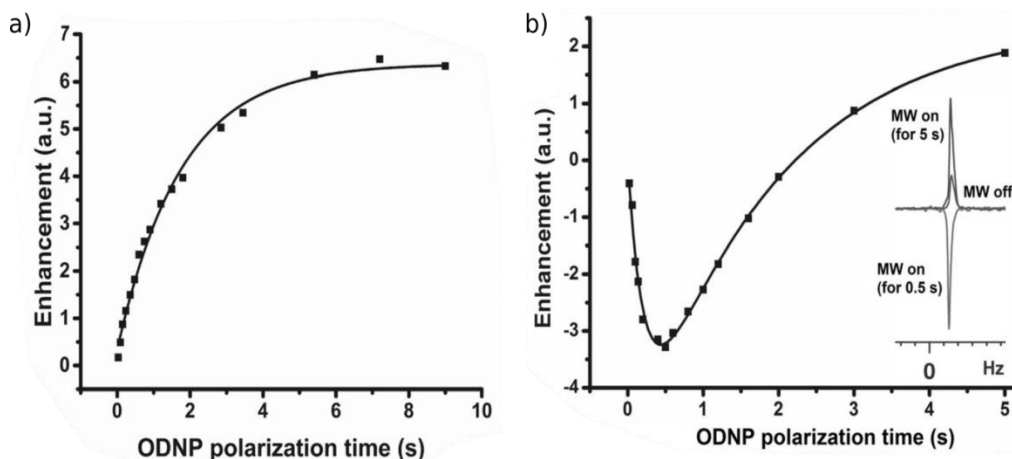


Figure 1-28: Polarization build-up curves of BMIM-TFSI with 15 mm galvinoxyl free radical for ^{19}F (a) and ^{19}F of a 1:1 v/v mixture of BMIM-TFSI and benzene (b). The inset in (a) displays ^{19}F spectra under Boltzmann conditions ("MW off") and under ODNP enhanced conditions ("MW on" for 0.5 s and 5 s polarization time, respectively). b) Displays the monotonic exponential build-up of ^{19}F polarization¹⁰⁷

1.III Conclusion and perspectives

It has been shown herein part of why ionic liquids raised a tremendous interest through the electrochemical community. The large number of potential systems makes the understanding of the internal structure and the ions motions unavoidable. Among all the techniques which can be used in order to study the ionic liquids structure, the nuclear magnetic resonance has already demonstrated the capability of extracting parameter such as the diffusion coefficient. However most studies only describe the behavior of individual species rather than an overall view of the system. Thus some research projects were oriented on the HOESY NMR experiments, which permit to study the interactions between different nuclei, and thus can lead to the interactions between ions, and then to distance extraction. Nevertheless, most of the studies only reported qualitative results. In order to be able to extract more quantitative results and to be able to compare systems on to another in a quantitative way, the HOESY experiment need to be developed both in the data acquiring, but also in the data processing. Other techniques such as the DNP or the ENMR experiments have the potential to correlate and complement quite well the results extracted by the HOESY experiments.

Chapter 2
Experimental NMR
theory and
methodology

2.1 Introduction

In order to study samples by NMR spectroscopy, magnetic nuclei are needed, meaning nuclei which will interact with the magnetic field. In the NMR magnet, the nucleus will interact with the main magnetic field B_0 . The magnetic moment μ of the nucleus interacts with B_0 with an energy described by Equation 2-1.

$$E = -\mu \cdot B_0$$

Equation 2-1

In a sample, all nuclei have their own magnetic moment pointing in a different direction for each of them. In fact these magnetic moments are characterized by a quantum property called spin S , and the magnetic moment and the spin are directly proportional (Equation 2-2), with γ corresponding to the gyromagnetic ratio

$$\mu = \gamma S$$

Equation 2-2

When these magnetic nuclei are put into a magnetic field, the Zeeman effect causes the nuclear spins to precess about the direction of the external magnetic field (Figure 2-1), at a characteristic frequency ω_0 for each nucleus, called the Larmor frequency, and described by Equation 2-3

$$\omega_0 = -\gamma B_0$$

Equation 2-3



Figure 2-1: Precession around the magnetic field¹⁰⁸

In a bulk sample, the distribution of spin orientations is initially random, but in a magnetic field B_0 , the individual magnetic moment of each nucleus will be affected by additional internal magnetic fields such as those arising from the surrounding nuclei, which will change their magnetic moment orientation. Over time, an anisotropic distribution of orientations will be created with magnetic moments along the field slightly more probable than orientations with magnetic moments opposed to the field. This creates a net bulk magnetization M_{eq} along the magnetic field, a state called thermal equilibrium (Figure 2-2).

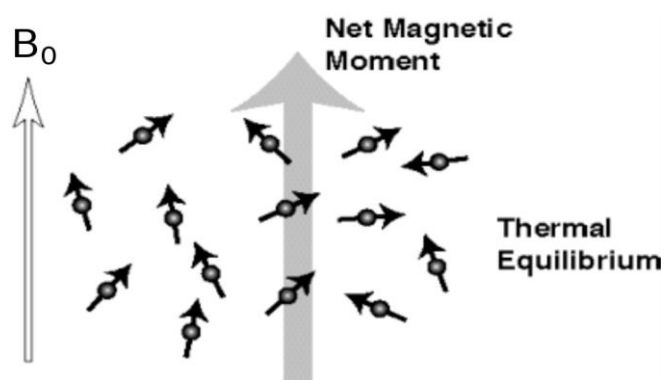


Figure 2-2: Net magnetization along the external magnetic¹⁰⁸

This process of rearrangement of magnetic moments in order to reach the thermal equilibrium is characterized by a time called T_1 , known as the longitudinal relaxation or spin lattice relaxation time. The timescale of the longitudinal T_1 relaxation is described by the following expression:

$$M(t) = M_{eq} \left(1 - e^{-\frac{t}{T_1}}\right)$$

Equation 2-4

Note that the T_1 parameter is not the time that the system takes to fully relax. According to the Equation 2-4, when $t = 5.T_1$, 99.3% of the whole equilibrium magnetization is recovered. In order to carry out quantitative NMR experiments, at least five times T_1 of the nuclei of interest is necessary between each experiment (scans). Otherwise, if only a qualitative experiment is needed, only 1.256 times T_1 is

required, as it will give the best sensitivity, and thus the best signal over noise ratio, as shown in Figure 2-3.

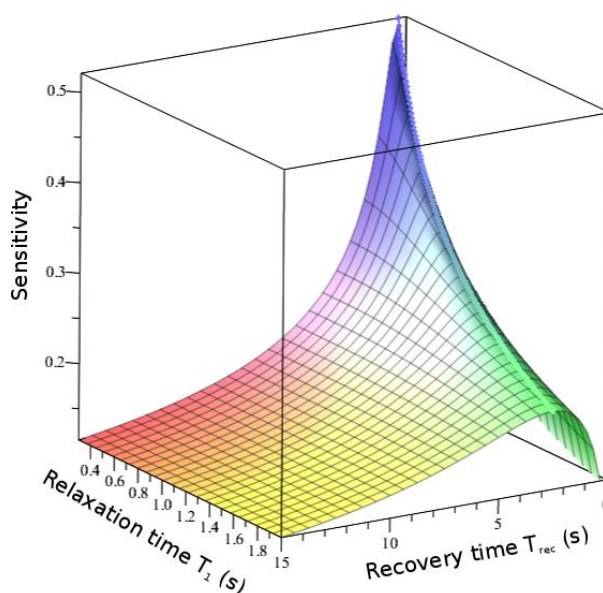


Figure 2-3: Sensitivity as a function of T_1 relaxation and recovery time

The principle of NMR is to apply a radio frequency pulse (RF) at the Larmor frequency, in order to create a rotation of the net magnetization away from the external magnetic field. The RF field changes the orientation of the spins which rotate around the RF field, modifying the angle of the net magnetization. After a 90° pulse the magnetisation precesses around B_0 , inducing an electric current in a wire coil near the sample. It is possible to detect this small oscillating current by using a sensitive detector. The detected signal is called the FID (free induction decay) and the Fourier transform of the signal gives the NMR spectrum on a frequency scale.

As the equilibrium situation has magnetization of size M_0 along the z axis and no transverse (x or y magnetization), by applying an electromagnetic pulse to tip the longitudinal magnetization vector through an angle of 90° , transverse magnetization is created as shown in Figure 2-4.

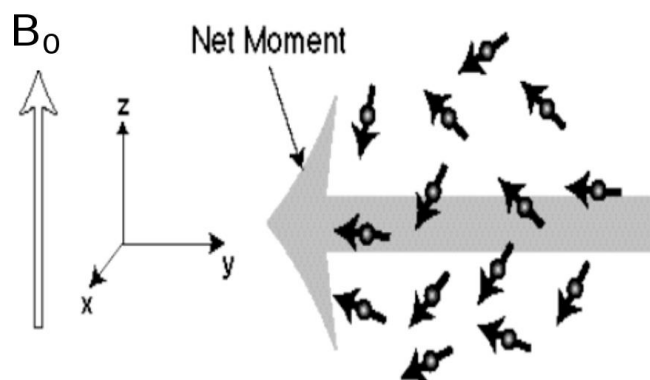


Figure 2-4: Net magnetization in the xy plan (transverse magnetization)¹⁰⁸

Over time, due to the fluctuating internal magnetic fields, relaxation will cause this transverse magnetization to decay away to zero. This relaxation process occurs in the xy plane, and is known as transverse relaxation, characterized by a time T_2 . The timescale of the transverse T_2 relaxation is described by the following expression:

$$M(t) = M_{eq} e^{-\frac{t}{T_2}}$$

Equation 2-5

In practice, the magnitude of B_0 is not perfectly the same in every position on the sample, and these slight differences in field in the sample are called inhomogeneities. Although these inhomogeneities are usually small, they can lead to an observable difference in Larmor frequency. Thus, individual magnetic moments will precess at slightly different frequencies. As some magnetic moments will therefore be faster and some slower, this is characterized in the transverse plane, by a dephasing between spins, thus leading to a shrinking of the net M_0 magnetization in the xy plane. The result of this effect is that M_0 will decay faster, and this decay of the observed FID is in fact characterized by a second parameter called T_2^* , corresponding to:

$$\frac{1}{T_2^*} = \frac{1}{T_2} + \frac{\gamma \Delta B_0}{2\pi}$$

Equation 2-6

In this expression, ΔB_0 is the variation in the external magnetic field experienced by the nuclei (the field inhomogeneity). Thus one should note that T_2^* is always shorter than (or equal to) T_2 .

2.II T_1 spin lattice relaxation

As explained earlier the T_1 parameter is very important for quantitative NMR, and it is also useful to measure for other reasons. A commonly used experiment for measuring T_1 is called the inversion-recovery experiment as shown in Figure 2-5

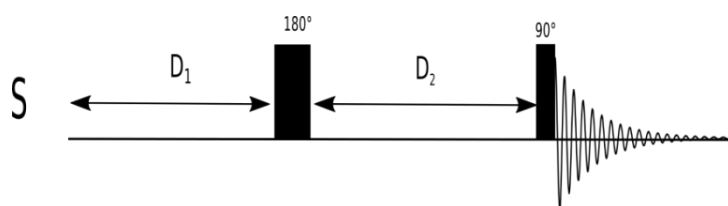


Figure 2-5: Inversion recovery pulse sequence (D_1 corresponds to the recycle delay between each experiments, in order for the magnetisation to reach back equilibrium before the new scan)

This experiment consists of a 180° pulse, which inverts the magnetization followed by a variable delay (D_2) before an excitation pulse (Figure 2-6). In order to measure T_1 , the D_2 delay is incremented. During D_2 the magnetisation relaxes along the z axis and the excitation pulse allows the size of the magnetisation vector to be measured during this process. For short D_2 , an inverted signal will appear and as the recovery time increases, the signal will pass through zero which at $D_2 = \tau_{\text{null}}$ and T_1 corresponds approximately to $1.44 \cdot \tau_{\text{null}}$.

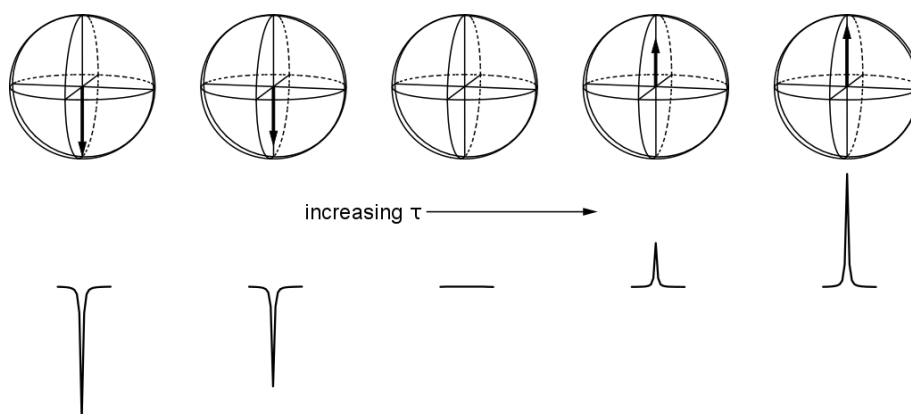


Figure 2-6: Evolution of the signal intensity due to longitudinal relaxation as function of D_2 , with the zero crossing⁶¹

2.III Relaxation theory

2.III.1 Spectral density

Relaxation is driven by statistical fluctuations in the internal magnetic fields that the nuclei experience over time. This can be caused by the rotational movements of molecules which modulate the interactions experienced by the relaxing spins.

Statistical fluctuations can be mathematically described by the autocorrelation function $G(\tau)$ which gives the time average of the difference between a spatial component of one spin's magnetisation between a time t and $t+\delta$. The autocorrelation function is usually assumed to take a simple, exponential form:

$$G(\tau) = \langle B_x^2 \rangle e^{-|\tau|/\tau_c}$$

Equation 2-7

Where B_x is the fluctuating magnetic field and the constant τ_c is called the *correlation time*. If a molecule rotates fast, and therefore experiences fast fluctuations, it will be characterised by a rapidly decaying autocorrelation function and a short τ_c . A slowly rotating molecule on the other hand has a large correlation time and a slowly decaying autocorrelation function.

Nuclear relaxation is driven by spin transitions caused by these randomly fluctuating fields. The transition probability between two spin states is dependent on the spectral density function $J(\omega)$, which is defined as the Fourier transform of the autocorrelation function. (Figure 2-7)

$$J(\omega) = \frac{\tau_c}{1 + \omega^2 \tau_c^2}$$

Equation 2-8

Specifically, the relaxation will depend on the value of the spectral density at particular frequency values (ω). For example at $\omega = 0$:

$$J(0) = \tau_c$$

Equation 2-9

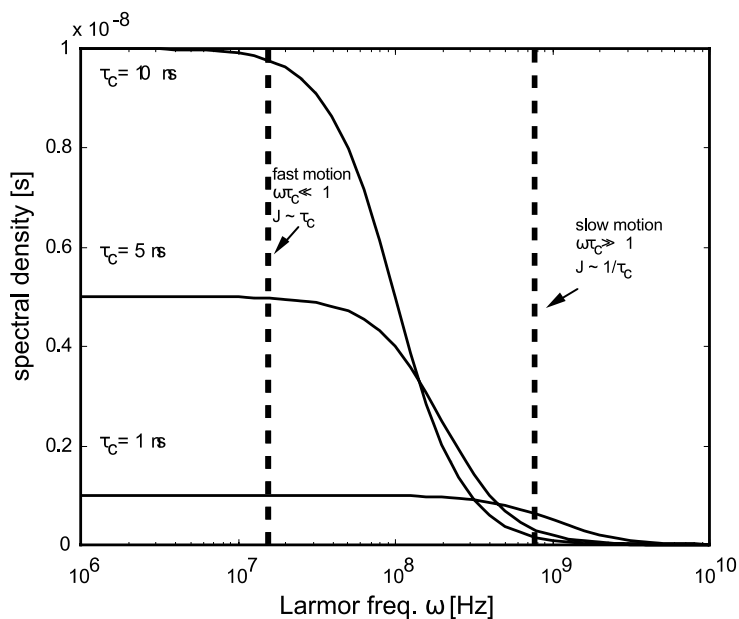


Figure 2-7: Spectral density representation (with different correlation time number) as a function of the Larmor frequency

2.III.2 Longitudinal relaxation against temperature

In fact, according to theory first derived by Bloembergen, Purcell and Pound (BPP)¹⁰⁹, the T_1 parameter, is in fact inversely proportional to the spectral density at the Larmor frequency $J(\omega_0)$:

$$T_1 \propto \frac{1}{\left(\frac{\tau_c}{1 + \omega_0^2 \tau_c^2}\right)}$$

Equation 2-10

According to this BPP theory¹⁰⁹, the constant of proportionality in the above expression depends on the nature of the interaction from which the fluctuating magnetic fields originate.

As τ_c is a temperature dependent parameter, the temperature dependence of $\log(T_1)$ can be plotted using the BPP equation and the Arrhenius equation (Equation 2-11):

$$\tau_c(T) = \tau_0 \exp\left(\frac{E_A}{RT}\right)$$

Equation 2-11

Therefore experimental plot of $\log(T_1)$ against temperature can be fitted and the correlation time and activation energy for the molecular motions causing the relaxation can be extracted. The results of this plot is a characteristic V shape as shown in Figure 2-8, with a minimum when the correlation time matches the inverse of the Larmor frequency, thus when $\omega_0\tau_c=1$.

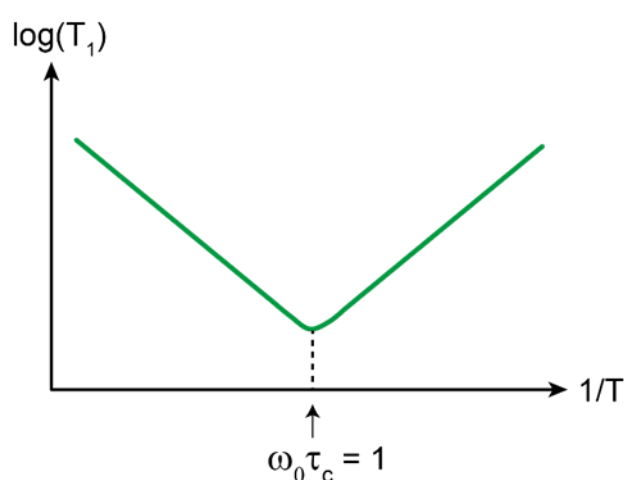


Figure 2-8: The temperature dependence of the T_1 parameter (figure taken from Dr Luke O'Dell lectures note)

However, in practice, the T_1 relaxation of a nucleus can be driven by several types of interactions.

2.III.3 Transverse relaxation against temperature

Similarly, in the case of transverse relaxation, the T_2 can be related to the correlation τ_c as shown in Equation 2-12

$$T_2 \propto \frac{1}{A\tau_c + B\left(\frac{\tau_c}{1 + \omega_0^2\tau_c^2}\right)}$$

Equation 2-12

In this expression, the constants A and B depend on the particulars of the interaction causing the relaxation. In the case of very small τ_c values, the A term is negligible. This case is called the motional narrowing limit, where T_2 is on the similar size as T_1 (Figure 2-9). This conditions is often encountered for very small molecules and/or in low viscosity samples, as in that case, the molecular motions represented by the correlation time are fast (τ_c is small). On the other hand, with very viscous samples, or even solids, the A term dominates, and T_2 becomes very short.

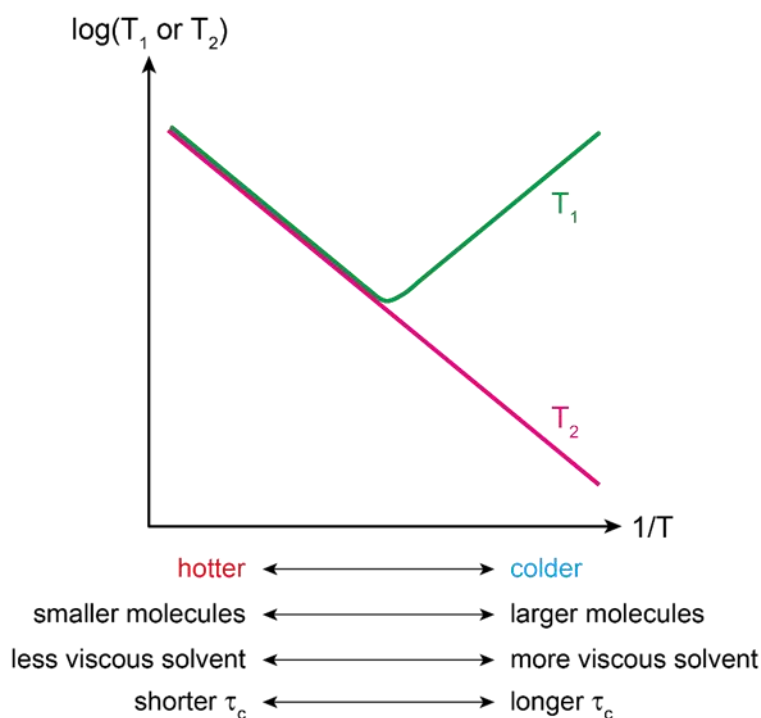


Figure 2-9: Temperature dependence of T_1 and T_2 parameter (figure taken from Dr Luke O'Dell lectures note)

2.III.4 Different relaxation interactions

In general, there are five NMR interactions that can contribute to the T_1 relaxation:

$$\frac{1}{T_1} = \frac{1}{T_1^{DD}} + \frac{1}{T_1^{CSA}} + \frac{1}{T_1^{SR}} + \frac{1}{T_1^{Sc}} + \frac{1}{T_1^Q}$$

Equation 2-13

Where T_1^{DD} , T_1^{CSA} , T_1^{SR} , T_1^{Sc} and T_1^Q are the relaxation times associated with the magnetic dipole-dipole interaction, chemical shift anisotropy, spin rotation, scalar coupling, and the quadrupolar interaction respectively.

In order to understand relaxation process in an ionic liquid system, the following section will focus on the study at a two spin system. By considering a two spin system, the energy level diagram will be represented as shown Figure 2-10.

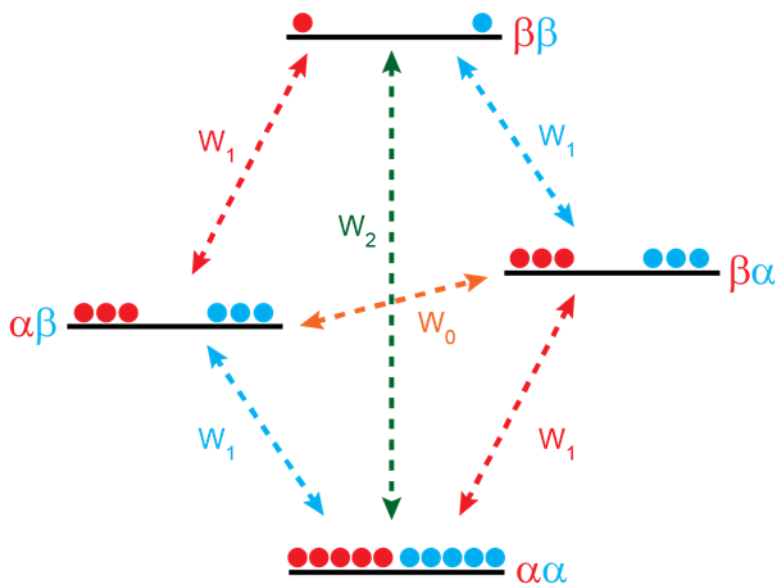


Figure 2-10: Energy level of a two spins system (figure taken from Dr Luke O'Dell lectures note)

In such a system, relaxation can occur *via* different transitions, known as the zero quantum transition W_0 , the single quantum transition W_1 and the double quantum transition W_2 . The longitudinal relaxation can be described as the rate of change of the z component of the angular momentum of both spins:

$$\frac{d\langle\hat{I}_{1z}\rangle}{dt} = -R_1(\langle\hat{I}_{1z}\rangle - \langle\hat{I}_{1z}\rangle^{eq}) - \sigma_{12}(\langle\hat{I}_{2z}\rangle - \langle\hat{I}_{2z}\rangle^{eq})$$

Equation 2-14

$$\frac{d\langle\hat{I}_{2z}\rangle}{dt} = -\sigma_{12}(\langle\hat{I}_{1z}\rangle - \langle\hat{I}_{1z}\rangle^{eq}) - R_1(\langle\hat{I}_{2z}\rangle - \langle\hat{I}_{2z}\rangle^{eq})$$

Equation 2-15

Where

$$R_1 = W_0 + W_1^{1\alpha} + W_1^{1\beta} + W_2$$

Equation 2-16

$$R_2 = W_0 + W_1^{2\alpha} + W_1^{2\beta} + W_2$$

Equation 2-17

$$\sigma_{12} = W_2 - W_0$$

Equation 2-18

In the case of homonuclear spins, the equation of motion for the observable quantity can be written as the sum of the magnetization, thus:

$$\begin{aligned} \frac{d(\langle \hat{I}_{1z} \rangle + \langle \hat{I}_{2z} \rangle)}{dt} &= \frac{d\langle \hat{I}_{1z} \rangle}{dt} + \frac{d\langle \hat{I}_{2z} \rangle}{dt} \\ &= -(2W_1 + 2W_2)(\langle \hat{I}_{1z} \rangle + \langle \hat{I}_{2z} \rangle) - (\langle \hat{I}_{1z} \rangle^{eq} + \langle \hat{I}_{2z} \rangle^{eq}) \end{aligned}$$

Equation 2-19

Leading to a solution with T_1 where T_1 in this case is given by:

$$\frac{1}{T_1} = (2W_1 + 2W_2)$$

Equation 2-20

The expression of the transition probabilities can be calculated to be

$$W_0 = \frac{1}{10} \left(\frac{\mu_0}{4\pi} \right)^2 \frac{\hbar^2 \gamma_1^2 \gamma_2^2}{r^6} \frac{\tau_c}{1 + (\omega_1^2 - \omega_2^2) \tau_c^2}$$

Equation 2-21

$$W_1^1 = \frac{3}{20} \left(\frac{\mu_0}{4\pi} \right)^2 \frac{\hbar^2 \gamma_1^2 \gamma_2^2}{r^6} \frac{\tau_c}{1 + \omega_1^2 \tau_c^2}$$

Equation 2-22

$$W_2 = \frac{3}{5} \left(\frac{\mu_0}{4\pi} \right)^2 \frac{\hbar^2 \gamma_1^2 \gamma_2^2}{r^6} \frac{\tau_c}{1 + (\omega_1^2 + \omega_2^2) \tau_c^2}$$

Equation 2-23

By including these values of transitions probabilities in eq, the homonuclear dipole relaxation can be written as follow:

$$\frac{1}{T_1^{DD}} = \frac{3}{10} \left(\frac{\mu_0}{4\pi} \right)^2 \frac{\gamma^4}{r^6} \left(\frac{\tau_c}{1 + \omega^2 \tau_c^2} + \frac{4\tau_c}{1 + 4\omega^2 \tau_c^2} \right)$$

Equation 2-24

Corresponding to

$$\frac{1}{T_1^{DD}} = \frac{3}{10} d_{12}^2 \left(\frac{\tau_c}{1 + \omega^2 \tau_c^2} + \frac{4\tau_c}{1 + 4\omega^2 \tau_c^2} \right)$$

Equation 2-25

With d_{12} corresponding to the dipolar constant:

$$d_{12} = -\frac{\hbar \mu_0 \gamma_1 \gamma_2}{4\pi r^3}$$

Equation 2-26

Using the same methodology, the dipolar relaxation equation of an heteronuclear coupling with one spin relaxation much faster than the other spin can be calculated.

$$\frac{1}{T_1} = (W_0 + W_1^1 + W_2)$$

Equation 2-27

Thus,

$$\frac{1}{T_1^{DD}} = \frac{1}{10} \left(\frac{\mu_0}{4\pi} \right)^2 \frac{\hbar^2 \gamma_1^2 \gamma_2^2}{r^6} \left(\frac{\tau_c}{1 + (\omega_1 - \omega_2)^2 \tau_c^2} + \frac{3\tau_c}{1 + \omega_1^2 \tau_c^2} + \frac{6\tau_c}{1 + (\omega_1 + \omega_2)^2 \tau_c^2} \right)$$

Equation 2-28

Additionally, it should be noted that this expression corresponds to an heteronuclear relaxation between two spin half nuclei. Thus, on a precautionary basis, Equation 2-29 correspond to the heteronuclear relaxation between a half integer spin and a quadrupole spin.

$$\frac{1}{T_1^{DD}} = \frac{2}{15} \left(\frac{\mu_0}{4\pi} \right)^2 I_2(I_2 + 1) \frac{\hbar^2 \gamma_1^2 \gamma_2^2}{r^6} \left(\frac{\tau_c}{1 + (\omega_1 - \omega_2)^2 \tau_c^2} + \frac{3\tau_c}{1 + \omega_1^2 \tau_c^2} + \frac{6\tau_c}{1 + (\omega_1 + \omega_2)^2 \tau_c^2} \right)$$

Equation 2-29

As the quadrupolar relaxation is usually more efficient than the dipolar relaxation, the homonuclear dipolar relaxation of quadrupolar nuclei does not need to be considered.

2.IV Structural experiments

2.IV.1 Spin Echoes

Spin echoes are a basic principle in NMR and are used in many different NMR pulse sequences. After an excitation pulse, the signal decay due to relaxation and the signal dephasing due to inhomogeneity of B_0 can be distinguished. Unlike the transverse relaxation T_2 , the signal dephasing can be reversed. Then the magnetization lost due to field inhomogeneity or interactions such as the chemical shift, can be recovered by just applying a second RF pulse with a nutation angle of 180° , called a refocusing pulse. This is called the spin echo experiment.

An example of a spin echo experiment is shown below (Figure 2-11). Firstly a 90° pulse is applied in order to put the magnetization into the transverse plane (y axis). Then after a delay, during which transverse relaxation and dephasing occurs (inhomogeneity or interactions causing some magnetization vectors to precess faster than others) a 180° pulse is applied in order to invert the magnetization along the y axis. Because all of the magnetization vectors continue to precess at their individual speeds, all of the vectors are refocused in the transverse plane after another delay of equal length. Therefore the refocusing pulse reverses the effect of signal dephasing, by bringing back the NMR signal in an echo. This experiment is often called the Hahn echo.

Experimental NMR theory and methodology

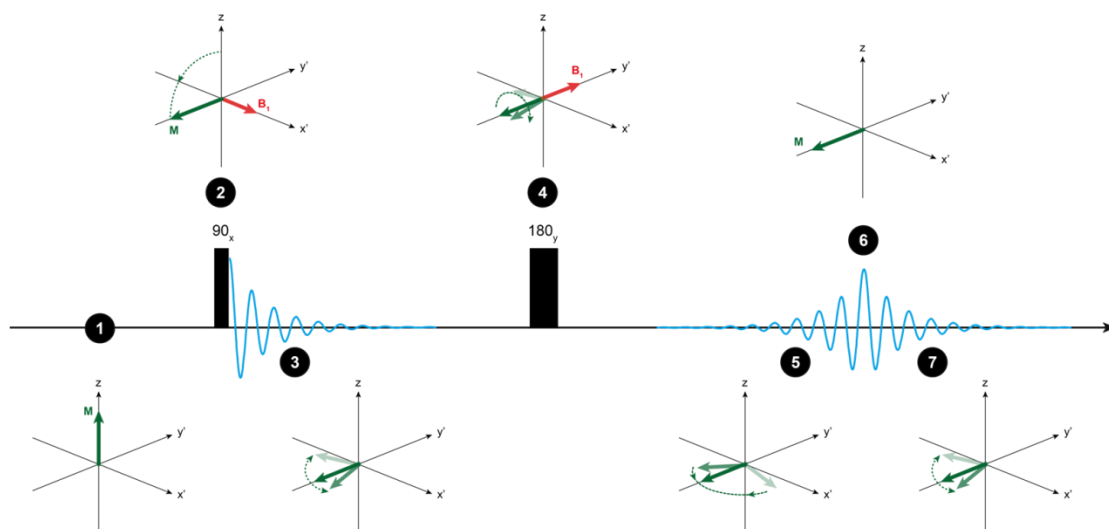


Figure 2-11: A spin echo experiment (figure taken from Dr Luke O'Dell lectures note)

The spin echo experiment can be used also to refocus the chemical shift, as spins at different offsets (chemical shifts) don't have the same precession frequency. Then by using a refocusing pulse, the different chemical shifts can be refocused, while other interactions such as the J coupling (a through-bond interaction between two magnetic nuclei) continue to evolve (Figure 2-12). This can be useful in 2D experiments.



Figure 2-12: Effect of a 180° pulse

By looking at a two spins coupled together by the J interaction, the effect of a refocusing pulse depending on how the pulse is applied can be analyzed (Figure 2-13). Assuming the two species have different Larmor frequencies, the refocusing pulse can be applied to either nucleus selectively or both simultaneously.

By applying the 180° pulse on one nucleus, either ^1H or ^{13}C in the example below, the J -coupling will be refocused, as will be the chemical shift of the nucleus to which the refocused pulse was applied. By applying the 180° pulse on both nuclei

simultaneously, both chemical shifts will be refocused but the J -coupling will be allowed to evolve.

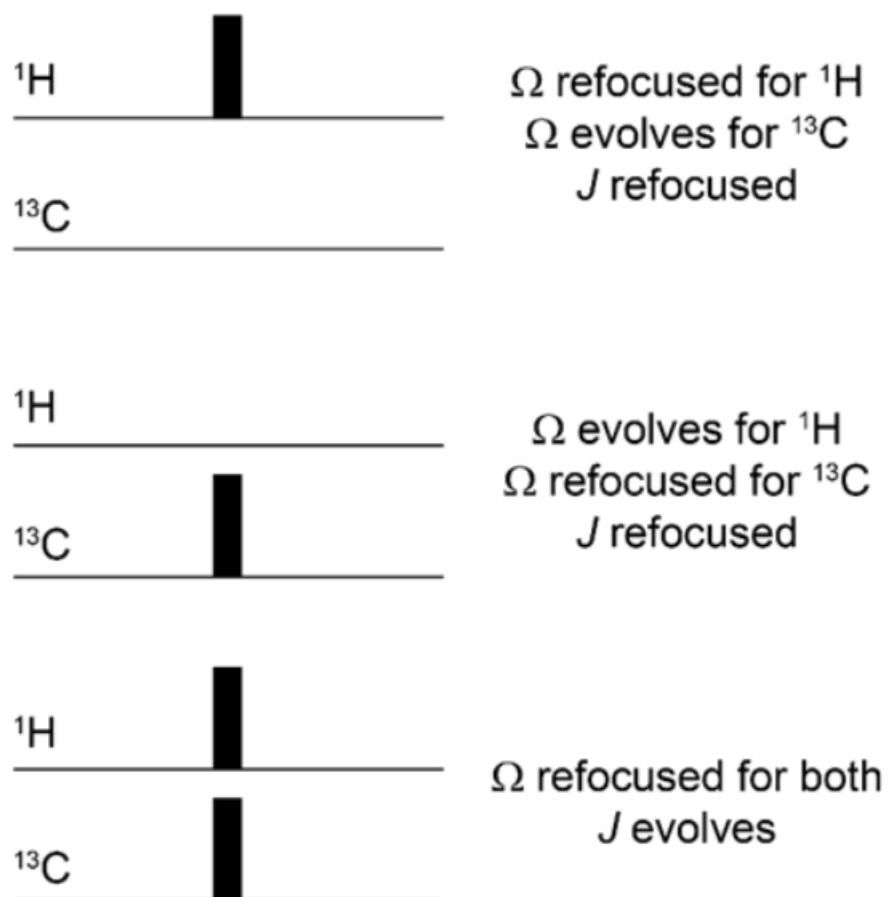


Figure 2-13: The effect of 180° pulses on a system of two coupled spins. (figure taken from Dr Luke O'Dell lectures note)

2.IV.2 HMQC

The HMQC experiment (Heteronuclear Multiple Quantum correlation) is a widely used pulse sequence for structural determination. This experiment provides a 2D heteronuclear chemical shift correlation map between directly bonded protons and X nuclei (Figure 2-14). Most commonly HMQC experiments are between ^1H and

^{13}C with proton detection, which offers a higher sensitivity when compared to ^{13}C experiments.

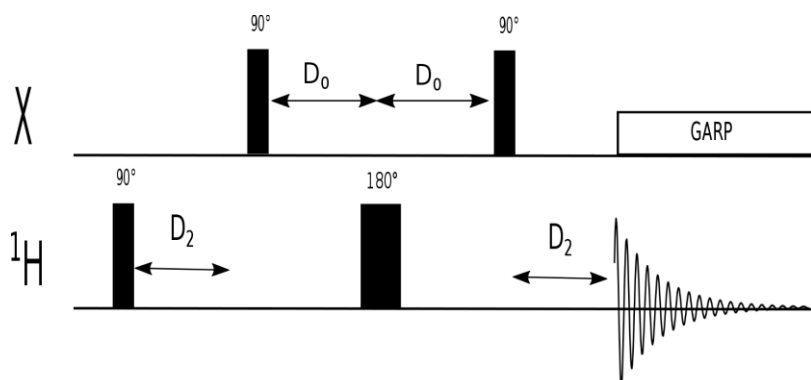


Figure 2-14: HMQC pulse sequence

As shown above, the HMQC pulse sequence consists of a 90° pulse on the ^1H channel in order to create a transverse magnetization that evolves during a D_2 period under the effect of the heteronuclear coupling. At the end of the D_2 period, a 90° pulse on the X channel creates the heteronuclear multiple-quantum coherences that evolve during the variable evolution period $2D_0$.

The 180° pulse on channel ^1H , insert in the middle of the variable evolution period will removes the evolution of the heteronuclear couplings and proton chemical shift. At the end of this period, a last 90° on channel X is applied in order to create antiphase single quantum coherences proton magnetization which will be refocused after a second D_2 delay.

This experiment was used in this work in order to solve hydrogen peak attribution in different samples.

2.IV.3 HSQC

The HSQC (Heteronuclear Single Quantum Correlation) experiment provides a 2D heteronuclear chemical shift correlation map, usually between ^1H and ^{13}C or ^{15}N that

are linked by a single bond. The pulse sequence (shown to the below) starts with an INEPT block that transfers the ^1H magnetisation to the ^{13}C nuclei, resulting in (enhanced) transverse ^{13}C magnetisation. This evolves under the ^{13}C offset during t_1 with the J_{HC} coupling refocused by the 180° pulse applied to the ^1H nuclei. Finally the two simultaneous 90° pulses convert this evolved ^{13}C magnetisation back to the ^1H nuclei for observation.

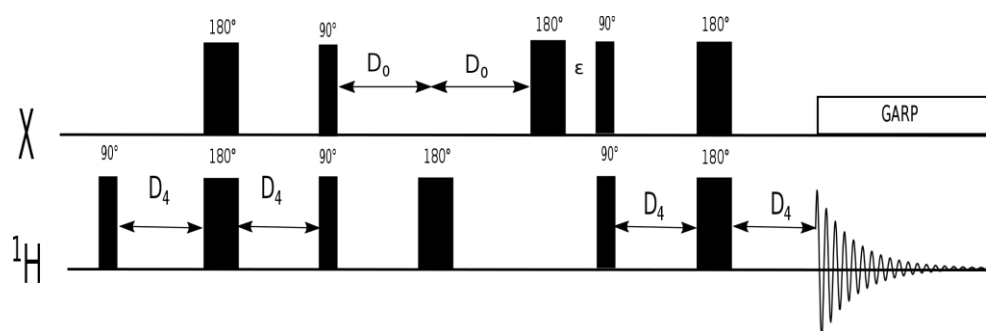


Figure 2-15: HSQC pulse sequence

2.IV.4 Diffusion measurements

The diffusion NMR technique is achieved by combining NMR pulses and pulsed magnetic field gradients applied across the sample, which encode spatial information¹¹⁰. The most commonly used diffusion experiment is called Pulse Field Gradient Spin Echo (PFGSE).

In such experiments, various spectra are acquired, each using a different pulsed magnetic field gradient strength. The pulsed field gradients (PFGs) create a linear spatial variation in the magnetic field which affects the nuclear Larmor frequencies. In the pulse sequence below one can see that a first 90° pulse is applied and then a magnetic field gradient pulse is applied in order to disperse the magnetization. Then a period of $\Delta/2$ allows diffusion to occur, followed by a 180° pulse in order to invert the dispersed magnetization. After another period of $\Delta/2$, a second gradient pulse is applied to refocus the signal.

Experimental NMR theory and methodology

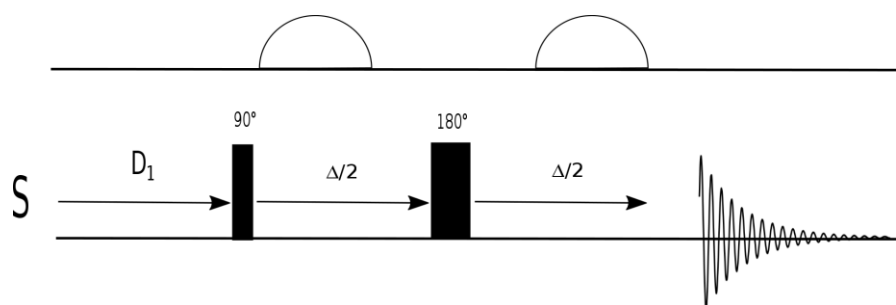


Figure 2-16: A basic diffusion NMR pulse sequence. The semi-circles represent field gradient pulses.

The refocusing will be only achieved for those nuclei that have not moved significantly along the direction of the gradient as shown on the figure below (Figure 2-17).

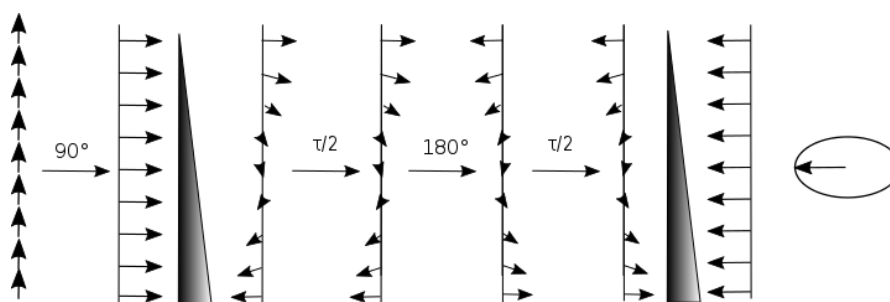


Figure 2-17: The effect of gradients during a diffusion experiment assuming no movement of the nuclei.

If a nucleus moves along the direction of the applied field gradient during the diffusion time Δ , then its precession frequencies during the dephasing and refocusing periods will not be the same, and the spin will not be perfectly refocused, and the signal will be attenuated (Figure 2-18).

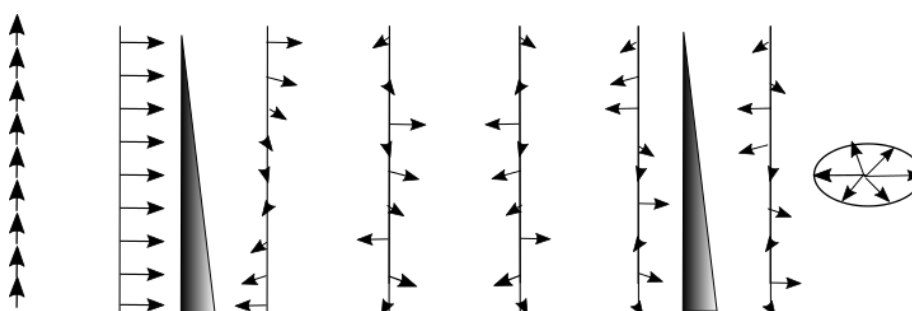


Figure 2-18: The effect of gradients during a diffusion experiment assuming diffusion of the nuclei along the gradient direction.

By repeating this experiment with incremental increases in the magnetic field gradient strength or pulse length, a 2D map showing a decay of the peak intensity

will be created. The measured signal is the integral over the whole sample volume and the NMR signal intensity is attenuated depending on the diffusion time Δ , the gradient strength g and the gradient pulse length δ . This decay can then be fitted with the Stejskal-Tanner equation:

$$I = I_0 e^{-D\delta^2\gamma^2 g^2 (\Delta - \frac{\delta}{3})}$$

Equation 2-30

I is the observed intensity, I_0 the reference intensity, D the diffusion coefficient, γ the gyromagnetic ratio of the observed nucleus.

2.IV.5 The Nuclear Overhauser Effect

The Nuclear Overhauser Effect (NOE) was first proposed in 1953 by Albert W. Overhauser¹⁰², demonstrated experimentally the same year by Carver and Slichter¹⁰³, and fully verified experimentally in 1962 by Anderson and Freeman¹¹¹. The NOE is a transfer of spin polarization *via* cross relaxation in a dipolar coupled spin system. It comes from dipole-dipole interactions and is therefore mediated through space, not through chemical bonds.

The simplest experiment to observe the NOE is the steady state experiment, which consists of selective saturation of a spin I_1 and then application of a 90° pulse to observe the change in polarization on spin I_2 . In order to understand the NOE effect, a system of two coupled spins which share a dipolar (through space) coupling have to be considered. Let's assume a spin system I_1 and I_2 who do not share a J coupling. The NOE effect concerns changes in spin polarization, *i.e.* the difference of populations between the energy states.

At equilibrium, the population differences between energy levels are determined by the Boltzmann distribution. By looking at the two spins system energy level diagram as shown in Figure 2-19, one should recall that three type of transitions lead relaxation processes.

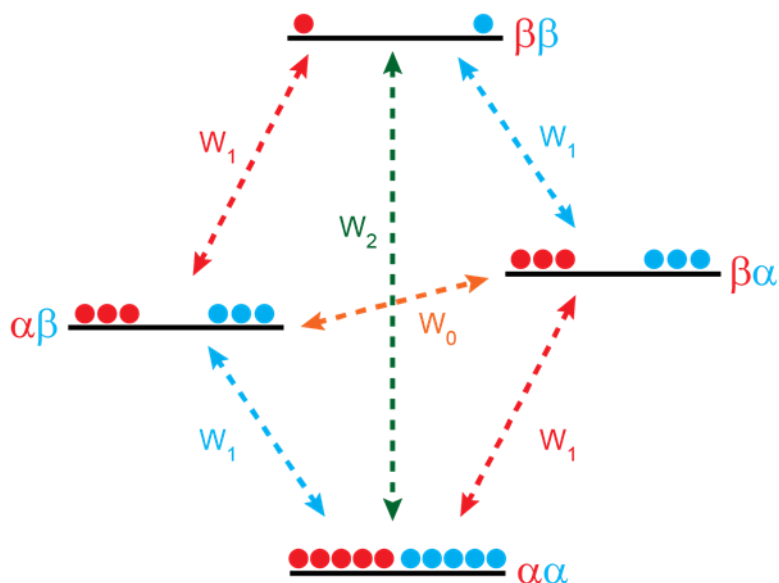


Figure 2-19: Energy level and possible transitions of a two spins system (figure taken from Dr Luke O'Dell lectures note)

In fact, the NOE corresponds to the combination of only two of these transitions, the double quantum and the zero quantum transition as shown in Equation 2-31.

$$\sigma_{12} = W_2 - W_0$$

Equation 2-31

As shown earlier, these two transitions can be developed as follow:

$$W_0 = \frac{1}{10} \left(\frac{\mu_0}{4\pi}\right)^2 \frac{\gamma_1^2 \gamma_2^2}{r^6} \frac{\tau_c}{1 + (\omega_1^2 - \omega_2^2)\tau_c^2}$$

Equation 2-32

$$W_2 = \frac{3}{5} \left(\frac{\mu_0}{4\pi}\right)^2 \frac{\gamma_1^2 \gamma_2^2}{r^6} \frac{\tau_c}{1 + (\omega_1^2 + \omega_2^2)\tau_c^2}$$

Equation 2-33

Thus it is easy to see that the cross relaxation value σ depends on the Larmor frequencies of the studied nuclei. Furthermore as these transitions are dependent on the correlation time, the cross relaxation rate is also dependent on the correlation time, thus depending on the molecules or system studied, one transition will be greater than the other and vice versa. This in fact can lead to negative or positive sigma, for example, for large molecules and/or viscous system, the molecular

motions and thus the correlation time will tend to be slow. In that case, the W_0 transitions will begin to be efficient and thus, under these conditions, negative NOE can be observed.

The other major contribution to the cross relaxation rates is the distance parameter (r) present in the different transitions. Indeed, this parameter is thus the most important in our study of the cross relaxation rates, as it means that cross relaxation rate is one over distance dependant, and thus the closer spins are one to each other's, the stronger the cross relaxation rate σ will be. One should note that in the specific equations describe above, the distance dependence is a r^{-6} , meaning that the cross relaxation rate will get weak very fast as spins get further one to each other. It will be shown in the following chapters that different theories can in fact described the σ distance dependence, highlighting that the distance dependence is not always an r^{-6} dependence, and that the cross relaxation rates can sometimes be relayed from several coordination sphere number.

2.IV.6 The NOESY experiments

Among all of the experiments taking advantage of the NOE effect, the 2D NOESY (Nuclear Overhauser Effect Spectroscopy) experiment, is one of the simplest ways to obtain NOE information. The NOESY experiment offers a simple way to observe spatial correlations in a molecule using a single experiment.¹¹²

The most basic NOESY pulse sequence is shown in Figure 2-20, and is the same as a classical two-dimensional exchange experiment. After an excitation 90° pulse creating the transverse magnetization evolving during a variable t_1 period, a subsequent 90° pulse will create the chemical shift-encoded longitudinal magnetization. Then, during a period τ_m called the mixing time, the magnetization will transfer between nuclei by cross relaxation or chemical exchange. The last 90° creates a transverse magnetization which can be therefore detected.

Experimental NMR theory and methodology

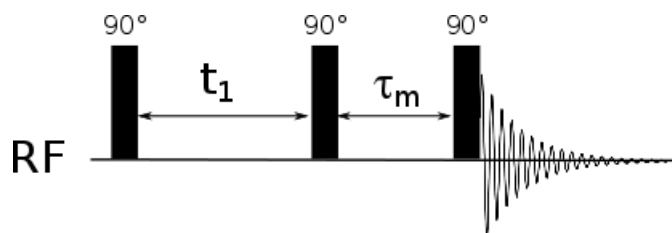


Figure 2-20: NOESY basic pulse sequence

As an example, Figure 2-21 shows a 2D ^1H - ^1H NOESY experiment of a pyrrolidinium cation (*N*-butyl-*N*-methyl pyrrolidinium: C_4mpyr shown on Figure 2-22). First of all peaks highlighted in red correspond to the auto-correlation ^1H peaks. Secondly as the intensity of the transfer depends on the mixing time (the longer it is the more intense peak will be, as more magnetization get the time to be transferred) and on the distance between nuclei, by adjusting the mixing on different experiments, correlation peaks between different hydrogen can appear (in black in figure), which can help to determine the sample structure.

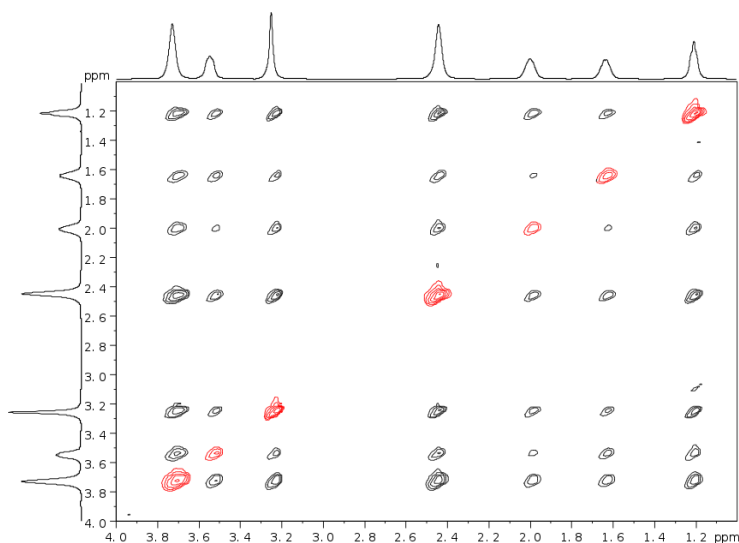


Figure 2-21: ^1H - ^1H NOESY experiment realised on C_4mpyr FSI doped with 1 molal LiFSI sample, therefore corresponding to the hydrogen on the cation.

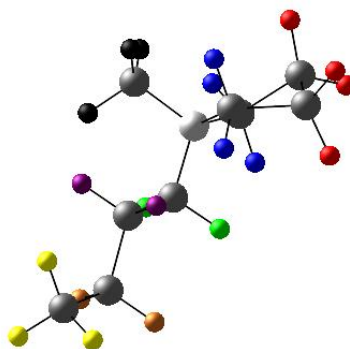


Figure 2-22: Representation of Campyr cation with a colour labelling use later on for build up curves.

In the following work, a modified version of the classical NOESY pulse sequence is used. This pulse sequence present two additional 180° pulses just after the first and the third 90° , combine with a gradient selection (Figure 2-23). Furthermore, a spoiler gradient is present just after the mixing time, in order to remove all of the unwanted signals.

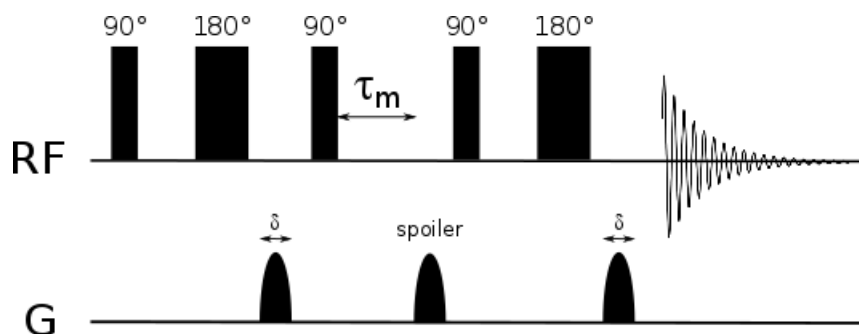


Figure 2-23: NOESYgtp pulse sequence

2.IV.7 The HOESY experiment

The Heteronuclear OverHauser Effect Spectroscopy (HOESY) experiment allows the NOE occurring between different nuclear isotopes to be observed, which as discussed above can potentially provide information on how the anions and the cations are

arranged relative to each other in an ionic liquid. In our ionic liquid, for example P_{111i4} TFSI Li⁺, the TFSI contains ¹⁹F nuclei, and the P_{111i4} contains ¹H nuclei. So for example, the proximities of the two cations and the anion can be studied using ¹H-⁷Li HOESY, ¹H-¹⁹F HOESY or ⁷Li-¹⁹F HOESY.

The most basic pulse sequence for HOESY experiments is shown in Figure 2-24. It corresponds firstly to a 90° pulse on the ¹H nuclei, which creates the transverse magnetization that evolves during 2*d₀ (the Preparation section). A 180° pulse is applied after one delay d₀, on the X channel, to re-focus the ¹H-X J-coupling but allow the ¹H chemical shift to evolve (the Evolution section). After a second delay d₀, a 90° pulse of variable phase is applied on the ¹H channel, in order to return the ¹H magnetization to the ±z axis. When the ¹H magnetization is along the -z axis, it will relax during d₈ and magnetization will transfer between ¹H and the X nucleus *via* the NOE. The period τ_m is called the mixing time, transfer time or build up time (the Mixing section). Finally, a 90° pulse is applied on the X channel to observe the signal from the X nucleus, thus the magnetization transfer can be read (the Detection section).

This NOE-enhanced signal is dependent on the size and sign of the NOE effect (determined primarily by the proximity of the nuclei but, crucially, also by their dynamics), and contains the ¹H chemical shift information, allowing the ¹H signals to be resolved in a 2D experiment in which d₀ is incremented.

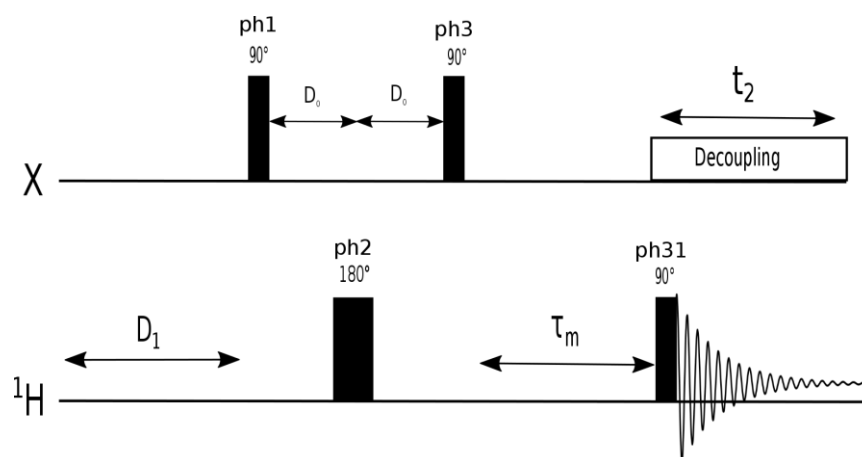


Figure 2-24: A basic 2D HOESY pulse sequence

During the detection part, in order to cancel the directly-excited signal from the X nuclei and just observe the signal transferred from the ^1H to X, phase cycling is used. One of the most basic phase cycling (see table below) creates an experiment with a positive regular signal plus a positive NOE enhancement and the next with a negative regular signal but still a positive NOE. By subtracting one from the other, only the NOE transfer will appear as shown on Figure 2-25.

Φ	1	2	3	4
ph1	0	0	0	0
ph3	0	2	0	2
ph2	0	0	2	2
ph31	0	2	0	2

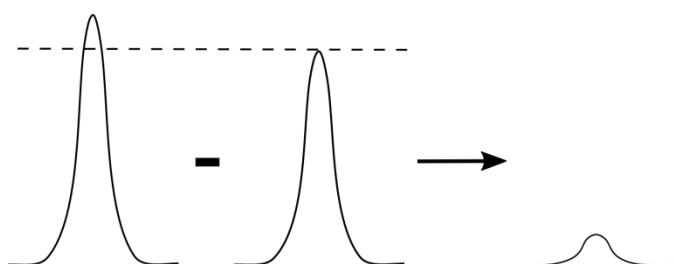


Figure 2-25: Substraction of two HOESY scans, leading to extraction of the NOE enhancement (0 stand for the x position and 2 for -x position of the receiver).

A number of different HOESY pulse sequences have been developed^{78,113–116}. The HOESY pulse sequence used for this work is actually different from the one described above (see Figure 2-26). Here gradient pulses are used to select the desired magnetization and remove unwanted signals, for example a spoiler gradient is applied at the end of the mixing time in order to eliminate any unwanted transverse magnetization. An extra 180° pulse is applied to refocus J couplings and ^1H chemical shifts during the Evolution section. Finally, and most importantly, the NOE transfer in this case goes from the X nucleus (^7Li or ^{19}F in this work) to ^1H and the signal is detected from the latter nucleus. This brings the major advantage of being able to resolve the ^1H chemical shifts in a one dimensional experiment. As the samples studied herein contain only a single lithium (or fluorine) environment (averaged over time), no ^7Li (or ^{19}F) chemical shift information is required and no acquisition of the second dimension is needed. This brings a considerable time saving.¹¹⁷

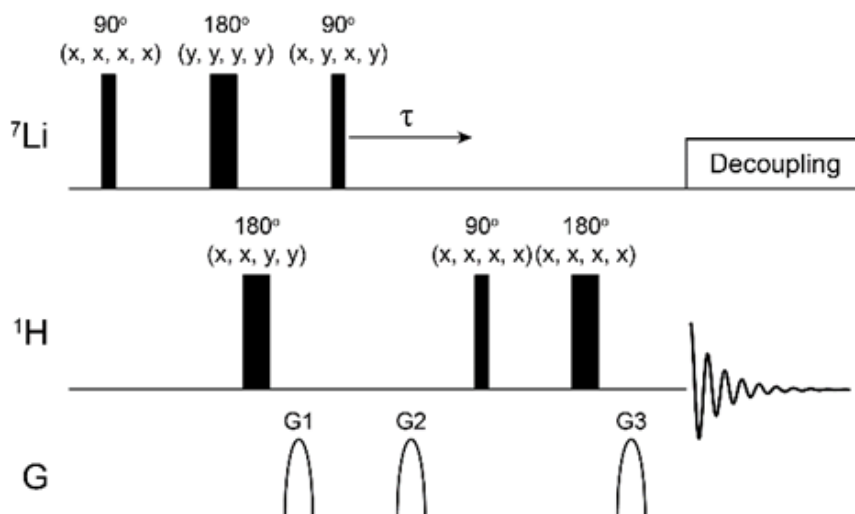


Figure 2-26: The HOESY pulse sequence used in this work

2.IV.8 ENMR experiments

The electrophoretic NMR (ENMR) is based on the idea of applying an electric field between two electrodes during a PFG NMR experiments. Under an applied magnetic field gradient the nuclei will resonate at different NMR frequencies depending on their position in the gradient. Isotropic ion motions caused by self-diffusion create a de-phasing of the signal which induces a loss of the observed signal intensity, whereas the anisotropic ion motion under the presence of an electric field create a systematic dephasing of the signal, which will be proportional to the magnetic field gradient strength and the applied electric field. Therefore, during an ENMR experiment, both the diffusion parameter and electrophoretic mobility can be quantified.

The equation describing the NMR signal resulting from an ENMR experiment is presented in Equation 2-34, with both the exponential term corresponding to the attenuation of the signal due to the pulse field gradient and a cosine term corresponding to the displacement of the species due to the electric field, thus to the

phase shift. One should note that the distance between electrodes $d_{\text{electrode}}$ and the voltage V will affect only the cosine term and not the exponential one. Indeed, the gradient strength, the gradient pulse duration and the diffusion time, will affect both the exponential term and the cosine term, creating a smaller intensity due to the loss of refocused magnetization. Thus one way, to be able to obtain larger phase shift without reducing the signal intensity, is to carry out experiments with a very high voltage or very small inter-electrode distances. Usually only a very high voltage is used, as having a very small distance between electrodes can create magnetic field inhomogeneity, due to the applied electric current.

$$S = S_0 e^{(-D\gamma^2 g^2 \delta^2 (\Delta - \frac{\delta}{3}))} * \cos\left(\frac{g\gamma\Delta\delta\mu V}{l}\right)$$

Equation 2-34

Different ENMR pulse sequences can be used to measure the phase shift and thus the mobility. An example is shown in Figure 2-27⁹⁷, corresponding to a pulse gradient spin echo with an applied electric field E gated on during the diffusion encoding time. Such as the PGSE experiment, in the absence of an electric field, the random motion such as the diffusion, of the species, in the direction of the applied magnetic field, will thus results of a random phase shift of the difference species and thus will correspond to a loss of the net magnetization. As the gradient is stronger, the loss will become more important, until no more signals are extractable.

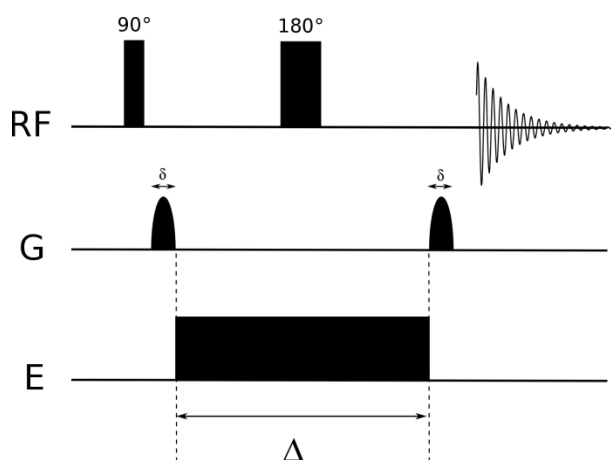


Figure 2-27: Pulsed-Gradient Spin Echo PGSE pulse sequence

Interestingly, as shown in Figure 2-28 if the electric field is applied in the direction of the magnetic field gradient, an additional phase shift will appear, but this time will not create any additional signal attenuation since the same phase shift is encoded in all spins. This net phase shift yields to the electrophoretic mobility.

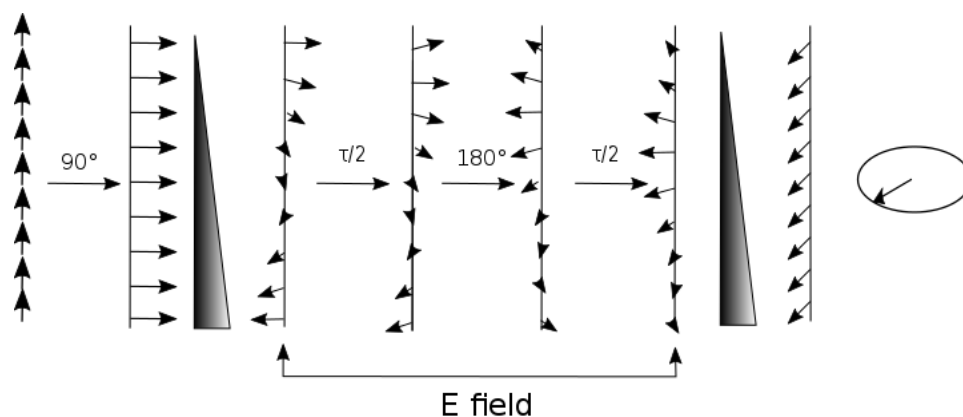


Figure 2-28: Dephasing of signal due to mobility during the PGSE pulse sequence with E field ON

Like the PGSE experiments, this ENMR PGSE is also subject to additional signal attenuation caused by thermal convection, as well as an additional bulk thermal convection due to the resistive heating at the interface of the electrodes. As explained in the literature review part, one way to overcome this problem is to optimize the cell design with for example capillaries in order to restrict the convection. In fact, in order to reduce this bulk convection, a pulse sequence composed of a combination of two spin echo as shown on Figure 2-29 can be used, thus a Pulse Gradient Double spin echo experiment^{97,98} (PGDSE). If an electric field is applied during each diffusion time, but with a different polarity on the two diffusion time sections, the thermal convection due to the Joule heating will be cancelled out. Indeed the electrophoretic flow will change with the applied field polarity but not the convective flow. Thus if the convective flow in the first $\Delta/2$ period is the same as the convective flow in the second $\Delta/2$ period, the two convective flow will be compensated and thus cancelled.

Experimental NMR theory and methodology

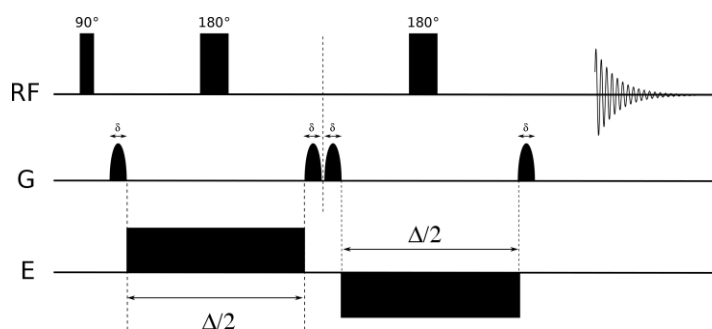


Figure 2-29: Pulsed-Gradient Double Spin Echo PGDSE pulse sequence

Another way to try to overcome the problem of thermal and electro-osmotic convection is to use a modified PGDSE-ENMR experiment⁹⁸, similar to CPMG experiments, corresponding to a truncated CPMG-like pulse train as shown on Figure 2-30.

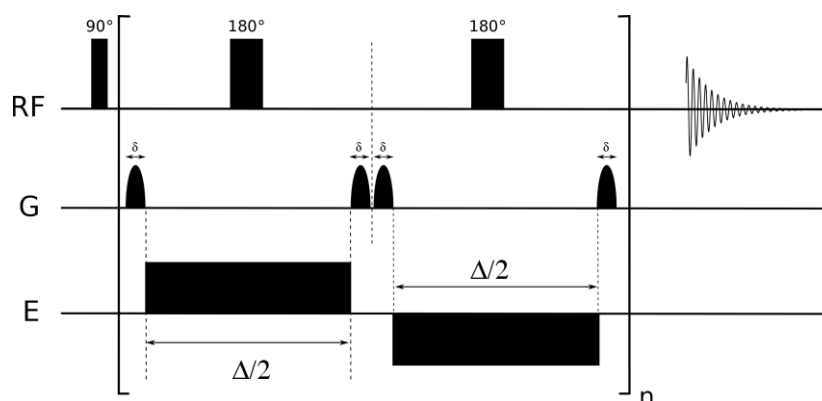


Figure 2-30: CPMG-like pulse gradient double spin echo

The main limitation of the PGSE or CPMG-like pulse sequences results from the potential long duration of the electric pulse. Indeed, as explained earlier long electric pulses are required in order to obtain large enough electrophoretic phase shifts, thus signals from samples having short T_2 relaxation times are greatly attenuated, but also in coupled spin systems the J modulation can be important. Unfortunately, both of these conditions can often be found in ionic liquids.

In order to avoid these pulse sequence limitations, a stimulated echo experiment with 90° pulse can be used, and as explained before, in order to avoid convection, doubling the echo and with field polarity inverted should be used, this is called a Double Stimulated Echo (DSTE). As shown on Figure 2-31, the 180° pulses present in Figure 2-29, are replaced by two 90° , changing the T_2 dependence into a T_1

dependence, and avoiding the J modulation limitations. Moreover homospoil gradient are added after the second and the fourth pulses in order to select the proper coherence pathway and suppress eventual artefacts¹¹⁸.

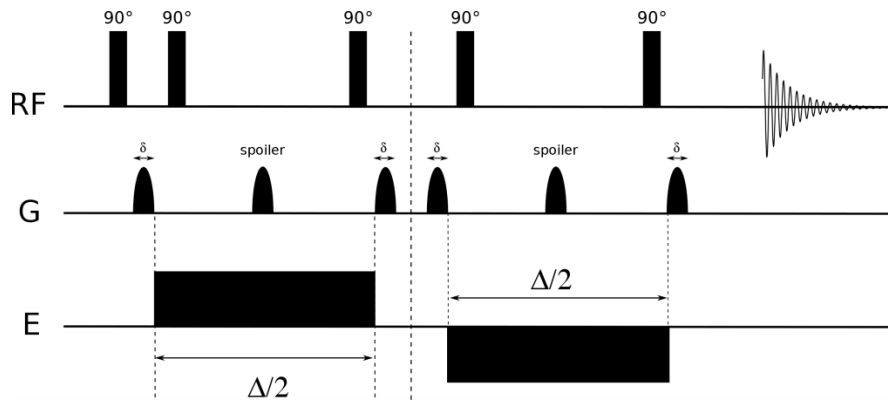


Figure 2-31: Double STimulated Echo (DSTE) pulse sequence

In fact, in the following work, a modified version of the DSTE experiment will be used. By following the electric current on an oscilloscope, one can see on Figure 2-32, that an over voltage can appear when turning the voltage on or off, or when switching polarity. Thus in order to avoid artefacts which can be created by this overvoltage, as shown in Figure 2-33 the pulse sequence was modified by adding two additional 90° pulse just before and just after the polarity witching with a homospoil gradient during the switching. Furthermore, a LED block with a homospoil gradient in the middle is added at the end of the pulse sequence.

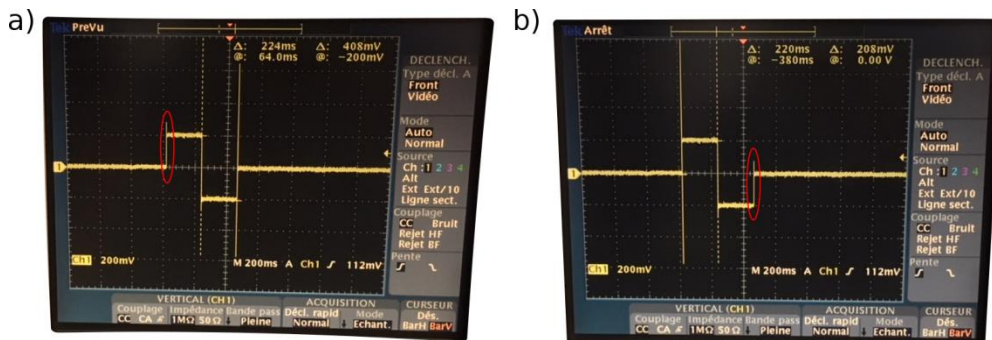


Figure 2-32: Electric overvoltage observe in situ on an oscilloscope

Experimental NMR theory and methodology

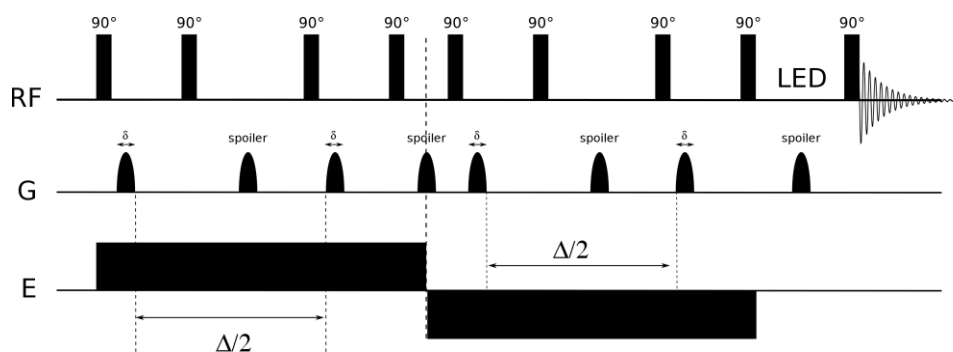


Figure 2-33: modified DSTE used in the following work

2.IV.9 DNP experiments

Dynamic nuclear polarization (DNP) was developed around the idea that the nuclear polarization can be greatly increased by transferring the larger polarisation of an unpaired electron. In our case, magic angle spinning DNP (MAS-DNP) was used to study ionic liquids in the solid state. An added nitroxide biradical and the cross effect DNP mechanism were used, which show greater polarisation transfer efficiency at lower temperature, thus these experiments were carried out at around 100 K. The MAS-DNP technique brings two interesting aspects for the study of ionic liquids. First, by quenching the sample at very low temperature in a sapphire rotor, a glassy state is obtained, corresponding therefore to a snapshot of the liquid structure, which can allow the measurement of inter-ionic distances. Secondly, the high polarization transfer from the unpaired electrons leads to a signal enhancement and thus a gain in sensitivity.

2.IV.9.1 REDOR experiments

In order to study the distances between the organic cation and the monatomic cation added for electrochemistry applications (lithium, sodium) using MAS-DNP experiments, two pulse sequence were used. First for measuring ^{13}C - ^6Li distances the Rotational Echo DOuble Resonance (REDOR)¹¹⁹ were used.

This pulse sequence consists of transferring ^1H polarization to the neighbouring ^{13}C nuclei through cross polarization. Then, as shown in Figure 2-34, which represent the REDOR pulse sequence, this experiment involves a simple spin echo on the ^{13}C nuclei, followed by n 180° pulses on the ^6Li nuclei. These 180° pulses are synced up with the MAS speed (such that $2\tau = n\tau_{\text{MAS}}$, where n is an integer), in order to re-introduce the ^{13}C - ^6Li dipolar coupling. Thus the aim of the experiment is to compare two spectra obtained with and without the 180° pulse train applied to the ^6Li nuclei. The signal arising from the ^{13}C that are in close proximity to some ^6Li nuclei, and therefore experiencing some dipolar coupling reintroduced thanks to the 180° pulse train, will show a decreased signal intensity in the REDOR spectrum. This is because the refocusing pulse applied on the ^6Li spins caused the magnetization from the ^{13}C spin to dephase and not be fully refocused. Thus, there is a signal intensity difference between the scans with and without the 180° pulse train on the ^6Li , which is usually quantified by the fraction $\Delta S/S_0$ of these scans, with ΔS corresponding to the difference in signal intensity, and S_0 corresponding to the signal intensity from the scans with the 180° refocusing.

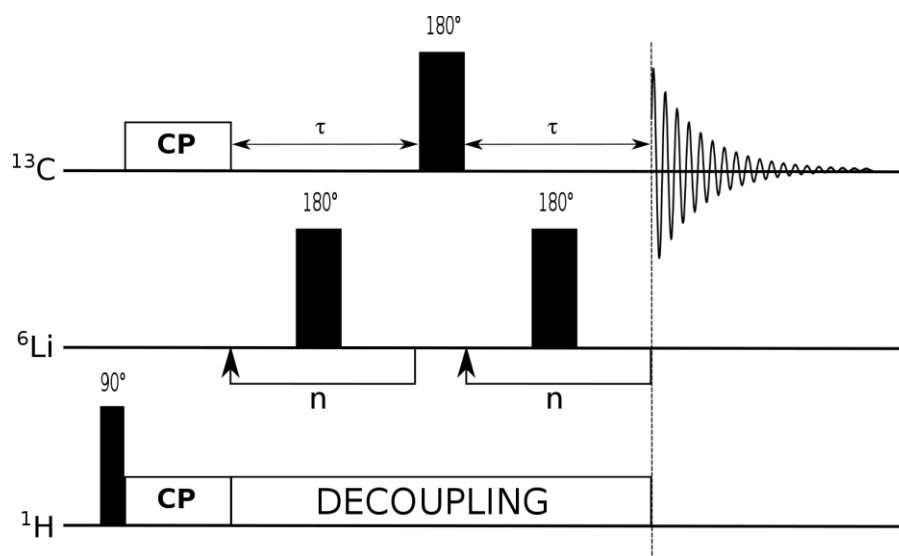


Figure 2-34: Rotational Echo DOuble Resonance REDOR pulse sequence

In order to extract the ^6Li - ^{13}C distance, the dephasing fraction can be measured as a function of the τ time. As shown in Figure 2-35, the dephasing fraction build-up in the initial part of the plot, and then characteristic wiggles can be seen. Thereby, the plot

can be fitted in order to extract the dipolar coupling constant $d_{^{13}\text{C}-^6\text{Li}}$ from which the distance between nuclei can be extracted.

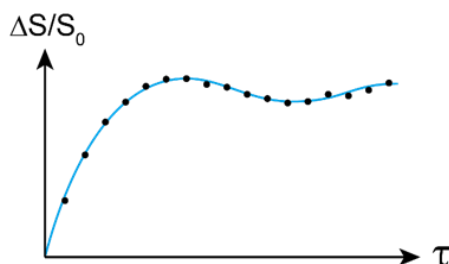


Figure 2-35: Theoretical representation of dephasing fraction of the signal as a function of τ

2.IV.9.2 REAPDOR experiments

Unfortunately, when measuring distances between a spin half nuclei and a quadrupolar nuclei such as ^{23}Na (^6Li is also a quadrupolar nuclei but his quadrupolar interaction is very small, and thus it can consider as a spin half nuclei), the REDOR pulse sequence is limited due to the difficulties associated with the application of n pulses to broad resonances such as the ^{23}Na satellite transitions, which are often as wide as many MHz.

Thus a new type of experiment was developed by T Gullion¹²⁰, combining the REDOR like π pulse train, with a single adiabatic pulse on the quadrupolar nuclei, and called the Rotational-Echo Adiabatic-Passage DOuble-Resonance-NMR, (REAPDOR), the pulse sequence is shown on Figure 2-36.

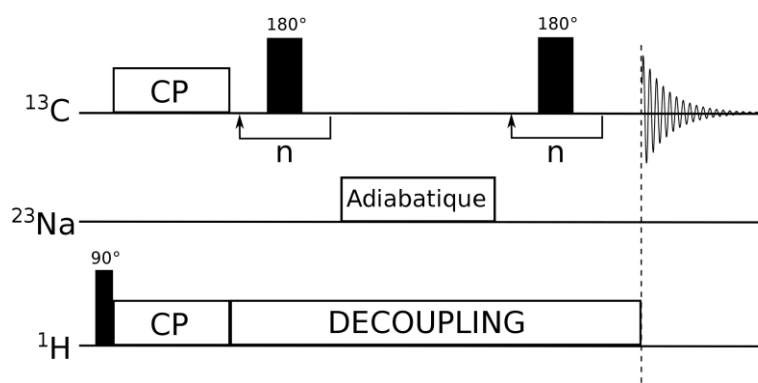


Figure 2-36: Rotational-Echo Adiabatic-Passage DOuble-Resonance REAPDOR pulse sequence

Chapter 3

Experimental details

3.I Sample preparation

The different ionic liquids studied were purchased from Solvionic® and mixed with LiFSI salt inside an argon glove box to obtain the required concentrations. The ionic liquid samples were then loaded into 3 mm capillary tubes inside the glove box, removed and then immediately flame sealed inside 3 mm diameter glass tubes order to avoid moisture contamination. The 3 mm tube was loaded in a 5 mm outer tube containing D₂O for use as an external chemical shift reference and a locking nucleus (²H). Additionally, this set-up minimises convection currents and temperature gradients within the IL.



3.II Diffusion measurements

Diffusion coefficients (*D*) were measured for the different ionic liquids over a range of temperatures using ¹H, ¹⁹F and ⁷Li pulsed field gradient NMR experiments performed at a magnetic field strength of 7.05 T (¹H Larmor frequency of 300 MHz) on a Bruker Avance III wide-bore spectrometer, using a 5 mm Bruker Diff50 probe with a maximum gradient strength of 3000 G cm⁻¹. A stimulated echo pulse sequence was used with 2–5 ms trapezoidal gradient pulses of varying gradient strength, and a diffusion time of 20–50 ms (optimized for each sample in order to obtain complete dephasing of the signals with the maximum gradient strength). In each experiment, between 12 to 48 scans (¹H and ¹⁹F) and 16 to 64 scans (⁷Li) were acquired at each gradient strength, with between 12 to 64 gradient steps used for each experiment. The sample temperature was set and controlled by a gas flow to avoid any temperature fluctuations within the sample. Variable temperature experiments were

Experimental details

performed depending on the sample, between 10 and 70 °C. Diffusion coefficients were extracted using the Stejskal Tanner equation (see section 2.IV.4).

3.III Longitudinal relaxation (T_1) measurements

Heteronuclear Over-hauser Effect Spectroscopy (HOESY) experiments were performed at a magnetic field strength of 11.7 T (^1H Larmor Frequency of 500 MHz). To obtain the full build-up curves, a series of HOESY experiments were carried out for each sample with different mixing times, on a range from 25 ms to 6.5 s, adjusted for each sample. Unless stated otherwise, the D_1 recycle delay was adjusted to be at least 5 times the measured T_1 values to ensure that the experiments will be quantitative. For most of the studies, experiments were carried out at 50 °C as sample are less viscous at this temperature and therefore a better signal over noise can be obtain. However some samples such as the C_3mpyr FSI at 1 m LiFSI, were from 20 to 60 °C for the ^1H - ^{19}F experiments in order to observe the dependence of the cross relaxation rate against temperature. Other aspects of the HOESY experimental details are discussed in detail in chapter 4.

3.IV Molecular dynamics simulation details

The MD simulations were carried our by Dr Fangfang Chen (Deakin University) and full experimental details can be found in supporting information of paper Martin *et al.*¹²¹ and in supporting info of reference Sani *et al.*¹²²

3.V DNP experiments

3.V.1 Sample preparation

The ^6Li -enriched ionic liquid samples were prepared by Dr Ruhamah Yunis (Deakin University) and the full details can be found in the supporting information of Sani *et al.*¹²²

3.V.2 NMR experimental details

The DNP NMR experiments were performed at a magnetic field strength of 9.4 T (^1H Larmor Frequency of 400 MHz) on a Bruker Avance III spectrometer with a 263 GHz gyrotron and a DNP probe in ^1H - ^{13}C - ^6Li configuration. The sample was cooled to a target temperature of 90 K, however the measured sample temperature was corresponding to 92 ± 0.5 K. Furthermore, it should be noted that microwave pulse can lead to a heating of the sample and thus an increase of the actual temperature by several degrees. All experiments were carried out using a MAS rate of 8 kHz and a ^1H 90° pulse width of 2.3 μs . Similarly, the ^{13}C CPMAS spectra were acquired with a SPINAL-64 decoupling (108 kHz), a contact time of 600 μs , and 80 scans acquired with a recycle delay of 6s. ^{13}C T_1 values were measured using a ^1H - ^{13}C CP saturation recovery pulse sequence. The ^{13}C - ^6Li REDOR spectra were acquired with ^1H - ^{13}C CP (600 μs contact time), a ^{13}C 180° pulse width of 8.5 μs , a ^6Li 180° pulse width of 10.0 μs . In addition, a SPINAL-64 1H decoupling were applied continuously throughout the dephasing period and acquisition time and a recycle delay of 6 s. A number of different dephasing times were used, ranging from 8 to 40 ms and a number of scans ranging between 64 and 320 scans for both the dephased (S) and reference (S0) acquisitions. The ^{13}C signal was fitted using the dmfit software.

Chapter 4

Results and discussion

PART 1:
Development of an
automatic data
fitting procedure

4.1.I. HOESY analysis method

The following sections will use the NMR nomenclature of source spin (S), and the spin of interest (I), corresponding to the observed spin. Indeed, in a NOESY experiment on protons for example, spin I and spin S are both ^1H . But for a heteronuclear experiment such as HOESY, the S spin differs from the I spin. Moreover, for clarity the corresponding nucleus will be indicated by a superscript. For example in a ^1H - ^7Li HOESY experiment, transferring magnetization from ^1H spins to ^7Li spins, the source spin will be written S^{H} , and the interest spin will be written I^{Li} thus the transfer direction can be noted $S^{\text{H}} \rightarrow I^{\text{Li}}$. If the nucleus is not specified, the nomenclature will be for example S^{X} or I^{Y} . For the HOESY experiments, only ^1H , ^7Li and ^{19}F will be studied, and ^2H will be used as a locking signal. In the case of DNP experiments or REDOR in general, ^6Li and ^{23}Na were also used.

4.1.I.1 The need for an improved equation for fitting the full HOESY build-up curve

One of the main goals of this PhD is to develop a better way to extract cross-relaxation rates from HOESY experiments, in order to be able to measure quantitative values. Indeed, as the cross-relaxation rates are correlated to the distances between nuclei but also the dynamics of the pair of ions studied, a quantitative extraction is crucial to have a correct determination of these distances and interactions between ions.

To extract the cross-relaxation rates, the following equation derived from the Solomon's equations was used (Equation 4-1).

$$NOE_H\{Li\}(\tau) = M_0\sigma \frac{2\sinh(\kappa\tau)}{\kappa} e^{\frac{-(R_{H,1}+R_{Li,1})\cdot\tau}{2}}$$

PART 1:
Development of an automatic data fitting procedure

$$\kappa = \sqrt{\frac{R_{(H,1)}^2 - 2R_{H,1} \cdot R_{Li,1} + R_{Li,1}^2 + 4\sigma_{H,Li}^2}{2}}$$

Equation 4-1

In this equation, σ is the cross-relaxation rate, M_0 represents the total initial source spin magnetization available and thus, in our case it corresponding to the X magnetization (^{19}F or ^7Li depending on the experiment). In practice M_0 acts as a scaling factor that adjusts the vertical height of the function, and R_H and R_{Li} correspond respectively to the inverse of the relaxation times T_{1H} and T_{1Li} . The measured T_1 values are used to calculate R_H and R_{Li} . The cross-relaxation rate σ is allowed to vary during the fitting of the HOESY build-up curves with M_0 fixed. The reason why it's fixed and to which number will be explained later.

The R_1/T_1 values are very important in fitting the HOESY build-up curve, because different hydrogen sites can have very different ^1H relaxation times which cause very different build-up curves if the same cross-relaxation rate (*e.g.* $\sigma = 2$ a.u.) is used (see below).

As explained in the literature review, many published HOESY investigations of ILS report σ values extracted by just fitting the beginning of the experimental build-up curve with a linear function. The Taylor expansion of Equation 4-1 at $\tau=0$ at the order 3 reveals the impact of the relaxation time.

$$NOE_H\{Li\}(\tau) = 2\sigma\tau + 2\sigma\left(-\frac{R_{H,1}}{2} - \frac{R_{Li,1}}{2}\right)\tau^2 + O(\tau^3)$$

Equation 4-2

This means that if the build-up curve is not fitted using the experimentally measured spin lattice relaxation times, but just by a linear function at short mixing times, this can result in a systematic error in the determined σ value.

In order to quantify this error and the potential impact on the fit, six build-up curves were simulated using Equation 4-1 as shown in Figure 4-1a. These six build-up curves were simulated with the same σ value, fixed at 2 a.u., but with different T_1 relaxation ranging from 0.5 seconds up to 2 seconds. Then, selected points of these build up

PART 1:
Development of an automatic data fitting procedure

curves were plotted as experimental data points, in order to simulate a linear fitting as shown in Figure 4-1 b, from 0 ms up to 150 ms of mixing time. The cross-relaxation rates extracted from these linear fits are plotted in Figure 4-1 c, showing that all the six relaxation rates depart from the one used to simulate the build-up curves (*e.g.* $\sigma = 2$ a.u.), and are all different, due to the different relaxation times. The impact of T_1 relaxation times on the extracted cross-relaxation rates can therefore be important even at short mixing times. A linear fitting at even shorter mixing times could give a more accurate value, but then the signal to noise ratio of the experiment will be very small, as short mixing times correspond to a very small amount of magnetization transfer.

Potentially a linear fitting of a build-up curve at short mixing times on nuclei with a very long T_1 could give accurate cross relaxation rate values, but in any case it's always preferable to use the fit of the full build-up curve with the T_1 relaxation parameters included in the equation, if aiming for quantitative values.

PART 1:
Development of an automatic data fitting procedure

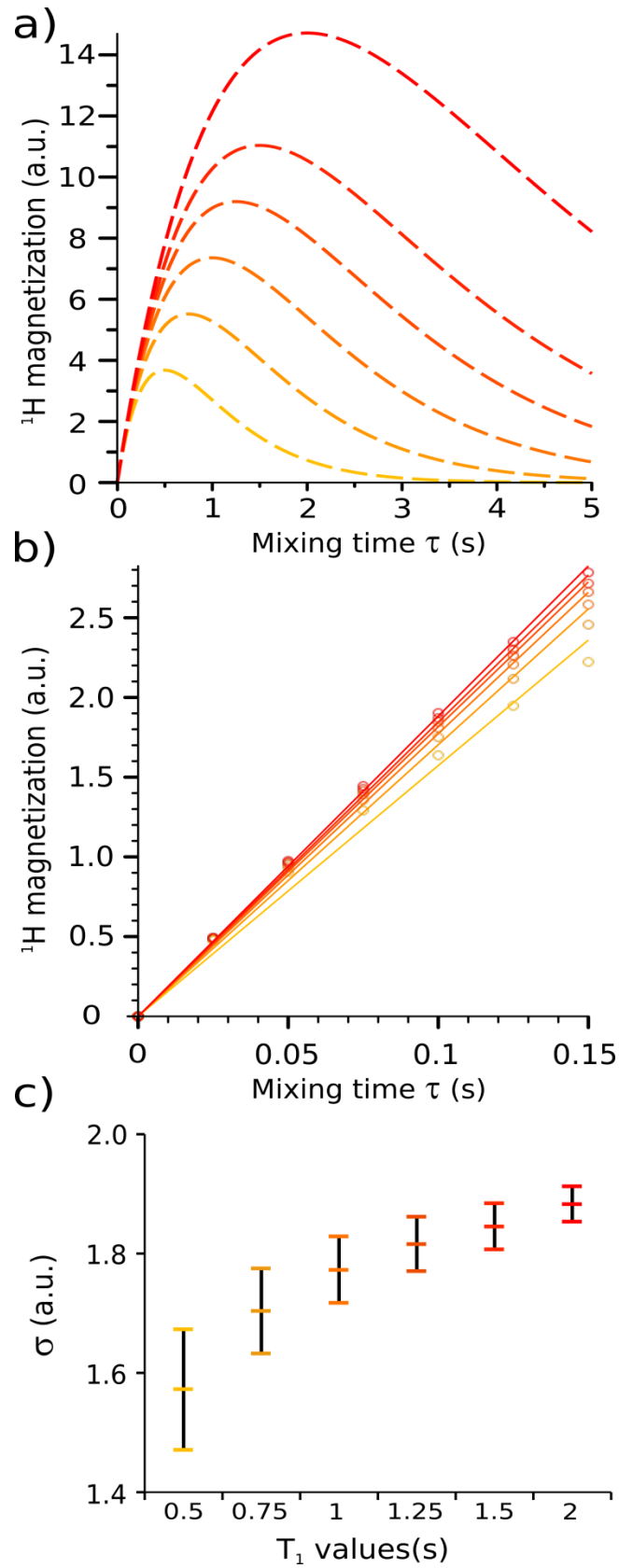


Figure 4-1: a) Simulated build-up curves T_1 values ranging from 0.5 (yellow) to 2 seconds (red), b) Linear fit of the build-up curves between 0 and 150 ms, c) Fitted cross-relaxation rates with confidence intervals, as a function of the T_1 values used for simulation

4.1.1.2 Intensity decay due to diffusion

Interestingly, even when Equation 4-1 was used with the experimental spin lattice relaxation parameters to fit the HOESY build-up curves, the fits obtained were not matching well with the experimental data. A detailed explanation of the fitting process will follow in the next part.

One of the reasons can in fact be found in the pulse sequence (Figure 4-2). The presence of the gradient pulses G_1 and G_3 can impact the observed HOESY signal intensity, due to the fact that the delay between the two gradient pulses can be up to 6 seconds. Indeed, the mixing time τ is present between the two gradients. Thus, even with very low gradient strengths (on the order of 54 G/cm see experimental details), the delay between these gradient pulses acts like the diffusion time Δ in the diffusion experiments. When the gradient G_3 at the end of the pulse sequence is used to refocusing the spins, due to diffusion some spins will have moved from one gradient position to another, thus part of the signal will not be refocused and the observed signal will be attenuated.

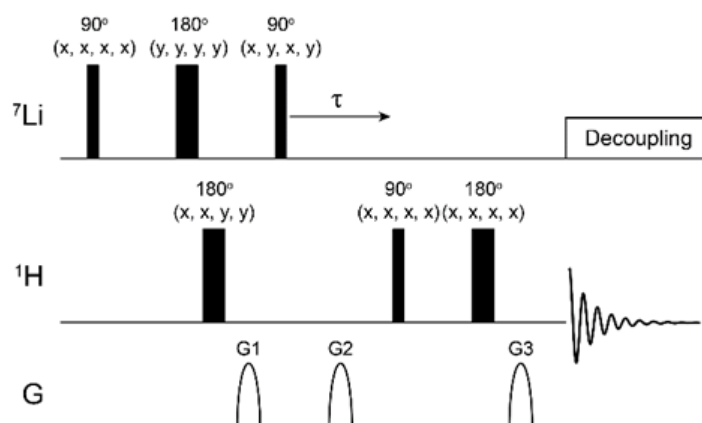


Figure 4-2: The ${}^7\text{Li}$ - ${}^1\text{H}$ HOESY pulse sequence used in this work, with phase cycling shown above pulses

By using the Stejskal-Tanner equation described in the diffusion section (see Chapter 2 Experimental NMR theory and methodology), the decay of the signal intensity is simulated with a diffusion coefficient of $4.63 \times 10^{-11} \text{ m}^2 \cdot \text{s}^{-1}$ (Figure 4-3). This shows that in fact at long mixing times, the percentage of signal intensity extracted is significantly attenuated ($\sim 25\%$ attenuation after 5000 ms).

PART 1:
Development of an automatic data fitting procedure

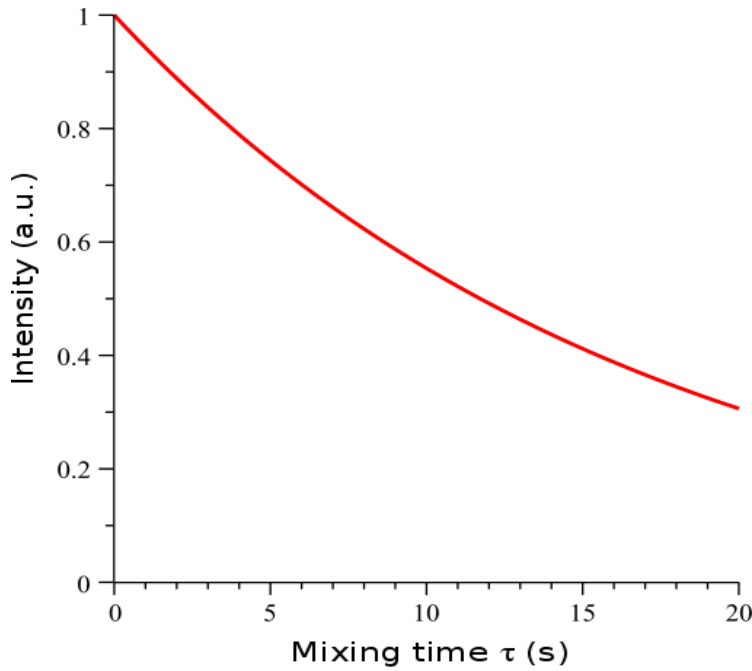


Figure 4-3: Theoretical signal intensity decay due solely to diffusion during the HOESY pulse sequence (experimental parameters as specified in main text). This signal intensity can drop by 30% at the longest mixing time used in this work ($\tau_m = 5.5$ s, $D = 4.63 \times 10^{-11}$ m².s⁻¹, $\delta = 1$ ms, $g = 0.5$ T/m and $\gamma_H = 2,68 \times 10^8$ rad.s⁻¹.T⁻¹).

In fact, neglecting the effects of diffusion on a particular sample will result in a systematic error for the σ values measured, thus this has no impact when these values are normalized. However, in order to enable a quantitative comparison of σ values between different types of IL systems, or at different concentrations or even at different temperatures the diffusion coefficients must be accounted for, and measured independently. Equation 4-1 was therefore modified in order to include a Stejskal-Tanner term accounting for the effects of signal attenuation due to diffusion as shown in Equation 4-3

$$M(\tau) = M_0 \sigma \frac{2 \sinh(\kappa \tau)}{\kappa} e^{-\frac{(R_I + R_S)\tau}{2}} e^{-\left(\frac{D_I + D_S}{2}\right) \gamma_I \gamma_S g^2 \delta^2 \left(\Delta - \frac{\delta}{3}\right)}$$

Equation 4-3

Figure 4-5 shows an example of the difference in the fit of a HOESY build-up curve using the equation with and without diffusion included. Similarly to the spin lattice relaxation experiment, the impact is more predominant at longer mixing times as these correspond to a longer diffusion time. This Figure shows data for the C₃mpyr FSI sample doped with 1 molal lithium FSI (this sample was choose for testing the fitting procedure, as the hydrogen spectrum was very well resolve with no

PART 1:

Development of an automatic data fitting procedure

overlapping peaks), and corresponds to the cross-relaxation between ^{19}F spins and ^1H spins in blue in Figure 4-4 (anion to cation transfer). Figure 4-6 correspond to the extracted cross-relaxation rates for each hydrogen peaks present in the cation, with and without the diffusion correction. One can notice that all peaks are impacted, and not by the same amount, thus this correction is mandatory.

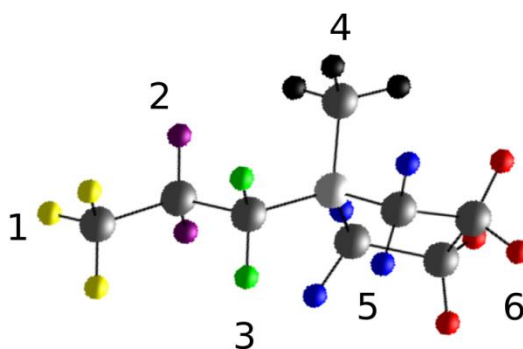


Figure 4-4: C₃mpyr cation with hydrogen sites numbering

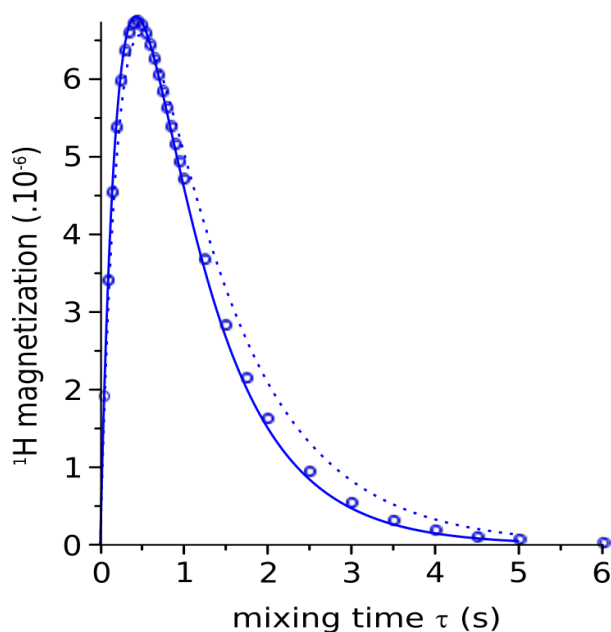


Figure 4-5: Build-up curve fitted by taking into account diffusion (solid line) and not taking into account diffusion (dot line) realised on C₃mpyr FSI sample doped with 1 molal lithium FSI

PART 1:
Development of an automatic data fitting procedure

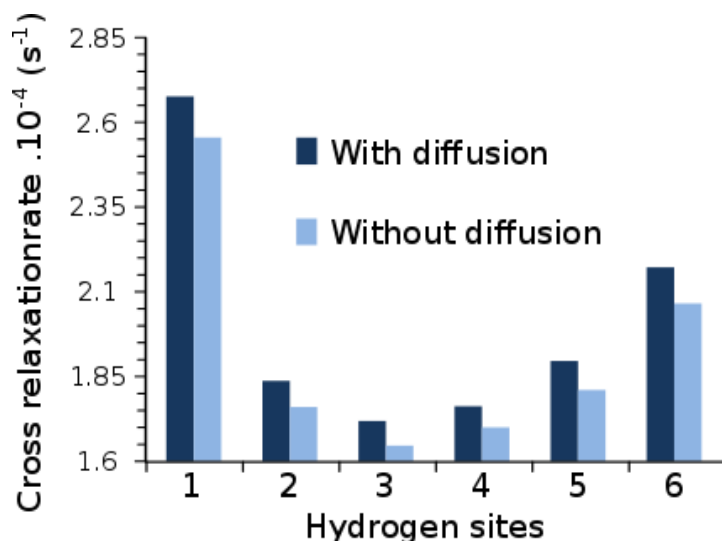


Figure 4-6: Measured cross-relaxation rates for the different ¹H sites in C₃mpyrFSI with 1 mol.kg⁻¹ of LiFSI, with and without taking account diffusion effects. Without accounting for diffusion, the cross-relaxation rates are smaller by around 5%.

4.1.I.3 Extracting quantitative cross relaxation rates

One of the more important aims of this work is to be able to extract the cross-relaxation rate in a quantitative way. Indeed a correct and quantitative extraction will allow us to compare these values for different ionic liquids or even different concentrations.

To extract an accurate cross-relaxation rate from the HOESY build-up curves using Equation 4-3, all of the other variables in this equation thus need to be measured.

The spin lattice relaxation parameters T_1 can be measured independently using inversion-recovery experiments (see details “Experimental NMR theory and methodology”). Moreover, as the decay due to the diffusion also needs to be taken into account, the self-diffusion coefficients of both spin-bearing species need to be measured independently.

With the relaxation rates and diffusion effects measured independently, M_0 is the last quantity in Equation 4-3 that needs to be determined in order to have the cross-relaxation rate σ as the sole variable in the fitting. When measuring weak

PART 1:

Development of an automatic data fitting procedure

intermolecular NOEs where $\sigma \ll R_{1/s}$, such as in the following experiments, M_0 and σ will play the same role in the equation and will affect the shape of the fit in essentially the same way, both acting as a vertical scaling factor. Thus it is particularly important to determine the M_0 factor in order to avoid a potential infinite number of solutions as shown on Figure 4-7.

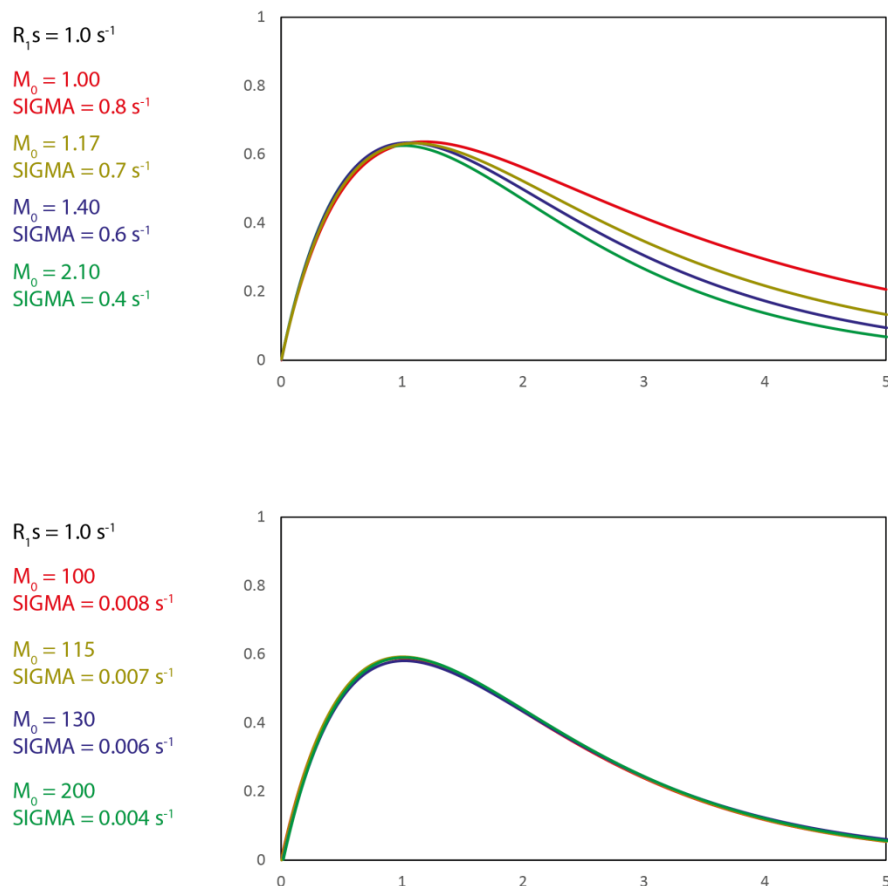


Figure 4-7: Theoretical HOESY build-up curves, with different M_0 and σ values. For small σ values, multiple solutions can give the same function shape. R_{1H} and R_{1Li} were both set to 1.0 s^{-1} for all curves.

In practice M_0 represents the total initial source spin X magnetization (S^X), available to participate in the NOE transfer (with X corresponding to either ^{19}F or either ^7Li spins). For the following work, as the HOESY experiments transfer magnetization from spin X to the ^1H spins, the total magnetization available corresponds to the Boltzmann equilibrium of either the ^7Li magnetization or the ^{19}F magnetization. The measured ^1H signals therefore need to be quantified as a fraction of this magnetisation^{76,77,123}. As shown in Figure 4-8, the HOESY experiments is not only

PART 1:
Development of an automatic data fitting procedure

dependent on the number of protons as the peak intensities do not correspond to the number of hydrogens nuclei for each specific sites. This is due to the distances between hydrogens sites and the lithium, indeed, if the lithium is close enough to a specific sites, some magnetization will be transferred, explaining why some peaks are more intense than expected.

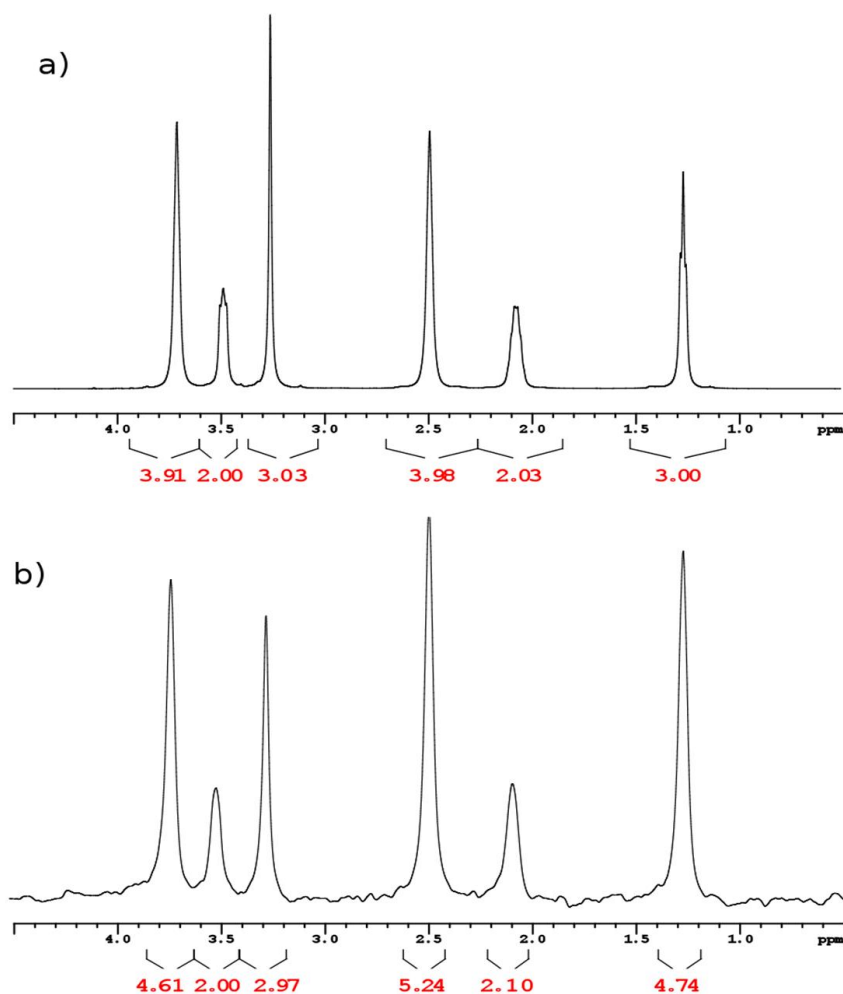


Figure 4-8: a) Quantitative single pulse ¹H spectrum with 4 scans corresponding to the pyrrolidinium cation (C₃mpyrFSI with 1 m. LiFSI), and b) 1D HOESY ⁷Li->¹H experiment at a mixing time of 700 ms, with 440 scans, normalized integrations show that the HOESY experiment is not only dependent of the number of protons

The normalization was realized in two steps. Firstly normalizing the integrated ¹H signal intensities extracted from the HOESY experiment to the ¹H Boltzmann polarization for each distinct ¹H peak, as measured using a single-pulse experiment. This normalization takes into account the effects of various parameters such as the different numbers of scans, or the different receiver gains, but also the normalization

PART 1:

Development of an automatic data fitting procedure

parameter used by the Bruker Topspin software (typically, NC_PROC equal to -9 corresponding to 2^{-9} factor for the HOESY experiment and 2^{-6} for the single pulse experiment). One should note that this normalization also accounts for any differences in the protons number contributing to each peak.

Secondly, after having carried out this signal normalization for the measured HOESY signals through the ^1H single pulse experiments, M_0 can then also be calculated as a fraction of the ^1H Boltzmann equilibrium magnetization (itself normalized to 1 as discussed above) using the following expression (Equation 4-4).

$$M_0 = \frac{\gamma(^7\text{Li})}{\gamma(^1\text{H})} \cdot \frac{n_{\text{Li}}}{n_{\text{C}_3\text{mpyr}}} \times n. a. (^7\text{Li})$$

Equation 4-4

which accounts for the ratio of the nuclear gyromagnetic ratios ($\gamma(^7\text{Li})/\gamma(^1\text{H}) = 0.389$), the ratio of the number of Li^+ relative to the number of C_3mpyr cations ($n_{\text{Li}}/n_{\text{C}_3\text{mpyr}}$), and the natural abundance of ^7Li ($n.a.(^7\text{Li}) = 0.9241$).

4.1.I.4 Fitting code using Maple

The first attempt to extract peaks intensities was made using Topspin software. Unfortunately this software is not flexible enough to provide all of the required data (*e.g.*, it cannot for example provide accurate T_{1s} from overlapping peaks in an inversion recovery data set). For example Figure 4-9 shows a studied sample, the 1-methyl-1-(2-methoxyethyl) pyrrolidinium bis(fluorosulfonyl)imide, which have the ^1H peaks arising from site 5 and site 3 overlapped.

PART 1:
Development of an automatic data fitting procedure

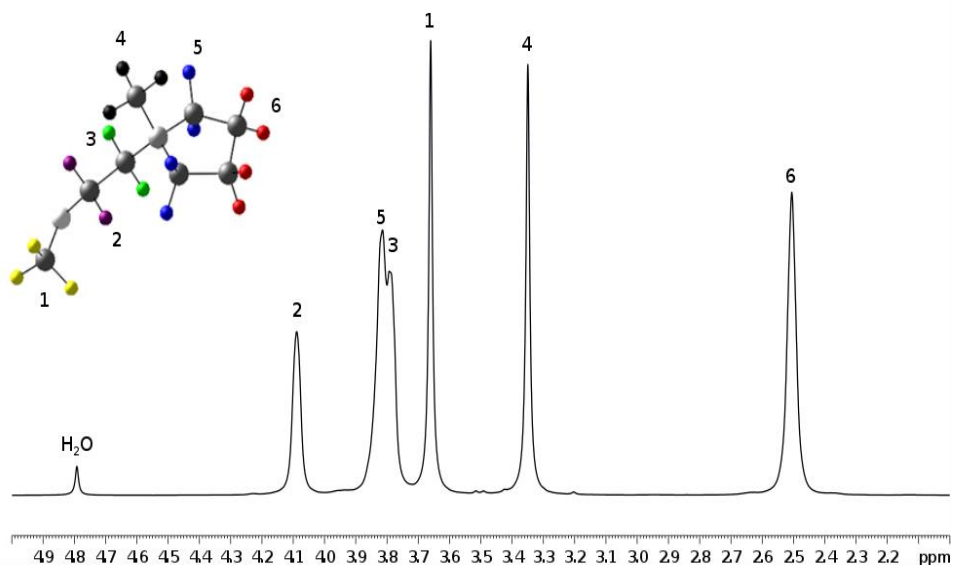


Figure 4-9: Single pulse ^1H spectrum of 1-methyl-1-(2-methoxyethyl) pyrrolidinium bis(fluorosulfonyl)imide, with peak assignment to the corresponding atom labelling.

Thus, a MAPLE code was developed to deconvolute overlapping peaks, extract intensities, control the normalization procedure and automatically fit the HOESY build-up curves. This allowed the data to be extracted and analyzed in a quantitative way, and the automation provided significant time savings.

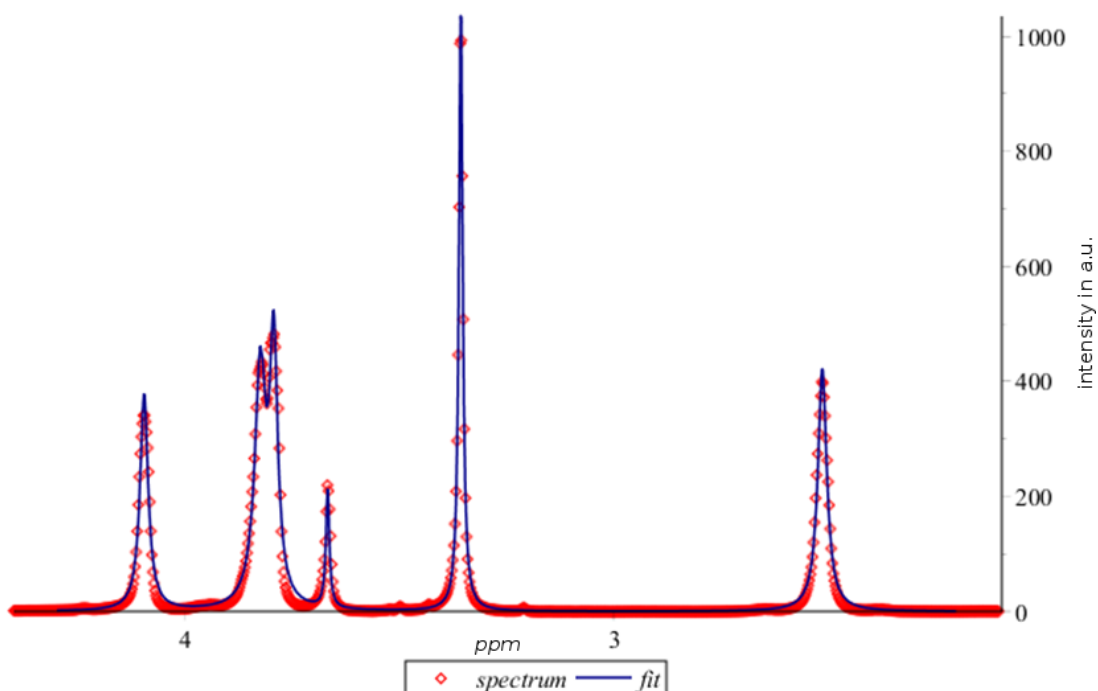


Figure 4-10: Single pulse ^1H spectrum of 1-methyl-1-(2-methoxyethyl) pyrrolidinium bis(fluorosulfonyl)imide fitted using Maple

PART 1:

Development of an automatic data fitting procedure

The Maple code was developed as follows. As shown in Figure 4-11, the T_1 relaxation data are opened as a 3D data set. By adjusting all the parameters in order to fit the whole 3D inversion recovery map in one step, the spin lattice parameter can thus be extracted for each site along with the peak widths, positions and intensities, even with overlapping peaks or low resolution.

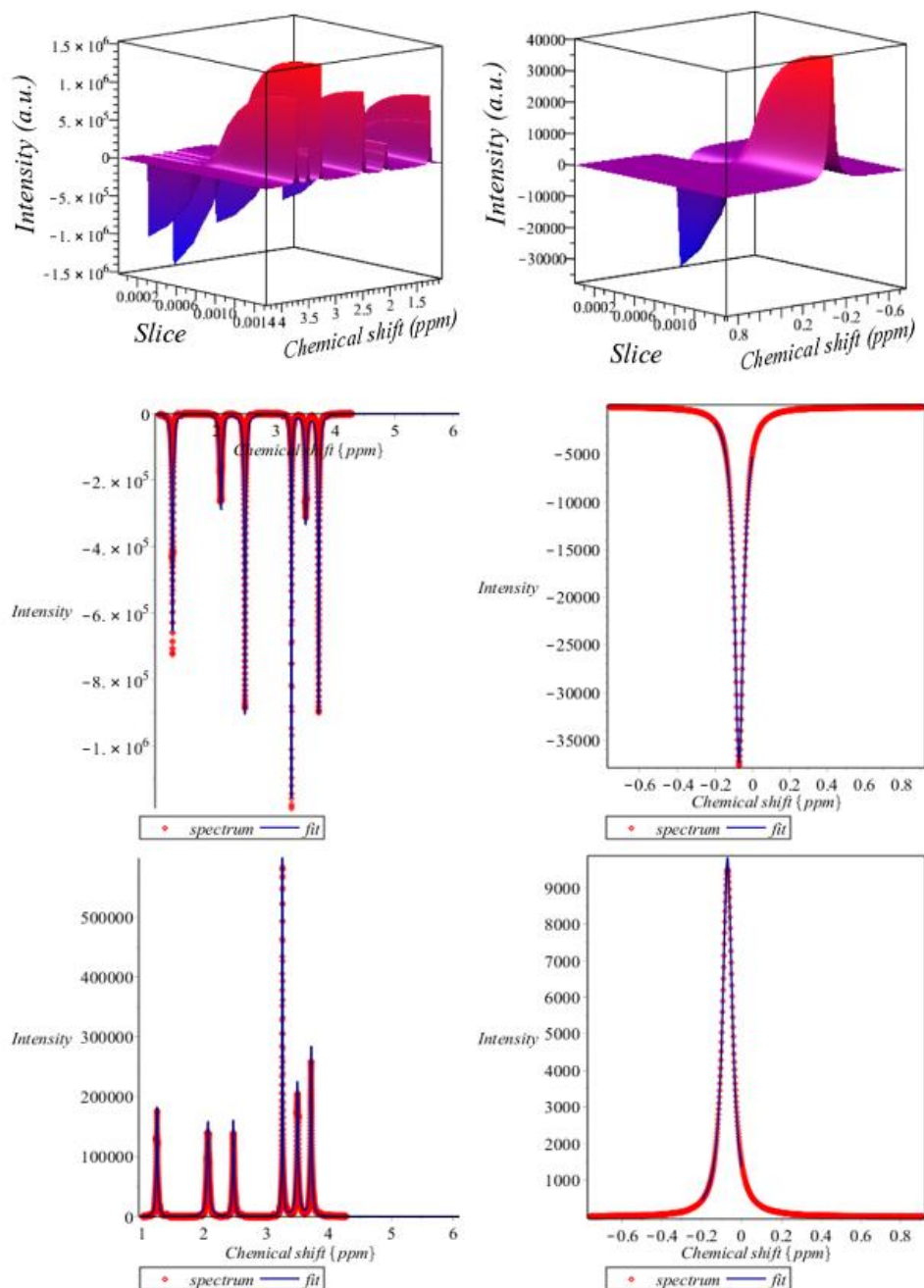


Figure 4-11: The top left figure correspond to the ^1H inversion recovery data set, follow by the fits of two different slices, corresponding to two different recovery delays. The right column corresponds to the ^7Li spin lattice relaxation

PART 1:
Development of an automatic data fitting procedure

The fully-relaxed ^1H NMR spectrum obtained by a single-pulse experiment is also fitted, providing a measure of the total ^1H magnetization to which the HOESY signals are normalised.

Figure 4-12 shows an example 3D HOESY data set, with the signal intensity displayed on the z axis (not yet normalized by the ^1H magnetization), and the mixing time and chemical shift on the x and y axis respectively.

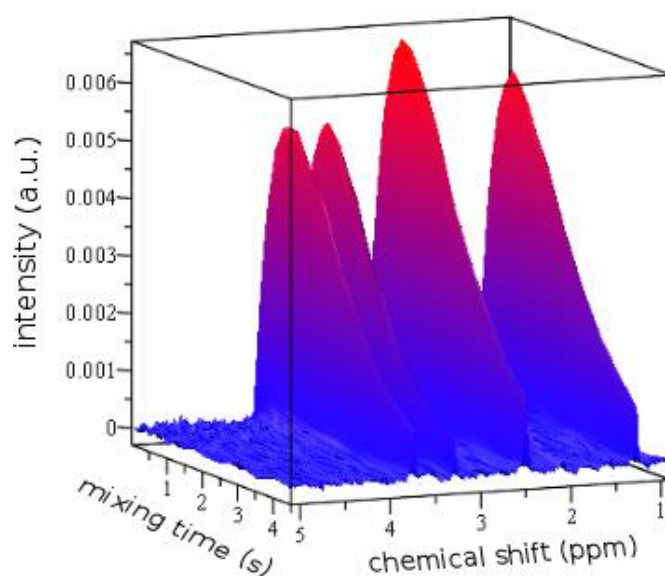


Figure 4-12: 2D ^1H - ^7Li HOESY data set obtained from 1-propyl-1-methylpyrrolidinium bis(fluorosulfonyl)imide doped with 1 m of lithium bis(fluorosulfonyl)imide.

Each slice is fitted independently, only using peak positions from the single pulse experiments as initial parameters, but all parameters such as peak positions, intensities or widths are allowed to vary. The software fits each slice using a least square minimization with a modified Newton algorithm (LSSolve function in Maple). Then the intensity for each peak is extracted and divided by the intensity of the corresponding peak in the single pulse experiment. Finally, all peaks intensities are plotted against mixing time, giving the build-up curves as shown in Figure 4-13

PART 1:

Development of an automatic data fitting procedure

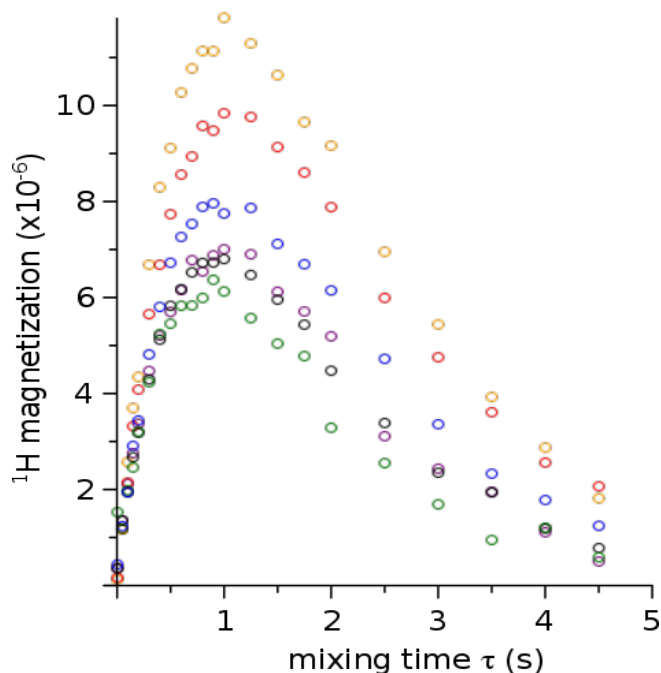


Figure 4-13: Build-up curves extracted from the ^1H - ^7Li HOESY experiment on 1-propyl-1-methylpyrrolidinium bis(fluorosulfonyl)imide doped with 1 m of lithium bis(fluorosulfonyl)imide

Now, using Equation 4-3, taking into account T_1 relaxation, self-diffusion coefficients and correcting the total magnetization when the recovery delay D_1 is not long enough compared to $T_1(^7\text{Li})$ (see below), all of the build-up curves can be fitted, and the corresponding cross-relaxation rates measured, as shown in Figure 4-14.

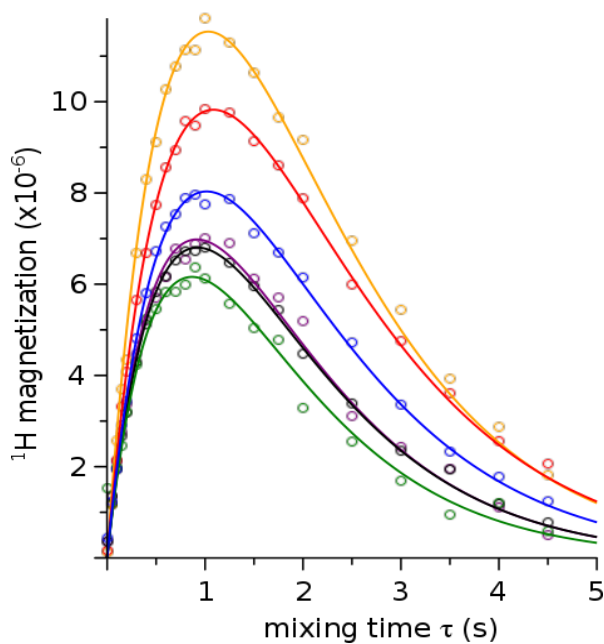


Figure 4-14: Build-up curves fitted to the ^1H - ^7Li HOESY data of 1-propyl-1-methylpyrrolidinium bis(fluorosulfonyl)imide, with the diffusion taken into account

PART 1:
Development of an automatic data fitting procedure

With the build-up curves normalized and the cross-relaxation rates extracted in a quantitative way, the molecule can be plot with a colour code corresponding to the cross relaxation rates. Therefore, assuming that the cross relaxation values scale inversely with the average inter-nuclear distances, as in Figure 4-15, showing where the X atoms (^7Li for the cation or ^{19}F for the anion) are located around the cation. The cross relaxation rates in this case correspond to the transfer from the X nuclei to the protons, but for clarity in the figure, the hydrogen atoms are removed and the carbons are colour coded. These cross relaxation rates and their significance in terms of the ionic liquid structure and interactions will be discussed in more detail in the C₃mpyr results chapter 3 part 2.

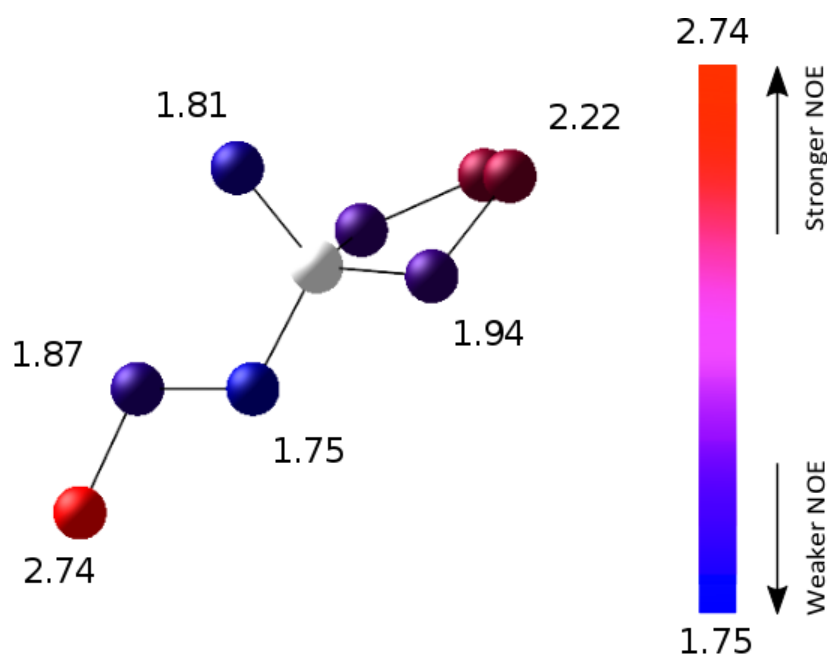


Figure 4-15: 1-propyl-1-methylpyrrolidinium cation with colour coding corresponding to the cross-relaxation rates in $(\times 10^{-4}) \text{ s}^{-1}$ between lithium and hydrogen for each hydrogen site (hydrogens sites were reduce to their corresponding carbon sites for clarity)

Extraction of cross relaxation rates were realised several times on the same sample with different number of mixing time for each experiments. The standard deviation of the cross relaxation rates was calculated for each peak and was found to be on average less than 2.5%. Therefore all cross relaxation rates will be presented with an uncertainty of 2.5%.

4.1.1.5 Experimental time optimization

PART 1:
Development of an automatic data fitting procedure

As explained earlier in the literature review, many researchers have used 2D HOESY experiments even if one of the studied nuclei shows only one site^{17,28,39,43,116,124}. Indeed, transferring magnetization from S^H to the other studied spin I^X (such as ^7Li or ^{19}F in our case) can potentially give the advantage of having a high sensitivity and thus a good signal to noise ratio with few scans due to the larger source magnetisation available to transfer by the NOE. Furthermore this transfer direction helps to avoid artefacts: due to field or RF phase instabilities, as the artefacts will be separated from the t_1 -modulated magnetization, either as a t_1 -noise along the indirect axis or as an unmodulated artefact appearing at the window center when 2D States mode is used. In 1D experiments, these artefacts can be present as “antiphase wobbles”, or as a signal present in the window center. In fact, the use of a pulse sequence using gradient coherence selection, as present in the following work, should normally reduce these problems, while the lock with an external deuterated sample is used to alleviate field instabilities.

However, when using $S^H \rightarrow I^X$, if multiple hydrogen sites are present, a 2D experiment is needed to resolve the different chemical shifts of the ^1H nuclei. In the following work, the signal will be acquired from the protons, because, as explained earlier, only ^{19}F and ^7Li are studied as the X spin, and in both cases for the samples studied here, only one site is present, thus, there is no need for an indirect dimension during the experiment. Moreover, the aim of this work is to obtain a quantitative extraction of the cross-relaxation rates, and this requires the quantification and normalization of the extracted HOESY signal, and 1D NMR peaks are simpler to integrate than 2D peaks.

One last advantage of using a 1D HOESY experiment instead of a 2D, is that the full build-up curve can be obtained in a single experiment by replacing the mixing time present in the pulse sequence by a variable delay (*i.e.*, different mixing time ranging from 50 ms up to 5.5 s) incremented as the second dimension. This procedure will create a 2D data set showing the time domain build-up curve in the indirect dimension. This way of acquiring the data keeps the HOESY results within a single data set that can be directly extracted by the Maple software for analysis.

PART 1:
Development of an automatic data fitting procedure

The experimental duration can be a limiting factor due to spectrometer availability, and this is particularly true for quantitative HOESY experiments as a large number of mixing times are needed to obtain complete build-up curves. Moreover, the magnetization transfer between nuclei during these types of experiments is very low, especially for intermolecular cross-relaxation. Thus, the signal is weak, and long signal accumulation times are required. With a typical T_1 of about one second, and a mixing time list of 22 values from 50 ms up to 5.5 s, these HOESY experiments took between 12 and 48 hours, depending both on the number of mixing times used and also the number of scans and the recycle delay between each scan. A reliable fit of the dataset typically requires a minimum signal to noise ratio of 25 for the shorter or longer mixing times (*i.e.*, the ones corresponding to the smallest intensities), and therefore, around 400 scans were required. One last correction factor equal to $[1-\exp(-d_1/T_1)]^{-1}$ was added for every peak, to account for incomplete relaxation when a recycle delay shorter d_1 than $5 \times T_1$ (^7Li or ^{19}F) is used.

In Figure 4-16, cross-relaxation data are plotted from five experiments carried out on (*N*-methyl-*N*-propyl-pyrrolidinium bis(fluorosulfonyl)imide ($\text{C}_3\text{mpyrFSI}$), containing 1.0 m lithium bis(fluorosulfonyl)imide. The experiments used the following recycle delay values: 10, 6.5, 4.5, 3 and 1.5 seconds. Therefore the recycle delay of 10 seconds is much greater than the time needed for quantitative experiments and so these data points are considered to be the most accurate. In the figure, the blue circles correspond to the cross-relaxation rates determined with the T_1 correction, and the red circles correspond to the values without this correction. Cross-relaxation rates are extracted for each peak.

At recycle delay over ~ 5 times the longest T_1 (corresponding approximately to 6.3 second in the present case), the extracted cross relaxation values are similar with and without the T_1 correction. But at shorter recycling delay, such as 3 or 4 seconds, the cross-relaxation rates without the T_1 correction, begin to deviate from the cross-relaxation rate with T_1 correction. Thus using this correction, the recycling delay can now be reduced to 1.26 times T_1 in order to maximize the optimum signal to noise ratio that can be achieved in a given experimental time, and still provide quantitative cross-relaxation rates. However, at short recycling delay such as 1.5 seconds, even

PART 1:

Development of an automatic data fitting procedure

with the T_1 correction, some cross-relaxation rates began to deviate by few percent ($\sim 5\%$) from the one measured for the fully relaxed system.

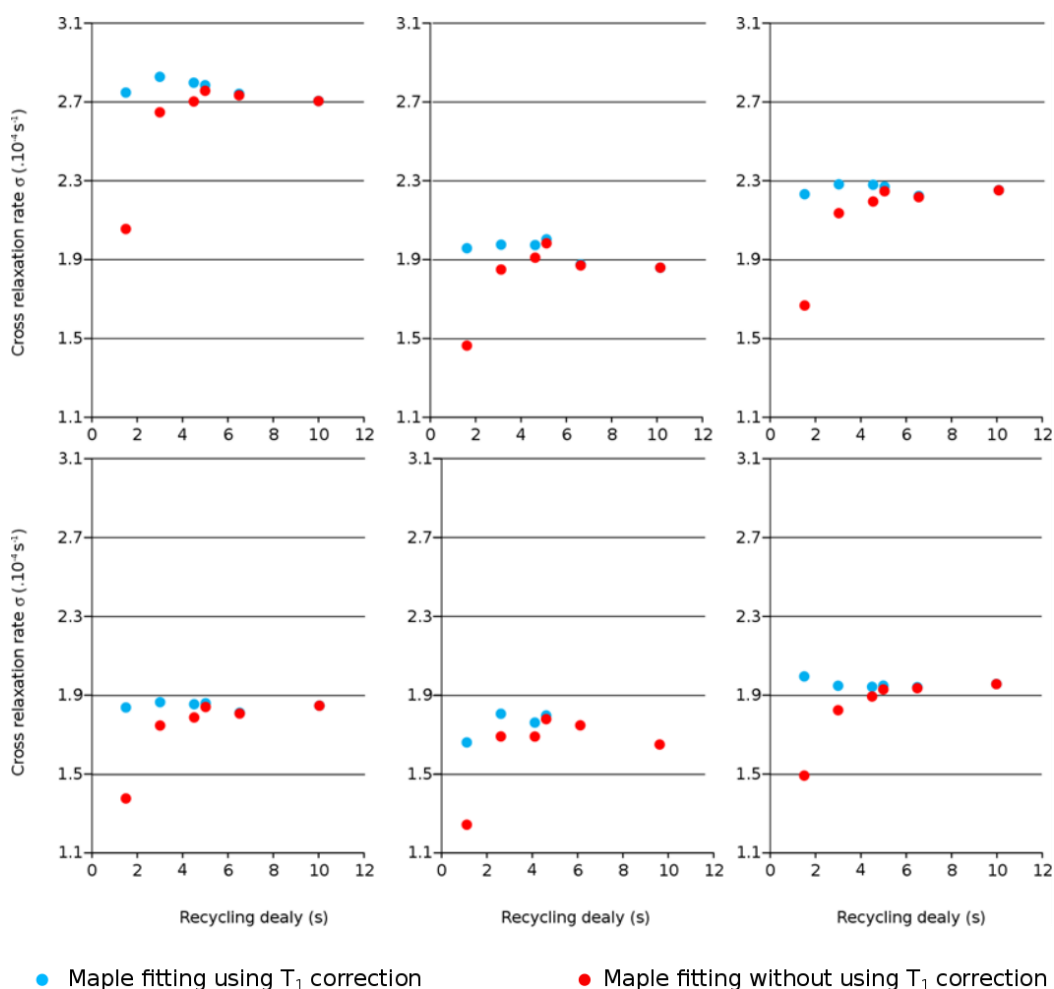


Figure 4-16: Six experiments carried out on the same sample, N-methyl-N-propyl pyrrolidinium ($C_3\text{mpyr}$ FSI) doped with 1 m of Lithium FSI, with different recycling delays (1.5s, 3s, 4.5s, 5s, 6.5s, 10s). The six graphs present the extracted ^7Li - ^1H cross-relaxation rates for the six hydrogen sites present on the pyrrolidinium cation, with and without taking into account the correction accounting for incomplete relaxation. (uncertainty of 2.5% for each cross relaxation rates)

Others studies were realized in order to optimize the experimental time. Indeed, despite the recycle delay, the number of scans and the number of mixing times are parameters that can impact the total experimental time. For example, three mixing time lists were tested, with 12, 22 and 32 mixing times. The results are presented in Figure 4-17 a), corresponding to the extracted cross-relaxation rates of the largest mixing time list in the set (32 mixing times) against the two other mixing time lists (22 mixing time in blue and 12 mixing time in red), for sample $C_3\text{mpyr}$ FSI doped with 1 m Li FSI at 20 °C, and Figure 4-17 b) which correspond to this same time of experiments, but this time for sample $C_3\text{mpyr}$ FSI doped with 3.2 m Li FSI at 20°C.

PART 1:
Development of an automatic data fitting procedure

One can see that the discrepancies of the results are pretty small, as the determination coefficient (R^2) is always over 95%, suggesting that there is no significant differences while using a short mixing time list with only 12 mixing times compared to a mixing time list of 32 mixing times, which reduces the total experimental time from 1.5 days to 6 hours.

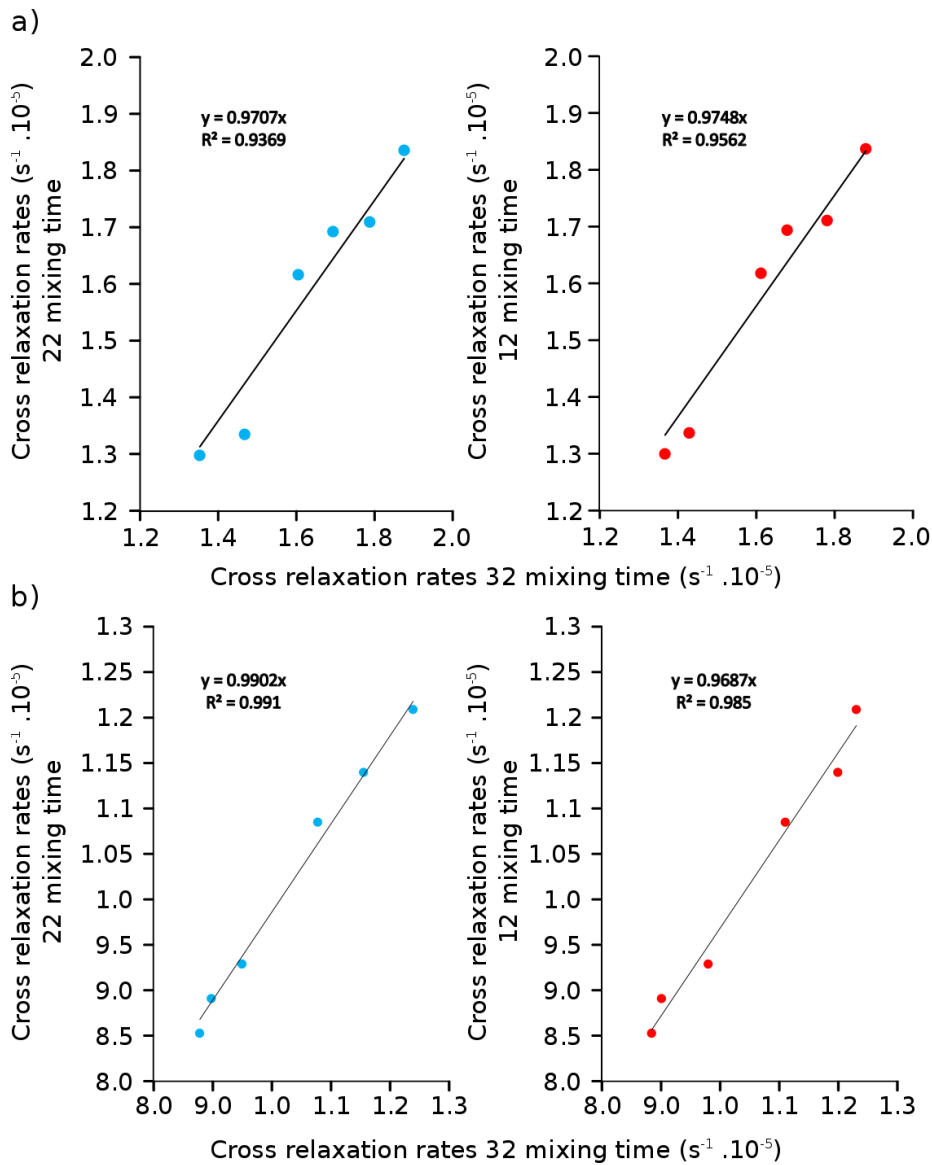


Figure 4-17: Extracted cross-relaxation values using 22 (in blue) and 12 (in red) mixing times as a function of the rates obtained with 32 mixing times, assuming these are the most exact ones. The lines are linear fits $y = ax$ (equation displayed on the graph with the coefficient of determination R^2). We showed the results obtained for samples C₃mpyr FSI at 20°C doped with 1 m Li FSI in a) and 3.2m Li FSI in b). (uncertainty of 2.5% for each cross relaxation rates)

In Figure 4-18, a similar type of representation is presented, but this time with 4 different numbers of scans: 80, 200, 440, 800 transients recorded, corresponding to a signal to noise ratio of 35, 70, 79, 130 for the twelfth mixing time or 900 ms,

PART 1:

Development of an automatic data fitting procedure

respectively, (*i.e.* near the top of the build-up curve, corresponding to the delay 10). The experiments with 80, 200 and 440 are plotted against the theoretical best experiments (800 number of scan). Similarly to a previous study, no significant discrepancies can be detected between experiments, and all yield a good coefficient of determination (R^2). Thus, even with a signal to noise ratio as low as 35 for the maximum transfer, cross-relaxation rates can be reliably extracted. Therefore, a significant gain in experimental time can be obtained by adjusting the number of scans. Thus, by optimizing all these parameters, we manage to record a full build-up curve, within an experimental time of ~ 2 h, compared to ~ 1.5 days in the beginning.

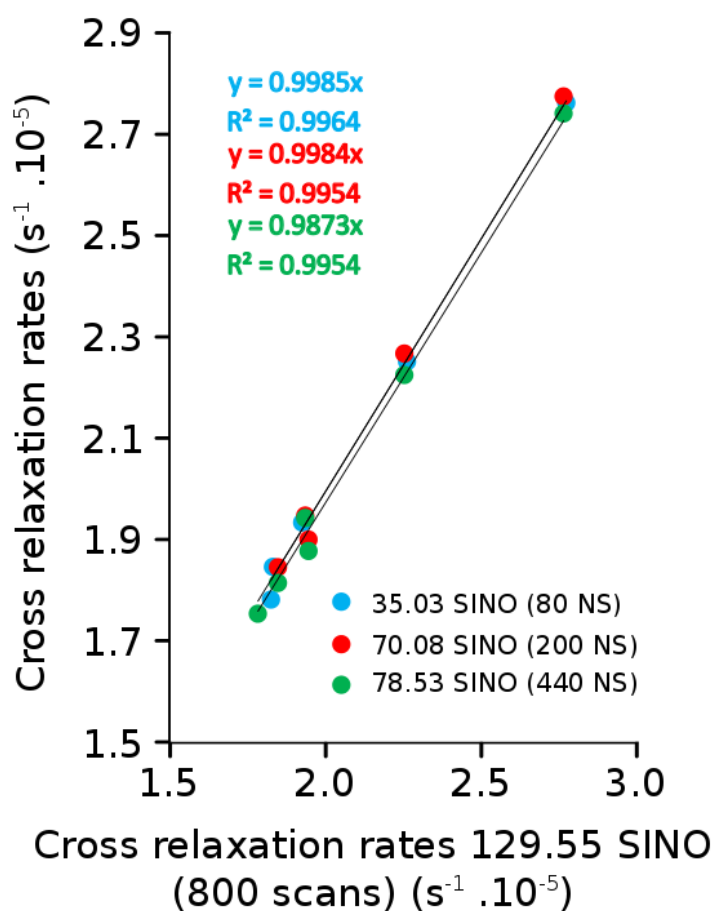


Figure 4-18: Extracted cross-relaxation values when 80 (blue), 200 (red) and 440 transients (green) are recorded, plotted as a function the theoretically better rates obtained with 800 transients recorded for each of the 22 mixing times and a recovery delay of 6.5 s. The lines corresponds to the linear fit $y = ax$ fit, displayed on top with the corresponding coefficient of determination R^2 . The sample was C_3mpyr FSI, doped with 1 m LiFSI at $50^\circ C$ (uncertainty of 2.5% for each cross relaxation rates).

4.1.II Conclusions

In order to extract heteronuclear, intermolecular cross relaxation rates from HOESY build-up curves in a quantitative manner, an improved data fitting procedure was developed. We have shown that diffusion coefficients must be measured and taken into account in the fitting due to the use of gradient pulses in the HOESY pulse sequence. Longitudinal relaxation times for the individual nuclei also need to be measured, and the normalisation of the HOESY signals relative to the equilibrium magnetisation is required to have the cross relaxation rate σ as the sole variable in the fitting. A home-written Maple code has been developed to achieve this fitting procedure. Prior to the cross relaxation rate extraction, this code automatically extracts required parameters from the raw data sets such as numbers of scans, receiver gains, etc., in order to normalize and fit build-up curves. By taking into account sample-specific factors such as the relative concentrations of the ions in the mixture, a quantitative comparison of cross relaxation rates in different ILs was made possible. Furthermore, we have considered ways to improve the time-efficiency of the HOESY experiment, showing that reliable and reproducible results can be obtained using shorter recycle delays, potentially reducing the experimental time by a factor of eight.

Part 2:
***N*-methyl-*N*-propyl
pyrrolidinium
bis(fluorosulfonyl)i
mide mixed with
lithium
bis(fluorosulfonyl)i
mide**

Part 2:

N-methyl-N-propyl pyrrolidinium bis(fluorosulfonyl)imide mixed with lithium bis(fluorosulfonyl)imide

The *N*-methyl-*N*-propyl pyrrolidinium bis(fluorosulfonyl)imide mixed with lithium bis(fluorosulfonyl)imide, was chosen as explained before due to the well resolved proton NMR spectrum, but also because this sample was a very commonly studied ionic liquid, therefore easy available on the shelf.

4.2.1 Spin lattice relaxation

The spin lattice relaxation times of the ^1H , ^{19}F and ^7Li nuclei were measured with inversion recovery experiments. Their longitudinal relaxation times measured at various temperatures can help to understand the dynamics (*via* the correlation time) for the C_3mpyr , FSI and lithium ions respectively. Moreover, the longitudinal relaxation times are also required for the quantitative measurements of the Overhauser effect (see previous chapter).

When relaxation rates are plotted as a function of the inverse of the temperature, a T_1 minima or R_1 maximum may be detected. At this temperature, the timescale for the underlying dynamics (which are responsible for the relaxation mechanism) is equal to the inverse of the nuclear Larmor frequency. In such cases, using the BPP theory (see Spectral density and relaxation theory in Materials and methods chapter) and assuming single relaxation processes with a single correlation time for each nucleus, the relaxation rates can be fitted and the correlation times can be retrieved. The presence of a T_1 minimum is necessary to precisely measure the magnitude of the interaction

As the T_1 relaxation data as a function of temperature exhibit a single T_1 minimum, only one relaxation process is assumed for each nucleus.

In the case of the ^1H T_1 measurements, the scalar, spin-rotation and chemical shift anisotropy relaxation were assumed to be negligible compared to the dipolar relaxation. Furthermore, the ^1H dipolar relaxation was assumed to be mostly due to the intramolecular homonuclear dipolar relaxation. The other dipolar relaxation mechanisms are neglected, as expected from the low abundance of ^{13}C and the long distance between ^1H and the other spin bearing ions. Thus as explained in the

Part 2:

N-methyl-N-propyl pyrrolidinium bis(fluorosulfonyl)imide mixed with lithium bis(fluorosulfonyl)imide

material and method section, in this case the data were fitted with the following equation:

$$\frac{1}{T_1(H)} = \frac{1}{T_1^{DD}(H)} = \frac{3}{10} \left(\frac{\mu_0}{4\pi} \right)^2 \frac{\gamma^4}{r^6} \left(\frac{\tau_c}{1 + \omega^2 \tau_c^2} + \frac{4\tau_c}{1 + 4\omega^2 \tau_c^2} \right)$$

Equation 4-5

While assuming that the correlation time follows an Arrhenius behavior:

$$\tau_c(T) = \tau_0 \exp\left(\frac{E_A}{RT}\right)$$

Equation 4-6

In the case of the ^{19}F nuclei of the FSI anion, several studies report¹²⁵ the quick reorganization of the FSI anion between the two potential configurations cis and trans, with a dipolar constant in the case of the cis conformer¹²⁵. In this case, intramolecular homonuclear dipolar relaxation can be assumed such as the hydrogen case.

However the proximity between C_3mpyr cations and anions let also presume that the intermolecular heteronuclear dipolar relaxation between the fluorine and the different hydrogen groups can be predominant. This behaviour has been actually reported by Kruk *et al*¹⁰⁹ in the case of a BMIM- BF_4 and BMIM- BF_6 . In the case of the intermolecular heteronuclear dipolar relaxation, the relaxation mechanism is described as follow:

$$\frac{1}{T_1^{DD}} = \frac{1}{10} \left(\frac{\mu_0}{4\pi} \right)^2 \frac{\hbar^2 \gamma_1^2 \gamma_2^2}{r^6} \left(\frac{\tau_c}{1 + (\omega_1 - \omega_2)^2 \tau_c^2} + \frac{3\tau_c}{1 + \omega_1^2 \tau_c^2} + \frac{6\tau_c}{1 + (\omega_1 + \omega_2)^2 \tau_c^2} \right)$$

Equation 4-7

Finally, in the case of the ^7Li T_1 measurements, the relaxation process can be more complicated. Indeed, ^7Li is a quadrupolar nucleus, and therefore the quadrupolar relaxation mechanism can play a significant role. In order to fit the ^7Li relaxation data, the quadrupolar relaxation will be assumed to be predominant and thus the fit will

Part 2:
N-methyl-N-propyl pyrrolidinium bis(fluorosulfonyl)imide mixed with lithium bis(fluorosulfonyl)imide

be restricted to the simple model of a quadrupolar relaxation as shown in Equation 4-11.

$$\frac{1}{T_1(H)} = \frac{1}{T_1^{Cq}(Li)} = C_q \left(\frac{\tau_c}{1 + \omega^2 \tau_c^2} + \frac{4\tau_c}{1 + 4\omega^2 \tau_c^2} \right)$$

Equation 4-8

The following chapter will focus only on the C₃mpyr-based IL sample at two concentrations, but also at different fields for some nuclei, as longitudinal relaxation rates were measured at 300 MHz, in parallel with the PFG experiments to measure the self-diffusion coefficients, but also at 500 MHz, as required for the fitting of the HOESY build-up curve. It should be noted that while the T₁ values are field dependent, the parameters extracted from the T₁ analysis, such as the correlation times and activation energies, are not.

4.2.I.1 Spin lattice relaxation for ¹H nuclei

As mentioned earlier, the spin lattice relaxation of ¹H nuclei against temperature were fitted assuming only one relaxation mechanism, with a single correlation time, the intramolecular homonuclear dipolar relaxation.

The color coding for ¹H spin lattice relaxation rate curves corresponds to the color coding of Figure 4-19 a).

Part 2:

N-methyl-*N*-propyl pyrrolidinium bis(fluorosulfonyl)imide mixed with lithium bis(fluorosulfonyl)imide

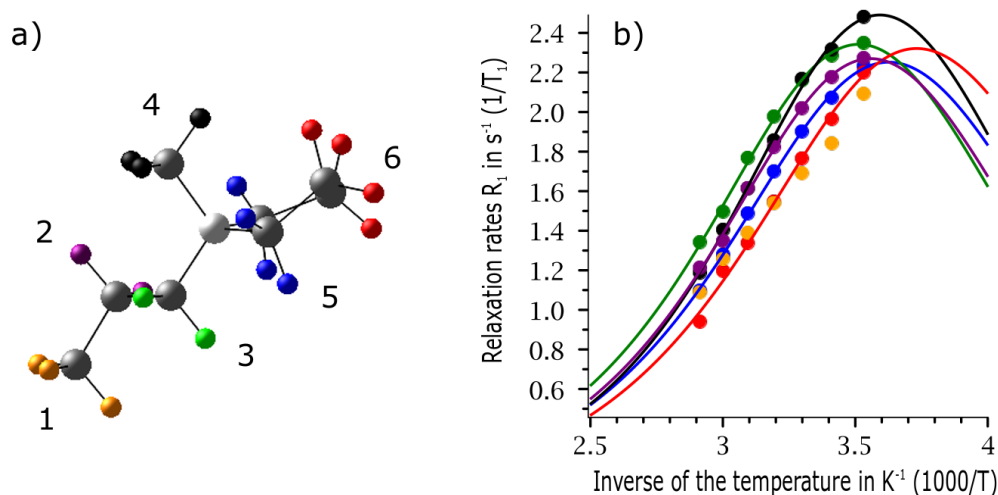


Figure 4-19: a) C₃mpyr cation with ¹H sites color coding and number and b) ¹H Spin lattice relaxation at 300 MHz as a function of temperature for sample C₃mpyr FSI with 3.2 m LiFSI

Unfortunately, the relaxation curves for sample C₃mpyr FSI with 1 m LiFSI and measured at 300 MHz, could not be reliably fitted, as no R_1 maxima were detected because of the limited temperature range of the probe used.

As shown in Figure 4-19 b) for the sample C₃mpyr FSI containing 3.2 m LiFSI, the ¹H spin lattice relaxation data points exhibit some curvature due to being close to the T_1 minima and can be thus fitted reliably, except for the methyl group at the end of the alkyl chain that does not show any T_1 minimum.

In table 1 below, the extracted results from the BBP fitting are presented, with the activation energy in $kJ.mol^{-1}$ and the correlation time at infinite temperature.

Part 2:
N-methyl-*N*-propyl pyrrolidinium bis(fluorosulfonyl)imide mixed with lithium
 bis(fluorosulfonyl)imide

Table 4-1 : Extracted activation energy E_a (in kJ/mol) and correlation time τ_0 at infinite temperature for ^1H T_1 measurements on $\text{C}_3\text{mpyrFSI}$ with 3.2 m LiFSI, measured at 300 MHz.

Peak		E_a kJ.mol $^{-1}$	$\tau_0 \times 10^{-12}$ s $^{-1}$	$\tau_c \times 10^{-10}$ s $^{-1}$ at 50°C
5	N-CH $_2$ -CH $_2$	16.38	1.61	7.2
3	CH $_3$ -CH $_2$ -CH $_2$	17.09	1.49	8.68
4	CH $_3$ -N	17.6	1.01	7.15
6	N-CH $_2$ -CH $_2$	15.92	1.61	6.06
2	CH $_3$ -CH $_2$ -CH $_2$	17.04	1.39	7.93
1	CH $_3$ -CH $_2$ -CH $_2$	-	-	-

Combining these results with Equation 4-5 allows us to plot the calculated correlation times as a function of $1000/T$ for each ^1H site (Figure 4-20). Even if the differences between the correlation times are small, one should note that the fastest motions (smaller τ_c) correspond to the pyrrolidinium ring. This results are in good agreement with a previous study⁵⁶, on a similar sample, which attributes these faster motions to the rapid inversion of the pyrrolidinium ring. The activation energy, present in Table 4-1, exhibits a similar trend as the correlation time, with the smallest activation energy for the ^1H sites on the pyrrolidinium ring.

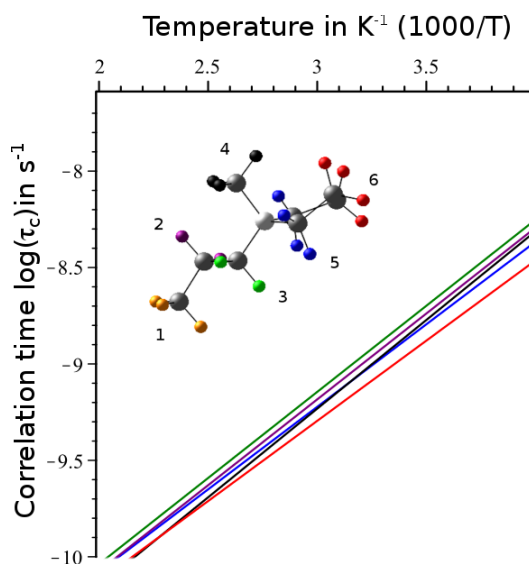


Figure 4-20: Correlation times τ_c obtained from the ^1H relaxation curves, as a function of $1000/T$ for sample $\text{C}_3\text{mpyrFSI}$ at 3.2 m LiFSI.

In the case of the $\text{C}_3\text{mpyrFSI}$ system doped with 1 molal LiFSI, the relaxation rate vs temperature curves recorded at 500 MHz showed a change of curvature hinting at a

Part 2:

N-methyl-*N*-propyl pyrrolidinium bis(fluorosulfonyl)imide mixed with lithium bis(fluorosulfonyl)imide

T_1 minimum, except for the CH_3 group attached to the nitrogen. Interestingly, the corresponding fits, as shown on Figure 4-21, show a trend similar to what was observed for the 3.2 m sample at 300 MHz, with faster motion for the two groups on the pyrrolidinium ring, as shown by their T_1 minimum occurring at a lower temperature.

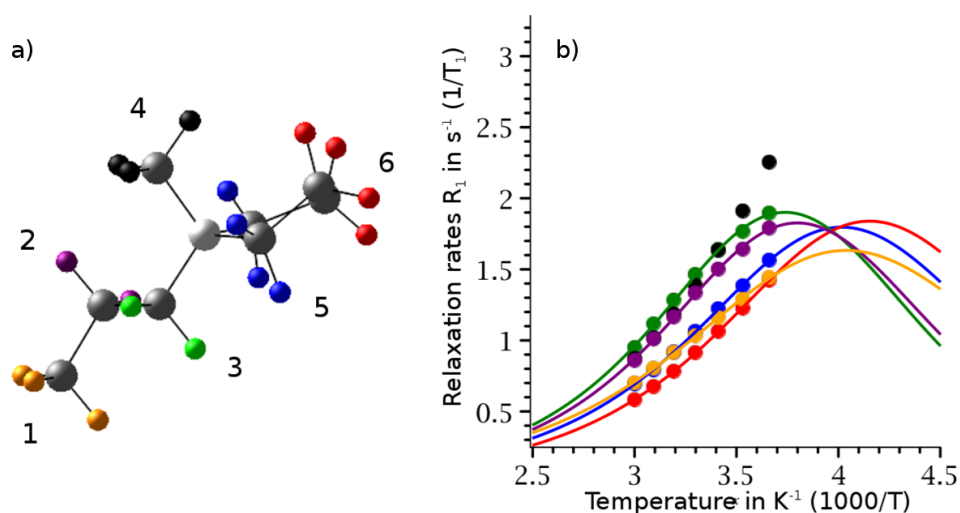


Figure 4-21: a) C_3mpyr cation with ^1H sites color coding and number and b) ^1H spin-lattice relaxation rates measured at 500 MHz as a function of temperature for sample C_3mpyr FSI with 1 m LiFSI.

The fitted activation energies (see Table 4-2) display a similar trend, as seen previously for the C_3mpyr with 3.2 m LiFSI, with ring protons presenting lower activation energies. All activation energies are slightly smaller, as expected for a sample with a lower viscosity¹²⁶. Moreover, the methyl group at the end of the alkyl chain presents the smallest activation energy, as expected for these more mobile protons due to the mobility of first the molecule, plus the rotation of each segment of the alkyl chain and then the rotation of the three hydrogens. It must be noted that in our analysis, we neglected the interplay between rotational diffusion and local motions, as only one relaxation rate was measured.

Part 2:
N-methyl-*N*-propyl pyrrolidinium bis(fluorosulfonyl)imide mixed with lithium
 bis(fluorosulfonyl)imide

Table 4-2: Extracted activation energies E_a and correlation times at infinite temperature for ^1H T_1 measurements on $\text{C}_3\text{mpyrFSI}$ with 1 m LiFSI at 500 MHz.

Peak		E_a $\text{kJ}\cdot\text{mol}^{-1}$	$\tau_0 \times 10^{-12} \text{ s}^{-1}$	$\tau_c \times 10^{-10} \text{ s}^{-1}$ at 50°C
5	N-CH ₂ -CH ₂	13.74	1.61	2.68
3	CH ₃ -CH ₂ -CH ₂	15.44	1.18	3.72
4	CH ₃ -N	-	-	-
6	N-CH ₂ -CH ₂	13.6	1.37	2.18
2	CH ₃ -CH ₂ -CH ₂	14.99	1.3	3.46
1	CH ₃ -CH ₂ -CH ₂	12.4	2.98	3.02

Using the parameters shown on Table 4-2 and Equation 4-5, correlation times can be calculated over a range of temperature (see Figure 4-22). Similar conclusions can be drawn on this second system. As expected from the lower viscosity, all correlation times are now shorter compared to the more concentrated sample. Indeed, the 1 m and 3.2m samples correspond to molar fractions of 25 and 50 mol% of LiFSI, respectively.

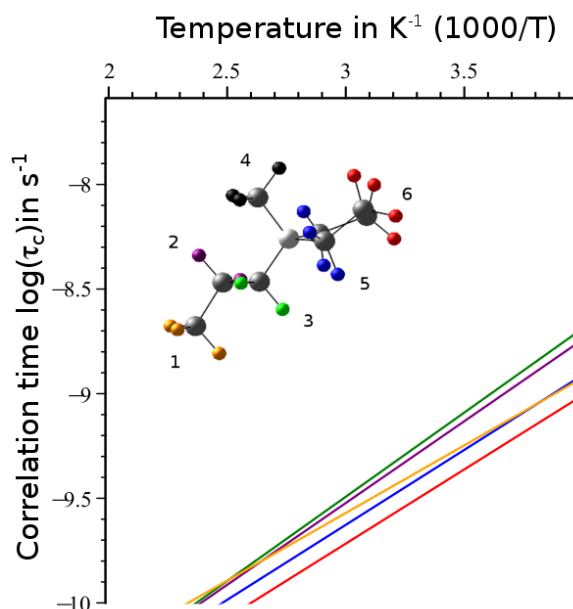


Figure 4-22: Correlation time τ_c calculated from ^1H longitudinal relaxation rates plotted as a function of $1000/T$ for sample $\text{C}_3\text{mpyrFSI}$ with 1 m LiFSI.

4.2.1.2 Spin lattice relaxation for ^{19}F nuclei

As discussed earlier, in the case of ^{19}F T_1 spin lattice relaxation, two different relaxation mechanisms can be studied, either the intramolecular homonuclear dipolar relaxation between two fluorine nuclei, and most likely when the FSI is on the cis-conformation, or the intermolecular heteronuclear dipolar relaxation between fluorine nuclei and the surrounding hydrogens as one would expect a great association between the cation carrying on the hydrogens and the anion carrying the fluorine.

The ^{19}F T_1 longitudinal relaxations were fitted using the intermolecular heteronuclear dipolar relaxation, which was supposed to be predominant. Thus Figure 4-23 reports the fit from the intermolecular mechanism for both concentrations. (Similar fit and results were in fact obtained separately in the intramolecular case)

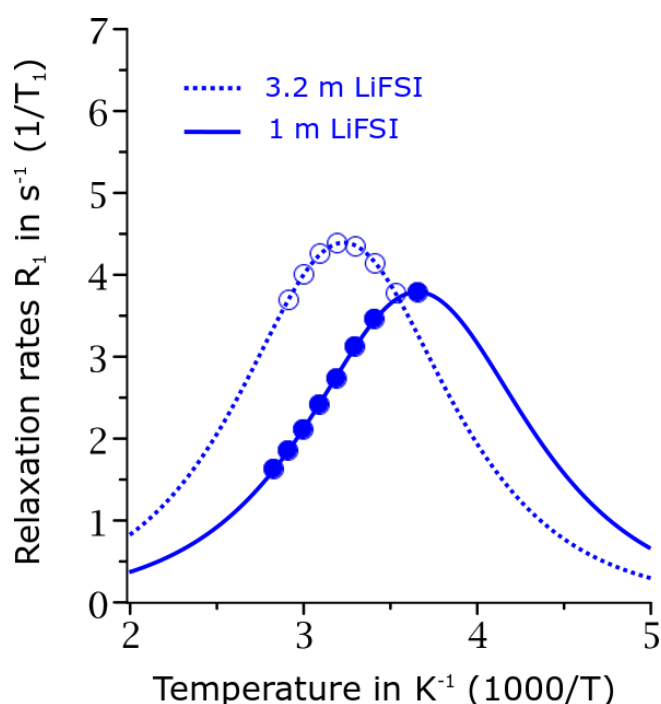


Figure 4-23 : ^{19}F longitudinal relaxation rates at 300 MHz as a function of temperature for $\text{C}_3\text{mpyrFSI}$ at 1 m and 3.2 m of LiFSI, using the intermolecular heteronuclear dipolar relaxation

According to Table 4-3, which represents the extracted activation energy E_A , the τ_0 and the correlation time τ_c at 50°C for the two concentrations, the fluorine and thus the anion have a higher activation energy at higher concentration, and a higher

Part 2:

N-methyl-N-propyl pyrrolidinium bis(fluorosulfonyl)imide mixed with lithium bis(fluorosulfonyl)imide

correlation time. This can be explained by the apparent higher viscosity of the sample at higher concentration. Correlation time trend are displayed in Figure 4-24.

Table 4-3: Extracted activation Energy and correlation time at infinite temperature for ^{19}F T_1 measurements on C_3mpyr FSI at 1 m and 3.2 m of Li FSI.

C° (mol/kg)	E_A $\text{kJ}\cdot\text{mol}^{-1}$	$\tau_0 \times 10^{-12} \text{ s}^{-1}$	$\tau_c \times 10^{-9} \text{ s}^{-1}$ at 50°C
1	15.13	4.24	1.19
3.2	15.94	6.74	2.55

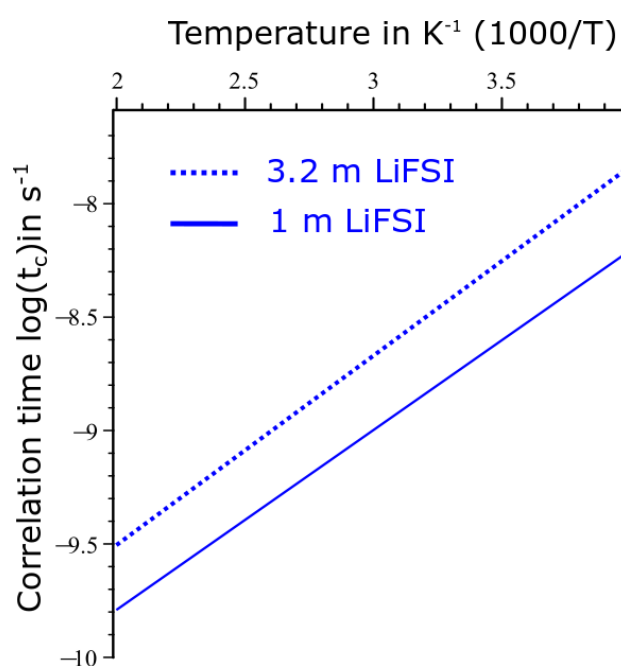


Figure 4-24: ^{19}F calculated correlation time τ_c as a function of $1000/T$ for sample C_3mpyr FSI at 1 m and 3.2 m Li FSI in the intermolecular heteronuclear dipolar relaxation

4.2.1.3 Spin lattice relaxation for ^7Li nuclei

As mention earlier, the ^7Li T_1 relaxations at two concentrations were fitted using the quadrupolar relaxation equation (Equation 4-8). Figure 4-25 represent the plot of the T_1 parameter as function of temperature, and the corresponding fits.

Part 2:
N-methyl-N-propyl pyrrolidinium bis(fluorosulfonyl)imide mixed with lithium bis(fluorosulfonyl)imide

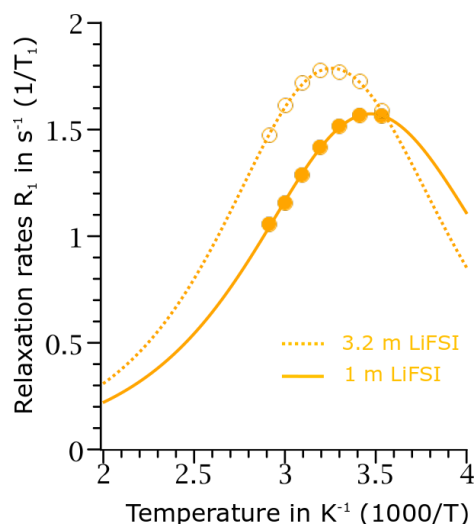


Figure 4-25: ^7Li spin lattice relaxation at 300MHz as a function of temperature for sample $\text{C}_3\text{mpyr FSI}$ at 1 m and 3.2 m of Li FSI

Similarly to the fluorine relaxation, according to Table 4-4, which represents the extracted activation energy E_A , the τ_0 and the correlation time τ_c at 50°C for the two concentrations, the lithium have a higher activation energy at higher concentration, and a higher correlation time. This can be explained by the apparent higher viscosity of the sample at higher concentration. Correlation time trend are displayed in Figure 4-26.

Table 4-4: Extracted activation Energy and correlation time at infinite temperature for ^7Li T_1 measurements on $\text{C}_3\text{mpyr FSI}$ at 1 m and 3.2 m of Li FSI.

C° (mol/kg)	E_A $\text{kJ}\cdot\text{mol}^{-1}$	$\tau_0 \times 10^{-12} \text{ s}^{-1}$	$\tau_c \times 10^{-9} \text{ s}^{-1}$ at 50°C
1	15.4	8.47	2.63
3.2	16.6	7.8	3.82

Part 2:
N-methyl-*N*-propyl pyrrolidinium bis(fluorosulfonyl)imide mixed with lithium bis(fluorosulfonyl)imide

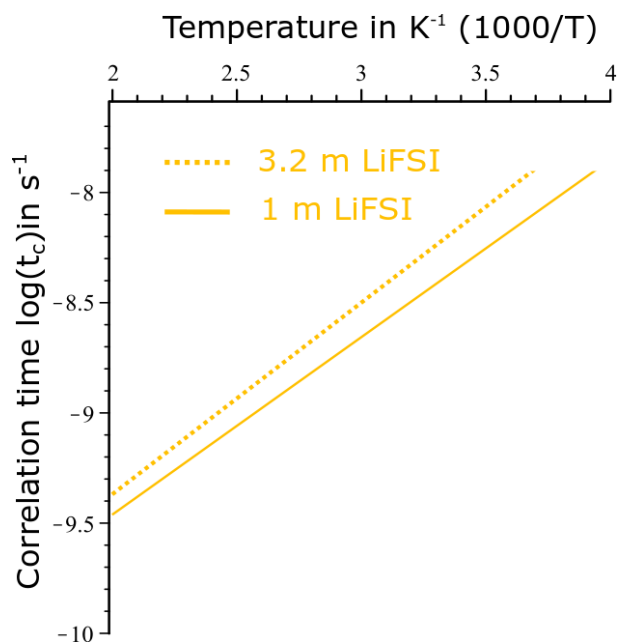


Figure 4-26: ⁷Li calculated correlation time τ_c as a function of $1000/T$ for sample C₃mpyr FSI at 1 m and 3.2 m Li FSI

The T_1 longitudinal relaxations were analysed as shown in the last sub-chapters, unfortunately there were not enough results for the extraction of the correlation time for the ¹H T_1 longitudinal relaxation. This prevented us from comparing the extracted correlation times of the different species present in the ionic liquid. However it should be noted that extraction of these parameters will be important in the future in order to correlate with NOE transfer.

4.2.II NOESY H-H measurements

As shown in Figure 4-27, one of the first experiments carried out in order to prepare for the HOESY experiments was the single pulse ¹H experiment on the *N*-methyl-*N*-propyl pyrrolidinium bis(fluorosulfonyl)imide (C₃mpyr FSI) mixed with 1 molal of lithium bis(fluorosulfonyl)imide (LiFSI). Therefore, the different peaks corresponding to the different hydrogen sites on the C₃mpyr cation were assigned. The methyl group on the nitrogen, attributed to the peak position four, corresponds to a singlet, as there no hydrogen neighbours but also due to the peak intensity corresponding to three (display in red). The methyl groups at the end of the chain, corresponding to

Part 2:
N-methyl-N-propyl pyrrolidinium bis(fluorosulfonyl)imide mixed with lithium bis(fluorosulfonyl)imide

peak 1 has been attributed to the triplet due to the two neighbours, and furthermore due to the peak intensity corresponding to three. Peak 5 and 6 has been attributed due to the peak intensity of four, and has been distinguished one to the other, due to the stronger chemical shift of the CH₂ group the closer to the nitrogen. Similar reasoning has been used to distinguish peak 2 and 3.

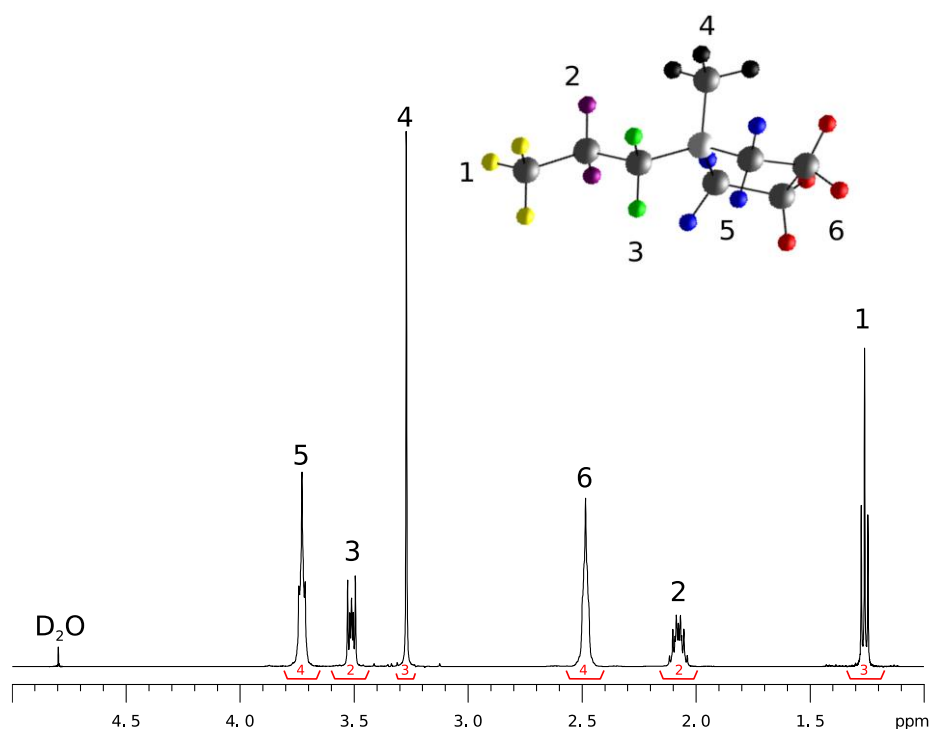


Figure 4-27: ¹H spectrum corresponding to the C₃mpyr FSI IL doped with 1 m LiFSI

Subsequently, ¹H-¹H NOESY experiments were carried out at different fields. First of all, these NOESY experiments help to confirm the peak assignments, as the spatial correlations for the different hydrogen sites can be observed. But secondly, these NOESY experiments were realized in order to observe the intensity of the ¹H-¹H NOESY transfer. Indeed, as the aim of this work is to realize some heteronuclear transfer between either ⁷Li or ¹⁹F nuclei to the surroundings hydrogens, it is also interesting to see during the HOESY experiments, there will be some homonuclear relayed NOE through bonds.

Part 2:
N-methyl-*N*-propyl pyrrolidinium bis(fluorosulfonyl)imide mixed with lithium bis(fluorosulfonyl)imide

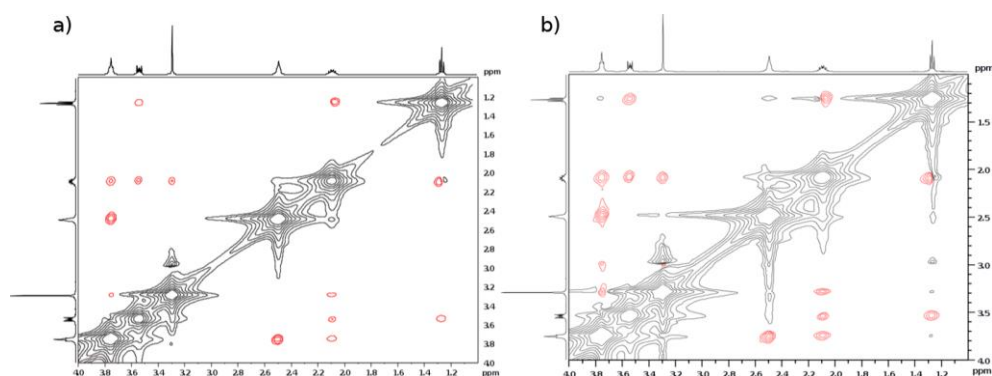


Figure 4-28: ^1H - ^1H NOESY experiments realized at a) 17.61 T and b) 11.74 T

As presented in Figure 4-28, two NOESY experiments were realized at two different fields (17.61 T and 11.74 T), in order to see the impact of the field on the NOE transfer during NOESY experiments. It is quite clear that the NOE transfer between hydrogens, despite the close distance between nuclei, is weak. The NOE transfer is actually even weaker at lower field which corresponds to the field strength at which HOESY experiments will be carried out. Thus in the further work, as the HOESY transfer is already weak, the potential NOESY transfer relayed through bonds, will be assumed negligible beyond the direct HOESY transfer.

4.2.III Cross relaxation rates measurements

4.2.III.1 ^1H - ^7Li HOESY experiments

4.2.III.1.1 C_3mpyr 1 m Li FSI

The first HOESY measurements were carried out on $\text{C}_3\text{mpyrFSI}$ with 1 molal LiFSI at 50°C as at this temperature the ionic liquid is fluid enough and thus the NMR signal present a good enough signal over noise ratio. As the major interest was to understand the interactions of the lithium cations with its surroundings, we began

Part 2:

N-methyl-*N*-propyl pyrrolidinium bis(fluorosulfonyl)imide mixed with lithium bis(fluorosulfonyl)imide

with ^1H - ^7Li HOESY experiments, thus probing the cation-cation interactions. Build-up curves were extracted and using the previously extracted self-diffusion coefficients for both cations, and the calculated spin lattice relaxation for each hydrogen sites and for the lithium, these build-up curves were fitted following the methods outlined in the previous chapter (see Figure 4-29).

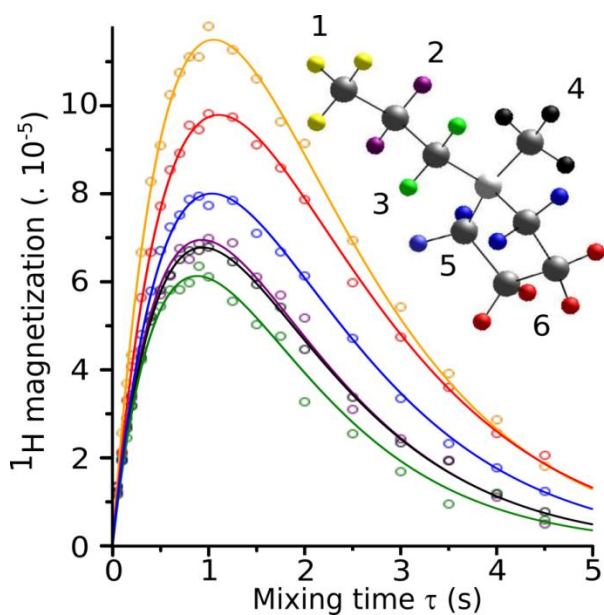


Figure 4-29: ^1H - ^7Li HOESY build-up curves for $\text{C}_3\text{mpyrFSI}$ with 1 m LiFSI at 50°C

In Figure 4-30, the cation C_3mpyr is represented with hydrogen atoms coloured according to the intensity of the cross-relaxation rates, red standing for the largest σ value, and blue for the smallest one. Figure 4-30 a) correspond ^1H - ^7Li experiments at 50°C and b) at 20°C . The same colour coding will be used for the other experiments and the others cations, as an aid to highlight the variations of cross-relaxation rates within the same molecule. The colour coding should not be used in order to compare different systems, only the cross-relaxation numbers displayed in the different figures can be compared.

Part 2:

N-methyl-*N*-propyl pyrrolidinium bis(fluorosulfonyl)imide mixed with lithium bis(fluorosulfonyl)imide

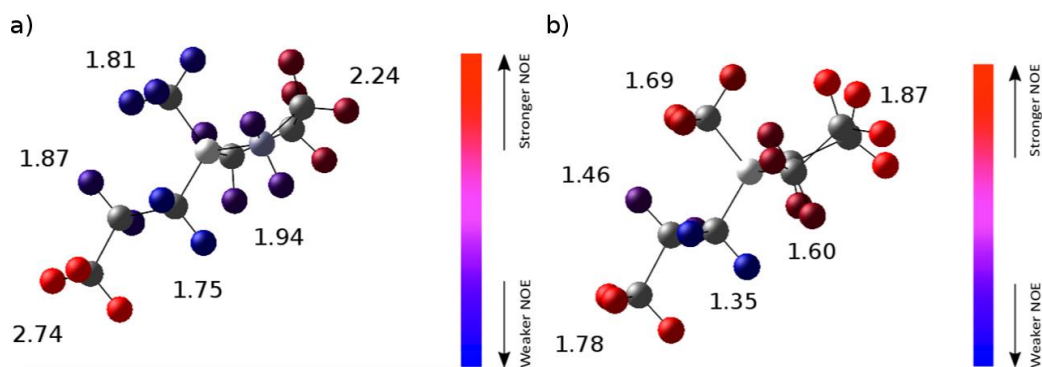


Figure 4-30: ^1H - ^7Li Overhauser rates for the C₃mpyr and lithium cations (1 molal LiFSI). Cross-relaxation rates are in 10^{-4} s^{-1} and the colour coding corresponds to the relative intensities of the NOE at a) 50°C and b) 20°C (uncertainty of 2.5% for each cross relaxation values)

According to the colour coding on Figure 4-30 a), it is easy to see that the highest ^1H - ^7Li cross relaxation rate value by far correspond to methyl group at the end of the alkyl chain. The second strongest value is reported on the CH₂ on the cycle the further away from the nitrogen site. The four other cross-relaxation rate which are closer to the nitrogen site, all exhibits lower cross relaxation rates values. This trend can be explained due to the repulsion between the Li⁺ and the nitrogen positively charges.

As shown in Figure 4-30 b) which represents the extracted ^1H - ^7Li cross-relaxation rates for the same system, but this time at 20°C, a similar trend can be noticed. However, by directly comparing the cross relaxation values at 50°C and at 20°C, one should note that at 20°C, the methyl group on the nitrogen and the CH₂ close to the nitrogen on the cycle, exhibiting quite higher values compared to the two CH₂ on the alkyl chain, which was not the case at 50°C. Thus by decreasing the temperature, the lithium looks like to exhibit a higher interaction with the cycle and the methyl group compared at higher.

Figure 4-31 represents a bar graph of the extracted cross-relaxation rates, with the one corresponding to the 1 molal concentration in blue. First, there is clear correlation between the Overhauser effects measured at the two temperatures, indeed all hydrogens atoms the further away from the nitrogen exhibits a higher cross relation values, thus experiencing a stronger effect, again, probably due to repulsion between the Li⁺ and the nitrogen positively charges. Secondly, cross-relaxations rates are all lower at 20°C than the ones at 50°C, and the spread in values is also lower.

Part 2:

N-methyl-*N*-propyl pyrrolidinium bis(fluorosulfonyl)imide mixed with lithium bis(fluorosulfonyl)imide

Lower cross-relaxation rates at lower temperature may be explained by slower dynamics and/or increasing average distances between the two cations.

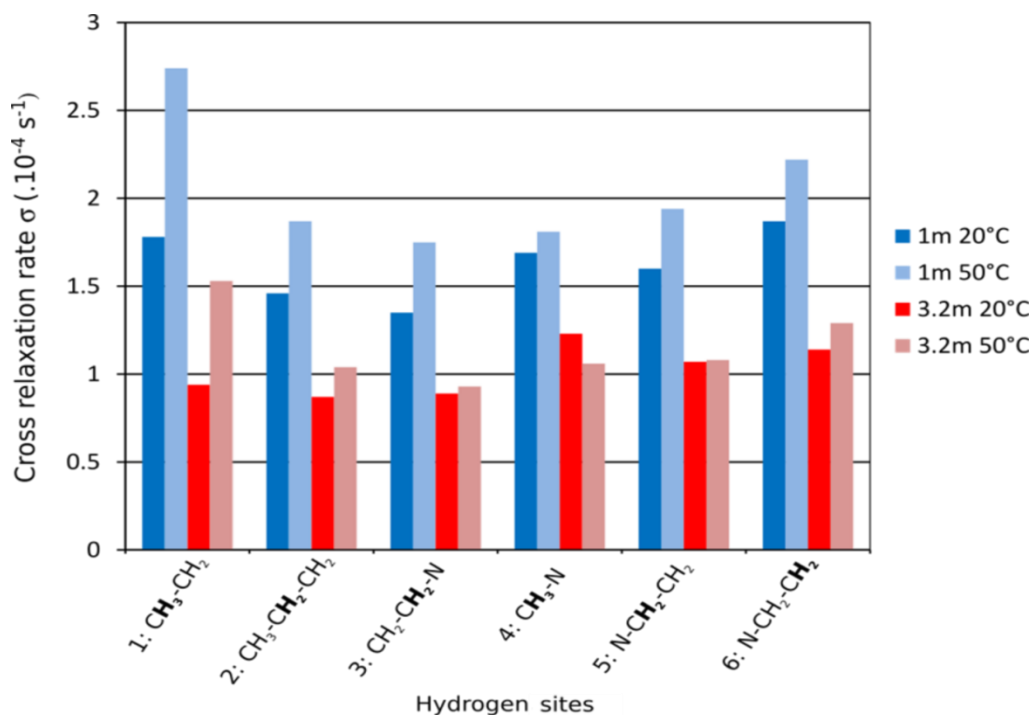


Figure 4-31: Cross-relaxation rates measured for C₃mpyr FSI doped with 1 molal and 3.2 molal Li FSI at 20°C and 50°C (uncertainty of 2.5% for each cross relaxation values)

4.2.III.1.2 C₃mpyr 3.2m Li FSI

In order to see the impact of the LiFSI concentration, similar experiments were carried out at 20°C and 50°C for a LiFSI molality of 3.2 mol.kg⁻¹. Again, Figure 4-32 a) and b) represent the experimental cross-relaxation rates for C₃mpyrFSI with 3.2m LiFSI, at 50°C and 20°C respectively.

Part 2:
N-methyl-*N*-propyl pyrrolidinium bis(fluorosulfonyl)imide mixed with lithium bis(fluorosulfonyl)imide

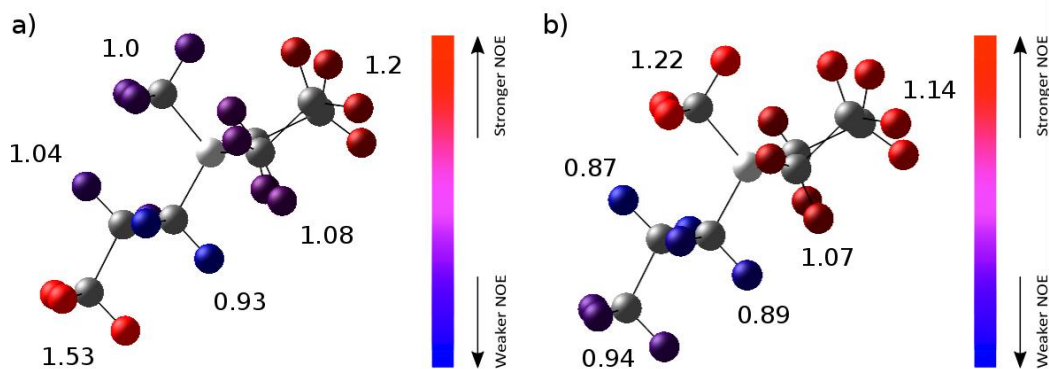


Figure 4-32: ^1H - ^7Li Overhauser rates for the C_3mpyr and lithium cations (3.2 molal LiFSI). Cross-relaxation rates are in $\cdot 10^{-4} \text{ s}^{-1}$ and the colour coding corresponds to the relative intensities of the NOE at a) 50°C and b) 20°C (uncertainty of 2.5% for each cross relaxation values)

Interestingly, in Figure 4-32 a), corresponding to ^1H - ^7Li experiment at 50°C , the cross-relaxation rates exhibit a similar trend as for the previous concentration at the same temperature. Indeed, except for the methyl group on the nitrogen, all other hydrogens sites exhibit a cross relaxation rates smaller at lower temperature, which can be potentially explained a slower dynamics due to the apparent higher viscosity. For the extracted cross relaxation on Figure 4-32 b), still corresponding to the 3.2 molal concentration but this time at 20°C , this time the highest value is reported from the methyl group on the nitrogen, followed by the two CH_2 groups on the cycle and then the methyl group at the end of the alkyl chain. The two last sites in the middle of the alkyl chain are still some of the lowest reported values, but not by far. In fact, according to Figure 4-31 in red, the cross relaxation values extracted for the 3.2 molal concentration at 20°C corresponds (almost all) to the smallest extracted.

This behavior can be potentially explained by a higher viscosity leading to slower motions, which leading the NOE transfer.

4.2.III.2 ^1H - ^{19}F HOESY experiments

In order to have a better understanding of interactions between ions in the ionic liquid, we decided to record ^1H - ^{19}F Overhauser cross-relaxation rates. Similarly to the ^1H - ^7Li experiments the same acquisition and fitting procedure was followed for ^1H -

Part 2:

N-methyl-N-propyl pyrrolidinium bis(fluorosulfonyl)imide mixed with lithium bis(fluorosulfonyl)imide

¹⁹F experiments. However, the Overhauser effect between two nuclei of close gyromagnetic ratio can be either positive or negative, as commonly seen in homonuclear NOEs. That is indeed what was observed in our case, further complicating their interpretation. In the following section, the discussion will be focused on the C₃mpyrFSI sample mixed with 1 m LiFSI at various temperatures.

As an example, Figure 4-33 shows the HOESY build curves carried out at 40°C, with the fits. At this temperature, it appears that some signals are the reverse than the others.

This negative cross-relaxation rate can be explained with Equation 4-9. Indeed, the cross-relaxation rate is the difference between the double quantum transition and the zero quantum transition probabilities, thus if the zero quantum mechanism is predominant over the double quantum one, the cross-relaxation rate will be negative.

Equation 4-9

$$\sigma_{12} = W_2 - W_0$$

Equation 4-10

$$W_0 = \frac{1}{10} \left(\frac{\mu_0}{4\pi} \right)^2 \frac{\hbar^2 \gamma_1^2 \gamma_2^2}{r^6} \frac{\tau_c}{1 + (\omega_1^2 - \omega_2^2) \tau_c^2}$$

Equation 4-11

$$W_2 = \frac{3}{5} \left(\frac{\mu_0}{4\pi} \right)^2 \frac{\hbar^2 \gamma_1^2 \gamma_2^2}{r^6} \frac{\tau_c}{1 + (\omega_1^2 + \omega_2^2) \tau_c^2}$$

Part 2:
N-methyl-*N*-propyl pyrrolidinium bis(fluorosulfonyl)imide mixed with lithium bis(fluorosulfonyl)imide

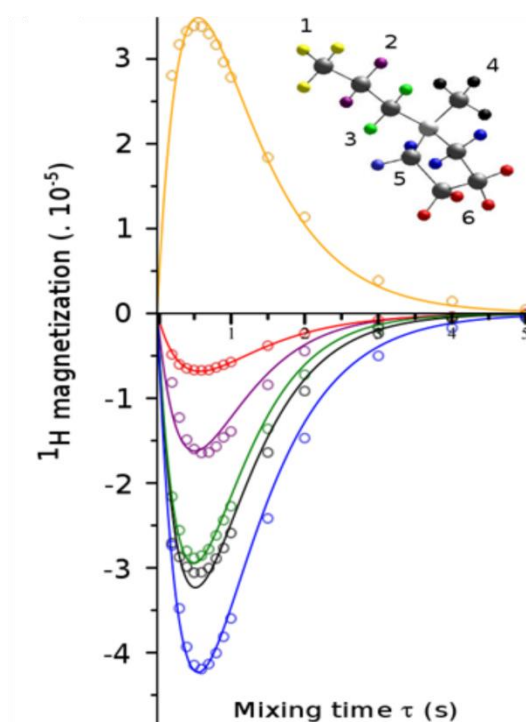


Figure 4-33: ^1H - ^{19}F Overhauser build-up curves for C_3mprFSI doped with 1 m LiFSI at 40°C , with the corresponding fits.

Figure 4-34 represents the extracted cross-relaxation rates for each of the hydrogen sites, at four temperatures (20-30-40-50°C). For each specific site, the cross-relaxation rates follow the same trend, and one can see that the zero crossing occurs at different temperatures for each site. (See Figure 4-34). Interestingly, a closer look at Equation 4-9, combined with the expression of the transition probabilities from Equation 4-10 and Equation 4-11, reveals that the zero and double quantum transition probabilities correspond to the spectral densities at the difference and sum of the Larmor frequencies of ^1H and ^{19}F at 11.74 T or 500 MHz for ^1H , which corresponds to $\omega_{\text{H}} - \omega_{\text{F}} = 30$ MHz and $\omega_{\text{H}} + \omega_{\text{F}} = 970$ MHz, therefore corresponding respectively to 5.3×10^{-9} and 0.16×10^{-9} . Therefore, the zero quantum transition probability will mostly result from the contribution of “slow” dynamics and the double quantum transition probability from “fast” dynamics.

In the case of the cross-relaxation rates extracted from ^1H - ^{19}F Overhauser transfers (see Figure 4-34), negative cross-relaxation rates can be observed at low temperature, which is expected as the zero quantum process and slow dynamics are then predominant. Considering the associated timescales ($\omega_{\text{H}} + \omega_{\text{F}} = 970$ MHz and $\omega_{\text{H}} - \omega_{\text{F}} = 30$ MHz), “slow” dynamics will correspond to self-diffusion and rotational

Part 2:
N-methyl-*N*-propyl pyrrolidinium bis(fluorosulfonyl)imide mixed with lithium bis(fluorosulfonyl)imide

diffusion of the whole ion usually above the nanosecond scale and “fast” dynamics will be considered as resulting from the rotation of the different groups or chain¹²⁷ usually from the nano to the pico second scale. Therefore, two atoms close to each other are expected to undergo faster fluctuations of their dipolar interaction, while two atoms which are further away may experience slower reorientations and fluctuations of the dipolar vector. It might imply that slow dynamics may correlate well with long range NOEs while fast dynamics may be linked with short range NOEs. Therefore, when a negative NOE is detected, one can expect slow dynamics to dominate the Overhauser transfer, and the ranking of NOEs may be related to the longer distances. At higher temperature and when positive NOEs are detected, the opposite may be true, and shorter distances may be probed. In fact, this behaviour is suggest by a theory from Gable et al^{81,128}, which will be describe later on.

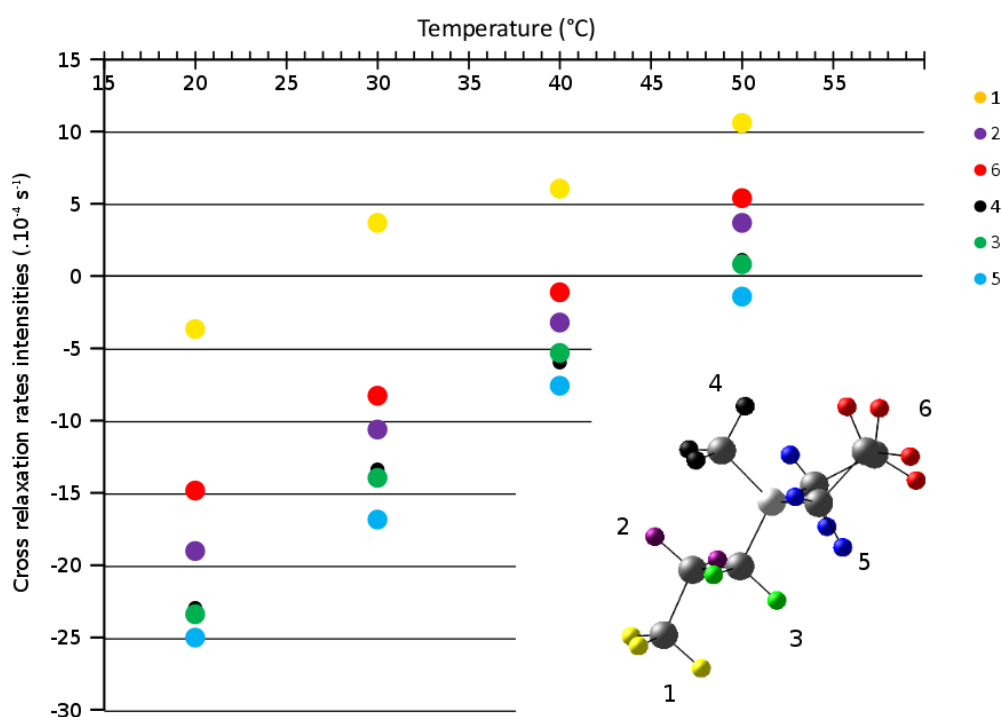


Figure 4-34: Cross-relaxation rates as a function of temperature extracted for C₃mpyrFSI with 1 mol.kg⁻¹ LiFSI (C₃mpyrFSI cation with hydrogen sites colours and numbers in insert) (uncertainty of 2.5% for each cross relaxation values)

As the interplay between the distances and dynamics becomes complex, one can see that it becomes difficult to theorize on which site is closer to fluorine of the FSI anion as the order of magnitude of the cross-relaxation rates will be depend upon the

Part 2:

N-methyl-N-propyl pyrrolidinium bis(fluorosulfonyl)imide mixed with lithium bis(fluorosulfonyl)imide

temperature. Similarly to the ^1H - ^7Li HOESY experiments, it is thus difficult to directly correlated with distances.

4.2.IV Interpreting the cross-relaxation values in terms of spatial proximities

In order to correlate the cross-relaxation rates σ and the proximity between ions, a deeper understanding is needed. Different theoretical studies are presented in the literature and three models are presented and applied in the following sections.

4.2.IV.1 Model A: Fluctuation of the intermolecular dipolar interaction with a single correlation time and a fixed distance, the strong ion pairing case

The simplest interpretation of the Overhauser rate is obtained with the standard equation derived for *intramolecular* heteronuclear dipolar cross-relaxation rates: it is derived for a pair of spins at a fixed distance from each other, in the same molecule, and experiencing a single motion (and a single correlation time describing it), generally resulting from rotational diffusion. As mentioned earlier, the cross-relaxation rate σ corresponds to the difference of probabilities between the two possible transitions for population transfer in the four state spin systems, as shown on Equation 4-12:

$$\sigma = W_2 - W_0$$
$$W_0 = \frac{1}{10} b^2 J(\omega^1 - \omega^2)$$

Part 2:
N-methyl-N-propyl pyrrolidinium bis(fluorosulfonyl)imide mixed with lithium bis(fluorosulfonyl)imide

$$W_2 = \frac{6}{10} b^2 J(\omega^1 + \omega^2)$$

Equation 4-12

The magnitude of the effect, b , is obtained from the standard equation for dipolar relaxation, where r is the fixed distance between spins 1 and 2.

$$b = \frac{\mu_0}{4\pi} \frac{h\gamma^2}{r^3}$$

Equation 4-13

Thus the cross-relaxation between spin 1 and 2 can be written as follow:

$$\sigma = \left(\frac{\mu_0}{4\pi} \frac{h\gamma_1\gamma_2}{r^3} \right)^2 (0.6 \times J(\omega^1 + \omega^2) - 0.1 \times J(\omega^1 - \omega^2))$$

Equation 4-14

In the case of an intra-molecular dipolar magnetization transfer with the underlying motion described by a single correlation time τ_c , the spectral density is given by Equation 4-15

$$J(\omega) = \frac{\tau_c}{1 + \omega^2\tau_c^2}$$

Equation 4-15

And the cross-relaxation rate σ can be now written as

:

$$\sigma = \left(\frac{\mu_0}{4\pi} \frac{h\gamma_H\gamma_X}{r^3} \right)^2 \left(0.6 \times \left(\frac{\tau_c}{1 + (\omega_H + \omega_X)^2\tau_c^2} \right) - 0.1 \times \left(\frac{\tau_c}{1 + (\omega_H - \omega_X)^2\tau_c^2} \right) \right)$$

Equation 4-16

One should note that in this case, the cross-relaxation rates are d^{-6} distance dependent.

4.2.IV.2 Model B: Hard sphere model and distance of closest approach

In previous studies, ions in ionic liquids have been modelled as hard spheres, in order to calculate how the intermolecular interactions are modulated by the relative translational diffusion of the interacting molecules^{129–131}. An expression for the spectral density of the dipolar interaction, was calculated, with two parameters: the translation correlation time τ_{trans} and the distance of closest approach between the two interacting spins d :^{129,130}

$$J_{DD}^{inter}(\omega, d, D_H, D_X) \propto \frac{72}{d^3} \int_0^\infty \frac{u^2}{(u^6 - 2u^4 + 9u^2 + 81)} \frac{u^2 \tau_{trans}}{(u^4 + (\omega \tau_{trans})^2)} du$$

Equation 4-17

In the case of “standard” self-diffusion, τ_{trans} is defined as $\tau_{trans} = d^2/D_{12}$, with D_{12} corresponding to the relative translation diffusion coefficient, which is given as the sum of the self-diffusion coefficient of the participating molecule. Thus Equation 4-17 can be re-written as follows:

$$J_{DD}^{inter}(\omega, d, D_H, D_X) \propto \frac{72}{d^3} \int_0^\infty \frac{u^4 d^2}{(u^6 - 2u^4 + 9u^2 + 81)(D_H + D_X)(u^4 + \frac{\omega^2 d^4}{(D_H + D_X)^2})} du$$

Equation 4-18

Now, by combining Equation 4-14 and Equation 4-18, and by doing a series development of the cross-relaxation rate expression at the first order for short distances, (including the calculated diffusion coefficient) the cross-relaxation rates scale as:

$$\sigma \propto 1.4 \times 10^{10} d^{-1} - 2.7 \times 10^{19} + O(d^2)$$

Equation 4-19

In that case, we can correlate cross-relaxation rates with one over the distance of closest approach.

4.2.IV.3 Model C: Inter molecular dipolar spin pair transfer: short to long range NOE

Interestingly, according to a new study, carried on by Gabl, Steinhauser and Weingärtner^{81,128}, the first model, which takes into account the intramolecular cross-relaxation between isolated pairs of spin, obviously neglects the modulation of the vector between spins resulting from the translational diffusion of both ions. Indeed, the earlier model (as in the BPP theory) only takes into account the rotational motions of ions, characterized by a single correlation time in the isotropic case. However, it has been known for a long time, from the theories of intermolecular spin lattice relaxation, that translational dynamics renders the spectral density $J(\omega)$ long range¹³²⁻¹³⁷.

Taking into account both rotational and translational dynamics of ions, Weingärtner and co-workers calculated the spectral density for the dipolar interaction between the two interacting spins using parameters typical for ILs, and pointed out that the function is no longer Lorentzian but is instead stretched out to higher frequencies as represented in Figure 4-35.

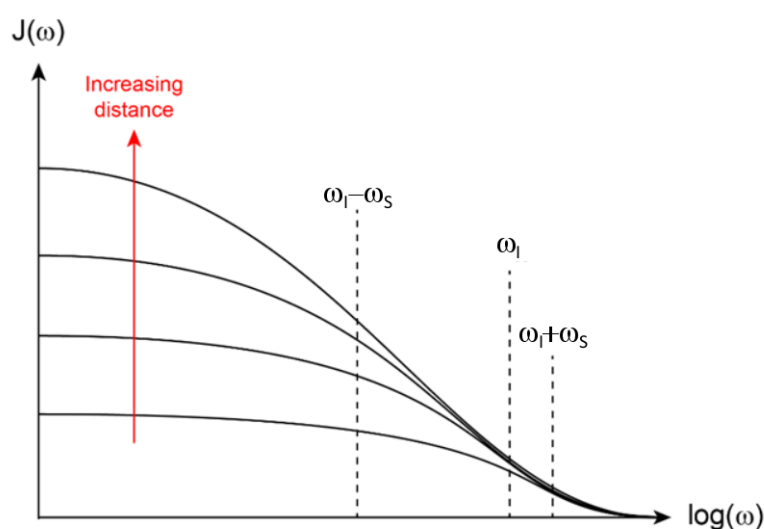


Figure 4-35: Representation of the spectral density as a function of $\log(\omega)$ according to the GSW model (reproduction of the figure from the original work⁸¹)

Part 2:

N-methyl-N-propyl pyrrolidinium bis(fluorosulfonyl)imide mixed with lithium bis(fluorosulfonyl)imide

In that case, one can see that $J(\omega_I - \omega_S)$ is of intrinsic long range nature $J(\omega_I + \omega_S)$ have a short range one. Furthermore, $J(\omega_I - \omega_S)$ will be always larger than the $J(\omega_I + \omega_S)$, and will vary much more with the distance between spins. Furthermore, the effect will be increased as the spins frequencies become closer to each other. The descriptions of the full theory is beyond the scope of this work, but can be found in detailed in the different publication from gabl *et al*^{81,128}.

4.2.V Application of these models to the HOESY data

4.2.V.1 ¹H-⁷Li HOESY experiments

In order to convert the cross-relaxation rates into distances, we applied the first model corresponding to the *intra* molecular spin pair transfer using Equation 4-14.

Thus in Equation 4-14, only two parameters are left unknown and able to vary, the correlation time τ_c and the distance r . Figure 4-36 represents a 3D plot of Equation 4-16 with the correlation time of fluctuation process and the distance between them as variables. On this figure, on the one hand, the value of σ increases as the correlation time gets higher, therefore, one can expect that as the temperature gets higher, the Overhauser effect will pass through a maximum, and then decrease. On the other hand, the sigma values at all correlation times increase as r becomes smaller, which is expected. Interestingly, as shown in Figure 4-31, (σ for each ¹H peaks for the C₃mpyrFSI with 1 m Li FSI, between 20 and 50 °C), all the σ values increase with temperature. As the temperature increase from the left to the right in Figure 4-36, the increase of cross-relaxation rates means that these points are located on the right hand side of the peak.

Part 2:
N-methyl-*N*-propyl pyrrolidinium bis(fluorosulfonyl)imide mixed with lithium
bis(fluorosulfonyl)imide

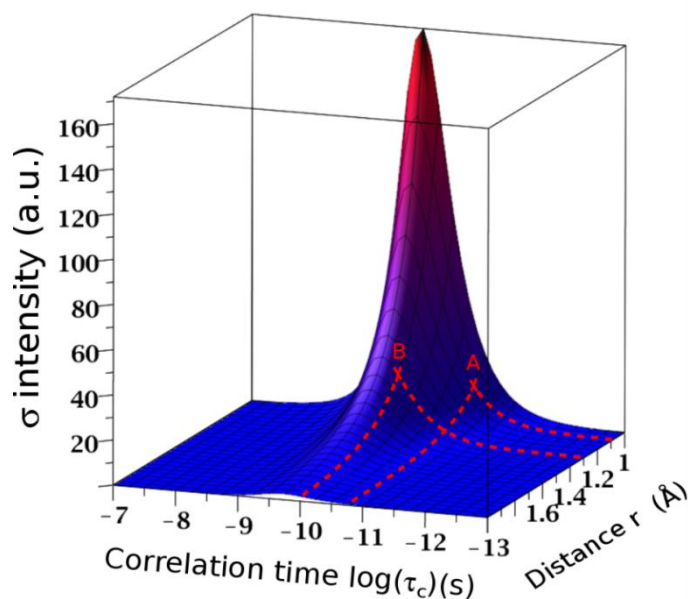


Figure 4-36: 3D representation of the cross-relaxation rate expression in the case of an intramolecular spin pair transfer with two theoretical spin pair example

Unfortunately, as neither the correlation time nor the distances between spins are known, no immediate conclusion can be provided for the distance between the ^7Li and the ^1H sites. Indeed, for two different pairs of spins A and B, as shown in Figure 4-36, even if spins in A are closer to each other compared to the spins in pair B, due to the smaller τ_c of pair B, the extracted cross-relaxation rate σ for pair B is higher.

However, this equation for the spectral densities was used here under the assumption that strong ion pairing between the molecules bearing the interacting spins would validate the use of the equations derived for intra-molecular magnetization transfer, *i.e.* with the Overhauser effect driven by the fluctuations of the dipolar interactions coming from rotational diffusion. In our case, for ^1H - ^7Li experiments, as both ions are cations, strong ions pairing is unlikely. In such ionic liquids, hydrogen-lithium interactions can be better described in the framework of Model B (the hard sphere model using the distance of closest approach). In this case, we will assume that the strongest cross relaxation rate is obtained for the smallest distance of closest approach.

Thus, using the cross-relaxation numbers report in Figure 4-30, relative distances of closest approach between lithium and the different hydrogen atoms can be extracted. Several assumptions have to be made: first, the d^{-1} dependency of the

Part 2:

N-methyl-N-propyl pyrrolidinium bis(fluorosulfonyl)imide mixed with lithium bis(fluorosulfonyl)imide

cross-relaxation rate, second, that the closest approach of the Li⁺ to the cation corresponds to the strongest cross-relaxation rate, third, that the shortest distance of closest approach is equal to the the sum of the hydrogen atomic radius (0.38 Å) and the lithium ionic radius (0.9 Å). Therefore, if the strongest cross-relaxation rate corresponds to 1.28 Å, the others distance of closest approach can be deduced from the ratio of cross-relaxation rates as presented in Table 4-5 .

Table 4-5: Distance of closest approach between lithium and the different hydrogen sites for C₃mpyr FSI with LiFSI 1 molal at 20°C and 50°C

¹ H sites	d _{Li-H} / Å	d _{Li-H} / Å
	20°C (1 mol/kg LiFSI)	50°C (1 mol/kg LiFSI)
1: CH ₃ -CH ₂	1.34	1.28
2: CH ₃ -CH ₂ -CH ₂	1.64	1.88
3: CH ₂ -CH ₂ -N	1.77	2.00
4: CH ₃ -N	1.42	1.94
5: N-CH ₂ -CH ₂	1.50	1.81
6: N-CH ₂ -CH ₂	1.28	1.58

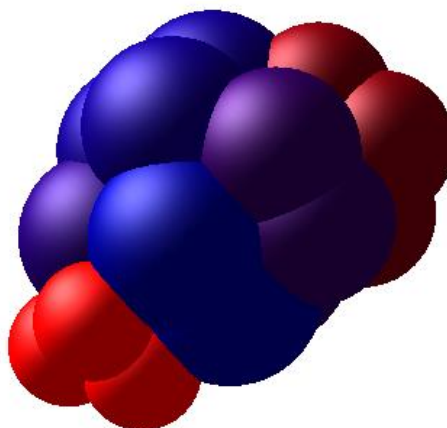


Figure 4-37: Representation of C₃mpyr cation with the hard sphere model corresponding to the region of closest approach for the lithium to each hydrogen sites

Part 2:
N-methyl-N-propyl pyrrolidinium bis(fluorosulfonyl)imide mixed with lithium bis(fluorosulfonyl)imide

Table 4-6: Distance of closest approach between lithium and the different hydrogen sites for C₃mpyrFSI with LiFSI 3.2 molal at 20°C and 50°C

¹ H sites	d _{Li-H} / Å	
	20°C (3.2 mol/kg LiFSI)	50°C (3.2 mol/kg LiFSI)
1: CH ₃ -CH ₂	1.67	1.28
2: CH ₃ -CH ₂ -CH ₂	1.81	1.88
3: CH ₂ -CH ₂ -N	1.77	2.11
4: CH ₃ -N	1.28	1.85
5: N-CH ₂ -CH ₂	1.47	1.81
6: N-CH ₂ -CH ₂	1.38	1.52

4.2.V.2 ¹H-¹⁹F HOESY experiments

4.2.V.2.1 Model A

In the case of the ¹H-¹⁹F Overhauser transfer, the first model, involved a pair of spins with a fixed distance between them and a single correlation time for the rotational diffusion. As the ¹H atoms belong to a cation and the ¹⁹F to the FSI anion, the first model was considered as relevant as electrostatic interactions may lead to strong ion pairing and long-lived ion pairs, in which the fluctuation of the inter-nuclear distance may be too slow to play a significant role in dipolar relaxation. As in the ¹H-⁷Li expression, only two parameters are left unknown and able to vary, the correlation time τ_c and the distance r . Figure 4-38 represents a 3D plot of Figure 4-38, with the correlation time of the pair of spins and the distance between the pair of displayed on the x and y axis respectively.

Part 2:
N-methyl-N-propyl pyrrolidinium bis(fluorosulfonyl)imide mixed with lithium bis(fluorosulfonyl)imide

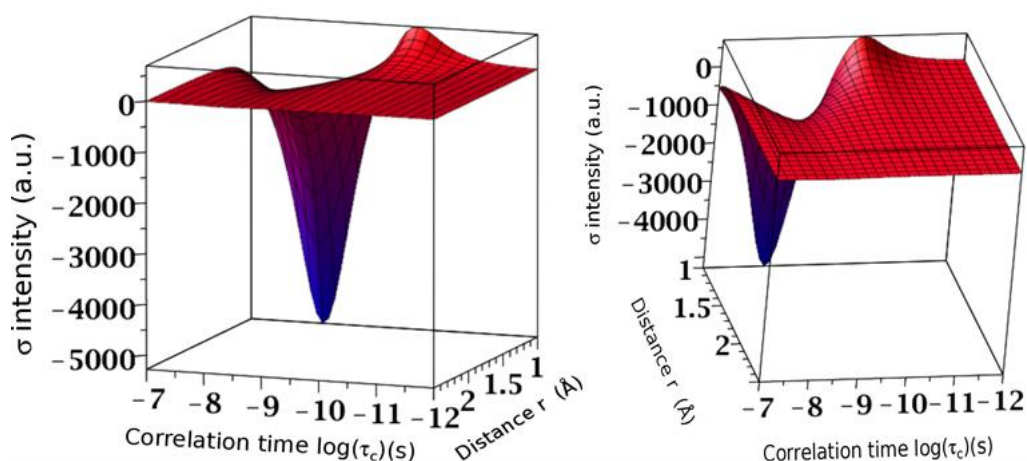


Figure 4-38: 3D representation of the cross-relaxation rate expression in the case of a fixed distance r between spins and a single correlation time describing the fluctuation of the dipolar vector's orientation (two different views).

A completely different behavior is highlighted here: as shown in Figure 4-39, for short correlation times, the cross-relaxation rate is positive, and reaches a maximum around 0.1 ns. For a correlation time of 3.16×10^{-10} s, the cross-relaxation rate vanishes and later becomes negative at larger correlation times, reaching a minimum around 10 ns before vanishing again around 1 μ s. This negative cross-relaxation rate is due to the close proximity between the gyromagnetic ratios of both nuclei ($\gamma_H = 267.51 \times 10^6$, $\gamma_F = 257.66 \times 10^6 \text{ rad}\cdot\text{s}^{-1}\cdot\text{T}^{-1}$). Thus for slower motions, the $J(\omega_H - \omega_F)$ term becomes dominant and the transfer is negative.

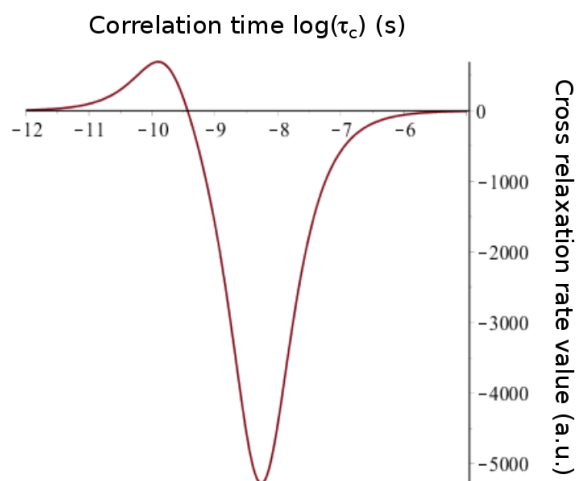


Figure 4-39: Plot of the cross-relaxation rate as a function of the correlation time (log scale) assuming a fixed distance $r=1\text{\AA}$ between the ^1H and ^{19}F spins.

Interestingly, the range of correlation times between 10^{-10} to 10^{-9} s which is the range obtained from the spin lattice relaxation experiments covers exactly the region where

Part 2:

N-methyl-N-propyl pyrrolidinium bis(fluorosulfonyl)imide mixed with lithium bis(fluorosulfonyl)imide

the zero-crossing is detected (see Figure 4-40). Furthermore, as the correlation time is expected to increase from low temperature measurements to high temperature ones, a negative cross-relaxation rate is expected for low temperatures, and a positive one at high temperatures. This behavior corresponds quite well with what was experimentally observed experimentally for the ^1H - ^{19}F heteronuclear Overhauser transfer, as shown in Figure 4-34.

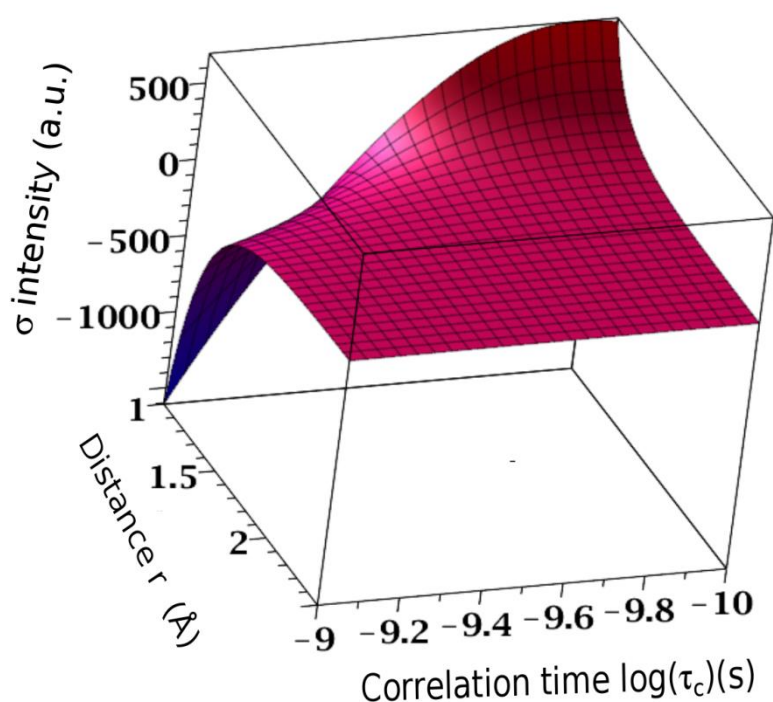


Figure 4-40: 3D representation of the cross-relaxation rate expression in the case of a fixed distance r between spins and a single correlation time describing the fluctuation of the dipolar vector's orientation with correlation time range corresponding to range extracted from T_1 experiments.

Unfortunately, as in the ^7Li - ^1H experiments, neither the correlation τ_c nor the distance r are known, thus it is difficult to theorize directly on the distance r . However, there is one potential way to overcome the issue of the two unknown variables. Indeed, as shown on Figure 4-41, the minimum, the zero crossing, and the maximum occurs always at the same correlation time, corresponding to 5.43×10^{-9} , 3.68×10^{-10} and 1.25×10^{-10} seconds, respectively, whatever the distance between spins. Thus, if at least two of these minima are detected on the studied range of temperature, an equation for the correlation time can be extracted, and the correlation can be calculated at each temperature, leaving only one variable. Unfortunately, in the

Part 2:

N-methyl-*N*-propyl pyrrolidinium bis(fluorosulfonyl)imide mixed with lithium bis(fluorosulfonyl)imide

present case of Figure 4-34, only the zero crossing appears, thus the correlation time was kept as a variable and no more information can be extracted.

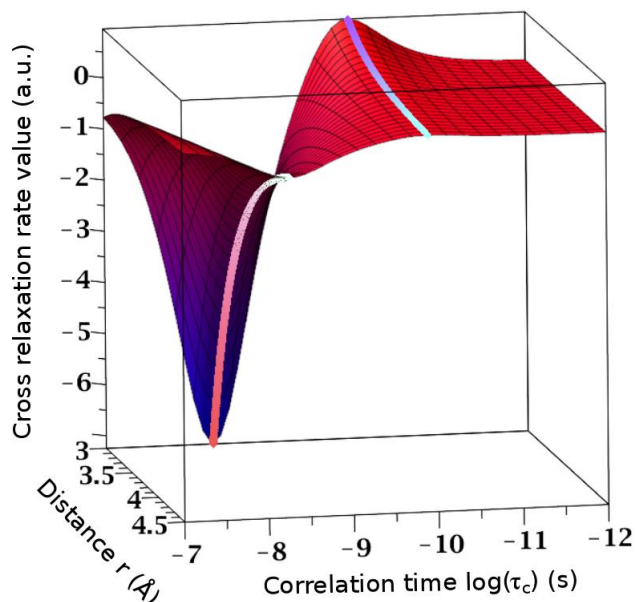


Figure 4-41: 3D representation of the cross-relaxation rate in the case of a fixed distance r between spins and a single correlation time describing the fluctuation of the dipolar vector's orientation. The lines show the positions of the minimum and maximum.

4.2.V.2.2 Model B

The hard sphere model was not used in the case of ^1H - ^{19}F experiments as the hydrogen sites are present on a cation and the fluorine sites are present on an anion. Therefore, the non-repulsive nature of the interaction makes the hard sphere model less relevant as one would expect the distance of closest approach to be the same or at least similar for all H-F pairs.

4.2.V.2.3 Model C

In fact, a better model to interpret the ^1H - ^{19}F Overhauser magnetization transfer is based on the GSW theory. As explained earlier, this model takes into account both translational and rotational dynamics of ions, which is a key point for an ^1H - ^{19}F spin

Part 2:

N-methyl-*N*-propyl pyrrolidinium bis(fluorosulfonyl)imide mixed with lithium bis(fluorosulfonyl)imide

pairs, as their gyromagnetic ratios are very close. Thus the sum of the gyromagnetic ratio is at relatively high frequency, and the subtraction of the gyromagnetic ratio is very low:

$$\text{At } 11.7 \text{ T: } \quad \omega_{\text{H}} + \omega_{\text{F}} = 970 \text{ MHz} \quad \omega_{\text{H}} - \omega_{\text{F}} = 30 \text{ MHz}$$

In order to be able to extract the different inter-nuclear distances for each site, we will consider the σ values measured at a temperature of 20 °C (as shown in Figure 4-42). Indeed at this temperature, the cross-relaxation rates are negative, and the furthest from the zero-crossing region. The magnitudes of the rates are also distributed over a wide range of values. We then assume that the differences in σ values at this temperature are predominantly due to variations in the average inter-nuclear distance rather than the dynamics. Thus as shown in Figure 4-41, at a fixed correlation time, the stronger the magnitude of the cross-relaxation rate, the closer the spins are to each other.

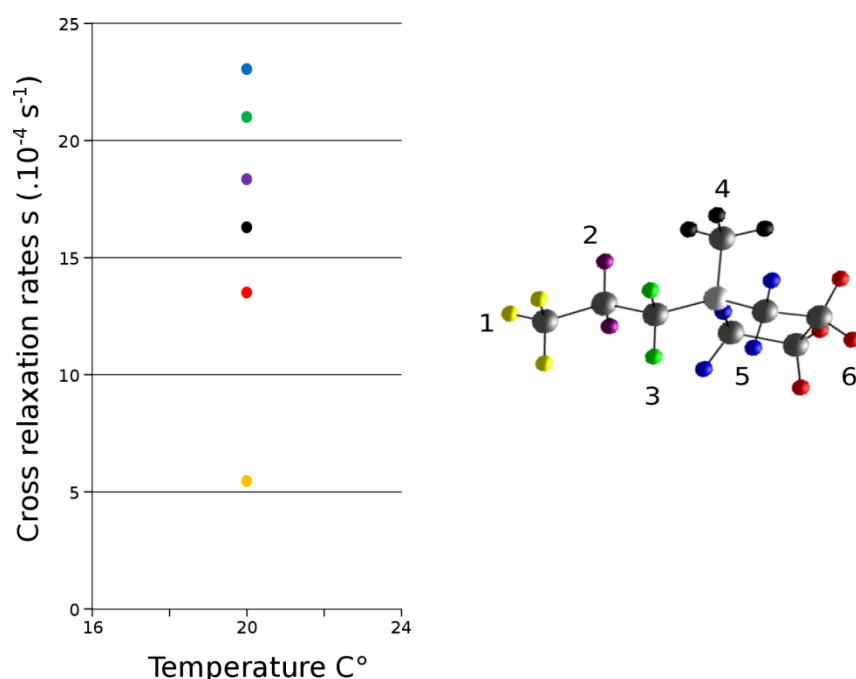


Figure 4-42: Magnitude of cross-relaxation rates extracted for the C₃myprFSI sample doped with 1 molal LiFSI at 20 °C (uncertainty of 2.5% for each cross relaxation values)

First, ^1H - ^{19}F cross-relaxation rates show the opposite trend as the one observed for ^1H - ^7Li rates: indeed, fluorine sites show a greater correlation with hydrogen sites close to the positively charge nitrogen sites. This behaviour can be explained if one

Part 2:

N-methyl-N-propyl pyrrolidinium bis(fluorosulfonyl)imide mixed with lithium bis(fluorosulfonyl)imide

considers the attraction between the negatively charged anion to the positively charged region of the cation. Indeed, even if the steric hindrance makes this behaviour unlikely, the potential strong coordination between the positive charge delocalized on the nitrogen of the cation and the negative charge delocalized on the nitrogen of the anion, can be predominant beyond the steric hindered.

4.2.VI Comparison with Molecular Dynamics simulations

In order to test the different models, for both series of cross-relaxation rates (^1H - ^7Li and ^1H - ^{19}F), molecular dynamics simulations can be used to extract the coordination sphere of lithium or fluorine around the C_3mpyr cation.

4.2.VI.1 Cation-Cation interactions

To summarize, the ^1H - ^7Li cross-relaxation rates were compared to one another using the second model (hard sphere model and distance of closest approach), in order to extract distances of closest approach between the lithium cation and the different hydrogen atoms of the C_3mpyr cation. It turns out that the lithium gets closer to the hydrogen atoms which are located far away from the positive charge. For the ^1H - ^7Li Overhauser rates, (on the $\text{C}_3\text{mpyrFSI}$ sample doped with 1 molal LiFSI at 50°C), the lithium to hydrogen distances are ordered as follow:

$$\text{C1} > \text{C6} > \text{C5} > \text{C2} > \text{C4} > \text{C3}$$

Part 2:
N-methyl-*N*-propyl pyrrolidinium bis(fluorosulfonyl)imide mixed with lithium bis(fluorosulfonyl)imide

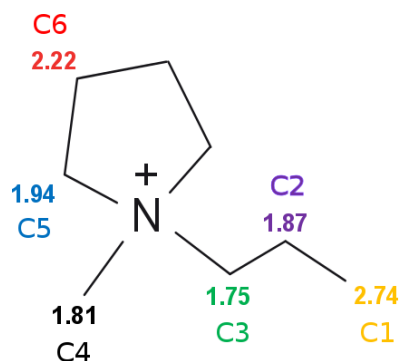


Figure 4-43: C₃mpyr cation with numbering, colour coding and experimental cross-relaxation rates (x10⁻⁴ s⁻¹) between ¹H and ⁷Li for C₃mpyrFSI with 1 molal LiFSI at 50°C

MD simulations provide the carbon-lithium radial distribution functions (RDF) and coordination numbers (CN), obtained after equilibrating the two systems at 353 K (as shown in Figure 4-44). The RDF peaks are relatively broad due to the significant variations in the C-Li distances.

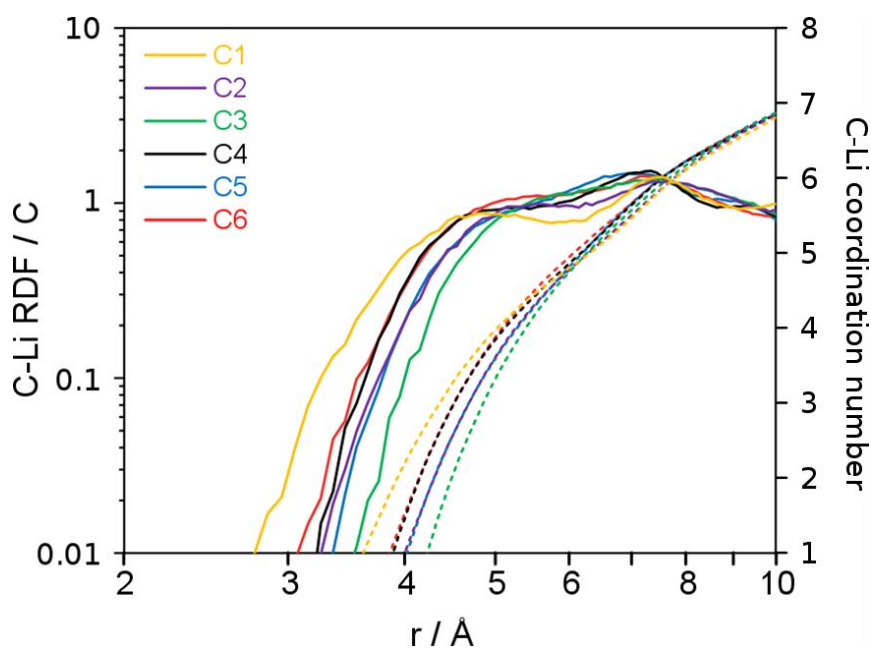


Figure 4-44: Carbon-lithium radial distribution functions (RDF) in solid line, and coordination numbers (CN) in dashed line obtained from the MD simulations for C₃mpyrFSI with 1 molal LiFSI at 50°C

The RDFs in Figure 4-44 shows a first coordination shell at a distance of around 4-5 Å and the carbon-lithium distance range in the following order:

$$C1 > C6 > C4 > C2 > C5 > C3$$

By looking at the Figure 4-45, one can see that the correlation with cross relaxation numbers trend extract from HOESY experiments are in good correlation with the

Part 2:

N-methyl-N-propyl pyrrolidinium bis(fluorosulfonyl)imide mixed with lithium bis(fluorosulfonyl)imide

carbon-lithium distance of closest approach trend extract from the MD simulation. Thus, this confirms the choice of the second model used later on and thus confirms that the lithium appears to be further away from the positive charge carry on by the nitrogen, and in fact closer to the end of the alkyl chain and the CH₂ on the cycle the furthest from the nitrogen.

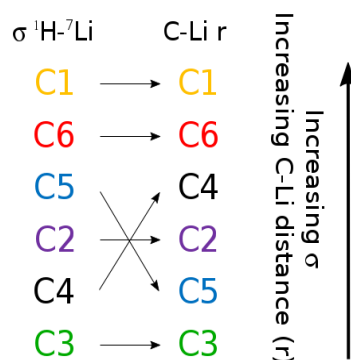


Figure 4-45: Graphical illustration of the correlations between the experimentally measured ¹H-⁷Li cross relaxation rates and carbon-lithium distance derived from the MD, corresponding to Figure 4-43 and Figure 4-44 data respectively.

4.2.VI.2 Cation-anion interactions

In the case of the ¹H-¹⁹F HOESY cross-relaxation rates, as the hydrogen sites are located on a cation and fluorine on an anion, the electrostatic attraction between the two ions makes the hard sphere model most likely not applicable, and also that the third model using the GSW theory looks like to be the more accurate for the ¹H-¹⁹F spin pair. By making the assumption that the influence of the correlation is negligible beyond the influence of the distances, for the ¹H-¹⁹F Overhauser experiments realized on the C₃mpyrFSI doped with 1 molal LiFSI at 20°C, the fluorine to hydrogen distances are ordered as follow:

$$\text{C5} > \text{C3} > \text{C2} > \text{C4} > \text{C6} > \text{C1}$$

Part 2:
N-methyl-*N*-propyl pyrrolidinium bis(fluorosulfonyl)imide mixed with lithium bis(fluorosulfonyl)imide

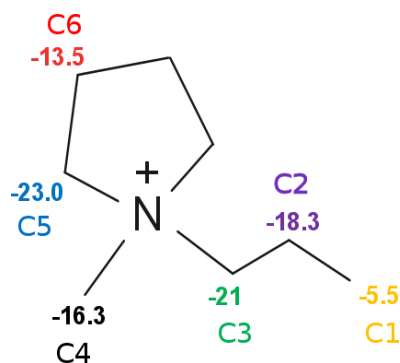


Figure 4-46: C₃mpyr cation with numbering, colour coding and experimental cross-relaxation rates ($\times 10^{-4}$) of ¹H-¹⁹F experiments for C₃mpyr FSI with 1 molal Li FSI at 20°C (uncertainty of 2.5% for each cross relaxation values)

Now, similarly to the ¹H-⁷Li experiments, by looking at the carbon fluorine radial distribution functions (RDF) and coordination numbers (CN) calculated from the MD simulations after equilibrating the two systems at 353 K shown in Figure 4-47, comparison with the cross-relaxation rates experiments can be done. The RDF peaks are relatively broad due to significant variations in the C-Li distances.

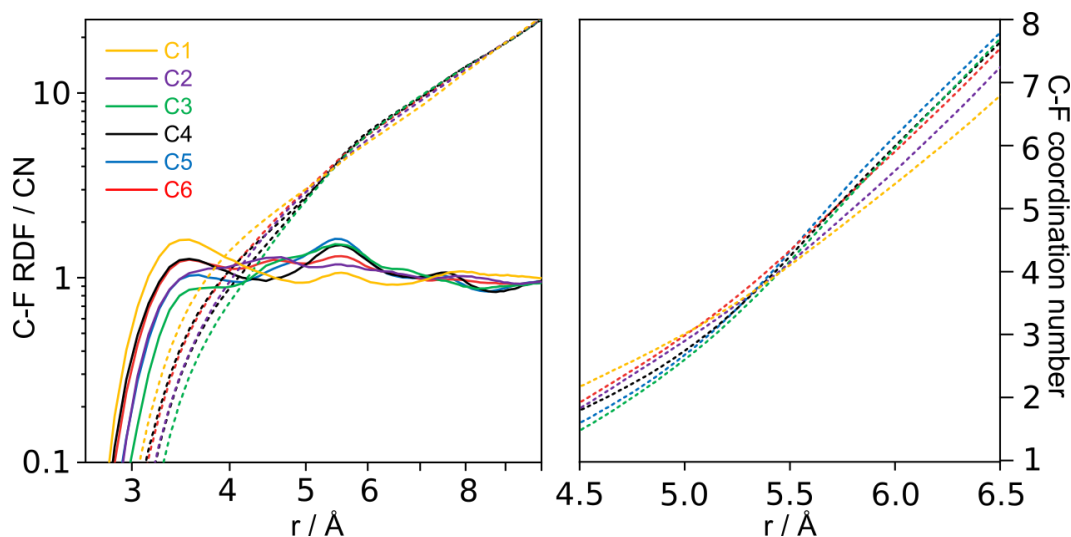


Figure 4-47: Carbon-fluorine radial distribution functions (RDF) and coordination numbers (CN) obtained from the MD simulations for C₃mpyrFSI with 1 molal LiFSI at 20°C

First of all, from the RDF plot, one can notice that all the distance of closest approach for the different C-F groups are more or less similar, around 2.8 Å, confirming the assumption that the fluorine can approach all sites at a similar distance.

Secondly, at a first glance, the CN shown in Figure 4-47 exhibit the following trend

Part 2:
N-methyl-N-propyl pyrrolidinium bis(fluorosulfonyl)imide mixed with lithium bis(fluorosulfonyl)imide

$$C1 > C6 > C2 > C4 > C5 > C3$$

But interestingly, while taking a closer look at the coordination numbers, a cross-over region can be seen at around 5.5 Å. This can be understood due to the structure of the FSI anion, featuring two fluorine sites. As the FSI anion can be oriented in different ways relatively to the cation, at a given time some fluorine sites are at a distance over 5.5 Å and the others at a distance smaller than 5.5 Å. Thus over 5.5 Å, the CN exhibit a different trend, as follow:

$$C5 > C3 > C4 > C6 > C2 > C1$$

In fact, as shown in Figure 4-48, between these two distance ranges, the longer range order of coordination numbers (at 6.5 Å) is the one that correlates best with the magnitudes of the ^1H - ^{19}F cross-relaxation rates. It should be noted that the correlation between these longer range C-F coordination numbers and the ^1H - ^{19}F σ values is much better compared to the shorter range, however the correlation is still not perfect. In fact the cross relaxation rates will correspond to a combination of both short range and long range dynamics. However, overall, this result seems to corroborate the theory of Weingärtner and co-workers, as indeed the ^1H - ^{19}F cross-relaxation rates appear to correlate best with longer-range interactions than the ^1H - ^7Li values.

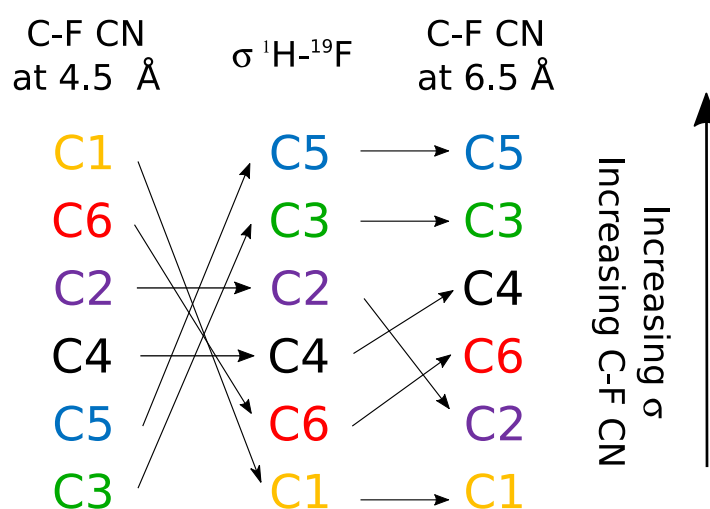


Figure 4-48: Graphical illustration of the correlations between the experimentally measured ^1H - ^{19}F cross-relaxation rates and carbon-lithium coordination numbers (CN) derived from the MD, corresponding to Figure 4-46 and Figure 4-47 data respectively

Part 2:

N-methyl-N-propyl pyrrolidinium bis(fluorosulfonyl)imide mixed with lithium bis(fluorosulfonyl)imide

In fact, this trend showing a strong correlation of the FSI with the hydrogens sites around the nitrogen correlates with the ^1H - ^7Li results. Indeed, on the one hand, if one assumes the lithium is surrounded by anions, at high temperature, the close approach of the lithium to the methyl group at the end of the alkyl chain can be explained by some lithium having enough energy to break the activation energy barrier and momentarily escape the coordination with the FSI. In this case, this free lithium will tend to be repelled by the nitrogen's positive charge, as explained by the stronger correlation with the methyl group at the end of the alkyl chain. In the other hand, a lower temperature or /and a higher LiFSI concentration (leading to less disrupted/stronger ion pairing and a higher viscosity), will induce a potentially stronger coordination between the lithium cation and FSI anion. In that case the lithium is trapped in a poly-ion structure that is negatively charged and end up being more around the nitrogen atom. This phenomenon seems to be observed in the structural studies of solid state samples (*vide infra*).

4.2.VII Conclusions

Quantitative ^1H - ^7Li and ^1H - ^{19}F cross relaxation rates have been measured from the $\text{C}_3\text{mpyrFSI}$ system mixed with LiFSI and interpreted in terms of the ion interactions and internuclear distances based on different models. Regarding the ^1H - ^7Li HOESY, it has been shown that at high temperature (50°C) and low concentration (1 molal), the lithium cation seems to be able to get closer to the methyl group at the end of the alkyl chain and to the ring CH_2 the furthest from the nitrogen, rather than the hydrogens sites close to the nitrogen. This trend can be explained by the repulsion of the lithium cation by the positive charge centred on the nitrogen. Interestingly, by lowering the temperature or increasing the concentration, and even more by doing both simultaneously, the distribution of the cross relaxation rates becomes narrower and shows that the lithium ions can approach closer to the hydrogen groups on the ring and to the methyl group on the nitrogen. This result has been attributed to a potentially stronger coordination between the lithium and the FSI anion. According

Part 2:

N-methyl-N-propyl pyrrolidinium bis(fluorosulfonyl)imide mixed with lithium bis(fluorosulfonyl)imide

to the ^1H - ^{19}F experiments, the anion seems to more strongly associate with the hydrogen groups close to the nitrogen.

The interpretation of the extracted cross relaxation rates in terms of distances has also been discussed with different models considered. Using a hard sphere model and interpreting the cross relaxation rates in terms of a distance of closest approach, the ^1H - ^7Li experiment at 50 °C at 1 molal LiFSI was in good agreement with the distances of closest approach obtained from the RDF plots extracted from the molecular dynamics simulation. In the case of the ^1H - ^{19}F experiments, it has been shown that in fact the trend displayed by the extracted cross relaxation rates correlates better with C-F coordination numbers (obtained from MD simulations) at longer distances, as predicted by the GSW theory⁸¹.

Part 2:

*N-methyl-N-propyl pyrrolidinium bis(fluorosulfonyl)imide mixed with lithium
bis(fluorosulfonyl)imide*

**Part 3:
Influence of ionic
liquid cation
structure**

Part 3:
Influence of ionic liquid cation structure

Part 3:
Influence of ionic liquid cation structure

The last two chapters have demonstrated the capacity of the developed Maple code to extract different parameters from NMR data sets, such as the spin lattice relaxation time, or cross-relaxation rates through the fit of build-up curves extracted from 2D HOESY experiments in a systematic manner. Moreover, the extracted cross relaxation rates for each specific proton sites on the C₃mpyr cation, exhibit different trends that can be correlated with the position of the other studied ion, *i.e.*, the lithium for the ¹H-⁷Li experiments or the anion for the ¹H-¹⁹F experiments. By using different models in order to convert the cross relaxation rates into distances, it has been highlighted on the one hand, that a hard sphere model and distance of closest approach can be used in order to convert the ¹H-⁷Li cross relaxation rates into distances, which correlate well with RDF and CN numbers extracted from molecular dynamics simulations. On the other hand, regarding the ¹H-¹⁹F experiments, the model of distance of closest approach is unlikely to be valid as one would expect the distance of closest approach to be similar for all H-F pairs which has been confirmed by the RDF plots extracted from the MD simulations, were all C-F distances of closest approach looks pretty similar one to each other in Figure 4-47, compare in the case of the C-Li distances of closest approach in Figure 4-44. Interestingly, the trend of magnitudes for the ¹H-¹⁹F cross relaxation rates, correlates well with the C-F CN at longer ranges extracted from the MD simulations. This behaviour was predicted by another model (so-called GSW theory), which takes into account both translational and rotational dynamics of ions. Thus in the rest of this report, all results corresponding to ¹H-⁷Li HOESY experiments will be assumed to correlate with the Li-H distance of closest approach, and all results corresponding to ¹H-¹⁹F experiments will be treated as being reflective of longer range polarisation transfer from the more distance fluorine site on the FSI anion. We note that in both cases the numbers still reflect interactions between the IL cation and the first shell of Li⁺ or FSI⁻ ions around it.

In this chapter we study other IL samples in order to compare how these cation-cation and cation-anion interactions vary depending on the IL cation structure. Only the IL cation structure is varied, and the concentration of LiFSI will be fixed at around 25% mol.

4.3.I Effect of an additional carbon group on the alkyl chain

The first new sample studied corresponds to the N-methyl-N-butyl pyrrolidinium bis(fluorosulfonyl)imide (C₄mpyr FSI) doped with LiFSI at 1 mol.kg⁻¹, which contains one additional carbon group on the alkyl chain. Cross-relaxation parameters were extracted using the same procedure as before, with the diffusion coefficients and relaxation parameters extracted separately.

4.3.I.1 ¹H-⁷Li HOESY experiments

As shown in Figure 4-49, which represents the extracted cross-relaxation rates from the ¹H-⁷Li HOESY experiments for each specific proton sites of the C₄mpyr cation, one should that the highest cross relaxation rates corresponds to the CH₂ site on the ring, the furthest from the positive charge. Then the two hydrogens sites at the end of the alkyl chain, the methyl group on the nitrogen, and the CH₂ the closest to the nitrogen on the ring, all exhibits similar cross relaxation rates. Finally the two last hydrogen sites on the alkyl chain, corresponding to the two CH₂ group the closest to the nitrogen, exhibits both the smallest cross relaxation rates. Thus, according to these values, it suggesting that the lithium looks like to be able to approach closer to the hydrogens sites the most far away from the nitrogen site on the carbon cycle, and less closer to the protons on the chain close to the nitrogen. In fact, the cross relaxation intensity trend is pretty similar to the one extracted from the C₃mpyr system (Figure 4-30), except that in the case of the C₄mpyr, the lithium looks like as close to the carbon group on the cycle close to the nitrogen and the methyl group and the nitrogen than the two carbon group at the end of the alkyl chain. One potential explanation of this trend could be firstly, due the motion of the alkyl which can prevent the lithium to approach close to the hydrogen groups close to the

Part 3:
Influence of ionic liquid cation structure

nitrogen and secondly, a potential sterical hindered due the longer alkyl chain, indeed some research already study the impact on the nanostructure of ionic liquids in the case of long alkyl chain, and highlight solvophobic segregation of the polar and apolar domains^{60,138}

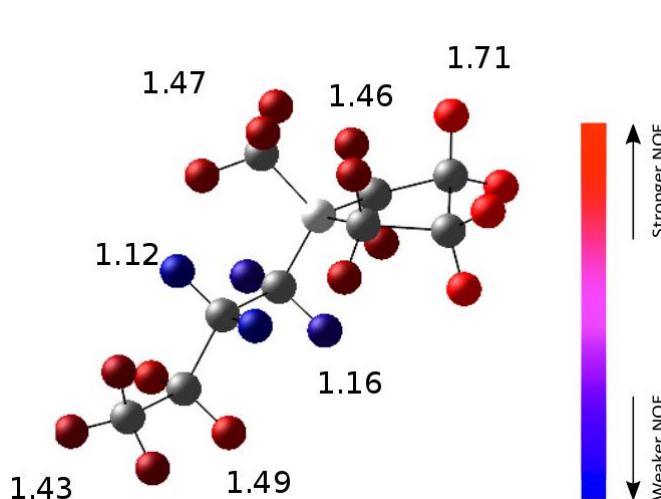


Figure 4-49: ^1H - ^7Li cross relaxation rates for the Campyr and lithium cations (1 molal LiFSI at 50°C). Cross-relaxation rates are in $\cdot 10^{-4} \text{ s}^{-1}$ and the colour coding corresponds to the relative intensities of the NOE. (uncertainty of 2.5% for each cross relaxation values)

4.3.I.2 ^1H - ^{19}F HOESY experiments

The ^1H - ^{19}F cross relaxation rates shown in Figure 4-50 are larger for the groups located closer to the nitrogen center of the cation. The largest value is for the CH_2 group on the alkyl chain that is closest to the nitrogen site. Note that these particular protons showed one of the lowest ^1H - ^7Li cross relaxation rates. This suggests that the FSI anions may be clustering around this group and thereby preventing the Li^+ cations from getting close to it. The lowest ^1H - ^{19}F cross relaxation rate is seen for the terminal methyl group on the alkyl chain. This is the group that is furthest from the positively charged region of the cation, so this could be explained by the lack of electrostatic attraction between the FSI anions and this part of the molecule, and it is also consistent with the closer distance of approach suggested by the relatively high ^1H - ^7Li cross relaxation rate for this group. Comparing the CH_2 groups on the ring, the groups more distant from the nitrogen again show a smaller ^1H - ^{19}F cross relaxation

Part 3:
Influence of ionic liquid cation structure

rate combined with a larger ^1H - ^7Li value. These trends were also observed in the C_3mpyr system.

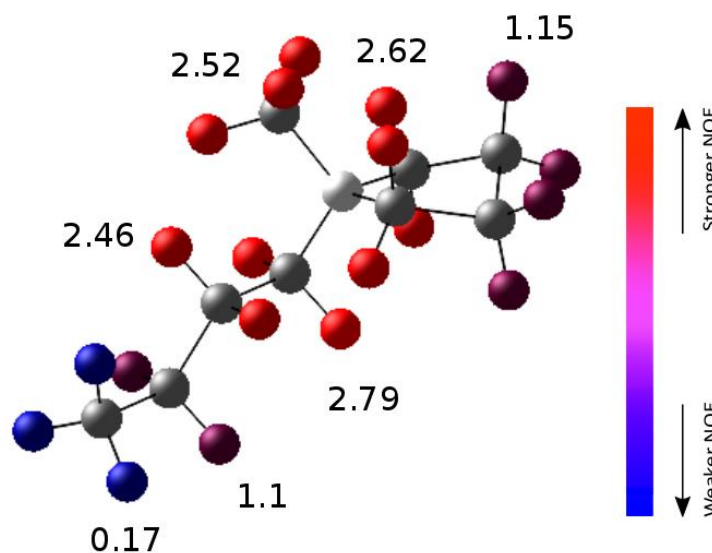


Figure 4-50: ^1H - ^{19}F Overhauser rates for the C_4mpyr and FSI anions (1 molal LiFSI at 50°C). Cross-relaxation rates are in $\cdot 10^{-4} \text{ s}^{-1}$ and the colour coding corresponds to the relative intensities of the NOE. (uncertainty of 2.5% for each cross relaxation values)

4.3.II Effect of an additional carbon group on the cycle

The next sample studied was *N*-methyl-*N*-propyl piperidinium bis(fluorosulfonyl)imide (C_3mpip FSI) mixed with LiFSI at $1 \text{ mol}\cdot\text{kg}^{-1}$, in order to investigate the effects of adding a CH_2 group in the cycle instead of on the alkyl chain.

4.3.II.1 ^1H peak assignment

The *N*-methyl-*N*-propyl piperidinium bis(fluorosulfonyl)imide (C_3mpip FSI) ^1H peak assignment could not be found in the literature. As the peak assignment is obviously required for the HOESY analysis, some single pulse experiments were carried out as

Part 3:
Influence of ionic liquid cation structure

shown in Figure 4-51. Interestingly the ^1H NMR spectrum contains 8 peaks compared to the seven expected for the C_3mpip structure as shown in Figure 4-51.

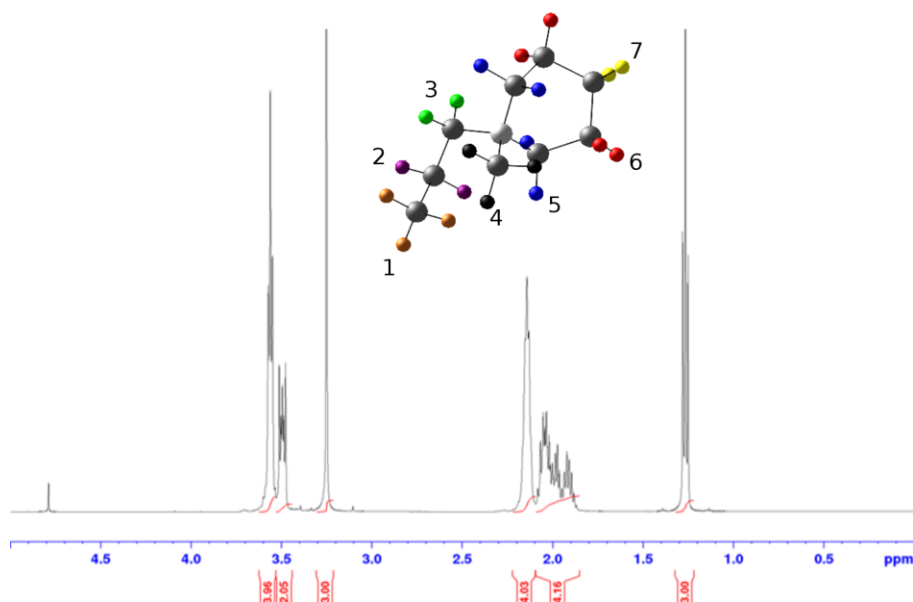


Figure 4-51: Single pulse ^1H experiments corresponding to the cation structure of the N-methyl-N-propyl Piperidinium bis(fluorosulfonyl)imide (C_3mpip FSI) doped with LiFSI at 1 mol.kg^{-1}

Thanks to the peak integration and J splittings shown in Figure 4-51, and the ^1H spectrum of the N-propyl-N-methyl pyrrolidinium cation, most of the peaks were easily assigned as shown in Figure 4-52. However, only one site is left to assign, and two multiplets are still visible in the NMR spectrum.

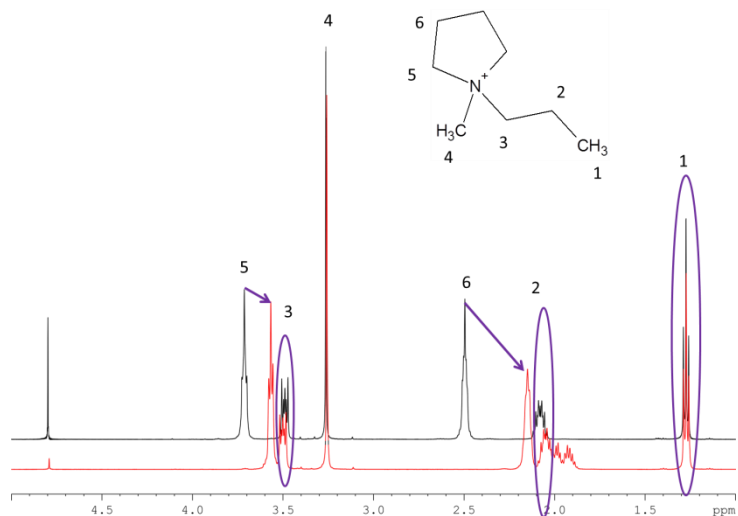


Figure 4-52: ^1H single spectrum of the N-methyl-N-propyl Piperidinium bis(fluorosulfonyl)imide in red and the N-propyl-N-methyl Pyrrolidinium in black, with the hydrogens sites correspondence.

Part 3:
Influence of ionic liquid cation structure

Thus a ^1H - ^{13}C HSQC experiments were carried on as shown in Figure 4-53 (a single pulse ^{13}C spectrum is presented as an external projection that shows the J splittings of the different peaks). From this experiment, it can be concluded that these final two peaks correspond to the hydrogens on site 7 (numbering in Figure 4-51), with a strong J coupling creating the two multiplets. Indeed, normally these protons should be equivalent by symmetry and would therefore have an identical chemical shift without J coupling to one another, but a break in the symmetry, presumably due to the conformation of the ring, makes these two protons non-equivalent. However, the almost identical environment of these two protons lead to an almost identical chemical shift, and the close proximity lead to a strong J coupling.

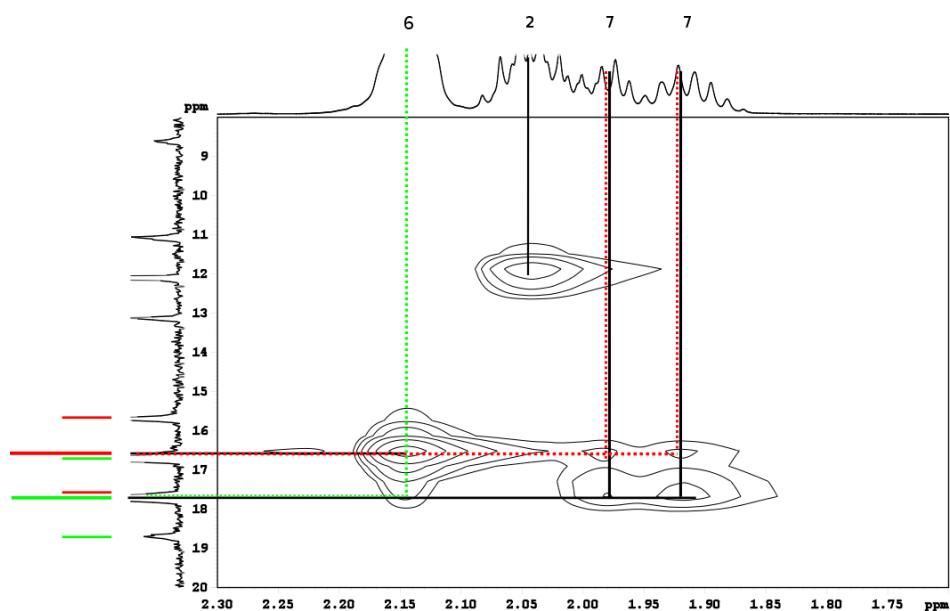


Figure 4-53: Zoom of an ^1H - ^{13}C HSQC experiments with a ^{13}C single pulse experiments as an external projection for the indirect dimension.

Thus the ^1H spectrum of the *N*-methyl-*N*-propyl piperidinium bis(fluorosulfonyl)imide ($\text{C}_3\text{mpip FSI}$) can be assigned as shown in Figure 4-54. However, as the two peaks corresponding to the two hydrogens of site 7 can't be assigned, both peaks are treated separately during the HOESY curve fitting, and the average of both cross relaxation rates will be reported herein.

Part 3:
Influence of ionic liquid cation structure

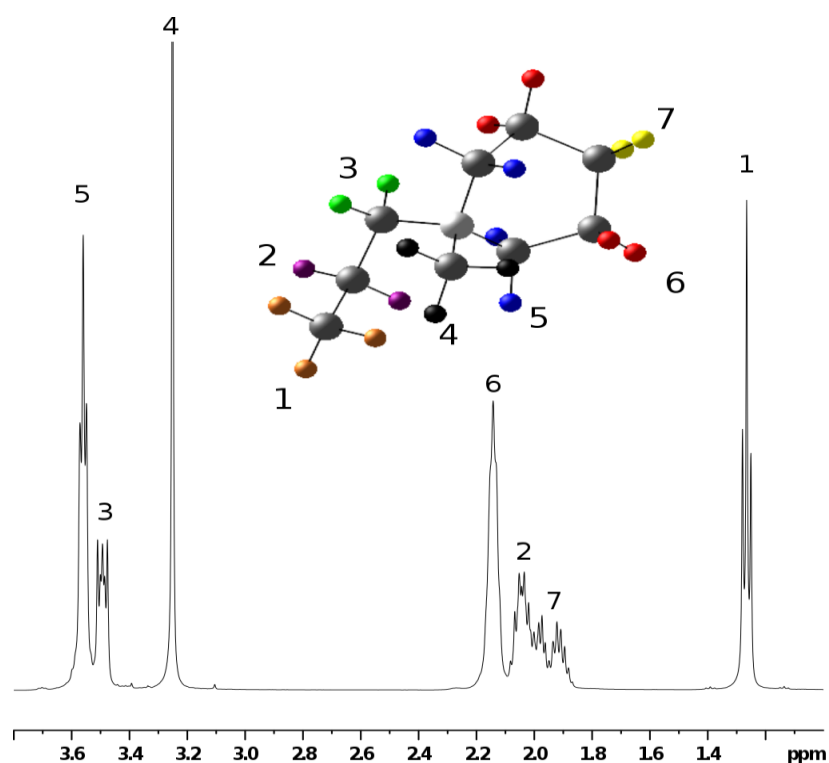


Figure 4-54: Assigned ^1H spectrum of *N*-methyl-*N*-propyl piperidinium bis(fluorosulfonyl)imide (C_3mpip FSI) cation

4.3.II.2 ^1H - ^7Li HOESY experiments

As shown in Figure 4-55, which represents the extracted cross-relaxation rates from the ^1H - ^7Li HOESY experiments for each specific carbon sites of the C_3mpip cation, one can see that the strongest reported cross relaxation value corresponds to the CH_2 group on the alkyl chain that is furthest away from the nitrogen, thus corresponding to the two strongly J coupled protons. Thus, according to these values, the trend is very similar to the one extracted for the ionic liquid with the C_3mpyr cation, with the lithium more strongly correlated with the hydrogen sites the further away they are from the nitrogen, which carries the positive charge.

Part 3:
Influence of ionic liquid cation structure

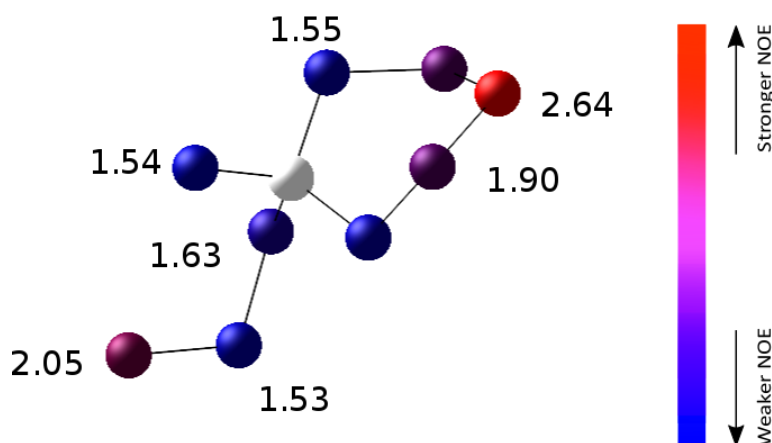


Figure 4-55: ^1H - ^7Li Overhauser rates for the C_3mpip and lithium cations (1 molal LiFSI at 50°C). Cross-relaxation rates are in $\cdot 10^{-4} \text{ s}^{-1}$ and the colour coding corresponds to the relative intensities of the NOE. (uncertainty of 2.5% for each cross relaxation values)

4.3.III Effect of a methoxy group at the end of the alkyl chain

The next studied sample still contains a pyrrolidinium cation structure, but this time with an oxygen site incorporated on the alkyl chain. This 1-methyl-1-(2-methoxyethyl) pyrrolidinium bis(fluorosulfonyl)imide ($\text{C}_{201}\text{mpyr}$) sample was mixed with 1 molal of lithium bis(fluorosulfonyl) imide (LiFSI). This modification of the cation structure is potentially interesting as another type of heteroatom is added to the cation and the oxygen is expected to interact strongly with the lithium.

4.3.III.1 ^1H - ^7Li HOESY experiments

Figure 4-56 presents the extracted cross relaxation rates for the ^1H - ^7Li HOESY experiments for each specific carbon site of the $\text{C}_{201}\text{mpyr}$ cation. Interestingly, one can see that the largest value of cross relaxation rate occurs for the methyl group next to the oxygen at the end of the heteroalkyl chain. Furthermore, the next two largest values correspond to the two CH_2 groups on the alkyl chain, the larger of these being the one closer to the oxygen site. Regarding the cross relaxation rates for the

Part 3:
Influence of ionic liquid cation structure

other three sites, corresponding to the cycle and the N-methyl group, the values are much lower, with the lowest one corresponding to the ring CH₂ group close to the nitrogen. This trend suggests that the lithium approaches more closely to the hydrogen sites on the alkyl chain, and in fact the strongest cross relaxation rates are specifically located either side of the oxygen. This behavior can be explained due to the electronegativity of the oxygen and its solvation to the lithium cation. This makes intuitive sense in that one would expect the lithium to be repelled by the positively charged nitrogen site and attracted to the alkyl chain due to the electronegativity of the oxygen.

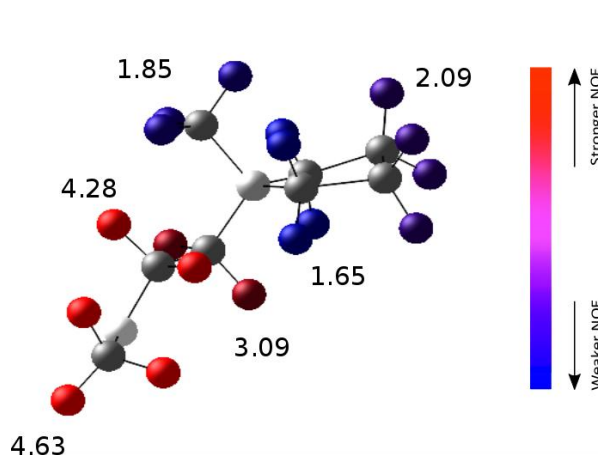


Figure 4-56: ¹H-⁷Li Overhauser rates for the C₂₀₁mpyr and lithium cations (1 molal LiFSI at 50°C). Cross-relaxation rates are in $\cdot 10^{-4} \text{ s}^{-1}$ and the colour coding corresponds to the relative intensities of the NOE. (uncertainty of 2.5% for each cross relaxation values)

4.3.III.2 ¹H-¹⁹F HOESY experiments

The ¹H-¹⁹F cross relaxation rates shown in Figure 4-57 are larger for the groups located closer to the nitrogen center of the cation. One should notice that the largest value, similarly to the C₄mpyr cation, is for the CH₂ group on the alkyl chain that is the closest to the positive nitrogen site. Then the lowest cross relaxation values are observed for the sites that are the furthest away from this positively charged nitrogen, *i.e.*, the methyl group at the end of the alkyl chain, and the more distant CH₂ group on the cycle. Although this trend corresponds to the ¹H-¹⁹F cross relaxation rates

Part 3:
Influence of ionic liquid cation structure

trends observed on the different samples described above, and as expected correspond to the inverse as the ^1H - ^7Li cross relaxation trend observe earlier on the same system.

Secondly, it is also interesting to note that the ^1H - ^{19}F σ magnitudes overall are larger in the $\text{C}_{201}\text{mpyrFSI}$ system than the $\text{C}_3\text{mpyrFSI}$, implying an overall closer association of the FSI to this cation. Based on the former discussion about the cation-cation interactions, one would expect to see the opposite trend, as a stronger interaction between the $\text{C}_{201}\text{mpyr}$ cation and the Li cation would have the potential effect of displacing the anion. These apparent discrepancies can be potentially explained by either a variation in the dynamics between the different ILs or either described by other ranged of NOE effect such as described in the GSW theory. Thus similarly to the cation-cation interactions, molecular dynamics simulations were carried out in order to try to find a correlation.

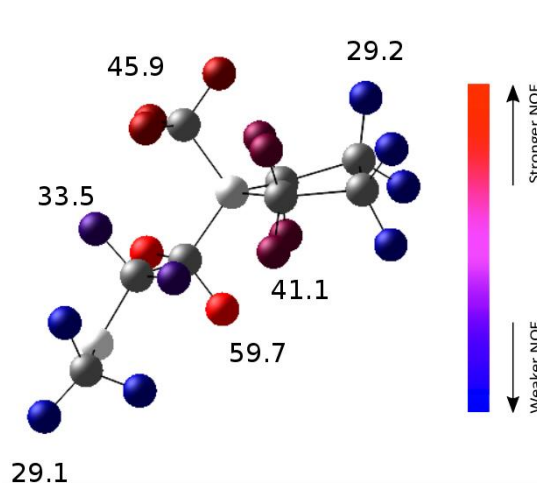


Figure 4-57: ^1H - ^{19}F Overhauser rates for the $\text{C}_{201}\text{mpyr}$ and FSI anions (1 molal LiFSI at 50°C). Cross-relaxation rates are in $\cdot 10^{-4} \text{ s}^{-1}$ and the colour coding corresponds to the relative intensities of the NOE. (uncertainty of 2.5% for each cross relaxation values)

As the extracted cross correlation rates for the $\text{C}_{201}\text{mpyr}$ cation showed the biggest difference to the $\text{C}_3\text{mpyrFSI}$ system, molecular dynamics simulations were carried out to see if the results correlate well.

4.3.III.3 Comparison with Molecular dynamics

Similarly to the C₃mpyr, molecular dynamics simulations were carried out in order to extract the RDF plots and the coordination number between the different carbon sites and both lithium and fluorine sites for the C₂₀1mpyr FSI ionic liquid doped with 1 molal LiFSI.

4.3.III.3.1 Cation-Cation interactions

The extracted ¹H-⁷Li cross relaxation rates for the C₂₀1mpyr cation are summarized in Figure 4-58. It turns out that compare to the C₃mpyr cation, in the case of C₂₀1mpyr the lithium to be strongly correlated to the carbon sites around the oxygen rather than the rest of the molecule. The ¹H-⁷Li cross-relaxation rates for the C₂₀1mpyrFSI sample doped with 1 molal LiFSI at 50°C are ordered as follows:

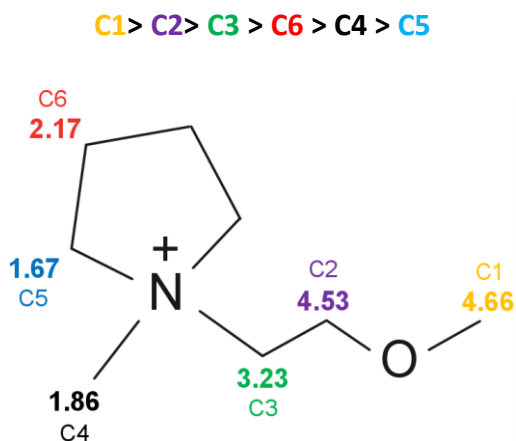


Figure 4-58: C₂₀1mpyr cation with numbering, colour coding and experimental cross-relaxation rates ($\times 10^{-4} \text{ s}^{-1}$) between ¹H and ⁷Li for C₂₀1mpyrFSI with 1 molal LiFSI at 50°C (uncertainty of 2.5% for each cross relaxation values)

MD simulations provide the carbon-lithium radial distribution functions (RDF) and coordination numbers (CN), obtained after equilibrating the two systems at 353 K (as shown in Figure 4-59). The RDF peaks are relatively broad due to the significant variations in the C-Li distances.

Part 3:
Influence of ionic liquid cation structure

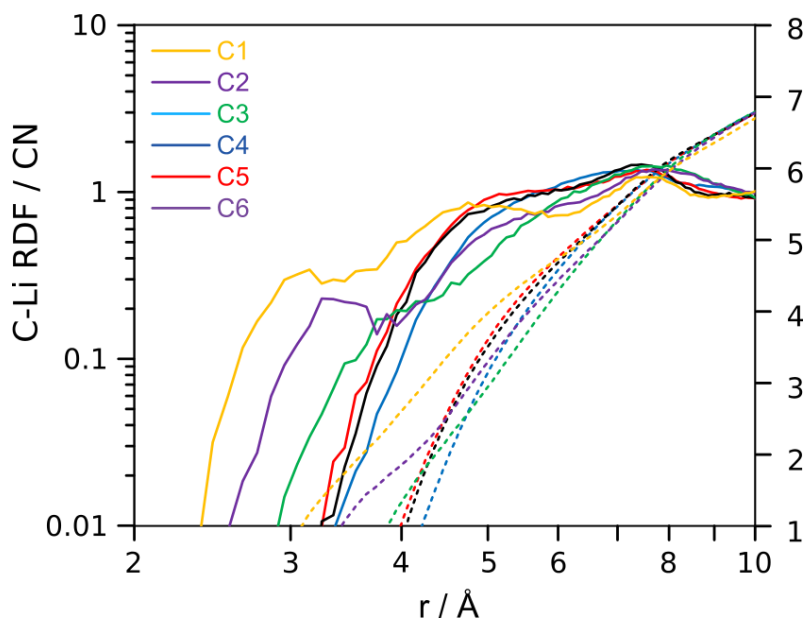


Figure 4-59: Carbon-lithium radial distribution functions (RDF) and coordination numbers (CN) obtained from the MD simulations for C_{201mpyr}FSI with 1 molal LiFSI at 50°C

The RDFs in Figure 4-59 shows a first coordination shell at a distance of around 4-5 Å and the C-Li distances for the different carbon are in the following order:

$$C1 > C2 > C3 > C6 > C4 > C5$$

Again, by looking at the Figure 4-60, one can see that the correlation with cross relaxation numbers extract from HOESY experiments are in perfect correlation with the distances numbers extract from the MD simulation. So according to the molecular dynamics simulations, this result confirms again the choice of the second model and confirms that the lithium is strongly correlated to the oxygen site in the middle of the alkyl chain of the C_{201mpyr} cation.

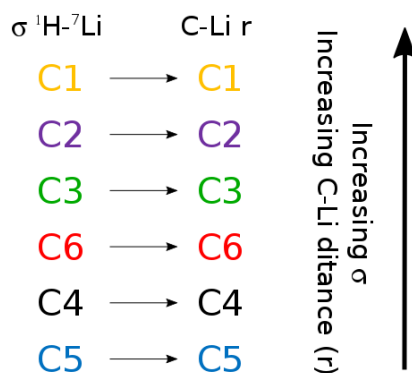


Figure 4-60: Graphical illustration of the correlations between the experimentally measured ¹H-⁷Li cross relaxation rates and carbon-lithium distance derived from the MD, corresponding to Figure 4-58 and Figure 4-59 data respectively.

4.3.III.3.2 Cation-Anion interactions

For the C₃mpyr cation, in the case of the ¹H-¹⁹F HOESY cross-relaxation rates, the influence of the correlation time was assumed negligible compared to the influence of the distances. By applying a similar assumption in the case of the C₂₀₁mpyrFSI doped with 1 molal LiFSI at 20°C, the fluorine to hydrogen distances according to the HOESY data are ordered as follow:

$$C5 > C4 > C2 > C6 > C3 > C1$$

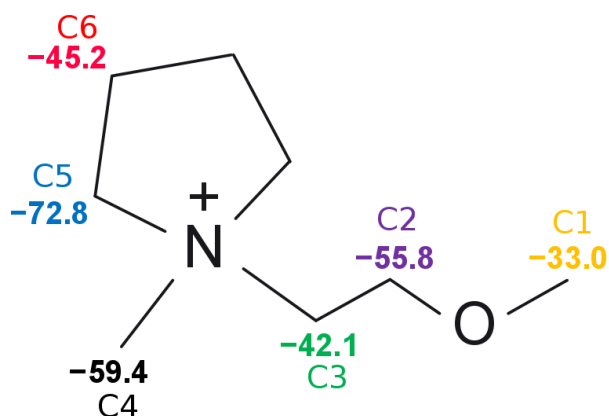


Figure 4-61: C₃mpyr cation with numbering, colour coding and experimental cross-relaxation rates ($\times 10^{-4}$) of ¹H-¹⁹F experiments for C₃mpyr FSI with 1 molal LiFSI at 20°C (uncertainty of 2.5% for each cross relaxation values)

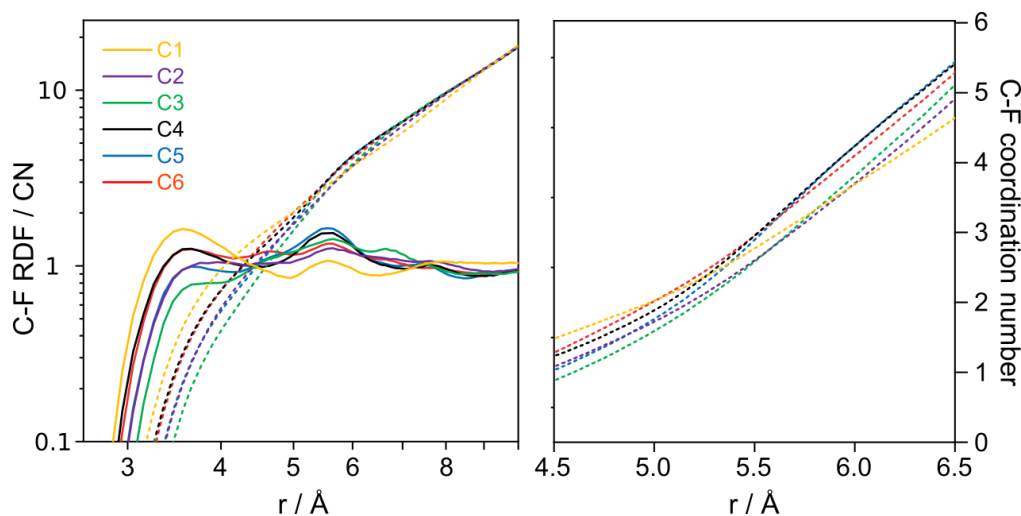
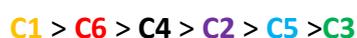


Figure 4-62: Carbon-fluorine radial distribution functions (RDF) and coordination numbers (CN) obtained from the MD simulations for C₂₀₁mpyrFSI with 1 molal LiFSI at 20°C

Part 3:
Influence of ionic liquid cation structure

The carbon fluorine radial distribution functions (RDF) and coordination numbers (CN) extracted from the molecular dynamics simulation carried out on the C₂₀₁mpyr FSI system exhibit a similar behaviour than the C₃mpyr cation. Indeed, all the minimum distances between the different carbon sites and the fluorine site appear to be similar, around ~3 Å, and the RDF curves also exhibit a second bump around 5.5 Å. Secondly the order of the coordination numbers also changes at a distance of around 5.5 Å.

Thus the C-F coordination numbers order at distances below 5.5 Å is:



and the order of the C-F coordination numbers at distances greater than 5.5 Å is:



When comparing the extracted cross relaxation rates to the two different trends extracted from the C-F coordination numbers as shown in Figure 4-63, the cross relaxation numbers exhibit a much closer correlation to the CN numbers at the longer distances, thus confirming again the potential importance of the long range interactions described by the GSW theory.

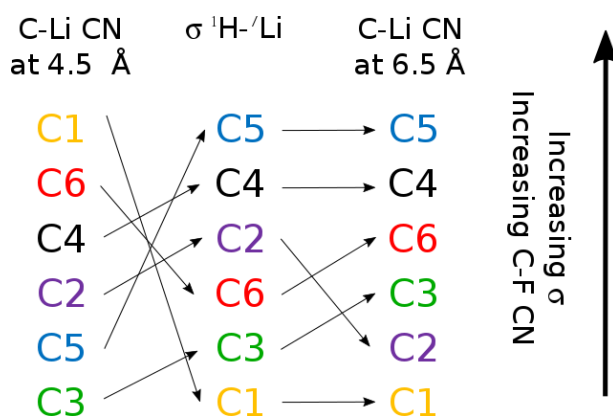


Figure 4-63: Graphical illustration of the correlations between the experimentally measured ¹H-¹⁹F cross-relaxation rates and carbon-lithium coordination numbers (CN) derived from the MD, corresponding to Figure 4-46 and Figure 4-47 data respectively

4.3.IV Conclusions

The extraction of ^1H - ^7Li and ^1H - ^{19}F cross relaxation rates has been carried out on a series of ionic liquid electrolytes with differences in the structure of the cation in order to observe the effect on the lithium-cation and anion-cation interactions. Interestingly, it has been shown that changing the alkyl chain length or the cycle length does not appear to have a major impact on these interactions. However, the addition of an ether group on the alkyl chain leads to a completely different behavior in the case of the ^1H - ^7Li HOESY experiments: in this case, the lithium displays a strong association with the hydrogen groups closest to the ether oxygen. This specific feature has been related to the ability of oxygen atoms to coordinate lithium ions. Furthermore, similarly to what was shown for the C_3mpyr cation, this specific behavior is in excellent agreement with the molecular dynamics simulations for this system. The ^1H - ^{19}F cross relaxation rates are larger by an order of magnitude in the methoxy system, seemingly resulting from slower dynamics (longer τ_c) as implied by the apparent larger viscosity.

Part 3:
Influence of ionic liquid cation structure

Part 4:
Structural studies
of solid state *N*-
methyl-*N*-propyl
pyrrolidinium
bis(fluorosulfonyl)i
mide mixed with
lithium

Structural studies of frozen N-methyl-N-propyl pyrrolidinium bis(fluorosulfonyl)imide mixed with lithium

As discussed in the previous chapters, the HOESY experiment is a useful technique for studying ion interactions in ionic liquids. We demonstrated that it was possible to extract quantitative cross relaxation rates that provide information on the organization of ions relative to each other, and that the order of extracted cross relaxation rates can correlate well with the order of distances and coordination numbers extracted from molecular dynamics simulations. But in fact, as explained earlier in the literature review section, HOESY is not the only NMR pulse sequence which can help to extract distances between ions. The following section outlines a potential complementary approach based on DNP NMR of ionic liquids in the glassy state.

4.4.I DNP

Dynamic Nuclear Polarization (DNP) is a rapidly developing NMR technique which has several advantages in our case. First of all, one of the primary features of DNP is to enhance the NMR signal using magnetization transfer from the electron spins. As samples need to be cooled down to low temperatures (~ 100 K) in order to achieve this signal enhancement most efficiently, samples such as ionic liquids will be therefore in a solid state. In our case, as the sample is quenched rapidly from room temperature to ~ 100 K, it is possible to make the assumption that the cooling is quick enough to obtain a glassy state of the ionic liquid and thus obtain static snapshot of the liquid state structure.

For the following study, the C₃mpyr FSI sample at 1 molal of LiFSI was used (Figure 4-64 (a)) as it was the first sample used for the HOESY experiments and as explained earlier a commonly studied ionic liquid. As the REDOR experiment first involves a cross polarization transfer from the ¹H nuclei to the ¹³C nuclei, Cross Polarisation Magic Angle Spinning (CPMAS) experiments were carried out in order to observe the increase in sensitivity due to the DNP mechanism. As shown in Figure 4-64b), which represents a ¹³C CPMAS spectrum recorded from the sample, all six distinct carbon sites of the cation are resolved and assigned. The spectrum with DNP enhancement

Structural studies of frozen N-methyl-N-propyl pyrrolidinium
bis(fluorosulfonyl)imide mixed with lithium

but without ^1H decoupling is shown in Figure 4-64 d). The peak at 0 ppm corresponds to the silicon plugs used to seal the rotor.

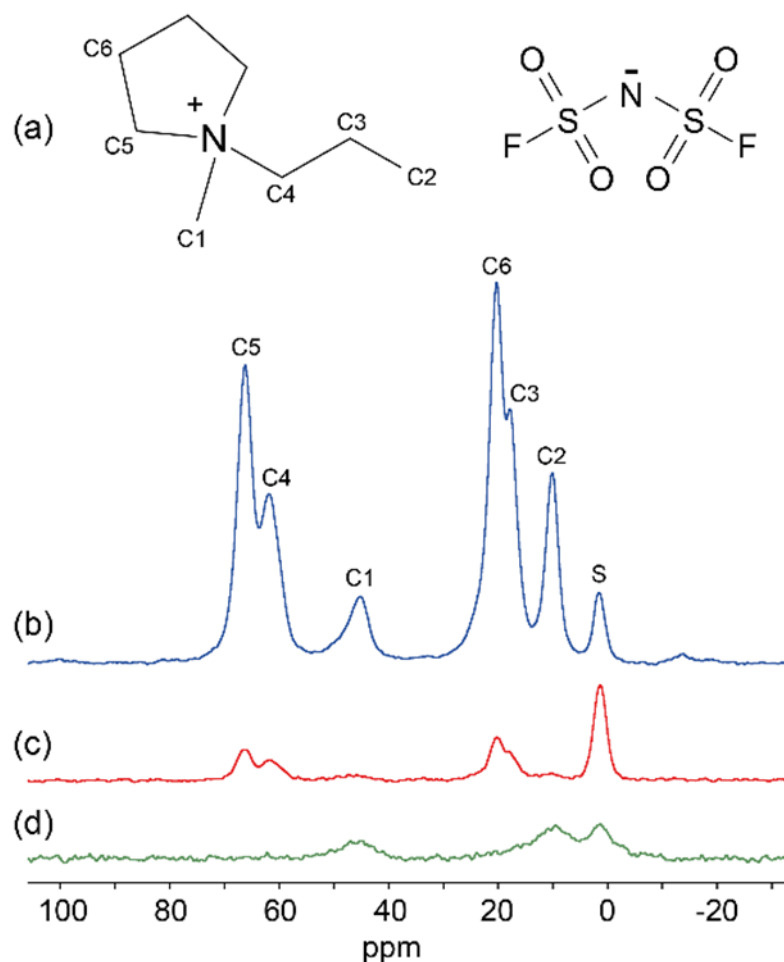


Figure 4-64: (a) The molecular structure of the C₃mpyrFSI ionic liquid with the six inequivalent carbon sites labelled. ¹³C CPMAS spectra obtained from the solid state C₃mpyrFSI-⁶LiFSI-TEKPol solution are shown with (b) DNP enhancement and ¹H decoupling, (c) no DNP enhancement and ¹H decoupling, and (d) DNP enhancement but no ¹H decoupling. All spectra were acquired at 9.4 T and 8 kHz MAS with 80 scans acquired, a 6s recycle delay, and a sample temperature of approximately 92 K. The peak assignment is shown in (b), where S denotes the signal from the silicone plug.

A summary of the different chemical shifts and peak widths is presented in Table 4-7, alongside their measured polarization build-up times (denoted T_{1}^{*}) and the different DNP enhancement factors (ϵ_{DNP}). In order to calculate the different DNP enhancement, the peaks intensities obtained with microwave irradiation applied (DNP enhancements occurring) in Figure 4-64 b), are divided by their corresponding peaks intensities in the absence of microwaves irradiation, in Figure 4-64 c).

Structural studies of frozen N-methyl-N-propyl pyrrolidinium
bis(fluorosulfonyl)imide mixed with lithium

Table 4-7: ^{13}C Isotropic Chemical Shifts (δ_{iso}), Peak Widths ($\Delta\delta$), Polarization Buildup Times (T_1^*), and DNP Enhancement Levels (ϵ_{DNP}) for the six Carbon Sites on the Pyrrolidinium Cation (as indicated in Figure 4-64 (a))

Carbon	$^{13}\text{C} \delta_{\text{iso}} / \text{ppm}$	$^{13}\text{C} \Delta\delta / \text{ppm}$	T_1^* / s	ϵ_{DNP}
C1	45.0	5.1	2.5	15.0
C2	9.7	3.0	2.9	29.0
C3	17.0	2.7	3.8	9.0
C4	60.9	4.5	3.9	8.6
C5	65.5	3.5	3.8	9.7
C6	19.8	3.5	3.6	9.0

One should note that in Table 4-7, peaks widths range from 2.7 to 5.1 ppm. As the IL was mixed with a biradical (the nitroxide biradical TEKpol¹³⁹ at a concentration of 15 mM) in order to obtain the DNP enhancement, a separate experiment was carried out on the same IL without any biradical and showed similar peak widths. This implies that the peak widths arise from a structural disorder rather than paramagnetic effects due to the presence of the biradical. This is consistent with the assumption that the biradical does not alter the structure and short range order of the IL. Moreover, these values are consistent with values observed in another glassy IL system (C₄mimTFSI) studied by ^{13}C solid-state NMR at 175 K. However, it was noted that peaks can narrow over time (several hours), which can be due to some slow crystallisation of the sample. Ejecting and re-inserting the sample returned it to the glassy state.

The aim of these experiments was to extract distances between the lithium and the different carbon sites on the cation, through for example ^7Li - ^{13}C REDOR experiments. Unfortunately, the ^7Li isotope, the one with the highest natural abundance (92.5%) was unable to be studied due to the probe configuration, and thus the IL was mixed with a ^6Li -enriched Li FSI (95% ^6Li). However, the ^6Li isotope gives the additional advantage of a small quadrupolar moment (~50 times smaller than the quadrupolar moment of ^7Li), thus ^6Li can be treated as a spin half nucleus in the rest of this work, which justifies the use of a REDOR¹¹⁹ pulse sequence instead of a REAPDOR¹²⁰ one.

Structural studies of frozen N-methyl-N-propyl pyrrolidinium bis(fluorosulfonyl)imide mixed with lithium

As explained in the Methodology chapter, the REDOR experiment works by comparing two spectra obtained with and without the 180° pulse train on the dephasing nucleus (in this case ^6Li). As shown in Figure 4-65, we can see the ^{13}C signal difference of the two spectra with and without the train of ^6Li pi pulses, and the difference spectrum. Note that the peak from the silicone plug shows no dephasing due to having no ^6Li present.

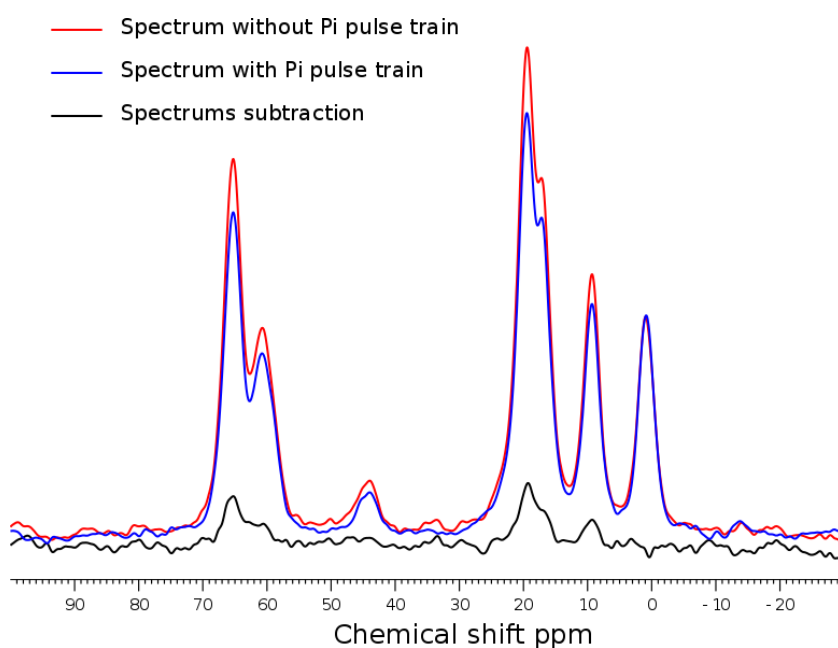


Figure 4-65: Spectrum with and without the pi pulse train, and the spectrum corresponding to the subtraction of both, extracted from a REDOR experiment realised on the C_3mpyr FSI sample doped with 1 molal ^6Li FSI at 8 ms of dephasing time

4.4.I.1 Universal curve fitting

Thus, different spectra at different dephasing times are recorded, and the difference in signal is plotted against the dephasing time, resulting in a so-called dephasing curve (Figure 4-66). In order to extract the ^6Li - ^{13}C distances from these curves, different models can be used. The most commonly used model is the universal REDOR curve expression, described K.T. Mueller¹⁴⁰.

Using Equation 4-20, which is given by Mueller¹⁴⁰:

Structural studies of frozen N-methyl-N-propyl pyrrolidinium
bis(fluorosulfonyl)imide mixed with lithium

$$\frac{\Delta S}{S_0} = 1 - [J_0(\sqrt{2}\lambda_n)]^2 + 2 \sum_{k=1}^{\infty} \frac{1}{16k^2 - 1} [J_k(\sqrt{2}\lambda_n)]^2$$

Equation 4-20

Where J_k represent the k^{th} order of the Bessel function and $\lambda_n = D\tau_d$, D corresponds to the dipolar coupling in Hz, and τ_d corresponds to the dephasing time in seconds. Thus, the dephasing plot can be fitted using the above equation, as shown in Figure 4-66. The expression was truncated to the 5th order Bessel function, and a linear scaling factor f was also incorporated and allowed to vary in the fits.

This way of fitting leads to the extraction of a single ${}^6\text{Li}$ - ${}^{13}\text{C}$ distance (Table 2). However, in the glassy IL electrolyte studied here, we expect multiple Li-C distances to co-exist due to the structurally disordered glass. A more advanced method that can fit the dephasing curve to multiple distances and distance distributions was therefore used. Figure 4-66 shows the universal REDOR curve fitting of all six carbon sites of the C_3mpyr cation, and the extracted distances are presented in Table 4-8

Structural studies of frozen N-methyl-N-propyl pyrrolidinium bis(fluorosulfonyl)imide mixed with lithium

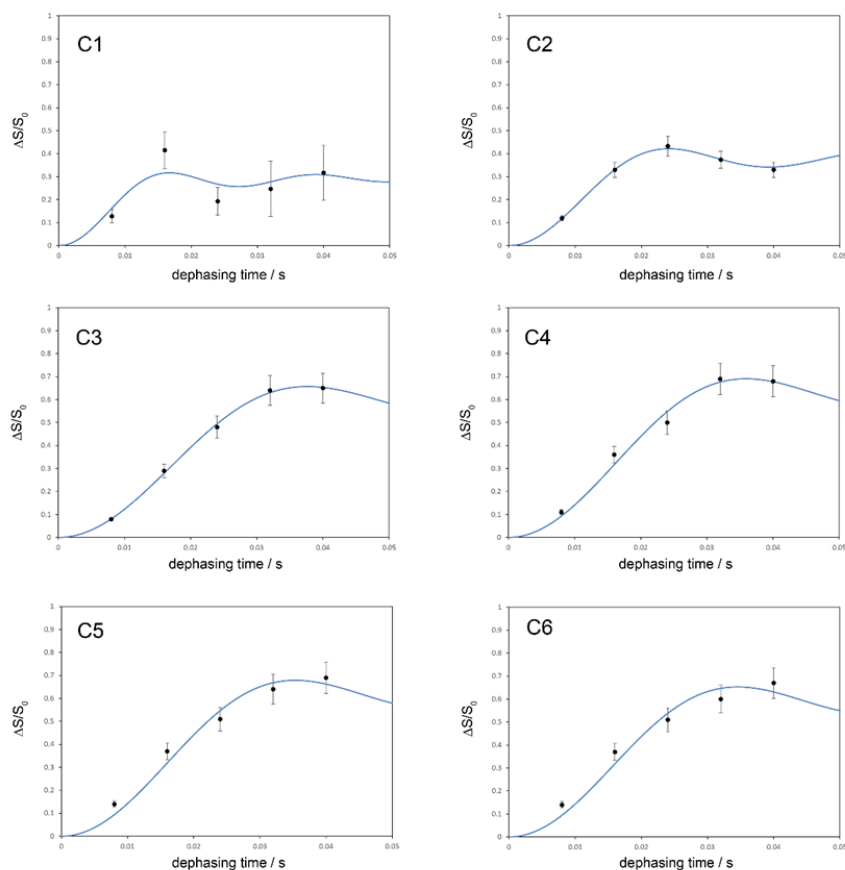


Figure 4-66: ^{13}C - ^6Li dephasing data fitted according to Equation 4-20.

Table 4-8: Li-C distances d and scaling factors f extracted from the ^{13}C - ^6Li dephasing data using the universal REDOR dephasing curve.

Carbon	$d / \text{Å}$	f
C1	3.54	0.30
C2	4.01	0.40
C3	4.64	0.63
C4	4.57	0.66
C5	4.55	0.65
C6	4.51	0.63

4.4.1.2 BS-REDOR curve fitting

The BS-REDOR analysis method¹⁴¹ uses maximum entropy Boltzmann statistics, and can provide unbiased fits to multiple distances and distance distributions, better accounting for the structural disorder in the glassy state IL. Figure 4-67 represent the same data as shown in Figure 4-66, but inverted (as required by the fitting software $1-\Delta S/S_0$), and fitted using the BS-REDOR model.

Figure 4-67 shows the fitting for the six carbon sites of the C₃mpyr cation, with their corresponding C-Li distance distributions.

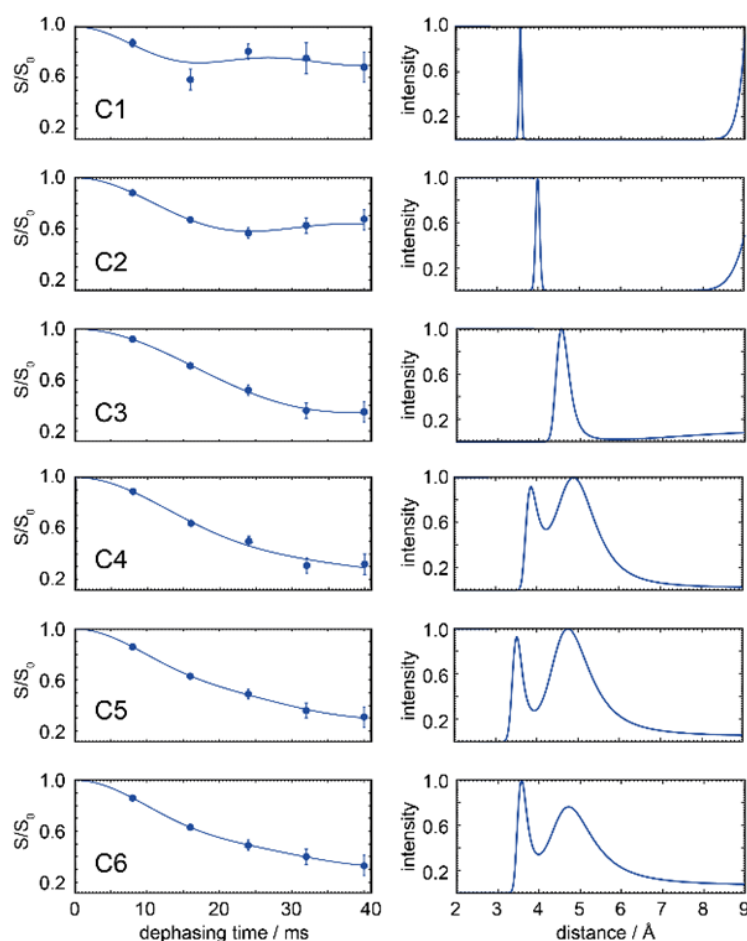


Figure 4-67: ¹³C-⁶Li REDOR dephasing plots for the six ¹³C signals of the C₃mpyr cation (left) fitted using the BS-REDOR method with extracted C-Li distance distributions (right).

Structural studies of frozen N-methyl-N-propyl pyrrolidinium bis(fluorosulfonyl)imide mixed with lithium

The extracted Li-C distances are summarized in Table 4-9. Interestingly, one should note that the three last carbons corresponding to C4, C5 and C6 ($C_3\text{mpyr}$ cation with corresponding sites in Figure 4-68), present two distinct Li-C distance, one around 3.6 Å and the other one around 4.75 Å. Furthermore, the probability of presence at these distances corresponds to around 20% at the closer distance and thus around 80% at the longer one.

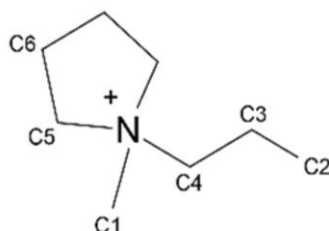


Figure 4-68: The molecular structure of the $C_3\text{mpyrFSI}$ ionic liquid with the six inequivalent carbon sites labelled

By looking at the distances extracted for all sites, the lithium exhibits a clear affinity to the carbon sites on the heterocyclic carbon ring, and distances get larger as the carbon sites get further away from this cycle.

Thus the order of the distances of closest approach extracted from the BS-REDOR fitting as presented in table 8 corresponds to the following:

$$C5 < C1 < C6 < C4 < C2 < C3$$

This trend can be explained by the potential clustering of the Li^+ cation with the FSI^- anions. Indeed, as the positive charge of the $C_3\text{mpyr}$ cation is delocalised on the heterocyclic carbon ring, the negatively charged $\text{Li}(\text{FSI})_n$ clusters will tend to be closer to this part of the cation. In fact this can also explain the long distance between carbon site on the ring as the most commonly found cluster corresponds to $\text{Li}(\text{FSI})_3^{2-}$ with a van der Waals radius of 4.07 Å⁵⁶. Thus the shorter distance, which is also less common (20%), may correspond to smaller cluster such as $\text{Li}(\text{FSI})_2^-$, with a smaller radius and lower abundance.

Structural studies of frozen N-methyl-N-propyl pyrrolidinium bis(fluorosulfonyl)imide mixed with lithium

Table 4-9: Lithium-carbon distances (d_n), distribution widths (Δd_n) and relative fractions (f_n) extracted for each of the carbons on the C₃mpyr cation using BS-REDOR analysis. The distribution widths Δd_n for C1, C2 and C3 are unspecified due to the 9 Å cut-off used in the fitting.

Carbon	$d_1 / \text{Å}$	$\Delta d_1 / \text{Å}$	f_1	$d_2 / \text{Å}$	$\Delta d_2 / \text{Å}$	f_2
C1	3.55	0.10	0.32	>8	-	0.68
C2	4.00	0.10	0.47	>8	-	0.53
C3	4.55	0.35	0.72	>6	-	0.28
C4	3.85	0.45	0.22	4.90	1.20	0.78
C5	3.50	0.30	0.18	4.75	1.15	0.82
C6	3.60	0.30	0.21	4.70	1.40	0.79

4.4.I.3 Comparison with molecular dynamics

In order to verify these distances extracted through solid-state NMR, it is interesting to compare them with the results of molecular dynamics simulations. Thus the extracted distances were converted into a 3D plot of the lithium probability of presence around the C₃mpyr cation. The molecular dynamics simulation were carried out on a room temperature liquid phase [C₃mpyrFSI]_{0.9}[LiFSI]_{0.1}. Figure 4-69 shows a) the extracted REDOR distances converted in a 3D plot from the REDOR experiment, and b) the results of the molecular dynamics simulation.

In the case of the REDOR experiment, the BS-REDOR analysis yielded a distribution of ¹³C-⁶Li distances that we model as the sum of two Gaussian curves. Thus, the probability p_i for the lithium to be at the distance r_i of C_i is calculated using a sum of two Gaussian curves centered at $d_{1,i}$ and $d_{2,i}$ with widths at half-maximum equal to $\Delta d_{1,i}$ and $\Delta d_{2,i}$ and of respective areas $f_{1,i}$ and $f_{2,i}$ correspond to:

$$P_i(r_i) = f_{1,i} 2 \left(\frac{\ln(2)}{\pi} \right)^{\frac{1}{2}} \frac{e^{-\frac{4 \ln(2)(r_i - d_{1,i})^2}{\Delta d_{1,i}^2}}}{\Delta d_{1,i}} + f_{2,i} 2 \left(\frac{\ln(2)}{\pi} \right)^{\frac{1}{2}} \frac{e^{-\frac{4 \ln(2)(r_i - d_{2,i})^2}{\Delta d_{2,i}^2}}}{\Delta d_{2,i}}$$

Equation 4-21

Then the probability to find a lithium nuclei at certain Cartesian position in space is obtained by calculated the product of the $P_i(r_i)$ for I from 1 to 6. Using the extracted

Structural studies of frozen N-methyl-N-propyl pyrrolidinium
bis(fluorosulfonyl)imide mixed with lithium

parameters display in Table 4-9, the 3D plot with the lithium preferential positions around the cation were realized with maple.

The two methods appear to be in good agreement, and exhibit similar locations for the lithium, with a preferential location above and below the pyrrolidinium ring and a higher probability to exist on the same side of the ring as the methyl group. This also provides evidence that the glassy state of the IL does indeed mimic the solution-state structure.

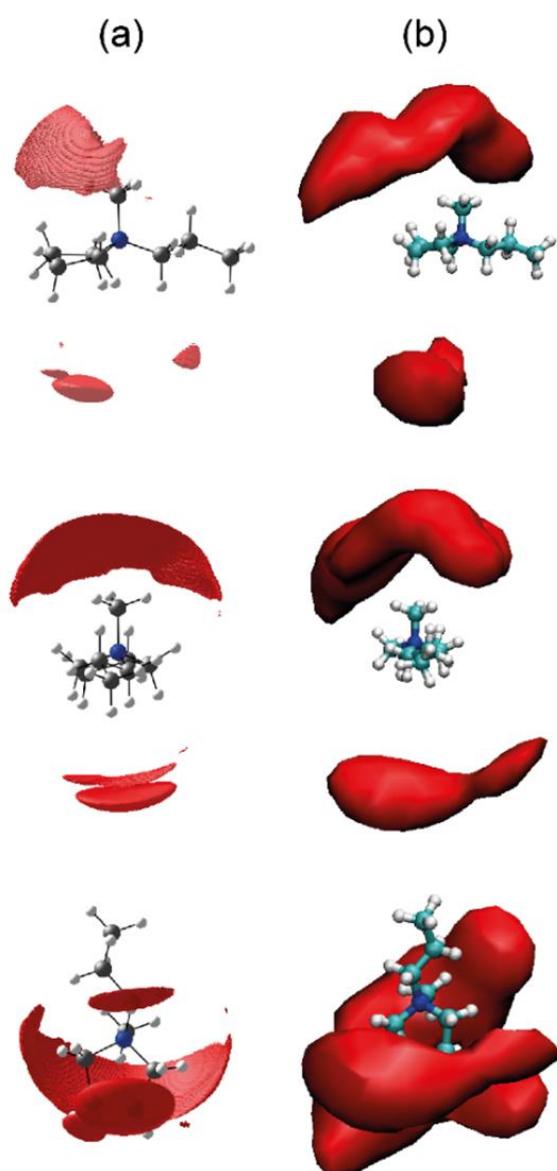


Figure 4-69: Plots of Li^+ spatial distribution around the C_3mpyr cation constructed from (a) the 92 K solid-state ^{13}C - ^6Li REDOR distance data in Table 2 and (b) a molecular dynamics simulation carried out on a liquid-phase $[\text{C}_3\text{mpyrFSI}]_{0.9}[\text{LiFSI}]_{0.1}$ system with a simulated temperature of 298 K. As a reference for scale, the carbon-carbon bond lengths on the C_3mpyr cation are 1.23 Å.

4.4.II Comparison with HOESY

The extracted spatial distribution of the lithium cation around the C₃mpyr cation according to the solid-state DNP NMR experiments can also be compared with the results of the HOESY experiments carried out on the same sample in the liquid phase. Indeed both experiments were carried out on the C₃mpyr FSI system, mixed with 1 molal LiFSI (⁶Li enriched in the case of the DNP experiments). The ¹H-⁷Li HOESY experiments were carried out at 293 and 323 K while the DNP experiments were carried out at 92 K. In the liquid state at high temperature (323 K) the ¹H-⁷Li HOESY experiments highlight a strong correlation of the lithium cation to the methyl at the end of the alkyl chain and then to the CH₂ group on the ring, the further away from the nitrogen. At lower temperature (293 K), which still corresponds to the liquid state, the extracted cross relaxation rates tend to exhibit a different behavior, indeed, in this case the lithium appears to be less correlated to the methyl group at the end of the alkyl chain, and more correlate with the hydrogen sites around the nitrogen. In fact, this trend correlates quite well with the spatial distribution around the C₃mpyr cation extracted from the DNP experiments, which highlights a strong correlation with the carbon groups around the ring. These results may be due to the fact that at lower temperatures, when the system has less energy, the reduced dynamics of the lithium ions results in a stronger association with the FSI anions, with longer-lived Li(FSI)_n clusters that interact more with the positively charged region of the IL cation.

4.4.III Conclusions

The DNP experiments allowed the extraction of the carbon-lithium distances from the C₃mpyrFSI mixed with 1 m of ⁶Li enriched LiFSI in the glassy state (92 K). These results provided the most probable positions of the lithium cations around the C₃mpyr cation, and highlighted that the lithium appears to be more strongly associated with the carbon groups on the cycle and the N-CH₃ group compared to the

Structural studies of frozen N-methyl-N-propyl pyrrolidinium
bis(fluorosulfonyl)imide mixed with lithium

rest of the molecule. These results were in good agreement with room temperature liquid-phase molecular dynamics simulations carried out on the same sample, and thus, this behaviour has been attributed to a strong coordination of the lithium with the FSI. It has been shown that this result is also in good agreement with the extracted cross relaxation rate trend from ^1H - ^7Li HOESY experiments at 293 K. This can be explained by the theory that at lower temperature, the lithium is more strongly coordinated with the FSI anions and as a result it more strongly associates with the positively charged part of the C_3mpyr cation.

Chapter 5

Conclusions and outlook

Conclusions and outlook

5.I Conclusions

5.I.1 An improved HOESY build-up curve fitting method

A new way of extracting heteronuclear intermolecular cross relaxation rates from HOESY experiments has been developed in order to extract the cross relaxation rates in a quantitative and systematic manner and also to improve the fit quality of the build-up curves. By including some sample-specific factors into the fitting procedure, quantitative comparisons of the extracted NOEs between different samples was made possible. Moreover, we have demonstrated a way to improve the time efficiency of the HOESY experiment as reliable and reproducible results can be obtained using shorter recycle delays or numbers of mixing time steps, potentially reducing the experimental time by a factor of eight.

5.I.2 Quantitative comparison of cross-relaxation rates in ionic liquids

It has been demonstrated herein that measuring the cross relaxation rates is a powerful way to probe ion interactions in ionic liquid systems. These parameters can be interpreted in terms of inter-ionic distances. In the C₃mpyrFSI ionic liquid doped with LiFSI, it has been shown that the lithium cation is able to get close to the methyl group at the end of the alkyl chain at high temperature and low lithium concentration. Interestingly, this is not the case at lower temperature or higher lithium concentration: this can potentially be due to a stronger coordination between the lithium and the FSI anions, leading to longer-lived Li(FSI)_n clusters. Moreover, in the study of other ionic liquids systems with other cations of the same family such as C₄mpyr or C₃mpip, similar results were found, highlighting that at lower temperature and concentration, the lithium seems to be more closely associated with the positively charged region of the IL cation. However, in the case of the C₂₀₁mpyr with an ether-alkyl chain, the extraction of the cross-relaxation rates shows that the lithium cation associates strongly with the methyl and CH₂ groups neighboring the oxygen atom, rather than to the ring. This specific feature has been explained by the ability of the oxygen to coordinate to the lithium

ion. Regarding the cation-cation interactions, in all cases studied above, the FSI anion seems to be more strongly associated with the hydrogen groups close to the nitrogen which has been attributed to the presence of the positive charge centered on the nitrogen.

5.I.3 Correlating cross-relaxation rates with molecular dynamics simulations

The aim of the HOESY experiments is to extract the cross relaxation rates and convert them into information on the ionic liquid “structure”, and several models were studied. In the case of the ^1H - ^7Li HOESY experiments, a model developed around the distance of closest approach and the hard sphere model has been used to compare with the molecular dynamics simulations. The extracted cross relaxation rates and the distance of closest approach have shown a good correlation in both cases of the C_3mpyr cation and the $\text{C}_{201}\text{mpyr}$ cation. In the case of the ^1H - ^{19}F HOESY experiment, the hard sphere model is not applicable due to the attraction between the cation and anion, thus another theory, referred to as the “GSW theory” herein, has been considered. This theory highlights the fact that, in the case of nuclei with similar gyromagnetic ratios, the HOESY transfer can be mostly due to long range interactions, beyond the first sphere of correlation. Interestingly, the trends displayed by the extracted ^1H - ^{19}F cross relaxation rates have been shown to correlate better with C-F coordination numbers extracted from the molecular dynamics simulation at longer distances, as predicted by the GSW theory.

5.I.4 Qualitative comparison with glassy state studies

It has been found that studying ionic liquids *via* low temperature DNP NMR spectroscopy can be highly promising and complementary to the HOESY experiment for several different reasons. Firstly, the study of ionic liquids in the glassy state provides a snapshot of the liquid state structure, thereby allowing solid-state NMR experiments that can measure distances directly. Thus by probing the dipolar interactions between the lithium and the different carbons present on the cation, the REDOR experiment allowed the extraction of the carbon-

Conclusions and outlook

lithium distances of the C₃mpyrFSI mixed with 1 m of ⁶Li enriched LiFSI. Secondly, the addition of a biradical such as the TEKPol, in combination with microwave irradiation, increased the sensitivity of the experiments significantly, which is important to counteract the low natural abundance of the ¹³C. These experiments highlighted the fact that the lithium cation is strongly associated with the carbons group on the cycle and the N-CH₃ group compared to the rest of the molecule. These results showed a good agreement with MD simulations and correlated well the ¹H-⁷Li HOESY experiments. In the HOESY experiment, the lithium was shown to be strongly correlated with the end of the cation's alkyl chain at high temperature, but correlated more and more with the cycle carbons and the methyl group on the nitrogen as the temperature decreased and/or the concentration increased. This result was attributed to a stronger coordination of the lithium with the FSI anions at low temperatures and as a result a stronger association with the positively charged part of the C₃mpyr cation.

5.II Future work

As explained earlier, this thesis was focused on the quantitative extraction of cross relaxation rates in order to help refine our understanding of ionic liquid structure and thus potentially the ion transport mechanism. These results open a wide window of potential applications and further developments of the experimental methods.

5.II.1 Comparison with ⁷Li-¹⁹F HOESY experiments

In order to have a more complete understanding of the ion interactions in ionic liquid electrolytes, ⁷Li-¹⁹F HOESY experiments are promising. Indeed, having access to the lithium-anion cross relaxation rates, in combination with the lithium-cation and cation-anion cross relaxation, will lead to a better overall understanding of all the interactions between the three

Conclusions and outlook

ions, and thus can potentially lead to a clearer picture. Unfortunately, after several attempts, no ${}^7\text{Li}$ - ${}^{19}\text{F}$ HOESY signals were recorded. This issue is probably due to the slower dynamics between Li^+ and FSI, and long correlation times that may result in weak HOESY signals. This could potentially be solved by trying these HOESY experiments at lower fields or higher temperatures.

5.II.2 More accurate calculation of the spectral densities

The calculation of the spectral densities is one of the most crucial points to be developed. Spectral densities can potentially be extracted from the molecular dynamics simulations. However, in order to be able to calculate the values of the spectral density at the NMR frequencies required (*i.e.*, the sum and difference of the I and S resonance frequencies), longer simulations, up to 50 nanosecond need to be carried out. These long molecular dynamics simulations may be complicated, but can be possible as it has already been developed on proteins¹⁴².

5.II.3 Studies of the cross relaxation rate as a function of temperature

Regarding ${}^1\text{H}$ - ${}^{19}\text{F}$ HOESY experiments, because of the close proximity between the gyromagnetic ratios, negative NOEs can be observed and attributed to slow dynamics. Further studies with a wider range of temperature will be helpful in order to record the temperatures and cross relaxation rates at the maximum, minimum, and zero crossing. As these are found at specific values of the correlation time, a fit of the extracted cross relaxation rates could provide an easier access to both the correlation time and the magnitude of the dipolar constant, which can be translated in terms of distances and coordination numbers. Measuring the dipolar constants in the solid state state might also be useful to understand the dynamics in liquids with the HOESY experiment. Furthermore, molecular dynamics simulations with different sample temperatures would be interesting to also carry out in order to be able to understand the temperature variation of the cross relaxation rates and ion interactions.

5.II.4 Developing ^{13}C - ^{23}Na REAPDOR experiments

As sodium-based ionic liquids are attracting increasing interest, observing ion interactions in these systems would be highly valuable. ^1H - ^{23}Na HOESY experiments have been attempted during this project, and the ^{23}Na nuclei unfortunately exhibit very short T_{1s} , usually on the order of milliseconds. Thus, it was impossible to extract any signal using the HOESY experiment, as the signal relaxed too quickly. However, the solid-state ^{13}C - ^{23}Na REAPDOR experiment on the glassy-state IL with DNP should be possible and dipolar couplings are expected to be measurable. Some attempts have been already made at the NHFML in Tallahassee (in collaboration with Dr Frederic Mentink-Vigier), on a C_3mpyr FSI ionic liquid containing 1 molal NaFSI. Reliable dephasing time plots were difficult to extract as the signals obtained were too weak, and this data was therefore not presented here. However, these attempts revealed a very promising method, and further development of these methods, such as new bi-radicals and better optimization of the DNP enhancement should be tried.

5.II.5 Correlation with ENMR spectroscopy

Electrophoretic NMR spectroscopy is a powerful technique which can lead to the extraction of the mobility of the different ions under the influence of an applied electric field. Furthermore, the extraction of the mobilities can also give access to the ion drift direction, which can help to understand the different ion associations^{93,143}. During this PhD project, ENMR experiments were attempted in collaboration with Professor Louis Madsen in Virginia Tech, however unfortunately these did not lead to satisfactory enough results, mostly due to very low signal to noise ratios and/or sample degradation at high voltage. Thus, in order to reach more viable conditions for ionic liquids, tests at very low voltage and with very small distances between the electrodes (to maximise the electric field) were carried out at the CEMHTI laboratory, and the first results were encouraging. A cell is currently under development in order to optimize the distance between electrodes and facilitates the sample preparation.

Résumé

Etat de l'art

Ces dernières décennies, les liquides ioniques ont accru l'intérêt des chercheurs de par leurs propriétés étonnantes. En effet, les liquides ioniques, mélanges de sels purs le plus souvent liquides en-dessous de 100°C, voire à température ambiante, présentent des propriétés tel qu'une vapeur de pression saturante faible, une stabilité à haute température ou encore une capacité à dissoudre une large gamme d'échantillons. De plus, les liquides ioniques sont intéressants dans les domaines de l'électrochimie, puisqu'ils possèdent généralement une large fenêtre électrochimique, et surtout sont pour la plupart ininflammables.

Les liquides ioniques peuvent être étudiés de multiples façons et pour différents types d'application. Ce travail de thèse se concentre sur l'étude des liquides ioniques par Résonance Magnétique Nucléaire pour des applications à l'électrochimie. Plus précisément, ce travail porte sur l'étude de la structure et des associations ioniques au sein même de ces liquides. Pour ce faire, les expériences se concentrent sur une séquence d'impulsions RMN spécifique appelée Heteronuclear Overhauser Effect Spectroscopy (HOESY). Ce type d'expérience est connu depuis longtemps et est déjà fortement mentionné dans la littérature. En effet, les expériences d'HOESY consistent à étudier les transferts d'aimantation entre deux spins, via la mesure de la vitesse de relaxation croisée σ . L'intensité de la vitesse de relaxation croisée étant proportionnel à la distance entre les spins, son calcul peut permettre de remonter à la distance entre les spins et donc à la proximité des ions dans le liquide.

Cependant, l'extraction de la vitesse de relaxation croisée est compliquée, en effet, pour permettre l'extraction du paramètre σ , différents types d'équations peuvent être utilisés pour ajuster les données théoriques aux données expérimentales. De plus, dans la majeure partie des cas, un paramètre de normalisation doit être ajouté pour permettre un bon ajustement des courbes. Cependant ce paramètre de normalisation rend ainsi plus compliqué la comparaison entre différents échantillons, rendant ainsi l'expérience HOESY, dans la majeure partie des cas, uniquement qualitative et non quantitative.

Results and discussion:

Partie 1- Développement d'une procédure automatique d'extraction des paramètres

La première partie de ce travail de thèse fut de développer un code informatique permettant l'extraction du paramètre de vitesse de relaxation croisée entre les noyaux étudiés. Le traitement informatique est automatique et systématique et permet ainsi de comparer les différents taux de relaxation extraits, indépendamment du liquide ionique étudié. Ainsi différents types de liquide ionique, à différentes concentrations en sel de LiFSI, et/ou à différentes température, peuvent être comparés.

Pour extraire le paramètre de vitesse de relaxation croisée, une équation décrivant l'évolution du transfert NOE en fonction de différents paramètres est utilisée (Equation). Cette équation, décrite par Giernoth *et al*, et dérivée des équations de Solomon, prend en considération cinq paramètres, R_H , R_{Li} , M_0 , σ et τ . Les paramètres R_H et R_{Li} correspondent à la vitesse de relaxation des deux spins étudiés (l'hydrogène et le lithium dans ce cas). Le paramètre τ , « le temps de mélange », est intrinsèque à la séquence de pulse RMN et correspond au paramètre de temps pendant lequel le transfert d'aimantation entre les deux spins a lieu. Les deux derniers paramètres correspondent à la vitesse de relaxation croisée σ et au paramètre M_0 considéré ici comme le facteur d'échelle.

Equation 1

$$NOE_{H\{Li\}}(\tau) = M_0 \sigma \frac{2 \sinh(\kappa \tau)}{\kappa} e^{-\frac{(R_{H,1} + R_{Li,1}) \cdot \tau}{2}} \quad \kappa = \sqrt{\frac{R_{(H,1)}^2 - 2R_{H,1} \cdot R_{Li,1} + R_{Li,1}^2 + 4\sigma_{H,Li}^2}{2}}$$

Parmi les quatre paramètres présents dans l'équation ci-dessus, il a déjà été mentionné que le temps de mélange τ est intrinsèque à l'expérience réalisée. Les vitesses de relaxation R des deux différents spins étudiés peuvent être quant à elles extraites des différentes expériences de relaxation réalisées préalablement. Le paramètre M_0 , utilisé classiquement comme facteur d'échelle, est ici utilisé comme facteur de normalisation, pour permettre la comparaison de différents échantillons. En effet, dans ce paramètre est présent le rapport des deux rapports gyromagnétiques, le ratio du nombre de lithiums relativement au nombre de cations, ainsi

Résumé

que l'abondance naturelle du lithium (dans le cas d'un transfert lithium-cation). Ainsi, l'unique variable ajustable reste le taux de relaxation σ .

L'expérience ^1H - ^7Li est donc réalisée à différents temps de mélange, créant ainsi une série de spectres RMN comme présenté en trois dimensions en **Figure a)** présentant pour chaque site hydrogène une courbe croissante puis décroissante, communément appelée « courbe d'accroissement ». La **Figure b)** présente un exemple de courbe d'accroissement extrait dans le cas d'une expérience ^1H - ^7Li HOESY.

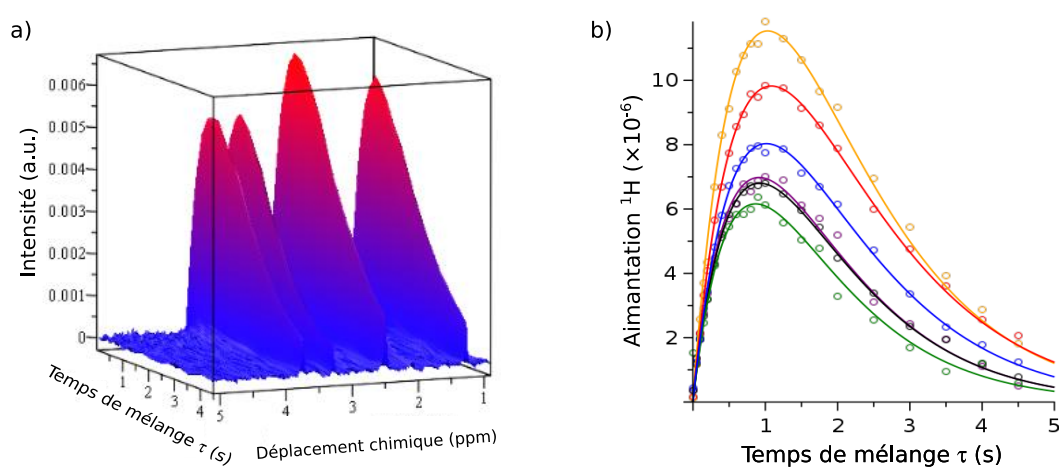


Figure 1 : a) Correspond au plot en trois dimensions d'une expérience ^1H - ^7Li HOESY et en b) les courbes d'accroissement correspondante pour les différents pics.

En utilisant l'Equation , la vitesse de relaxation croisée peut être extraite des courbes d'accroissement pour les différents sites hydrogènes. La Figure représente les différents vitesses de relaxation croisée extraits d'une expérience ^1H - ^7Li HOESY à 50°C réalisée sur l'échantillon 1-propyl-1-méthylpyrrolidinium bis(fluorosulfonyl)imide dopé à 1 molal de LiFSI. Le code couleur indique l'intensité de la vitesse de relaxation croisée extrait pour les différents pics. Sur l'exemple ci-dessous, il peut donc être observé que la vitesse de relaxation croisée est plus intense pour les sites hydrogène les plus éloignés de l'azote central.

Résumé

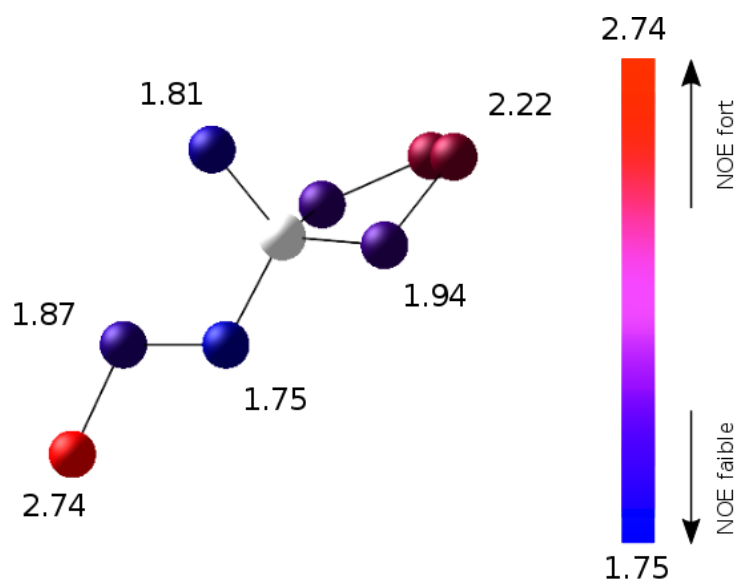


Figure 2: Cation 1-propyl-1-méthylpyrrolidinium avec le code couleur correspondant aux différentes vitesses de relaxation croisée extraites pour chaque site hydrogènes (Les sites hydrogènes sont réduits à leurs sites carbones correspondant)

Partie 2- N-methyl-N-propyl pyrolidinium bis(fluorosulfonyl)imide mélangé au lithium bis(fluorosulfonyl)imide

Les premières expériences HOESY ont été réalisées sur l'échantillon méthyl-N-propyl pyrolidinium bis(fluorosulfonyl)imide mélangé au lithium bis(fluorosulfonyl)imide à différentes concentrations (1 molal et 3,2 molal). Les premiers résultats consistent à comparer l'échantillon C₃mpyr FSI dopé à 1 molal de LiFSI et à deux températures, 20°C et 50°C. Ces résultats montrent que dans le cas de l'étude à 50°C présentée [Figure a\)](#), le lithium semble être plus corrélé avec le groupe méthyle en fin de chaîne, et les groupes CH₂ les plus éloignés de l'azote sur le cycle, plutôt qu'avec les sites hydrogènes proches de l'azote. Les études à 20°C quant à elles, montrent que, à plus faible température, le lithium semble toujours être plus corrélé avec le méthyl en fin de chaîne, et les groupes CH₂ en milieu de cycle. Cependant, dans ce cas le lithium semble être un peu plus corrélé que précédemment aux sites hydrogènes proches de l'azote. Dans un second temps, le même échantillon, C₃mpyrFSI a cette fois-ci été dopé à 3,2 molal de LiFSI. L'étude à deux températures de cet échantillon (20°C et 50°C), a montré des résultats similaires à l'étude à concentration plus faible. Cependant, une affinité croissante aux sites hydrogène les plus proches de l'azote et les sites situés sur le cycle peuvent être observés à plus faible températures et/ou plus fortes concentrations. Ce comportement est attribué à l'augmentation de la viscosité lorsque l'on abaisse la température et/ou augmente la concentration en LiFSI. En effet, dans ces cas, le lithium serait potentiellement plus coordonné avec les groupes FSI, et serait donc contraint de rester dans une position autour du cycle.

Dans l'optique d'avoir une vision plus complète des interactions ioniques dans le liquide, des expériences ¹H-¹⁹F HOESY ont été réalisées. Le processus d'extraction et de conversion des données utilisé, est identique à celui des expériences ¹H-⁷Li HOESY. Dans le cas des expériences ¹H-¹⁹F HOESY, en fonction de la température, des pics de corrélation positifs ou négatifs sont obtenus. Ce résultat était en effet prévisible du à la proximité des fréquences de résonance des deux noyaux étudiés. En [Figure b\)](#), est présenté un exemple de vitesse de relaxation croisée extraits pour l'échantillon C₃mpyr FSI mixé avec 1 molal de LiFSI à 20°C. Dans ce cas, tous les pics de corrélation sont négatifs.

Résumé

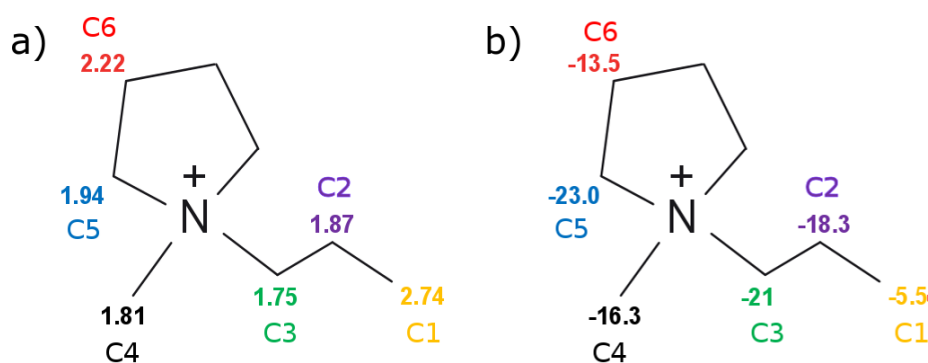


Figure 3: Vitesses de relaxation croisée ($\times 10^{-4} \text{ s}^{-1}$) extrait a) d'une expérience ^1H - ^7Li HOESY à 50°C et b) d'une expérience ^1H - ^{19}F HOESY à 20°C pour l'échantillon $\text{C}_3\text{mpyr FSI}$ mixé avec 1 molal de LiFSI .

La deuxième grande partie de cette étude est de convertir les vitesses de relaxation croisée en distances. Dans ce but, différents modèles permettant de convertir ces taux en distances ont été utilisés. Le premier modèle étudié, correspondant à l'interprétation la plus simpliste de l'effet Overhauser, est extrait des équations standard, dérivées des vitesses de relaxation croisées dipolaire hétéro-nucléaire intramoléculaire. Ce modèle est dérivé pour une paire de spins à une distance fixe, sous l'influence d'un seul mouvement résultant généralement de la diffusion rotationnelle. Le deuxième modèle étudié correspondant au modèle des sphères dures, permet le calcul d'une expression différente de la densité spectrale de l'interaction dipolaire avec seulement deux paramètres, le temps de corrélation translationnel et la distance d'approche minimale entre les deux spins étudiés. Dans ce cas, la vitesse de relaxation croisée est proportionnelle à l'inverse de la distance minimale d'approche. Le dernier modèle étudié, correspond à une théorie développée par Weingärtner *et al* (théorie GSW), utilisant la dynamique translationnelle et la dynamique rotationnelle. Ainsi, une nouvelle expression de la densité spectrale de l'interaction dipolaire entre deux spins peut être calculée, et montre que la fonction n'est désormais plus Lorentzienne, mais s'étend aux plus hautes fréquences. Cette nouvelle expression de la densité spectrale implique un impact important des interactions à longue distance. Cet impact est d'autant plus important que la fréquence de résonance des spins est proche.

Les différents modèles sont étudiés dans le cas des différentes expériences HOESY. Dans le cas des expériences ^1H - ^7Li HOESY, le modèle deux, prenant en considération le cas des sphères dures et des distances d'approche minimale, est retenu. Dans le cas des expériences ^1H - ^{19}F HOESY, dû à la forte proximité des fréquences des spins hydrogène et fluor, le modèle trois basé sur la théorie de Weingärtner *et al*, semble le plus cohérent. Pour tester les différents

Résumé

modèles utilisés, des expériences de dynamique moléculaire sont réalisées. La [Figure 70 a\)](#) représente les vitesses de relaxation croisée extraites des expériences ^1H - ^7Li HOESY, comparées aux distances carbone-lithium extraites de la dynamique moléculaire. L'ordre d'intensité des vitesses de relaxation croisée du plus faible au plus fort, correspondant à la distance de la plus grande à la plus faible, est en bon accord avec l'ordre des distances d'approche extraites de la dynamique moléculaire. Dans le cas des expériences ^1H - ^{19}F HOESY, la valeur absolue des vitesses de relaxation croisée est utilisée (les taux étant négatifs). Les expériences de dynamique moléculaire montrant une inversion des nombres de coordination à distances élevées, les vitesses de relaxation croisée sont comparées à faible et à grande distance ([Figure 70 b](#)). Il est facile d'observer [Figure 70 b](#)) que les vitesses de relaxation croisée sont en meilleur accord avec les nombres de coordination extraits à plus grande distance, confirmant ainsi le choix du troisième modèle, prédisant l'impact majoritaire des corrélations à longue distance.

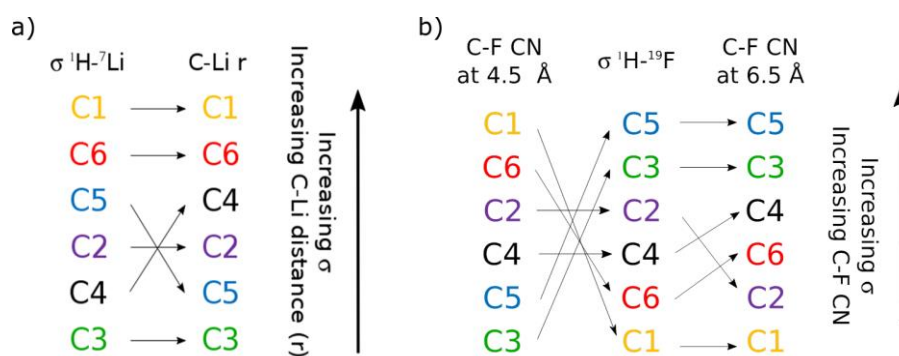


Figure 70: Comparaison des vitesses de relaxation croisée extraites par expérience HOESY et les plus courtes distances d'approche extraites par dynamique moléculaire pour a) les expériences ^1H - ^7Li HOESY, b) les expériences ^1H - ^{19}F HOESY de l'échantillon C_3mpyr FSI à 1m de LiFSI

Partie 3- Influence de la structure cationique du liquide ionique

Il a été démontré que des vitesses de relaxation croisée peuvent être extraites des expériences HOESY, que ce soient des HOESY ^1H - ^7Li ou des HOESY ^1H - ^{19}F . De plus, l'ordre de plus forte intensité des vitesses de relaxation croisée est en accord avec l'ordre des distances d'approche les plus faibles extraites de la dynamique moléculaire. Ainsi, l'influence de la structure cationique sur la proximité des ions peut être étudiée.

Les premiers changements sur la structure du cation constituent à ajouter un site carbone, soit sur la chaîne alkyl, soit dans le cycle. La **Figure a)** représente les vitesses de relaxation croisée extraites dans le cas du cation C_4mpyr . Il peut être observé que, dans ce cas, les σ extraits sont plus intenses en fin de chaîne alkyl et sur le cycle. Ce résultat est similaire à la vitesse de relaxation extraite dans le cas du C_3mpyr , à ceci près que, dans ce cas, les vitesses de relaxation sont aussi importantes sur les sites hydrogène proches de l'azote sur le cycle et du group méthyle fixé sur l'azote. Ce comportement peut être attribué au mouvement de la chaîne alkyl qui pourrait ainsi empêcher l'approche des atomes de lithium, expliquant ainsi la proximité accrue près des sites hydrogène proches de l'azote. La **Figure b)** représente les vitesses de relaxation croisée extraites dans le cas du cation C_3mpip . Dans ce cas, les vitesses de relaxation sont les plus intenses pour le site hydrogène en milieu de cycle et pour le groupement méthyle en fin de chaîne alkyl. Ceci correspond à la même tendance extraite dans le cas du C_3mpyr .

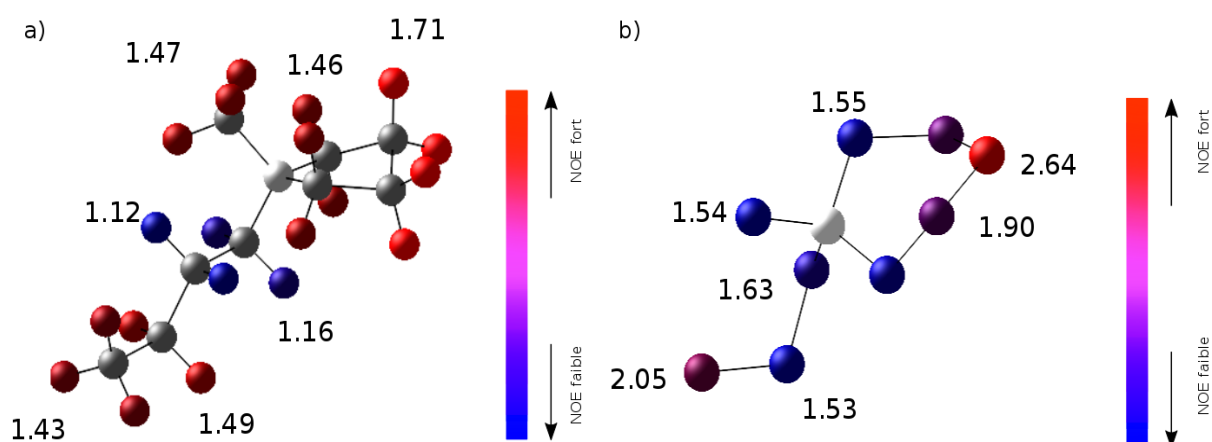


Figure 5: Vitesses de relaxation croisée extraites d'expérience ^1H - ^7Li dans le cas a) du C_4mpyr FSI dopé à 1 molal LiFSI et b) du C_3mpip FSI dopé à 1.1 molal LiFSI

Résumé

Au vu des études sur les cations $C_4\text{mpyr}$ et le $C_3\text{mpip}$ présentant des résultats similaires au cation $C_3\text{mpyr}$, le cation sélectionné pour la suite présente, cette fois-ci, des modifications beaucoup plus importantes. En effet, le dernier cation étudié correspond au 1-méthyl-1-(2-méthoxyéthyl) pyrrolidinium bis(fluorosulfonyl)imide ($C_{201}\text{mpyr}$) mélangé à 1 molal de lithium bis(fluorosulfonyl) imide (LiFSI). Les vitesses de relaxation présentées en [Figure a\)](#) sont extraits d'une expérience ^1H - ^7Li HOESY. Sur cette représentation du cation $C_{201}\text{mpyr}$, il peut être observé que les vitesses de relaxation croisée les plus intenses sont présents uniquement sur les sites hydrogène autour de l'oxygène. Ce comportement peut être expliqué par l'électronégativité de l'oxygène. Ce résultat est intuitif puisqu'on s'attend à ce que le lithium soit repoussé de l'azote portant la charge positive du cation, et en même temps attiré autour de la chaîne à cause de l'électronégativité de l'oxygène. En [Figure b\)](#) l'expérience ^1H - ^{19}F HOESY, quant à elle, présente des vitesses de relaxation croisée similaires au σ extraits pour le cation $C_3\text{mpyr}$. Il est cependant à noter que dans le cas de l'échantillon méthoxy, les σ extraits sont plus intenses d'un ordre de grandeur. Ce changement de tendance peut être potentiellement expliqué par une variation de la dynamique interne, décrite par exemple par la théorie GSW.

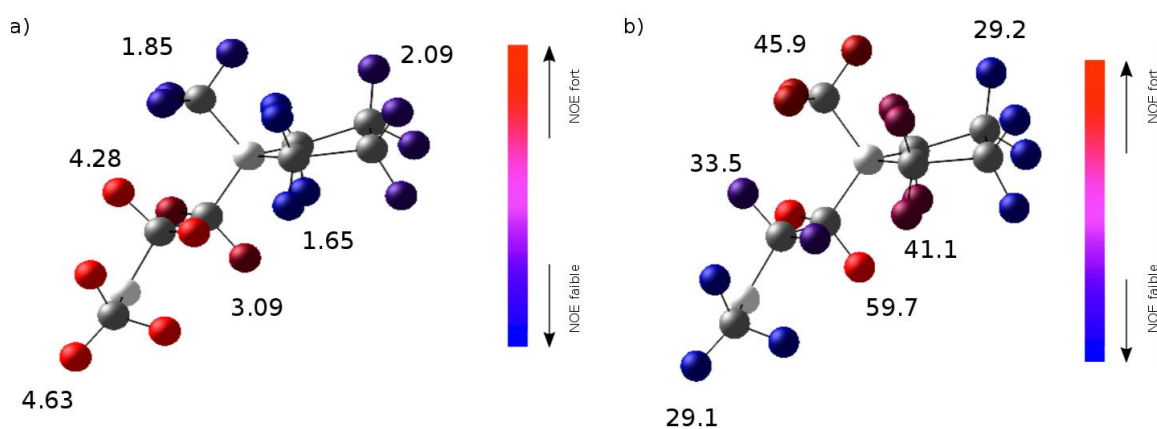


Figure 6: Vitesses de relaxation croisée extraites pour l'échantillon $C_{201}\text{mpyr}$ à 1 molal de LiFSI à 50°C , en a) d'une expérience ^1H - ^7Li HOESY, et en b) d'une expérience ^1H - ^{19}F HOESY. Les vitesses de relaxation croisée sont en $\cdot 10^{-4} \text{ s}^{-1}$ et le code couleur correspond aux intensités relatives des σ extraits.

Les vitesses de relaxation croisée montrent une tendance bien particulière dans le cas du $C_{201}\text{mpyr}$. Nous avons donc décidé, comme pour le cas du $C_3\text{mpyr}$, de comparer la tendance des différentes intensités du σ , à la tendance d'approche la plus faible extraite de la DM dans le cas du ^1H - ^7Li , et des nombres de coordination les plus faibles, dans le cas du ^1H - ^{19}F . Les corrélations entre les expériences HOESY et les expériences de DM sont présentées [Figure 71.a\)](#) pour la corrélation cation-cation, et [Figure 71 b\)](#) pour la corrélation cation-anion. Mieux que

Résumé

pour le cas du cation $C_3\text{mpyr}$, les résultats de DM et les vitesses de relaxation croisée dans le cas ^1H - ^7Li sont en parfait accord. Dans le cas des expériences ^1H - ^{19}F , de même que pour le cas du cation $C_3\text{mpyr}$, les vitesses de relaxation croisée sont en meilleur accord avec les nombres de coordination à plus grande distance (ici 6.5 Å).

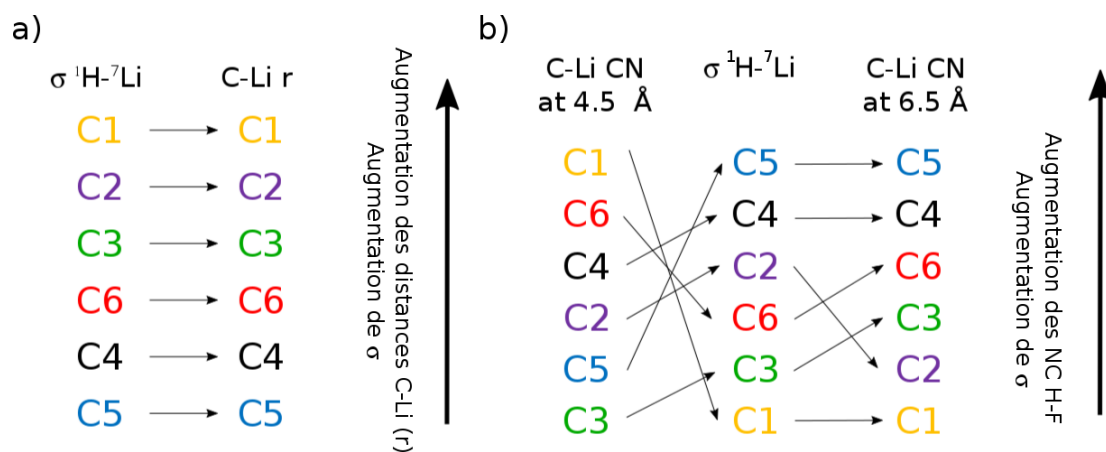


Figure 71: Comparaison des vitesses de relaxation croisée extraits par expérience HOESY et les plus courtes distances d'approches extraites par dynamique moléculaire pour a) les expériences ^1H - ^7Li HOESY, b) les expériences ^1H - ^{19}F HOESY de l'échantillon $C_{201}\text{mpyr}$ FSI à 1m de LiFSI.

Partie 4- Etudes structurales du N-methyl-N-propyl pyrrolidinium bis(fluorosulfonyl)imide mélangé avec du lithium à l'état gelé.

La dernière partie de cette thèse est consacrée à l'étude du premier échantillon, C₃mpyr FSI dopé à 1 molal de LiFSI. Cette étude se porte sur des expériences de polarisation dynamique nucléaire (PDN). La PDN est une technique de RMN complémentaire à l'expérience HOESY. En effet, lors d'une expérience PDN, l'échantillon est refroidi très rapidement, à très basse température (~100K). L'échantillon est donc étudié dans un état gelé, considéré comme un instantané de l'état liquide. De plus, l'ajout d'un biradical dans l'échantillon, couplé à un gyrotron, permet le transfert de la polarisation des spins électroniques aux noyaux voisins. Ainsi, le signal RMN peut être considérablement accru.

Dans l'étude qui suit, des expériences appelées REDOR (Rotational Echo Double Resonance) combinées avec la PDN sont utilisées pour permettre d'étudier les transferts de polarisation entre le lithium et les carbones voisins.

Pour permettre l'extraction des distances, différents spectres à différent temps de déphasage sont acquis, résultant ainsi à une courbe de déphasage. Cette courbe de déphasage peut être ajustée à l'aide de différents modèles, le plus courant étant le « Universal curve fitting ». Cependant, dans notre cas, un autre modèle est utilisé, le « BS-REDOR ». Ce modèle prend en compte différentes variables, mais surtout tient compte de la possibilité d'obtenir plusieurs distances, et leurs probabilités respectives. Le résultat de cette extraction est présenté dans le [Tableau](#) .

Résumé

Tableau 1: Distance carbone-lithium (d_n), la distribution de taille (Δd_n), et leurs fraction relative (f_n), extraites pour chaque site carbone du cation $C_3\text{mpyr}$ après analyse par BS-REDOR.

Carbone	$d_1 / \text{Å}$	$\Delta d_1 / \text{Å}$	f_1	$d_2 / \text{Å}$	$\Delta d_2 / \text{Å}$	f_2
C1	3.55	0.10	0.32	>8	-	0.68
C2	4.00	0.10	0.47	>8	-	0.53
C3	4.55	0.35	0.72	>6	-	0.28
C4	3.85	0.45	0.22	4.90	1.20	0.78
C5	3.50	0.30	0.18	4.75	1.15	0.82
C6	3.60	0.30	0.21	4.70	1.40	0.79

D'après ce résultat, on peut observer que le lithium semble être plus proche des carbones 1, 5 et 6, correspondant au groupement méthyl sur l'azote, au groupe CH_2 sur le cycle proche de l'azote, et au groupe CH_2 sur le cycle le plus loin de l'azote respectivement.

Ces résultats sont comparés à une étude de dynamique moléculaire sur le même système, mais à température ambiante, donc à l'état liquide. Comme présenté en [Figure 72](#), il peut être observé que les probabilités de présence du lithium par rapport au cation $C_3\text{mpyr}$ sont en très bon accord avec la probabilité de présence extraite par dynamique moléculaire. De plus, il est intéressant de noter que puisque les études de dynamique moléculaire ont été réalisées pour le système à l'état liquide, cela confirme l'hypothèse préalable, qui consistait à dire que les études structurales réalisées à froid avec la PDN correspondaient à un instantané de l'état liquide dû à la trempe thermique rapide.

Résumé

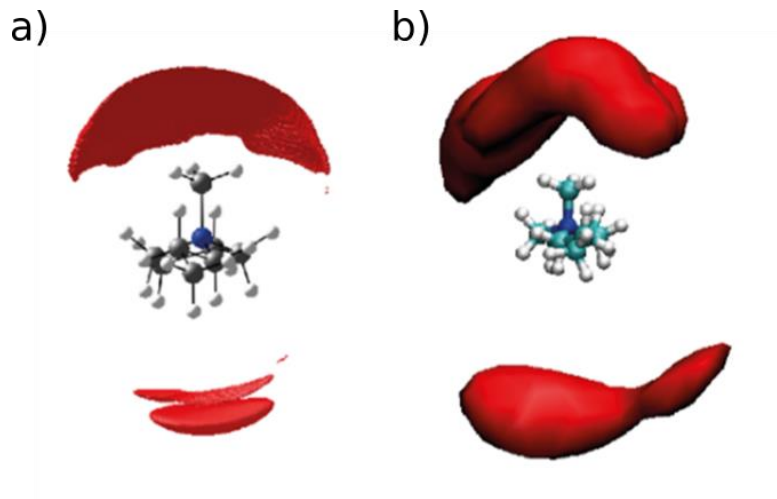


Figure 72: Représentation de la distribution spatiale du lithium autour des cation C₃mpyr construite à partir a) des données extraites des expérience DNP ¹³C-⁶Li REDOR à 92K et b) des données extraites de la dynamique moléculaire à 298K

Conclusion

Ce travail de thèse a permis de développer une nouvelle méthode d'extraction des vitesses de relaxation croisée hétéronucléaire et intramoléculaire des expériences HOESY. Ce code informatique permet d'extraire de façon systématique et automatique les vitesses de relaxation croisée. De plus, par la prise en compte des concentrations de chaque atome, de l'abondance naturelle et de la diffusion, des comparaisons quantitatives des σ peuvent être faites entre les différents échantillons. Ainsi, différentes expériences d'HOESY ont pu être réalisées, entre ^1H - ^7Li ou ^1H - ^{19}F , et ce, sur différents échantillons. Les premières expériences réalisées sur le C_3mpyr FSI mixé à 1 molal de LiFSI, ont permis d'observer la présence du lithium autour du cation C_3mpyr , mais aussi la présence de l'anion FSI autour du cation C_3mpyr . Ainsi, d'après les vitesses de relaxation croisée extraites de ces expériences, le lithium semble avoir plus d'interaction avec les sites hydrogènes les plus éloignés de l'azote central. Ce résultat concorde avec le fait que la charge positive du cation est délocalisée sur cet azote central. L'anion, quant à lui, semble avoir plus d'interaction, autour de cet atome central, ce qui, une fois de plus, concorde avec les prédictions dues à la localisation de la charge positive. La suite de cette étude s'est donc portée sur l'interprétation de ces vitesses de relaxation croisée en termes de distance. Pour ce faire, différents modèles pouvaient être utilisés. Dans le cas des interactions lithium-cation, un modèle basé sur le modèle des sphères dures et des distances d'approche minimale a démontré que les valeurs des différentes vitesses de relaxation croisée pour les différents sites hydrogène sont en accord avec les distances minimales d'approche extraites de la dynamique moléculaire. Dans le cas des interactions cation-anion, (^1H - ^{19}F HOESY), la théorie communément appelée GSW prédit que dans le cas de noyaux à rapports gyromagnétiques similaires, le transfert NOE est majoritairement dû à des interactions à longue distance. Les vitesses de relaxation croisée ont donc été comparées aux nombres des coordinances C-F extraits des expériences de dynamique moléculaire. Ils ont montré un très bon accord pour les nombres de coordinance extraits à plus longue distance. Ainsi, pour étudier l'impact de la structure cationique sur les interactions au sein du liquide,

Résumé

différents types de cation ont été étudiés. Le cation $C_{201}mpyr$, présentant donc un site oxygène sur la chaîne alkyl est celui qui a montré des interactions lithium-cation les plus différentes. En effet, dans ce cas, le lithium semble être localisé à proximité des sites hydrogène les plus proches de l'oxygène. Cette tendance, prévisible et due à l'électronégativité de l'oxygène, a elle aussi été confirmée par les résultats de dynamique moléculaire. La dernière étude de ce travail de thèse consiste à étudier le système C_3mpyr FSI par des expériences de polarisation dynamique nucléaire. Cela présente l'avantage d'étudier l'échantillon dans un état vitrifié, assimilé ainsi à un instantané de la structure du liquide, en ayant un rapport signal sur bruit amplifié grâce au transfert d'aimantation électronique. Cette étude a montré que le lithium semble être dans ce cas majoritairement positionné autour du cycle et du groupement CH_3 situé sur l'azote. Ce comportement, corrélé par la dynamique moléculaire, peut être expliqué par une forte association des ions lithium et des anions. Le lithium, fortement associé à l'anion serait donc contraint de rester dans une position autour de la charge positive du C_3mpyr , en deuxième sphère de coordination.

Conclusion and outlook

Bibliography

- 1 F. Perera, Pollution from Fossil-Fuel Combustion is the Leading Environmental Threat to Global Pediatric Health and Equity: Solutions Exist, *Int. J. Environ. Res. Public Health*, 2017, **15**, 16.
- 2 D. L. Turcotte, G. Schubert and D. L. Turcotte, *Geodynamics*, Cambridge University Press, Cambridge ; New York, 2nd ed., 2002.
- 3 D. O. Akinyele and R. K. Rayudu, Review of energy storage technologies for sustainable power networks, *Sustain. Energy Technol. Assess.*, 2014, **8**, 74–91.
- 4 A. Lewandowski and A. Świdarska-Mocek, Ionic liquids as electrolytes for Li-ion batteries—An overview of electrochemical studies, *J. Power Sources*, 2009, **194**, 601–609.
- 5 D. Bankmann and R. Giernoth, Magnetic resonance spectroscopy in ionic liquids, *Prog. Nucl. Magn. Reson. Spectrosc.*, 2007, **51**, 63–90.
- 6 F. A. Silva, Lithium-Ion Batteries: Fundamentals and Applications [Book News], *IEEE Ind. Electron. Mag.*, 2016, **10**, 58–59.
- 7 Q. Wang, J. Sun and G. Chu, Lithium ion battery fire and explosion, *Fire Saf. Sci.*, 2005, **8**, 375–382.
- 8 R. Hayes, G. G. Warr and R. Atkin, Structure and Nanostructure in Ionic Liquids, *Chem. Rev.*, 2015, **115**, 6357–6426.
- 9 E. J. Maginn, Molecular simulation of ionic liquids: current status and future opportunities, *J. Phys. Condens. Matter*, 2009, **21**, 373101.
- 10 D. Rooney, J. Jacquemin and R. Gardas, in *Ionic Liquids*, ed. B. Kirchner, Springer Berlin Heidelberg, Berlin, Heidelberg, 2009, vol. 290, pp. 185–212.
- 11 K.N Marsh, J.A Boxall and R Lichtenthaler, Room temperature ionic liquids and their mixtures—a review, *Fluid Phase Equilibria*, 2004, **219**, 93–98.
- 12 M. Galiński, A. Lewandowski and I. Stępniań, Ionic liquids as electrolytes, *Electrochimica Acta*, 2006, **51**, 5567–5580.
- 13 J. Wilkes, Properties of ionic liquid solvents for catalysis, *J. Mol. Catal. Chem.*, 2004, **214**, 11–17.
- 14 S. Gabriel and J. Weiner, Ueber einige abkömmlinge des propylamins, *Berichte Dtsch. Chem. Ges.*, 1888, **21**, 2669–2679.
- 15 U. A. Rana, M. Forsyth, D. R. MacFarlane and J. M. Pringle, Toward protic ionic liquid and organic ionic plastic crystal electrolytes for fuel cells, *Electrochimica Acta*, 2012, **84**, 213–222.
- 16 R. P. Swatloski, S. K. Spear, J. D. Holbrey and R. D. Rogers, Dissolution of Cellulose with Ionic Liquids, *J. Am. Chem. Soc.*, 2002, **124**, 4974–4975.
- 17 F. Castiglione, G. B. Appetecchi, S. Passerini, W. Panzeri, S. Indelicato and A. Mele, Multiple points of view of heteronuclear NOE: Long range vs short range contacts in pyrrolidinium based ionic liquids in the presence of Li salts, *J. Mol. Liq.*, 2015, **210**, 215–222.
- 18 I. A. Shkrob, T. W. Marin, Y. Zhu and D. P. Abraham, Why Bis(fluorosulfonyl)imide Is a “Magic Anion” for Electrochemistry, *J. Phys. Chem. C*, 2014, **118**, 19661–19671.
- 19 J. Pitawala, A. Martinelli, P. Johansson, P. Jacobsson and A. Matic, Coordination and interactions in a Li-salt doped ionic liquid, *J. Non-Cryst. Solids*, 2014, **407**, 318–323.

- 20 C. J. F. Solano, S. Jeremias, E. Paillard, D. Beljonne and R. Lazzaroni, A joint theoretical/experimental study of the structure, dynamics, and Li⁺ transport in bis([tri]fluoromethanesulfonyl)imide [T]FSI-based ionic liquids, *J. Chem. Phys.*, 2013, **139**, 034502.
- 21 J. Huang and A. F. Hollenkamp, Thermal Behavior of Ionic Liquids Containing the FSI Anion and the Li⁺ Cation, *J. Phys. Chem. C*, 2010, **114**, 21840–21847.
- 22 K. Hayamizu, S. Tsuzuki, S. Seki, K. Fujii, M. Suenaga and Y. Umebayashi, Studies on the translational and rotational motions of ionic liquids composed of N-methyl-N-propyl-pyrrolidinium (P[_{sub} 13]) cation and bis(trifluoromethanesulfonyl)amide and bis(fluorosulfonyl)amide anions and their binary systems including lithium salts, *J. Chem. Phys.*, 2010, **133**, 194505.
- 23 O. Borodin, W. Gorecki, G. D. Smith and M. Armand, Molecular Dynamics Simulation and Pulsed-Field Gradient NMR Studies of Bis(fluorosulfonyl)imide (FSI) and Bis[(trifluoromethyl)sulfonyl]imide (TFSI)-Based Ionic Liquids, *J. Phys. Chem. B*, 2010, **114**, 6786–6798.
- 24 A. S. Best, A. I. Bhatt and A. F. Hollenkamp, Ionic Liquids with the Bis(fluorosulfonyl)imide Anion: Electrochemical Properties and Applications in Battery Technology, *J. Electrochem. Soc.*, 2010, **157**, A903.
- 25 Y. Umebayashi, T. Mitsugi, K. Fujii, S. Seki, K. Chiba, H. Yamamoto, J. N. Canongia Lopes, A. A. H. Pádua, M. Takeuchi, R. Kanzaki and S. Ishiguro, Raman Spectroscopic Study, DFT Calculations and MD Simulations on the Conformational Isomerism of N -Alkyl- N -methylpyrrolidinium Bis-(trifluoromethanesulfonyl) Amide Ionic Liquids, *J. Phys. Chem. B*, 2009, **113**, 4338–4346.
- 26 A. Martinelli, A. Matic, P. Jacobsson, L. Börjesson, A. Fernicola and B. Scrosati, Phase Behavior and Ionic Conductivity in Lithium Bis(trifluoromethanesulfonyl)imide-Doped Ionic Liquids of the Pyrrolidinium Cation and Bis(trifluoromethanesulfonyl)imide Anion, *J. Phys. Chem. B*, 2009, **113**, 11247–11251.
- 27 M. Matsumiya, S. Suda, K. Tsunashima, M. Sugiya, S. Kishioka and H. Matsuura, Electrochemical behaviors of multivalent complexes in room temperature ionic liquids based on quaternary phosphonium cations, *J. Electroanal. Chem.*, 2008, **622**, 129–135.
- 28 F. Castiglione, M. Moreno, G. Raos, A. Famulari, A. Mele, G. B. Appetecchi and S. Passerini, Structural Organization and Transport Properties of Novel Pyrrolidinium-Based Ionic Liquids with Perfluoroalkyl Sulfonylimide Anions, *J. Phys. Chem. B*, 2009, **113**, 10750–10759.
- 29 K. Tsunashima and M. Sugiya, Physical and electrochemical properties of low-viscosity phosphonium ionic liquids as potential electrolytes, *Electrochem. Commun.*, 2007, **9**, 2353–2358.
- 30 K. Tsunashima, S. Kodama, M. Sugiya and Y. Kunugi, Physical and electrochemical properties of room-temperature dicyanamide ionic liquids based on quaternary phosphonium cations, *Electrochimica Acta*, 2010, **56**, 762–766.
- 31 T. Frömling, M. Kunze, M. Schönhoff, J. Sundermeyer and B. Roling, Enhanced Lithium Transference Numbers in Ionic Liquid Electrolytes, *J. Phys. Chem. B*, 2008, **112**, 12985–12990.
- 32 S. Fukuda, M. Takeuchi, K. Fujii, R. Kanzaki, T. Takamuku, K. Chiba, H. Yamamoto, Y. Umebayashi and S. Ishiguro, Liquid structure of N-butyl-N-methylpyrrolidinium

- bis-(trifluoromethanesulfonyl) amide ionic liquid studied by large angle X-ray scattering and molecular dynamics simulations, *J. Mol. Liq.*, 2008, **143**, 2–7.
- 33 O. Borodin, G. D. Smith and W. Henderson, Li⁺ Cation Environment, Transport, and Mechanical Properties of the LiTFSI Doped N-Methyl- N-alkylpyrrolidinium⁺ TFSI⁻ Ionic Liquids, *J. Phys. Chem. B*, 2006, **110**, 16879–16886.
- 34 O. Borodin and G. D. Smith, Structure and dynamics of N-methyl-N-propylpyrrolidinium bis (trifluoromethanesulfonyl) imide ionic liquid from molecular dynamics simulations, *J. Phys. Chem. B*, 2006, **110**, 11481–11490.
- 35 M. Castriota, T. Caruso, R. G. Agostino, E. Cazzanelli, W. A. Henderson and S. Passerini, Raman Investigation of the Ionic Liquid N-Methyl- N-propylpyrrolidinium Bis(trifluoromethanesulfonyl)imide and Its Mixture with LiN(SO₂CF₃)₂, *J. Phys. Chem. A*, 2005, **109**, 92–96.
- 36 W. A. Henderson and S. Passerini, Phase Behavior of Ionic Liquid–LiX Mixtures: Pyrrolidinium Cations and TFSI⁻ Anions, *Chem. Mater.*, 2004, **16**, 2881–2885.
- 37 I. Nicotera, C. Oliviero, W. A. Henderson, G. B. Appetecchi and S. Passerini, NMR Investigation of Ionic Liquid–LiX Mixtures: Pyrrolidinium Cations and TFSI⁻ Anions, *J. Phys. Chem. B*, 2005, **109**, 22814–22819.
- 38 R. K. Blundell and P. Licence, Quaternary ammonium and phosphonium based ionic liquids: a comparison of common anions, *Phys. Chem. Chem. Phys.*, 2014, **16**, 15278.
- 39 M. L. P. Le, L. Cointeaux, P. Strobel, J.-C. Leprêtre, P. Judeinstein and F. Alloin, Influence of Solvent Addition on the Properties of Ionic Liquids, *J. Phys. Chem. C*, 2012, **116**, 7712–7718.
- 40 S. Fang, Y. Jin, L. Yang, S. Hirano, K. Tachibana and S. Katayama, Functionalized ionic liquids based on quaternary ammonium cations with three or four ether groups as new electrolytes for lithium battery, *Electrochimica Acta*, 2011, **56**, 4663–4671.
- 41 K. Hayamizu, S. Tsuzuki, S. Seki, Y. Ohno, H. Miyashiro and Y. Kobayashi, Quaternary Ammonium Room-Temperature Ionic Liquid Including an Oxygen Atom in Side Chain/Lithium Salt Binary Electrolytes: Ionic Conductivity and ¹H, ⁷Li, and ¹⁹F NMR Studies on Diffusion Coefficients and Local Motions, *J. Phys. Chem. B*, 2008, **112**, 1189–1197.
- 42 H. Matsumoto, H. Sakaebe and K. Tatsumi, Preparation of room temperature ionic liquids based on aliphatic onium cations and asymmetric amide anions and their electrochemical properties as a lithium battery electrolyte, *J. Power Sources*, 2005, **146**, 45–50.
- 43 F. Castiglione, A. Famulari, G. Raos, S. V. Meille, A. Mele, G. B. Appetecchi and S. Passerini, Pyrrolidinium-Based Ionic Liquids Doped with Lithium Salts: How Does Li⁺ Coordination Affect Its Diffusivity?, *J. Phys. Chem. B*, 2014, **118**, 13679–13688.
- 44 Q. Zhou, W. A. Henderson, G. B. Appetecchi, M. Montanino and S. Passerini, Physical and Electrochemical Properties of N-Alkyl- N-methylpyrrolidinium Bis(fluorosulfonyl)imide Ionic Liquids: PY₁₃FSI and PY₁₄FSI, *J. Phys. Chem. B*, 2008, **112**, 13577–13580.
- 45 Y. Saito, T. Umecky, J. Niwa, T. Sakai and S. Maeda, Existing Condition and Migration Property of Ions in Lithium Electrolytes with Ionic Liquid Solvent, *J. Phys. Chem. B*, 2007, **111**, 11794–11802.

- 46 M. Forsyth, J. Huang and D. R. MacFarlane, Lithium doped N-methyl-N-ethylpyrrolidinium bis(trifluoromethanesulfonyl)amide fast-ion conducting plastic crystals, *J. Mater. Chem.*, 2000, **10**, 2259–2265.
- 47 H.-B. Han, S.-S. Zhou, D.-J. Zhang, S.-W. Feng, L.-F. Li, K. Liu, W.-F. Feng, J. Nie and H. Li, Lithium bis(fluorosulfonyl)imide (LiFSI) as conducting salt for nonaqueous liquid electrolytes for lithium-ion batteries: Physicochemical and electrochemical properties, *J. Power Sources*, 2011, **196**, 3623–3632.
- 48 E. Paillard, Q. Zhou, W. A. Henderson, G. B. Appetecchi, M. Montanino and S. Passerini, Electrochemical and Physicochemical Properties of PY[₁₄]FSI-Based Electrolytes with LiFSI, *J. Electrochem. Soc.*, 2009, **156**, A891.
- 49 P. J. Carvalho, S. P. M. Ventura, M. L. S. Batista, B. Schröder, F. Gonçalves, J. Esperança, F. Mutelet and J. A. P. Coutinho, Understanding the impact of the central atom on the ionic liquid behavior: Phosphonium vs ammonium cations, *J. Chem. Phys.*, 2014, **140**, 064505.
- 50 H. Y. Lee, H. Shirota and E. W. Castner, Differences in Ion Interactions for Isoelectronic Ionic Liquid Homologs, *J. Phys. Chem. Lett.*, 2013, **4**, 1477–1483.
- 51 K. Tsunashima, A. Kawabata, M. Matsumiya, S. Kodama, R. Enomoto, M. Sugiya and Y. Kunugi, Low viscous and highly conductive phosphonium ionic liquids based on bis(fluorosulfonyl)amide anion as potential electrolytes, *Electrochem. Commun.*, 2011, **13**, 178–181.
- 52 Krishnan Damodaran, in *Annual Reports on NMR Spectroscopy*, Elsevier, 2016.
- 53 P. Stilbs and I. Furo, Electrophoretic NMR, *Curr. Opin. Colloid Interface Sci.*, 2006, **11**, 3–6.
- 54 M. D. Lingwood and S. Han, in *Annual Reports on NMR Spectroscopy*, Elsevier, 2011, vol. 73, pp. 83–126.
- 55 A. W. Overhauser, Polarization of nuclei in metals, *Phys. Rev.*, 1953, **92**, 411.
- 56 K. Hayamizu, S. Tsuzuki, S. Seki, K. Fujii, M. Suenaga and Y. Umebayashi, Studies on the translational and rotational motions of ionic liquids composed of N-methyl-N-propyl-pyrrolidinium (P13) cation and bis(trifluoromethanesulfonyl)amide and bis(fluorosulfonyl)amide anions and their binary systems including lithium salts, *J. Chem. Phys.*, 2010, **133**, 194505.
- 57 C. R. Pope, M. Kar, D. R. MacFarlane, M. Armand, M. Forsyth and L. A. O'Dell, Ion Dynamics in a Mixed-Cation Alkoxy-Ammonium Ionic Liquid Electrolyte for Sodium Device Applications, *ChemPhysChem*, 2016, **17**, 3187–3195.
- 58 V. V. Matveev, D. A. Markelov, E. A. Brui, V. I. Chizhik, P. Ingman and E. Lähderanta, ¹³C NMR relaxation and reorientation dynamics in imidazolium-based ionic liquids: revising interpretation, *Phys Chem Chem Phys*, 2014, **16**, 10480–10484.
- 59 V. V. Matveev, D. A. Markelov, A. V. Ievlev, E. A. Brui, K. V. Tyutyukin and E. Lähderanta, Molecular mobility in several imidazolium-based ionic liquids according to data of ¹H and ¹³C NMR relaxation: ¹H and ¹³C NMR relaxation in imidazolium-based ionic liquids, *Magn. Reson. Chem.*, 2018, **56**, 140–143.
- 60 M. N. Garaga, M. Nayeri and A. Martinelli, Effect of the alkyl chain length in 1-alkyl-3-methylimidazolium ionic liquids on inter-molecular interactions and rotational dynamics, *J. Mol. Liq.*, 2015, **210**, 169–177.
- 61 J. Keeler, *Understanding NMR Spectroscopy*, 211.

- 62 C. S. Johnson, Diffusion ordered nuclear magnetic resonance spectroscopy: principles and applications, *Prog. Nucl. Magn. Reson. Spectrosc.*, 1999, **34**, 203–256.
- 63 S. Zugmann, M. Fleischmann, M. Amereller, R. M. Gschwind, H. D. Wiemhöfer and H. J. Gores, Measurement of transference numbers for lithium ion electrolytes via four different methods, a comparative study, *Electrochimica Acta*, 2011, **56**, 3926–3933.
- 64 J. H. Wang, Self-Diffusion Coefficients of Water, *J. Phys. Chem.*, 1965, **69**, 4412–4412.
- 65 H. Tokuda, K. Hayamizu, K. Ishii, M. A. B. H. Susan and M. Watanabe, Physicochemical Properties and Structures of Room Temperature Ionic Liquids. 1. Variation of Anionic Species, *J. Phys. Chem. B*, 2004, **108**, 16593–16600.
- 66 H. Tokuda, K. Hayamizu, K. Ishii, M. A. B. H. Susan and M. Watanabe, Physicochemical Properties and Structures of Room Temperature Ionic Liquids. 2. Variation of Alkyl Chain Length in Imidazolium Cation, *J. Phys. Chem. B*, 2005, **109**, 6103–6110.
- 67 H. Tokuda, K. Ishii, M. A. B. H. Susan, S. Tsuzuki, K. Hayamizu and M. Watanabe, Physicochemical Properties and Structures of Room-Temperature Ionic Liquids. 3. Variation of Cationic Structures, *J. Phys. Chem. B*, 2006, **110**, 2833–2839.
- 68 H. Tokuda, S. Tsuzuki, M. A. B. H. Susan, K. Hayamizu and M. Watanabe, How Ionic Are Room-Temperature Ionic Liquids? An Indicator of the Physicochemical Properties, *J. Phys. Chem. B*, 2006, **110**, 19593–19600.
- 69 A. Noda, K. Hayamizu and M. Watanabe, Pulsed-Gradient Spin-Echo ^1H and ^{19}F NMR Ionic Diffusion Coefficient, Viscosity, and Ionic Conductivity of Non-Chloroaluminate Room-Temperature Ionic Liquids, *J. Phys. Chem. B*, 2001, **105**, 4603–4610.
- 70 F. Castiglione, E. Ragg, A. Mele, G. B. Appetecchi, M. Montanino and S. Passerini, Molecular Environment and Enhanced Diffusivity of Li^+ Ions in Lithium-Salt-Doped Ionic Liquid Electrolytes, *J. Phys. Chem. Lett.*, 2011, **2**, 153–157.
- 71 K. Hayamizu, S. Tsuzuki, S. Seki and Y. Umebayashi, Nuclear magnetic resonance studies on the rotational and translational motions of ionic liquids composed of 1-ethyl-3-methylimidazolium cation and bis(trifluoromethanesulfonyl)amide and bis(fluorosulfonyl)amide anions and their binary systems including lithium salts, *J. Chem. Phys.*, 2011, **135**, 084505.
- 72 G. M. A. Girard, M. Hilder, H. Zhu, D. Nucciarone, K. Whitbread, S. Zavorine, M. Moser, M. Forsyth, D. R. MacFarlane and P. C. Howlett, Electrochemical and physicochemical properties of small phosphonium cation ionic liquid electrolytes with high lithium salt content, *Phys Chem Chem Phys*, 2015, **17**, 8706–8713.
- 73 A. Einstein, On the Motion of Small Particles Suspended in Liquids at Rest Required by the Molecular-Kinetic Theory of Heat, 7.
- 74 J. A. Hodgdon and F. H. Stillinger, Stokes-Einstein violation in glass-forming liquids, *Phys. Rev. E*, 1993, **48**, 207–213.
- 75 S. Zugmann, M. Fleischmann, M. Amereller, R. M. Gschwind, H. D. Wiemhöfer and H. J. Gores, Measurement of transference numbers for lithium ion electrolytes via four different methods, a comparative study, *Electrochimica Acta*, 2011, **56**, 3926–3933.
- 76 D. Canet, N. Mahieu and P. Tekely, Heteronuclear Overhauser effect measurements in surfactant systems. 1. The direct estimation of the distance

- between water and the micellar surface, *J. Am. Chem. Soc.*, 1992, **114**, 6190–6194.
- 77 N. Mahieu, P. Tekely and D. Canet, Heteronuclear Overhauser effect measurements in surfactant systems. 3. Average location of water with respect to surfactant polar head in micellized sodium octanoate and sodium dodecanoate, *J. Phys. Chem.*, 1993, **97**, 2764–2766.
- 78 C. Yu and G. C. Levy, Two-dimensional heteronuclear NOE (HOESY) experiments: investigation of dipolar interactions between heteronuclei and nearby protons, *J. Am. Chem. Soc.*, 1984, **106**, 6533–6537.
- 79 I. Furo, P. Mutzenhardt and D. Canet, X-filtered HOESY experiment for detecting intermolecular contact between identical sites, *J. Am. Chem. Soc.*, 1995, **117**, 10405–10406.
- 80 Yves Lingscheid, Sven Arenz and Ralf Giernoth, Heteronuclear NOE Spectroscopy of Ionic Liquids, *ChemPhysChem*, 2012, **13**, 261–266.
- 81 Sonja Gabl, Othmar Steinhauser and Hermann Weingärtner, From Short-Range to Long-Range Intermolecular NOEs in Ionic Liquids: Frequency Does Matter, *Angew. Chem.*, 2013, **125**, 9412–9416.
- 82 P. L. Rinaldi, Heteronuclear 2D-NOE spectroscopy, *J. Am. Chem. Soc.*, 1983, **105**, 5167–5168.
- 83 R. Giernoth, A. Bröhl, M. Brehm and Y. Lingscheid, Interactions in ionic liquids probed by in situ NMR spectroscopy, *J. Mol. Liq.*, 2014, **192**, 55–58.
- 84 I. Solomon, Relaxation processes in a system of two spins, *Phys. Rev.*, 1955, **99**, 559.
- 85 S. R. Heil and M. Holz, A mobility filter for the detection and identification of charged species in complex liquid mixtures by ENMR phase difference spectroscopy, *Angew. Chem. Int. Ed.*, 1996, **35**, 1717–1720.
- 86 M. Holz, O. Lucas and C. Müller, NMR in the presence of an electric current. Simultaneous measurements of ionic mobilities, transference numbers, and self-diffusion coefficients using an NMR pulsed-gradient experiment, *J. Magn. Reson.* 1969, 1984, **58**, 294–305.
- 87 M. Holz, C. Müller, A. M. Wachter, Modification of the pulsed magnetic field gradient method for the determination of low velocities by NMR, *J. Mag. Res.*, 1986, **69**, 108–115
- 88 M. Holz, D. Seiferling, X. Mao, Design of a new electrophoretic NMR probe and its application to ⁷Li and ¹³³Cs mobility studies, *J. Mag. Res.*, 1993, **105**, 90–94
- 89 M. Holz and H. Weingärtner, Calibration in accurate spin-echo self-diffusion measurements using ¹H and less-common nuclei, *J. Magn. Reson.* 1969, 1991, **92**, 115–125.
- 90 K. F. Morris, C. S. Johnson, Mobility-ordered 2D NMR spectroscopy for the analysis of ionic mixtures, *J. Mag. Res.*, 1993, **100**, 67–73
- 91 K. F. Morris and C. S. Johnson Jr, Mobility ordered 2D-NMR spectroscopy, *J. Am. Chem. Soc.*, 1992, **114**, 776–777.
- 92 T. R. Saarinen and C. S. Johnson, High-resolution electrophoretic NMR, *J. Am. Chem. Soc.*, 1988, **110**, 3332–3333.
- 93 M. Gouverneur, J. Kopp, L. van Wüllen and M. Schönhoff, Direct determination of ionic transference numbers in ionic liquids by electrophoretic NMR, *Phys. Chem. Chem. Phys.*, 2015, **17**, 30680–30686.

- 94 M. Kunze, S. Jeong, E. Paillard, M. Schönhoff, M. Winter and S. Passerini, New Insights to Self-Aggregation in Ionic Liquid Electrolytes for High-Energy Electrochemical Devices, *Adv. Energy Mater.*, 2011, **1**, 274–281.
- 95 K. Hayamizu, Y. Aihara, S. Arai and C. G. Martinez, Pulse-Gradient Spin-Echo ^1H , ^7Li , and ^{19}F NMR Diffusion and Ionic Conductivity Measurements of 14 Organic Electrolytes Containing $\text{LiN}(\text{SO}_2\text{CF}_3)_2$, *J. Phys. Chem. B*, 1999, **103**, 519–524.
- 96 M. Bielejewski, M. Giesecke and I. Furó, On electrophoretic NMR. Exploring high conductivity samples, *J. Magn. Reson.*, 2014, **243**, 17–24.
- 97 Z. Zhang and L. A. Madsen, Observation of separate cation and anion electrophoretic mobilities in pure ionic liquids, *J. Chem. Phys.*, 2014, **140**, 084204.
- 98 F. Hallberg, I. Furó, P. V. Yushmanov and P. Stilbs, Sensitive and robust electrophoretic NMR: Instrumentation and experiments, *J. Magn. Reson.*, 2008, **192**, 69–77.
- 99 M. Holz, Electrophoretic Nmr, *Chem. Soc. Rev.*, 1994, **23**, 165–174.
- 100 G. M., S. F. and S. M., Negative effective Li transference numbers in Li salt/ionic liquid mixtures: does Li drift in the “Wrong” direction?, *Phys. Chem. Chem. Phys.*, , DOI:10.1039/C7CP08580J.
- 101 T. Frömling, M. Kunze, M. Schönhoff, J. Sundermeyer and B. Roling, Enhanced Lithium Transference Numbers in Ionic Liquid Electrolytes, *J. Phys. Chem. B*, 2008, **112**, 12985–12990.
- 102 A. W. Overhauser, Polarization of nuclei in metals, *Phys. Rev.*, 1953, **92**, 411.
- 103 T. R. Carver, C. P. Slichter, Polarization of Nuclear spins in metals, *Phys Review*, 1953, **92**, 212–213
- 104 L. F. Pinto, I. Marín-Montesinos, V. Lloveras, J. L. Muñoz-Gómez, M. Pons, J. Veciana and J. Vidal-Gancedo, NMR signal enhancement of >50 000 times in fast dissolution dynamic nuclear polarization, *Chem. Commun.*, 2017, **53**, 3757–3760.
- 105 F. Mentink-Vigier, Ü. Akbey, H. Oschkinat, S. Vega and A. Feintuch, Theoretical aspects of Magic Angle Spinning - Dynamic Nuclear Polarization, *J. Magn. Reson.*, 2015, **258**, 102–120.
- 106 D. Lee, E. Bouleau, P. Saint-Bonnet, S. Hediger and G. De Paëpe, Ultra-low temperature MAS-DNP, *J. Magn. Reson.*, 2016, **264**, 116–124.
- 107 A. Banerjee, A. Dey and N. Chandrakumar, Slow Molecular Motions in Ionic Liquids Probed by Cross-Relaxation of Nuclear Spins During Overhauser Dynamic Nuclear Polarization, *Angew. Chem.*, 2016, **128**, 14976–14981.
- 108 M. H. Levitt, *Spin Dynamics: Basics of Nuclear Magnetic Resonance*, 2001.
- 109 N. Bloembergen, E. M. Purcell and R. V. Pound, Relaxation effects in nuclear magnetic resonance absorption, *Physical Review*, 1948, **73**, 679–712
- 110 J. E. Tanner, Pulsed field gradients for NMR spin-Echo diffusion measurements, *The review of scientific instruments*, 1965, **36**, 1086–1087
- 111 W. A. Anderson and R. Freeman, Influence of a Second Radiofrequency Field on High-Resolution Nuclear Magnetic Resonance Spectra, *J. Chem. Phys.*, 1962, **37**, 85.
- 112 N. E. Heimer, R. E. Del Sesto and W. R. Carper, Evidence for spin diffusion in a ^1H , ^1H -NOESY study of imidazolium tetrafluoroborate ionic liquids, *Magn. Reson. Chem.*, 2004, **42**, 71–75.
- 113 K. E. Kövér and G. Batta, Strong coupling effects and their suppression in two-dimensional heteronuclear NOE experiments, *J. Magn. Reson.* 1969, 1987, **74**, 397–405.

- 114K. E. Kövér and G. Batta, Sensitivity-Enhanced 2D heteronuclear NOE spectroscopy. Two-to threefold improved S/N ratio at quaternary carbons in the miemi experiment, *J. Magn. Reson.* 1969, 1988, **79**, 206–210.
- 115K. E. Kövér and G. Batta, Suppression of direct peaks in two-dimensional heteronuclear NOE spectra. Sensitivity-enhanced detection of weak indirect and relay peaks, *Magn. Reson. Chem.*, 1988, **26**, 181–184.
- 116B. Lix, F. D. Sönnichsen and B. D. Sykes, The role of transient changes in sample susceptibility in causing apparent multiple-quantum peaks in HOESY spectra, *J. Magn. Reson. A*, 1996, **121**, 83–87.
- 117T. M. Alam, D. M. Pedrotty and T. J. Boyle, Modified, pulse field gradient-enhanced inverse-detected HOESY pulse sequence for reduction of t1 spectral artifacts, *Magn. Reson. Chem.*, 2002, **40**, 361–365.
- 118E. Pettersson, I. Furó and P. Stilbs, On experimental aspects of electrophoretic NMR: Experimental Electrophoretic NMR, *Concepts Magn. Reson. Part A*, 2004, **22A**, 61–68.
- 119J. Schaefer, “Development of REDOR rotational-echo double-resonance NMR” by Terry Gullion and Jacob Schaefer [*J. Magn. Reson.* 81 (1989) 196–200], *J. Magn. Reson.*, 2011, **213**, 421–422.
- 120T. Gullion, Measurement of dipolar interactions between spin-12 and quadrupolar nuclei by rotational-echo, adiabatic-passage, double-resonance NMR, *Chem. Phys. Lett.*, 1995, **246**, 325–330.
- 121P.-A. Martin, F. Chen, M. Forsyth, M. Deschamps and L. A. O’Dell, Correlating Intermolecular Cross-Relaxation Rates with Distances and Coordination Numbers in Ionic Liquids, *J. Phys. Chem. Lett.*, 2018, **9**, 7072–7078.
- 122M.-A. Sani, P.-A. Martin, R. Yunis, F. Chen, M. Forsyth, M. Deschamps and L. A. O’Dell, Probing Ionic Liquid Electrolyte Structure via the Glassy State by Dynamic Nuclear Polarization NMR Spectroscopy, *J. Phys. Chem. Lett.*, 2018, 1007–1011.
- 123A. Belmajdoub, N. Mahieu, P. Tekely and D. Canet, Heteronuclear Overhauser effect measurements in surfactant systems. 2. Evidence of solvent penetration into micelles in a nonaqueous medium, *J. Phys. Chem.*, 1992, **96**, 1011–1013.
- 124C. Chiappe, A. Sanzone, D. Mendola, F. Castiglione, A. Famulari, G. Raos and A. Mele, Pyrazolium- versus Imidazolium-Based Ionic Liquids: Structure, Dynamics and Physicochemical Properties, *J. Phys. Chem. B*, 2013, **117**, 668–676.
- 125K. Fujii, S. Seki, S. Fukuda, R. Kanzaki, T. Takamuku, Y. Umebayashi and S. Ishiguro, Anion Conformation of Low-Viscosity Room-Temperature Ionic Liquid 1-Ethyl-3-methylimidazolium Bis(fluorosulfonyl) Imide, *J. Phys. Chem. B*, 2007, **111**, 12829–12833.
- 126T. Yamaguchi, K. Mikawa, S. Koda, N. Serizawa, S. Seki, K. Fujii and Y. Umebayashi, Effects of Lithium Salts on Shear Relaxation Spectra of Pyrrolidinium-Based Ionic Liquids, *J. Phys. Chem. B*, 2012, **116**, 7322–7327.
- 127M. G. Del Pópolo and G. A. Voth, On the Structure and Dynamics of Ionic Liquids, *J. Phys. Chem. B*, 2004, **108**, 1744–1752.
- 128S. Gabl, C. Schröder, D. Braun, H. Weingärtner and O. Steinhauser, Pair dynamics and the intermolecular nuclear Overhauser effect (NOE) in liquids analysed by simulation and model theories: Application to an ionic liquid, *J. Chem. Phys.*, 2014, **140**, 184503.
- 129L.-P. Hwang and J. H. Freed, Dynamic effects of pair correlation functions on spin relaxation by translational diffusion in liquids, *J. Chem. Phys.*, 1975, **63**, 4017.

- 130Y. Ayant, E. Belorizky, J. Aluzon and J. Gallice, Calcul des densités spectrales résultant d'un mouvement aléatoire de translation en relaxation par interaction dipolaire magnétique dans les liquides, *J. Phys.*, 1975, **36**, 991–1004.
- 131D. Kruk, R. Meier, A. Rachocki, A. Korpała, R. K. Singh and E. A. Rössler, Determining diffusion coefficients of ionic liquids by means of field cycling nuclear magnetic resonance relaxometry, *J. Chem. Phys.*, 2014, **140**, 244509.
- 132B. Halle, Theory of intramolecular spin relaxation by translational diffusion in locally ordered fluids: I. continuum diffusion versus discrete-state exchange in systems with planar interfaces, *Mol. Phys.*, 1984, **53**, 1427–1461.
- 133B. Halle, Theory of intramolecular spin relaxation by translational diffusion in locally ordered fluids: II. Further results for systems with planar interfaces, *Mol. Phys.*, 1985, **56**, 209–221.
- 134B. Halle, Theory of intramolecular spin relaxation by translational diffusion in locally ordered fluids: III. Cylindrical interfaces, *Mol. Phys.*, 1987, **60**, 319–370.
- 135B. Halle, Cross-relaxation between macromolecular and solvent spins: The role of long-range dipole couplings, *J. Chem. Phys.*, 2003, **119**, 12372.
- 136K. Modig, E. Liepinsh, G. Otting and B. Halle, Dynamics of Protein and Peptide Hydration, *J. Am. Chem. Soc.*, 2004, **126**, 102–114.
- 137H. Weingärtner, NMR studies of ionic liquids: Structure and dynamics, *Curr. Opin. Colloid Interface Sci.*, 2013, **18**, 183–189.
- 138R. Hayes, S. Imberti, G. G. Warr and R. Atkin, Effect of Cation Alkyl Chain Length and Anion Type on Protic Ionic Liquid Nanostructure, *J. Phys. Chem. C*, 2014, **118**, 13998–14008.
- 139A. Zagdoun, G. Casano, O. Ouari, M. Schwarzwälder, A. J. Rossini, F. Aussenac, M. Yulikov, G. Jeschke, C. Copéret, A. Lesage, P. Tordo and L. Emsley, Large Molecular Weight Nitroxide Biradicals Providing Efficient Dynamic Nuclear Polarization at Temperatures up to 200 K, *J. Am. Chem. Soc.*, 2013, **135**, 12790–12797.
- 140K. T. Mueller, Analytic solutions for the time evolution of dipolar-dephasing NMR signals, *J. mag. Res.*, 1995, **113**, 81–93
- 141J. D. Gehman, F. Separovic, K. Lu and A. K. Mehta, Boltzmann Statistics Rotational-Echo Double-Resonance Analysis, *J. Phys. Chem. B*, 2007, **111**, 7802–7811.
- 142J. L. Klepeis, K. Lindorff-Larsen, R. O. Dror and D. E. Shaw, Long-timescale molecular dynamics simulations of protein structure and function, *Curr. Opin. Struct. Biol.*, 2009, **19**, 120–127.
- 143M. Brinkötter, G. A. Giffin, A. Moretti, S. Jeong, S. Passerini and M. Schönhoff, Relevance of ion clusters for Li transport at elevated salt concentrations in [Pyr₁₂₀₁][FTFSI] ionic liquid-based electrolytes, *Chem. Commun.*, 2018, **54**, 4278–4281.

Pierre MARTIN

Etude de l'interaction entre les ions dans des électrolytes à base de liquides ionique par résonance magnétique nucléaire

Ce travail de thèse porte sur l'étude d'électrolytes pour utilisation dans des systèmes de stockage énergétiques tels que les batteries lithium-ions. Les matériaux spécifiques à cette étude sont des liquides ioniques à base de pyrrolidinium avec le fluorosulfonylimide (FSI) en tant que contre-ion, le tout dopé au lithium.

La méthode de caractérisation principale est la spectroscopie par Résonance Magnétique Nucléaire (RMN) qui peut être utilisée pour résoudre la structure, la dynamique ou encore l'arrangement spatial entre les anions et les cations. Des mesures de diffusion et des expériences de relaxation réseau-spin, utilisant ^1H pour les cations, ^{19}F pour les anions et ^7Li , sont effectuées pour étudier le transport ionique dans le liquide ainsi que la rotation moléculaire respective des différents ions.

Toutefois, dans le but de mieux comprendre le mécanisme de transport des ions à un niveau moléculaire dans ces liquides ioniques, l'expérience Heteronuclear Overhauser Effect Spectroscopy (HOESY) a été employée. Cette technique est basée sur le transfert d'aimantation entre deux isotopes nucléaires dans l'espace. Puisque le transfert est généralement dû à des interactions de courtes portées, des informations concernant les différentes proximités des espèces dans le liquide sont obtenues.

Une grande partie de cette étude est concentrée sur le développement de la technique HOESY elle-même, avec l'amélioration de la séquence d'impulsion RMN mais aussi de l'analyse du signal, dans l'optique d'une étude quantitative et du développement d'une procédure automatique et systématique d'ajustement des données théoriques aux données expérimentales. Des simulations par Dynamique Moléculaire (DM) et des mesures de relaxation RMN sont utilisées pour permettre l'analyse des expériences HOESY, permettant alors d'accéder à la corrélation des distances entre les noyaux et des paramètres de relaxation tels que les temps de corrélation, pouvant permettre une meilleure compréhension du transport ionique. En plus du développement de cette technique, de nouveaux liquides ioniques incluant des chaînes alkyles plus longues, des cycles plus longs ou encore un groupe ethero-alkyle sur la chaîne alkyle sont étudiés par HOESY dans le but d'observer l'impact de la structure du cation sur les interactions ioniques. Une autre technique complémentaire, la polarisation dynamique nucléaire, est aussi adoptée afin d'étudier les liquides ioniques dans un état vitreux imitant leur structure à l'état liquide.

Mots clés : Liquides ioniques, RMN, HOESY

Studies of the interactions between ions in ionic liquids electrolytes by nuclear magnetic resonance

This work is focused on the study of electrolytes for energy storage devices such as lithium ion batteries. The specific materials are pyrrolidinium-based ionic liquid electrolytes with bis-fluorosulfonylimide (FSI) as the counter anion, and also containing lithium.

The main experimental method of characterization is Nuclear Magnetic Resonance (NMR) spectroscopy, which can be used to probe structure, dynamics and spatial arrangements between anions and cations. NMR-based diffusion measurements or spin lattice relaxation experiments, using ^1H for cations, ^{19}F for anions and ^7Li , are used to study the ionic transport in the liquid and the molecular tumbling of the different ions respectively.

However, in order to attempt to better understand the ion transport mechanism at the molecular level in these ionic liquids, the HOESY (Heteronuclear Overhauser Effect Spectroscopy) experiment is used. This technique is based on a transfer of magnetization through space between two different nuclear isotopes. As this transfer is generally mediated by short-range interactions, it provides information on which species are close together in the liquid.

A large part of this work is based on the development of the HOESY technique itself, both improving the implementation of the NMR pulse sequence to reduce the experimental time, but also improving ways to analyze the resulting data in a quantitative way and developing an automatic and systematic data fitting procedure. Molecular Dynamics (MD) simulations and NMR relaxation measurements are also used to assist the HOESY analysis, allowing correlations with distances between nuclei and motional parameters such as correlation times to be established, which will lead to a better understanding of the ion interactions. In addition to this technique development, others ionic liquids including longer alkyl, longer cycle or even an ether-o-alkyl group on the alkyl chain, are studied by HOESY in order to observe the impact of the cation structure on the ionic interactions. Another complementary technique, dynamic nuclear polarization, is also used in order to study the ionic liquid in the glassy state structure which mimics the liquid state.

Keywords : Ionic liquids, NMR, HOESY



CEMHTI-UPR3079 CNRS
1D avenue de la Recherche Scientifique
45071 Orléans Cedex 2

